



**US Army Corps
of Engineers**
Waterways Experiment
Station

Technical Report GL-97-3
April 1997

Development of an Analysis System for Discontinuities in Rigid Airfield Pavements

by Michael I. Hammons

Approved For Public Release; Distribution Is Unlimited

DTIC QUALITY INSPECTED 3

The contents of this report are not to be used for advertising, publication, or promotional purposes. Citation of trade names does not constitute an official endorsement or approval of the use of such commercial products.



PRINTED ON RECYCLED PAPER

Technical Report GL-97-3
April 1997

Development of an Analysis System for Discontinuities in Rigid Airfied Pavements

by Michael I. Hammons

U.S. Army Corps of Engineers
Waterways Experiment Station
3909 Halls Ferry Road
Vicksburg, MS 39180-6199

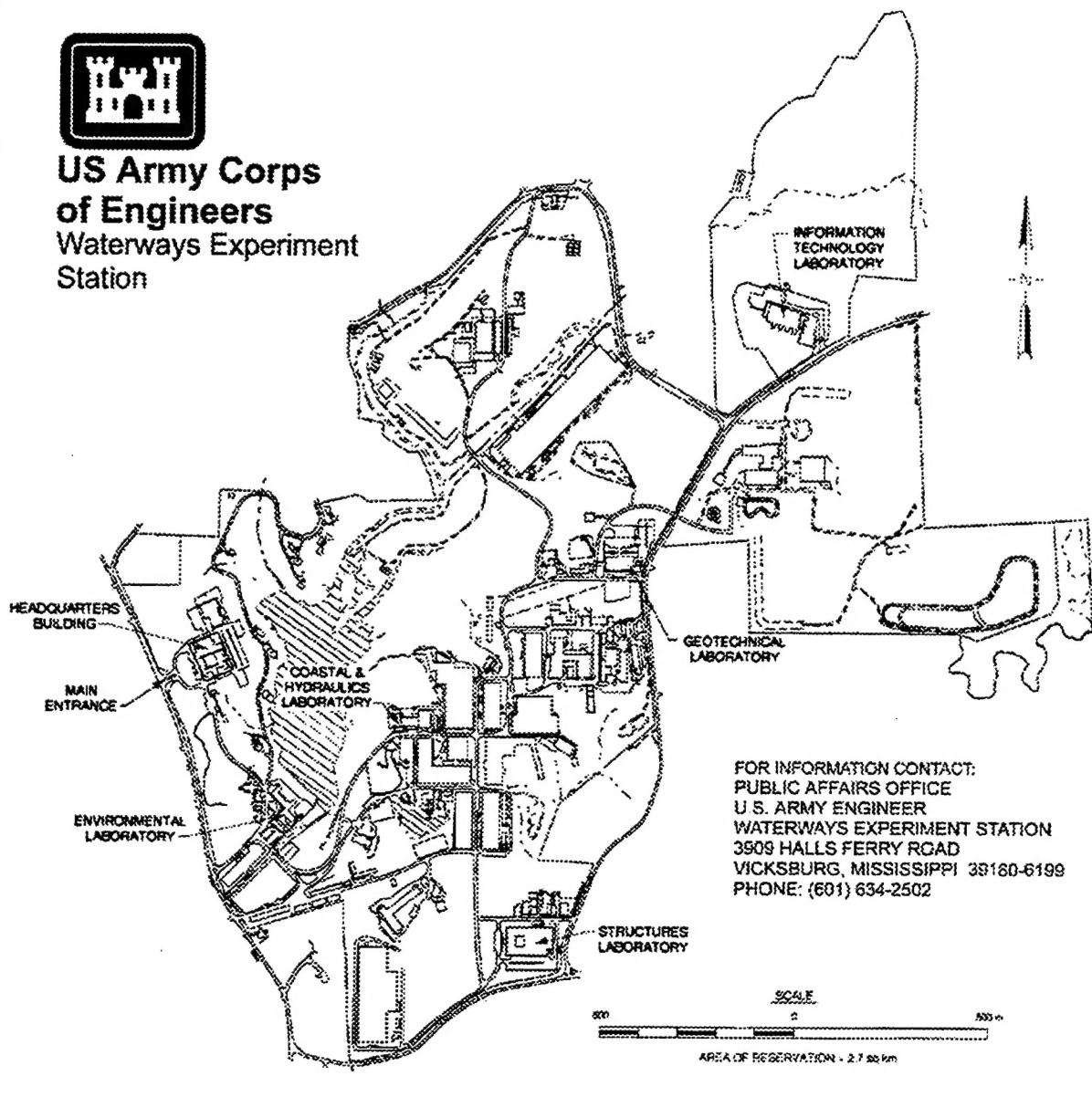
Final report

Approved for public release; distribution is unlimited

DTIC QUALITY INSPECTED 3



**US Army Corps
of Engineers**
Waterways Experiment
Station



Waterways Experiment Station Cataloging-in-Publication Data

Hammons, Michael I.

Development of an analysis system for discontinuities in rigid airfield pavements / by Michael I. Hammons ; prepared for U.S. Department of Transportation, Federal Aviation Administration.

332 p. : ill. ; 28 cm. — (Technical report ; GL-97-3)

Includes bibliographic references.

1. Runways (Aeronautics) — Mathematical models. 2. Dowels. 3. Finite element method.
- I. United States. Army. Corps of Engineers. II. U.S. Army Engineer Waterways Experiment Station. III. Geotechnical Laboratory (U.S. Army Engineer Waterways Experiment Station)
- IV. United States. Dept. of Transportation. V. United States. Federal Aviation Administration.
- IV. Title. VII. Series: Technical report (U.S. Army Engineer Waterways Experiment Station) ; GL-97-3.

TA7 W34 no. GL-97-3

TABLE OF CONTENTS

LIST OF TABLES	iv
LIST OF FIGURES	v
PREFACE	xii
CHAPTER	
1 INTRODUCTION	1
Background	1
Objectives	3
Scope	3
2 PROBLEM STATEMENT	5
Rigid Pavement System	5
Load Transfer Definitions	8
Load Transfer Mechanisms	9
Rigid Pavement Foundations	10
3 HISTORICAL DEVELOPMENTS	12
Response Model	14
Critical Design Stresses	14
Accelerated Trafficking Tests	15
Subgrade Characterization	17
Rigid Pavement Joints	19
Summary	25
4 CLASSICAL RESPONSE MODELS	27
Westergaard Theory	27
Response charts	28
Computerized solutions	29
Westergaard theory limitations	30
Elastic Layer Models	31
Models for Dowel Stresses	33
Westergaard-Type Solution for Load Transfer	38
5 FINITE ELEMENT RESPONSE MODELS	43
2D Finite Element Models	43
ILLI-SLAB models	45
3D Finite Element Models	58
GEOSYS model	58
ABAQUS models	60
6 SMALL-SCALE PHYSICAL MODEL STUDIES	64
Single-Slab Models	64
Test description	64
Test results and analysis	67

Doweled Joint Models	70
Test description	70
Test results	73
Analysis	73
7 FINITE ELEMENT RESPONSE AND SENSITIVITY STUDIES	78
Background	78
Purpose of sensitivity studies	78
Description of ABAQUS	79
Isoparametric element considerations	80
Element Descriptions	86
2D element description	86
3D element description	89
Example Problems for Sensitivity Studies	91
Interior Load Case I	91
Interior Load Case II	93
Interior Load Case III	94
Edge Load Case I	96
Edge Load Case II	96
Response and Sensitivity Study Results	99
Interior Load Case I	99
Interior Load Case II	110
Interior Load Case III	112
Edge Load Case I	114
Edge Load Case II	118
Jointed Rigid Pavement Models	127
Representation of Joint Stiffness	129
Example Problem	135
Contact Surfaces	143
Summary	147
8 EXPERIMENTS ON LABORATORY-SCALE PAVEMENT MODELS	151
Introduction	151
Experimental Plan	151
Materials	153
Concrete materials	155
Cement-stabilized base materials	156
Dowels	160
Model Construction	161
Base course construction	163
Slab construction	165
Loading	168
Instrumentation	169
Experimental Results	170
Materials	171
Experiment LSM-1	181
Experiment LSM-2	198
Experiment LSM-3R	201
Experiment LSM-4	208

Experiment LSM-5	210
Comparison of Experimental Results	217
9 ANALYTICAL MODEL DEVELOPMENT AND VERIFICATION	225
Analytical Model Description	225
Analytical Model Results	228
Case I	228
Case II	232
Case III	237
Case IV	243
Case V	247
Slab/Base Interaction and Joint Response	248
10 CONCLUSIONS AND RECOMMENDATIONS	255
Conclusions	255
Recommendations	257
REFERENCES	260
APPENDIXES	
A STRAIN PLOTS FROM 1950S MODEL TESTS	266
B TABULATED JOINT RESPONSES FROM 1950S MODEL TESTS	276
C ALGORITHM FOR ASSIGNING SPRING STIFFNESSES TO NODES USING ABAQUS "JOINTC" OPTION	286
D COMPILED INSTRUMENTATION TRACES FROM EXPERIMENTS	289
E SAMPLE ABAQUS INPUT FILE	313

LIST OF TABLES

3.1. Summary of Corps of Engineers Load Transfer Measurements For Full-Scale Test Sections and In-Service Pavements (Rollings 1989)	20
5.1. Overview of Finite Element Models for Rigid Pavements	44
6.1. Small-Scale Dowelled Joint Model Test Parameters	71
6.2. Backcalculated Dowelled Joint Response Parameters	75
7.1. Description of ABAQUS 2D Shell Elements Used in Sensitivity Study	88
7.2. Description of ABAQUS 3D Hexahedral Elements Used in Sensitivity Study	90
7.3. Results of 2D Convergence Study, Interior Load Case I	100
7.4. Results of 3D Convergence Study, Interior Load Case I	104
7.5. Results of Convergence Study, Interior Load Case II	112
7.6. Material and Structural Parameters, Jointed Slabs-on-Grade Example Problem	136
8.1. Laboratory-Scale Experiment Matrix	152
8.2. Concrete Mixture Proportions	156
8.3. Concrete Mixture Evaluation	156
8.4. Typical Physical Model Construction Schedule	163
8.5. Results of Tests on Cement-Stabilized Base	172
8.6. Results of Tests on Fresh Portland Cement Concrete	174
8.7. Results of Tests on Hardened Portland Cement Concrete	175
9.1. Considerations for Model Development	226
9.2. Experimental Model Parameters	229
9.3. Experimental Model Parameters for Base	235

LIST OF FIGURES

2.1. Typical rigid pavement system (after Larralde and Chen 1985)	6
2.2. Concept of load transfer	7
3.1. Dowel installations at Lockbourne and Sharonville test tracks	22
4.1. Friberg's (1940) analysis of dowel bar support	36
4.2. Loss of dowel-concrete interaction stiffness with increasing displacement (after Channakeshava, et al. 1993)	38
4.3. Variation of deflection load transfer efficiency with dimensionless joint stiffness and dimensionless load size ratio	41
4.4. Relationship between deflection and stress load transfer efficiencies with dimensionless load size ratio	42
5.1. Four-node plate bending element	45
5.2. Finite element model in ILLI-SLAB (after Tabatabaie 1978)	47
5.3. Equivalent sections for a two-layer system (after Korovesis 1990)	49
5.4. ILLI-SLAB joint models (after Larralde and Chen 1985)	50
5.5. Joint efficiency as a function of dimensionless joint stiffness for aggregate interlock joint (after Ioannides and Korovesis 1990)	51
5.6. Joint efficiency as a function of dimensionless joint stiffness for doweled joint (after Ioannides and Korovesis 1992)	53
5.7. Foundation displacement under a loaded plate for Winkler and elastic solid foundations (after Majidzadeh et al. 1981)	54
5.8. Vlasov or Plasternak foundation (after Kerr 1993)	56
5.9. Kerr foundation model (after Kerr 1993)	58
6.1. Photograph of small-scale physical models test setup	66
6.2. Edge loading deflection contours from small-scale model study (after Carlton and Behrman 1956)	68
6.3. Comparison of edge loading deflection basins from experiment and ILLI-SLAB	69

6.4. Typical small-scale dowel joint test slab showing approximate strain gage positions	72
6.5. Backcalculated dimensionless joint stiffness from small-scale model tests	76
6.6. Backcalculated modulus of dowel reaction from small-scale model tests	77
7.1. Interpolation functions, 2D Lagrangian isoparametric element	83
7.2. Interpolation functions, 2D serendipity isoparametric element	84
7.3. System configuration, Interior Load Case I	92
7.4. System configuration, Interior Load Case II	94
7.5. System configuration, Interior Load Case III	95
7.6. System configuration, Edge Load Case I	97
7.7. System configuration, Edge Load Case II	98
7.8. Definition of element dimensions for determining mesh fineness	101
7.9. Finite element meshes in plane of slab surface, Interior Load Case I	102
7.10. Finite element meshes in plane of slab thickness, Interior Load Case I	105
7.11. Dimensionless bending stress, Interior Load Case I	106
7.12. Dimensionless deflection, Interior Load Case I	107
7.13. CPU time, selected 3D runs, Interior Load Case I	108
7.14. Dimensionless bending stress summary, Interior Load Case I	109
7.15. Dimensionless deflection summary, Interior Load Case I	110
7.16. Finite element meshes in plane of slab surface, Interior Load Case II	111
7.17. Finite element meshes in plane of slab surface, Interior Load Case III	113
7.18. Stress ratio, Interior Load Case III	114
7.19. Deflection ratio, Interior Load Case III	115
7.20. Finite element meshes in plane of slab surface, Edge Load Case I	116
7.21. Dimensionless bending stress, Edge Load Case I	118

7.22. Summary of 2D and 3D runs, dimensionless bending stress, Edge Load Case I	119
7.23. Finite element meshes in plane of slab surface, Edge Load Case II	120
7.24. Dimensionless bending stress, default transverse shear stiffness, Edge Load Case II	121
7.25. Dimensionless bending stress, 100 times default transverse shear stiffness, Edge Load Case II	122
7.26. Dimensionless deflection, default transverse shear stiffness, Edge Load Case II	123
7.27. Dimensionless deflection, 100 times default transverse shear stiffness, Edge Load Case II	124
7.28. Effect of slab width to depth ratio on edge stresses	125
7.29. Finite element distribution of $\tau_x h^2/p$ through slab thickness	126
7.30. Theoretical and experimental dimensionless bending stress from small-scale model studies	128
7.31. Ratio of theoretical to experimental bending stress from small-scale model studies	129
7.32. Simply-supported beam problem to test JOINTC element	134
7.33. Results from simply-supported beam with JOINTC elements	135
7.34. Finite element mesh for 2D jointed rigid pavement model	138
7.35. Bending stresses predicted by 2D finite element model of a jointed pavement	139
7.36. Comparison of joint response parameters, 2D finite element model	140
7.37. Comparison of bending stresses predicted by 2D and 3D finite element models of a jointed pavement	142
7.38. Comparison of 3D finite element model with closed-form solution, dimensionless joint stiffness versus deflection load transfer efficiency	143
7.39. Comparison of 3D finite element model with closed-form solution, stress load transfer efficiency versus deflection load transfer efficiency	144
7.40. Example of over constraint for contact problem	147

7.41. Simply-supported beam problem to test contact interaction features of ABAQUS	148
7.42. Results from simply-supported beam with contact and friction	149
8.1. Test configurations for laboratory scale models	154
8.2. Grain size distribution of sand/silica flour blend	158
8.3. Moisture-density curves for cement-stabilized sand/silica flour blend	159
8.4. Compressive strength test results on cement-stabilized sand/silica flour blend compacted to maximum density	160
8.5. Dowel locations	161
8.6. Photograph of completed reaction box	162
8.7. Photograph of adjustable screed/compaction device	164
8.8. Installation of polyethylene film in reaction box	166
8.9. Placement of thin sand layer	166
8.10. Bond breaker and doweled joint just prior to concrete placement	167
8.11. Test setup for plate bearing test on rubber pad	178
8.12. Bearing stress-displacement data from plate bearing test on rubber block in load control	179
8.13. Corrected plate bearing stress	181
8.14. Bearing stress-displacement data from plate bearing test on rubber block in displacement control	182
8.15. Instrumentation plan, Experiment LSM-1A	183
8.16. Loading history, Experiment LSM-1A	184
8.17. Posttest photograph, Experiments LSM-1A and LSM-1B	185
8.18. Raw and corrected displacement data from LVDTs positioned perpendicular to edge, Experiment LSM-1A	187
8.19. Raw and corrected displacement data from LVDTs positioned parallel to edge, Experiment LSM-1A	188

8.20. Analytical relationship between modulus of subgrade reaction and deflection from ABAQUS models, Experiment LSM-1A	189
8.21. Comparison of experimental and analytical deflection basin profiles perpendicular to edge, Experiment LSM-1A	190
8.22. Comparison of experimental and analytical deflection basin profiles parallel to edge, Experiment LSM-1A	191
8.23. Instrumentation plan, Experiment LSM-1B	192
8.24. Loading history, Experiment LSM-1B	193
8.25. Raw and corrected displacement data from LVDTs, Experiment LSM-1B	195
8.26. Analytical relationship between modulus of subgrade reaction and deflection from ABAQUS models, Experiment LSM-1B	196
8.27. Comparison of experimental and analytical deflection basin profiles, Experiment LSM-1B	197
8.28. Loading history, Experiment LSM-2	198
8.29. Instrumentation plan, Experiments LSM-2, -3R, -4, and -5	200
8.30. Posttest photograph of slab top surface, Experiment LSM-2	201
8.31. Series of photographs in vicinity of joint, Experiment LSM-2	202
8.32. Selected deflection basin profiles, Experiment LSM-2	203
8.33. Loading history, Experiment LSM-3R	204
8.34. Posttest photograph of top surface of slabs, Experiment LSM-3R	205
8.35. Selected photographs of joint region during testing, Experiment LSM-3R	206
8.36. Selected deflection basin profiles, Experiment LSM-3R	207
8.37. Loading history, Experiment LSM-4	209
8.38. Posttest photograph of top surface of slabs, Experiment LSM-4	210
8.39. Selected photographs of joint region during testing, Experiment LSM-4	211
8.40. Selected deflection basin profiles, Experiment LSM-4	212
8.41. Loading history, Experiment LSM-5	213

8.42. Posttest photograph of top surface of slabs, Experiment LSM-5	214
8.43. Selected photographs of joint region during testing, Experiment LSM-5	215
8.44. Selected deflection basin profiles, Experiment LSM-5	216
8.45. Load-deflection curves from experiments, loaded side of joint	217
8.46. Load-deflection curves from experiments, unloaded side of joint	218
8.47. Deflection load transfer efficiencies from experiments	219
8.48. Effectiveness of slab end restraint	222
9.1. Analytical model case descriptions	227
9.2. Finite element model, Case I	230
9.3. Raw and corrected displacements, Experiment LSM-2	232
9.4. Experimental and analytical deflection basin profiles, Experiment LSM-2	233
9.5. Comparison of experimental deflection load transfer efficiency with analytical value, Experiment LSM-2	233
9.6. Finite element model, Cases II, III, IV, and V	234
9.7. Comparison of experimental deflection load transfer efficiency with analytical value, Experiment LSM-3R	236
9.8. Experimental and analytical deflection basin profiles, Experiment LSM-3R	237
9.9. Variation of analytical deflection load transfer efficiency with joint stiffness, Case II	238
9.10. Variation of analytical deflection load transfer efficiency with changes in aggregate interlock in cracked base, Case III	239
9.11. Postulated shift in analytical curve due to direct bearing in joint, Case III	241
9.12. Experimental and analytical deflection basin profiles, Experiment LSM-4	242
9.13. Variation of analytical deflection load transfer efficiency with friction between base course and slab, Case IV	243
9.14. Vertical deflection profiles along edge illustrating gap between slab and base, Case IV	244

9.15. Gap opening between slab and base, Case IV	245
9.16. Horizontal deflection profiles along edge illustrating slip between slab and base, Case IV	246
9.17. Relative slip between slab and base, Case IV	247
9.18. Experimental and analytical deflection basin profiles, Experiment LSM-5	248
9.19. Variation of analytical deflection load transfer efficiency with friction between base course and slab and aggregate interlock across crack, Case V	249
9.20. Comparison of joint responses from Cases III and V	250
9.21. Comparison of joint responses from Cases III, IV, and V	251
9.22. Comparison of joint responses from finite element models and experiments	252
9.23. Possible implications of slab/base interaction on joint performance	253

PREFACE

The research reported herein was sponsored by the U.S. Department of Transportation, Federal Aviation Administration (FAA), Airport Technology Branch, under Interagency Agreement DTFA03-94-X-00010 with the Airfields and Pavements Division (APD), Geotechnical Laboratory (GL), U.S. Army Engineer Waterways Experiment Station (WES), Vicksburg, MS. Dr. Xiaogong Lee, Airport Technology Branch, FAA, was technical monitor. Dr. Satish Agrawal is Manager, Airport Technology Branch, FAA.

This study was conducted under the general supervision of Dr. W. F. Marcuson III, Director, GL, Dr. G. M. Hammitt II, former Chief, APD, Mr. T. W. Vollor, Chief, Materials Analysis Branch, APD, Dr. R. S. Rollings, APD, and Dr. A. J. Bush, Acting Chief, APD. Direct supervision was provided by Mr. T. W. Vollor. Dr. Michael I. Hammons was the project principal investigator and author of this report. APD personnel engaged in the laboratory testing include Messrs. Bill Grogan and Dennis Mathews and Ms. Donna Day. Messrs. Billy Neeley, Dan Wilson, and Cliff Gill, Concrete and Materials Division (CMD), Structures Laboratory (SL), WES, also participated in the laboratory testing. This report was submitted to and accepted by the Graduate School at Louisiana State University as Dr. Hammons' dissertation.

Director of WES during the preparation and publication of this report was Dr. Robert W. Whalin. Commander was COL Bruce K Howard, EN.

The contents of this report are not to be used for advertising, publication, or promotional purposes. Citation of trade names does not constitute an official endorsement or approval for the use of such commercial products.

CHAPTER 1: INTRODUCTION

BACKGROUND

The commercial aviation industry has responded to increased demand for air travel by developing longer, wider, and heavier aircraft with complex, multiple-wheeled landing gear to support the aircraft while in ground operation. In order to maximize usable space for passengers and cargo as well as to reduce weight aircraft designers are developing landing gear layouts that are quite different from those on previous commercial aircraft. A new generation of such aircraft debuted in 1995 with the introduction of the Boeing B-777. The 2,630-kN (592,000-lb) B-777 features only two main landing gear assemblies, each in a triple-tandem configuration. New generation aircraft may precipitate the requirement for adjustments to airport pavement thickness to ensure serviceable pavements over design lives of 20, 30, or even 40 years.

Many design criteria in use today by the Federal Aviation Administration (FAA) for rigid airport pavement thickness design have their origin in research conducted by the U.S. Army Corps of Engineers between 1941 and 1955. These criteria are based upon theoretical studies, small-scale model studies, full-scale accelerated traffic tests, and various other field studies, including monitoring of performance of in-service rigid airport pavements (Hutchinson 1966). However, since 1955 aircraft landing gear geometry has become more complex as loads have continued to increase. In the 1970s a series of accelerated traffic tests were conducted to verify extrapolations beyond the original experimental database for specific loads and conditions (Ahlvin 1971). Recent development of new generation aircraft has caused

some concerns regarding the adequacy and applicability of current methods of structural design for airport pavements.

The response model which forms the basis for the FAA rigid pavement design procedure is the Westergaard idealization. In 1926 Westergaard developed a method for computing the response of rigid pavement slabs-on-grade subject to wheel loads by modeling the pavement as a thin, infinite or semi-infinite plate resting on a bed of springs (Winkler foundation) (Westergaard 1926). Although available Westergaard solutions have been used extensively, they are limited by two significant shortcomings: (1) only a single slab panel is accommodated in the analysis; therefore, load transfer at joints is not accounted for, and (2) the layered nature of the pavement foundation is not explicitly reflected in the Winkler foundation model. Multi-layered linear elastic models, as used in the new FAA design method released in 1995 (Federal Aviation Administration 1995), consider the complete layered system in the vertical direction, thereby addressing the second limitation. In the horizontal direction, however, the layers are assumed to be infinitely long with no discontinuities such as edges or joints. Consequently, the load transfer limitation remains unresolved.

Advances in electronic computing have revolutionized modern society, and the practice of engineering has benefitted from much of this revolution. The finite element modeling technique has matured as a powerful and efficient analysis tool for boundary value problems in engineering. For over twenty years pavement engineers have realized the potential of three-dimensional (3D) finite element analyses of jointed concrete pavements. The slab-joint-foundation system for a rigid pavement is 3D in nature; thus, comprehensive representation of this system requires a 3D analytical approach.

OBJECTIVES

The primary research objectives of this study were the following:

- Review currently-available rigid pavement models with particular emphasis on their joint and foundation modeling capabilities.
- Using modern analytical methods, analyze the yet unpublished scale-model studies on two-slab panel models with doweled joints performed by the U. S. Army Corps of Engineers Rigid Pavement Laboratory in the 1950s.
- Obtain data on the behavior of the rigid pavement slab-joint-foundation system by conducting scale-model studies of jointed rigid pavement slabs on cement-stabilized bases.
- Develop a comprehensive 3D finite element model of the rigid pavement slab-joint-foundation system that can be implemented in the advanced pavement design concepts currently under development by FAA.

SCOPE

This study offers a significant advancement in the state of the art for rigid pavement analysis by moving in the direction of a more comprehensive 3D finite element response model for rigid pavements. However, it is important that our perspective include the historical developments that have given rise to the current technology. Therefore, a survey of the problem addressed by this research along with the definitions of the fundamental joint response metrics for rigid airfield pavements are presented in Chapter 2 followed in Chapter 3 by a synopsis of the historical background for the current FAA rigid pavement design criteria. In Chapters 4 and 5 classical and finite element response models germane to this research are reviewed. Chapter 6 contains an analysis of doweled joint response data from small-scale model tests conducted in the 1950s by the Corps of Engineers. Chapter 7 describes in detail a comprehensive two-dimensional (2D) and 3D finite element response and sensitivity study for the

jointed rigid pavement problem. Experiments on laboratory-scale jointed rigid pavement models are described and their results presented in Chapter 8. These experimental results are used in Chapter 9 to verify the development of a comprehensive 3D finite element analysis procedure for discontinuities in rigid airfield pavements. Finally, conclusions and recommendations from this research are found in Chapter 10.

The Westergaard idealization layered elastic analysis, and finite element programs based on two-dimensional (2D) elements have proven to be useful tools in the design and analysis of rigid pavements. It is not likely that 3D finite element models will summarily replace these techniques in the near future. However, several very important physical processes cannot be adequately modeled without the 3D approach; furthermore, recent developments in engineering mechanics are best suited for 3D applications. Comprehensive 3D modeling provides a more fundamental understanding of certain aspects of pavement response that can be incorporated into the design process.

Although very important in understanding the overall response and performance of rigid pavement systems, environmental loadings were not considered as a part of this study. However, future studies including such effects could use the results of this study as a basis for research.

CHAPTER 2: PROBLEM STATEMENT

RIGID PAVEMENT SYSTEM

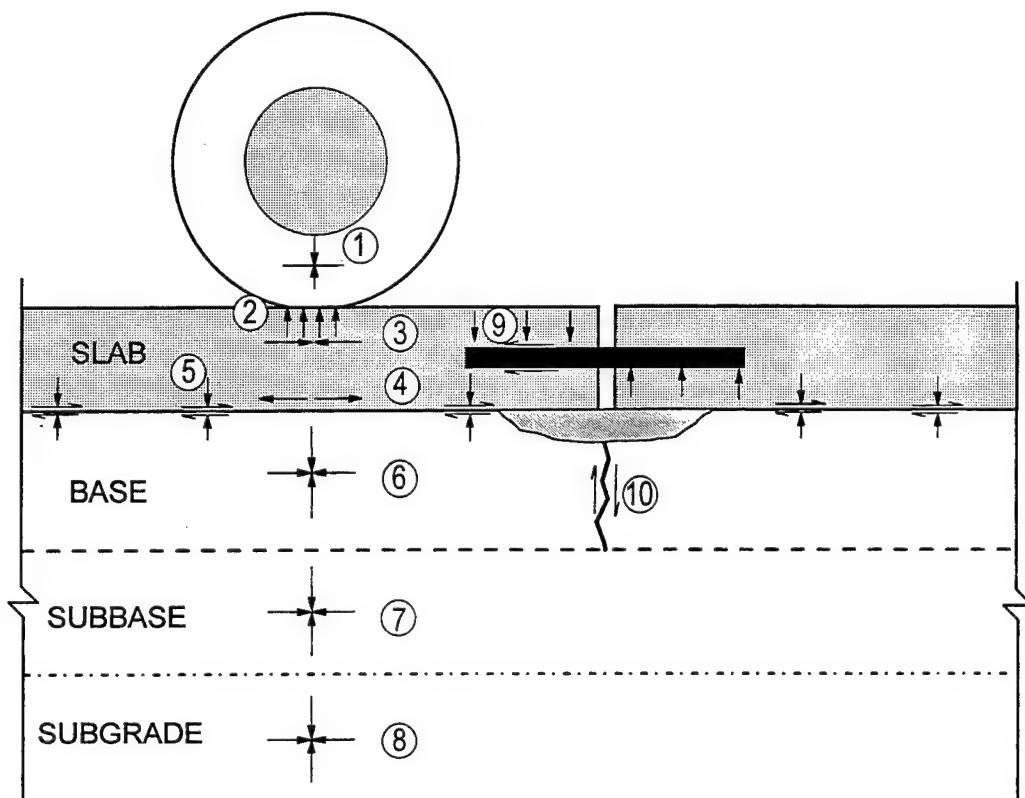
A rigid pavement system consists of a number of portland cement concrete slabs, finite in length and width, over one or more foundation layers. Figure 2.1 shows a representation of a typical rigid pavement system subjected to a static loading. When a slab-on-grade is subjected to a wheel load, it develops bending stresses and distributes the load over the foundation. The response of these finite slabs is controlled by joint or edge discontinuities. By their nature joints weaken the structural system. Thus, the response and effectiveness of joints are primary concerns in rigid pavement analysis and design.

Figure 2.2 presents a conceptual view of the mechanism of load transfer at a joint. The concept of load transfer is very simple: stresses and deflections in a loaded slab are reduced if a portion of the load is transferred to an adjacent slab. Load transfer is very important and fundamental to the FAA rigid pavement design procedure. A complex mechanism, load transfer varies with concrete pavement temperature, age, moisture content, construction quality, magnitude and repetition of load, and type of joint.

When a joint is capable of transferring load, statics dictates that the total load (P) must be equal to the sum of that portion of the load supported by the loaded slab (P_L) and the portion of the load supported by the unloaded slab (P_U), i.e.,

$$P_L + P_U = P \quad (2.1)$$

Load may be transferred across a joint by shear or bending moments. However, it has been commonly argued that load transfer is primarily caused by vertical shear and that moment transfer is negligible. In either case, the following relationship applies:



1. Tire Pressure
2. Bearing Stresses Caused by Tire
3. Flexural Stresses (Compression)
4. Flexural Stresses (Tension)
5. Stresses at the Slab-Base Interface
6. Vertical and Horizontal Stresses (Base)
7. Vertical and Horizontal Stresses (Subbase)
8. Vertical and Horizontal Stresses (Subgrade)
9. Stresses at Concrete-Dowel Interface
10. Stresses at Crack in Stabilized Base

Figure 2.1. Typical rigid pavement system (after Larralde and Chen 1985)

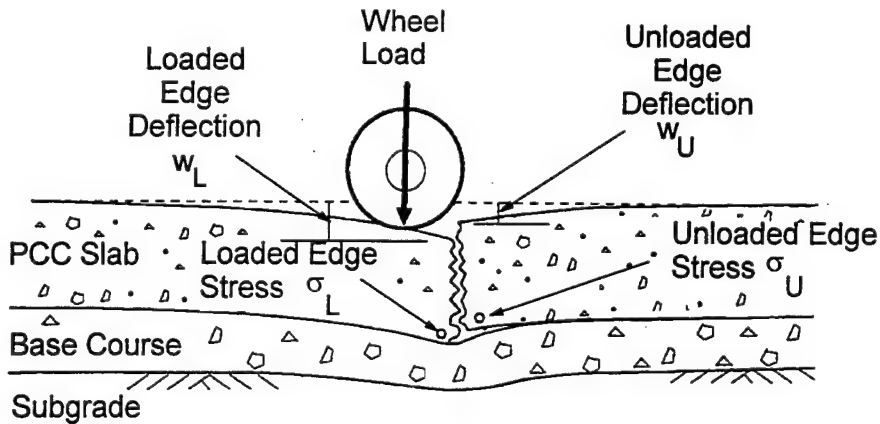


Figure 2.2. Concept of load transfer

$$\sigma_L + \sigma_U = \sigma_f \quad (2.2)$$

where

σ_L = maximum bending stress in the loaded slab

σ_U = maximum bending stress in the adjacent unloaded slab

σ_f = maximum bending stress for the free edge condition (no load transfer)

Likewise,

$$w_L + w_U = w_f \quad (2.3)$$

where

w_L = maximum edge deflection of the loaded slab

w_U = maximum edge deflection of the adjacent unloaded slab

w_f = maximum free edge deflection (no load transfer)

LOAD TRANSFER DEFINITIONS

Deflection load transfer efficiency (LTE_{δ}) is defined as the ratio of the deflection of the unloaded slab to the deflection of the loaded slab as follows:

$$LTE_{\delta} = \frac{w_U}{w_L} \quad (2.4)$$

Similarly, stress load transfer efficiency (LTE_{σ}) is defined as the ratio of the edge bending stress in the unloaded slab to edge stress in the loaded slab as follows:

$$LTE_{\sigma} = \frac{\sigma_U}{\sigma_L} \quad (2.5)$$

Load transfer (LT) in the FAA rigid pavement design procedure is defined as that portion of the edge stress that is carried by the adjacent unloaded slab:

$$\begin{aligned} LT &= \left(\frac{\sigma_U}{\sigma_f} \right) = \left(\frac{\sigma_f - \sigma_L}{\sigma_f} \right) \\ &= \left(1 - \frac{\sigma_L}{\sigma_f} \right) \end{aligned} \quad (2.6)$$

LT is commonly expressed as a percentage. It should be noted from the above equations that the ranges of LTE_{δ} and LTE_{σ} are from zero to one, while the range of LT is from zero to one half. Equation 2.6 can be related to Equation 2.5 as follows:

$$LT = \frac{LTE_{\sigma}}{1 + LTE_{\sigma}} \quad (2.7)$$

The FAA design criteria prescribe $LT = 0.25$, effectively reducing the design stress and allowing a reduced slab thickness. This accepted value is primarily based upon observations from experimental pavements trafficked from the mid-1940s to the mid-1950s. If the load

transfer requirement is violated through a degradation of the joint system, the pavement life can be significantly reduced.

LOAD TRANSFER MECHANISMS

Load transfer at joints is accomplished by three primary load transfer mechanisms: dowel bars, aggregate interlock, and keyways. Dowel bars are often placed across a joint to provide load transfer through dowel action and to maintain slab alignment. Dowels are smooth, round bars with bond intentionally broken on one end to allow limited horizontal movement of the slabs. Aggregate interlock is a load transfer mechanism that relies on shear forces developed at the rough interface of a concrete pavement joint. These shear forces are caused by mechanical interlock between the rough vertical surfaces of the joint and by sliding friction. Specially designed keyways may be formed in adjacent slabs at a joint to augment load transfer caused by aggregate interlock. The dimensions of the keyway depend upon the slab thickness.

Deformed steel bars, often called tie bars, can be placed across the joint (normal to the plane of the joint) to hold the slab faces in intimate contact. Bond between the concrete and bar develops in both slabs; thus, movement normal to the joint is restrained. Diameter, length, and spacing of tie bars is prescribed by the FAA design criteria. Load transfer due to dowel action of tie bars is small in comparison to that provided by dowel bars.

The three major types of joints are contraction joints, construction joints, and expansion joints. Contraction joints, used to control cracking in the concrete and to limit curling and warping stresses in the slab, are formed by introducing a weakened plane into the concrete and allowing a crack to form at the weakened plane. Typically, the weakened plane is created by sawing a groove in the concrete while it is curing. Contraction joints may be plain (often called dummy joints), doweled, or tied (often called hinged joints). Construction joints

are required between lanes of paving or where it is necessary to stop construction within a paving lane. The two most common types of load transfer devices in construction joints are dowels and keyways. Expansion joints are used at the intersections of pavements with structures, and in some cases, within pavements. Their primary purpose is to relieve compressive stresses induced by expansion of the concrete caused by temperature and moisture changes. Expansion joints may be doweled or thickened edge. To obtain load transfer at an expansion joint, a load transfer device is required (usually a dowel bar).

RIGID PAVEMENT FOUNDATIONS

The slabs may be placed directly on the subgrade; however, most current practice has slabs placed on an unbound or a bound base course. Such base course layers in airport pavements may be constructed to (a) provide uniform bearing support for the pavement slab; (b) replace soft, highly compressible or expansive soils; (c) protect the subgrade from frost effects; (d) produce a suitable surface for operating construction equipment; (e) improve foundation strength; (f) prevent subgrade pumping; and (g) provide drainage of water from under the pavement. An unbound base course may be a densely graded granular material or an open-graded or free-draining granular material. The base may be bound with portland cement, a lime-fly ash blend, bitumen, or other agent.

One or more subbases may be present in the pavement system. These subbases may be a lesser quality granular material and may be chemically stabilized. The subbase provides additional strength to the pavement system, provides more uniform support over variable soil conditions, and may provide protection against frost damage and swelling.

The subgrade is the naturally occurring soil, compacted naturally occurring soil, or compacted fill. It may be subject to pumping, frost damage, or swelling. Subgrade soils will

have very different values of strength depending on the soil classification, moisture conditions, and compaction.

CHAPTER 3: HISTORICAL DEVELOPMENTS

Many of the design criteria in use by the FAA for rigid airport pavements have their origin in research conducted by the U.S. Army Corps of Engineers between 1941 and 1955 (Hutchinson 1966). When the Corps was assigned responsibility for design and construction of military airfields in November, 1940, two major problems became immediately apparent. First, new heavy bomber aircraft, such as the B-17 Flying Fortress and B-24 Liberator, had maximum gross weights of 333 kN (75,000 lb) and produced single-wheel main gear loadings of 156 kN (35,000 lb), three to five times greater than any highway or airfield loadings previously encountered. The second problem was a lack of rational and valid design procedures by which rigid pavements could be designed to carry loads of these magnitudes (Sale and Hutchinson 1959). These problems were exacerbated during and after World War II as the demands upon rigid pavements continued to increase due to the development of ever heavier bomber aircraft including the propeller-driven B-29 and B-36 as well as the B-47 and B-52 jet bomber aircraft.

The technical issues faced by the early Corps' researchers were formidable. Many of the basic principles of airport pavement design accepted today concerning pavement response, design loadings, critical stresses, materials characterization, and others were not yet established in 1940. Among these technical questions were the following:

- What is an appropriate response model for rigid airfield pavements?
- What are the critical stresses that the pavement must be designed to resist?
- How should the subgrade be characterized for design? What type of tests should be conducted to characterize the support provided by the subgrade?

- Which loading is more severe: static loadings generated by fully loaded aircraft at rest or dynamic loadings which occur at the point of touchdown during landing operations?
- What effects do joints have on rigid pavement response and how should these be accommodated in design criteria?
- How can pavements be designed to resist repeated heavy loads over a given design life?
- What is an appropriate failure criteria?
- What is the effect of aircraft wander?

To provide answers for these questions, the Corps embarked on an investigational program in 1941 with a four-tiered approach involving theoretical studies, small-scale model studies, full-scale accelerated test track and miscellaneous field studies, and condition surveys of existing rigid airfield pavements.

A review of the available design methodologies revealed that substantial variations existed in design criteria from agency to agency. Design methodologies commonly used by state agencies or foreign governments relied heavily on local experience, materials, and empiricisms developed from performance records within the agency's purview. It was apparent that research was required to develop criteria that could be universally applied for all conditions that might be encountered, whether in the United States or abroad. The criteria needed to be simple, practical, and uniform. The objectives of the investigational program, as stated by Sale and Hutchinson (1959), were as follows: (a) eliminate the use of untried methods; (b) insure adequately designed pavements; (c) provide methods not subject to variation occasioned by arbitrary cost differences of local competitive materials; (d) avoid reductions in pavement thickness in order to balance costs; and (e) establish procedures that would readily lend themselves to further development through tests, investigations, and study of actual

pavement behavior. From these studies criteria were developed for plain and reinforced concrete pavements as well as rigid and flexible overlays.

RESPONSE MODEL

One of the first requirements in developing design criteria was to adopt an appropriate response model for rigid pavements. The theory of Professor Harald Malcolm Westergaard (1926) proved to approximate the observed response of rigid pavements. Westergaard assumed the slab to be a thin plate, the load to be circular, and the subgrade to be a bed of springs. By 1941 Westergaard's method of calculating stresses was considered to be the most advanced method for predicting critical stresses and deflections in rigid pavements and was adopted by the Corps as the response model for design (Sale 1977). Although Westergaard considered the interior, corner, and edge loading cases in his early works, he concentrated on interior loadings. It was not until 1948 that he published relationships that were valid for computation of stresses caused by large wheel loads on large contact areas at the edge of slabs (Westergaard 1948).

CRITICAL DESIGN STRESSES

In 1941 the Corps began a series of static and dynamic load tests on concrete slabs at Wright Field, Dayton, Ohio, in part to verify Westergaard's theory for airfield rigid pavement design (Sale and Hutchinson 1959). A set of 6 m (20 ft) square slabs was constructed on a number of subgrades of different strengths and tested to failure under static circular plate loadings. Also, dynamic loadings were generated by dropping loaded aircraft tires onto the pavement. The test slabs were instrumented with strain and deflection gages. The basic conclusions from these tests were that the Westergaard formula accurately predicted the critical stresses at structural failure, and dynamic loadings produced no greater stresses than equivalent static loadings.

The Wright Field Slab Tests conclusively demonstrated that edge and corner stresses were more critical than interior stresses. In 1942 and 1943 additional traffic tests at six airfields further confirmed that the interior load case was nonconservative without modification. Thus the design procedure produced by the Corps in 1943 included an empirically determined "design factor" of 1.75 to accommodate the differences in allowable interior and edge loadings and the effect of fatigue resulting from repetitive loadings (Sale 1977). The 1943 criteria also required load transfer devices or thickened edges at all construction and expansion joints in an attempt to enforce a "balanced" design between the stresses at the interior and edge (Ahlvin 1991).

Tests with B-26 aircraft were conducted in 1941 at Dayton Municipal Airport, Ohio, to determine whether impact loadings during landing were more critical than static loadings. The runway was dusted with lime so that the width of the tread mark of the B-26 tire could be accurately measured at point of touchdown. The width of these tread marks was correlated with the dynamic loading drop tests at Wright Field to estimate the magnitude of impact loadings. The results of the Dayton tests came as quite a surprise to those who had argued that dynamic loading at landing would be the critical load case. Under "normal" landing conditions, the observed dynamic loads were only 40 to 60 percent of the static load. Under cases of "hard" landings, where the aircraft was literally "flown into the ground," the dynamic loads were in the range of 150 to 200 percent of static loads. However, discussions with pilots indicated that hard landings of this sort would be indeed rare (Sale and Hutchinson 1959).

ACCELERATED TRAFFICKING TESTS

The first of a series of accelerated trafficking tests under controlled conditions was initiated at Lockbourne Army Airfield, Ohio, in June 1943. These ambitious tests were designed

to permit a comprehensive evaluation of many of the factors influencing rigid pavement design. Extensive strain and deflection measurements were made at slab interiors, edges, and corners.

The concept of coverages was introduced to account for distribution of traffic over the width of the pavement. Based upon probabilistic concepts, one coverage was said to occur when each point in the wander width of the pavement feature had been subjected to one maximum stress repetition by the operating aircraft. At the time of the Lockbourne tests, 5,000 coverages was considered to be representative of a design life of 10 years.

Among the conclusions of the Lockbourne accelerated trafficking tests as summarized by Sale and Hutchinson (1959) were the following:

- Stresses produced in a pavement slab by either traffic loadings or static loadings are more severe when the loading is applied at the corners and edges of a slab than when applied at the center.
- The Westergaard edge load equations (developed in 1943 and published in final form by Westergaard in 1948) were valid for a single loading condition, but an additional “design factor” must applied to account properly for stress repetitions (fatigue), temperature gradients, and other unknown variables.

Measurements from the Lockbourne tests showed that responses calculated by Westergaard's theory were conservative and followed the shape and form of the test track measurements. Therefore, the Corps revised its design criteria to edge stresses, adopting a 25 percent load transfer at the joints. A “design factor” of 1.3 was used for stress repetitions up to 5,000 coverages and to accommodate environmental stresses. The design factor (DF) was defined as the ratio of the design flexural strength of the concrete (R) to the maximum free edge stress. In its most general form, the DF is given by

$$DF = \frac{R}{(1 - LT) \times \sigma_f} \quad (3.1)$$

where

σ_f = Westergaard's edge stress

LT = load transfer from Equation 2.6 expressed as a fraction

The design factor is not a safety factor *per se*, but it takes into account the effects of fatigue due to aircraft and cyclic environmental loadings. The philosophical underpinnings of this approach are that the design factor has an initial value greater than one for design purposes, but continually decreases with time and repetitive loading until a design factor of 1.0 is reached at the end of the pavement's design life. Then, the pavement theoretically will crack under the design loading. As the effects of channelized traffic became more pronounced with steerable landing gear in the 1950's, the design coverages were increased from 5,000 to 30,000 with an increase in DF with increasing coverages.

SUBGRADE CHARACTERIZATION

Westergaard's analytical model characterized the support provided by the subgrade soil as a bed of springs with a stiffness defined by the modulus of subgrade reaction (k). However, he never proposed a test method for determining k . The results of the Wright Field Slab Tests indicated that k could be estimated by dividing the magnitude of a vertical force acting on a circular area located in the interior of a slab by the volume of the resulting deflection basin. Stresses predicted by a Westergaard analysis using a value of k determined by this method were in good agreement with stresses calculated from strains measured in the tests. However, this method, which came to be known as the volumetric displacement method, was unsuitable for design purposes, because it required constructing a test slab on a representative subgrade (Hutchinson 1966, Ahlvin 1991). In 1942 a series of plate bearing tests were

conducted on each subgrade for the Wright Field Slab Tests with plates varying in diameter from 305 mm (12 in.) to 1828 mm (72 in.). Almost without exception, tests made with a 762-mm (30-in.) diameter plate were in close agreement with k values determined from the volumetric displacement method (Sale and Hutchinson 1959). This plate bearing test, with minor variations, is still in use today to characterize the modulus of subgrade reaction for rigid pavement design.

The adequacy of the plate bearing test method has been questioned repeatedly in the past. One of the primary shortcomings of the test is that it requires a representative subgrade to be prepared before an accurate subgrade modulus can be obtained. The use of thick base courses and stabilized layers presents an obvious problem. However, one of the advantages of the plate bearing test is that it is a measure of the elastic (and plastic) properties of the soil at a unit loading which is approximately equal to the unit load to which the soil will be subjected (Hutchinson 1966). It can also be shown that the design pavement thickness is not particularly sensitive to typical variations in k ; therefore, the plate bearing value is considered adequate for design purposes.

In the 1950s the Corps began to require that the modulus of subgrade reaction for design of rigid pavements over base course be determined from plate bearing tests conducted on top of the base course. As these data accumulated, the Corps began to develop curves relating the k value on top of the base to the k value of the subgrade. In the 1970s these curves were approved by the Corps for design supplanting the requirement to conduct tests directly on the base (Ahlvin 1991). Later the FAA adopted this approach into its design doctrine. However, recent studies by Darter et al. (1995) have shown that the concept of the top-of-the-base k is not valid and that stabilized layers should be considered as a structural layer in analysis and design.

RIGID PAVEMENT JOINTS

Early experiences with highways revealed the importance of tying rigid pavement slabs together to prevent separation at the joints. Typically, deformed steel reinforcing bars were used in highway construction. However, an additional benefit was discovered: some load transfer was provided at the joint. Because highway slabs were being designed for interior loads, this advantage was not immediately appreciated. Later, as it became apparent that edge loadings were more critical than interior loadings, highway engineers began to construct rigid pavements with thickened edges. This practice was carried over into the first Corps' rigid pavement design procedure in 1943 (Hutchinson 1966).

Early work of the Corps of Engineers showed that the design thickness of rigid pavements was controlled by the tensile stress that occurred at the edge of the pavement slabs. This work also indicated that the edge stresses were reduced by properly designed load transfer devices at the joints. Thus, thinner, more economical pavement designs could be produced that would have satisfactory performance. A second benefit was increased surface smoothness as load transfer devices reduced differential vertical movements at the joints. Table 3.1 summarizes some of the values of load transfer from full-scale accelerated trafficking tests and in-service pavements.

Based upon the performance of the test items in the Lockbourne No. 2 Test Track and upon measured deflections and strains, the following ranking of joint types from the most effective to the least (in terms of load transfer) was made (Sale and Hutchinson 1959):

- Dowelled contraction joint.
- Dowelled construction joint.
- Keyed construction joint with tie bars.
- Contraction joint.

Table 3.1

Summary of Corps of Engineers Load Transfer Measurements For Full-Scale Test Sections and In-Service Pavements (Rollings 1989)

Type of Joint	Number of Data Points	Load Transfer, percent		
		Range	Mean	Coefficient of Variation, percent
Contraction joint with aggregate interlock	46	15.6-50.0	37.2	19.2
Doweled contraction joint	4	28.2-42.8	35.1	17.3
Doweled construction joint	195	0.0-50.0	30.6	38.0
Doweled expansion joint	15	15.4-42.6	30.5	24.4
Tied contraction joint	6	23.9-34.8	29.2	13.4
Tied key joint	2	25.6-26.1	25.8	----
Keyed joint	61	5.6-49.0	25.4	41.4
Lockbourne free (butt) joint	8	5.8-24.5	15.5	40.9

- Keyed construction joint.
- Doweled expansion joint
- Free-edge expansion joint.

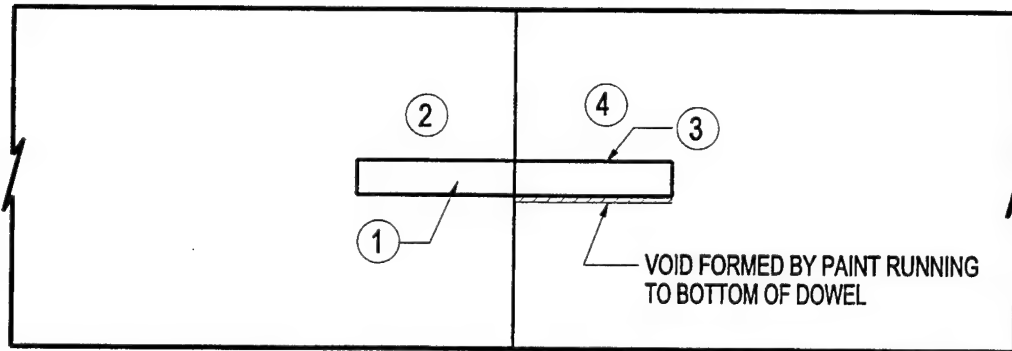
For doweled joints in thick pavements, it was found that there was no apparent advantage in using structural shapes over conventional round bars.

Observations at the test tracks at Lockbourne and later at Sharonville, Ohio, indicated that load transfer at doweled joints varied with the various methods of doweled joint construction.

At both Lockbourne and Sharonville, the concrete slabs were cast against forms, and the dowels were locked into place in the forms. At Lockbourne the dowels were installed by first bonding the one end in the concrete, pulling the forms off over the dowels, painting and greasing the exposed half of the dowel, and then paving the adjacent lane. At Sharonville the dowels were installed by painting and greasing the end of the dowel in the first paving lane, turning and removing the dowel, removing the forms, reinserting the painted and greased end

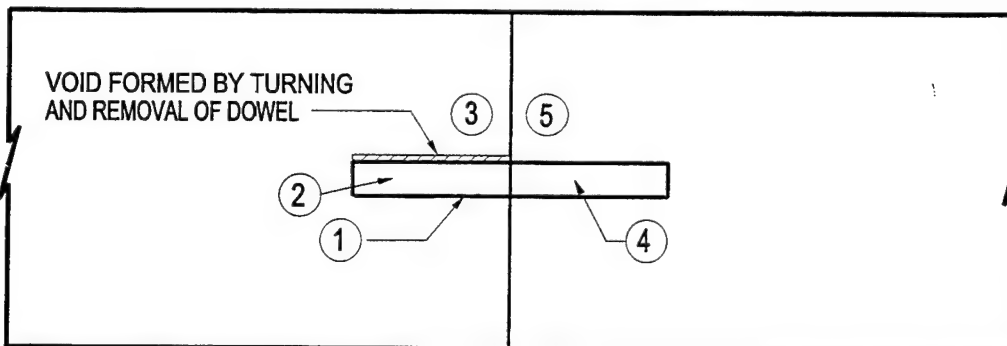
of the dowels into the same hole from which they were removed, and bonding the exposed end of the dowel into the adjacent lane. Strain gages and deflection gages were installed in the pavements on each side of the joints at both test tracks. A load cart with a twin tandem assembly was used to load the track in each case. The results of these tests can be summarized as follows:

- Cast-in-place dowels (at Lockbourne) performed better (higher load transfer) than reinserted dowels (at Sharonville).
- At Lockbourne the greatest load transfer was observed when the load was applied on the edge of the slab having the painted and greased dowel end. It was speculated that this was caused by the void created by the buildup of paint under the unbonded dowel (Figure 3.1a). When load was applied to the slab containing the bonded end, the unbonded end did not make contact with the concrete and contribute to load transfer until some amount of deflection occurred. When the load was applied to the slab containing the unbonded end, bearing contact was immediate on both ends of the dowel causing a more efficient transfer of load. Conversely, at Sharonville, the greatest load transfer was observed when the load was applied to the slab containing the bonded dowel. Again, it was speculated that the turning and removal of the dowel created looseness. When the dowel was reinserted, it lay on the bottom of the hole, thus creating a void at the crown of the painted and greased end (Figure 3.1b). As a result, the load on the slab containing the painted and greased end of the dowel deflected an amount equal to the void at the top of the dowel before any load was transferred to the adjacent slab. Thus, it was the recommended that the dowels be installed with no manipulation of the dowel after concrete was placed to maximize the load transfer obtained by the doweled joint.

CONSTRUCTION SEQUENCE

- (1) DOWEL ANCHORED FIRMLY TO FORM.
- (2) PAVEMENT PLACED AND BONDED TO END OF DOWEL.
- (3) FORM REMOVED OVER DOWEL, EXPOSED END OF DOWEL PAINTED AND GREASED.
- (4) ADJACENT PAVEMENT PLACED.

(a) Lockbourne test track

CONSTRUCTION SEQUENCE

- (1) DOWEL PAINTED AND GREASED.
- (2) DOWEL ANCHORED FIRMLY IN FORM.
- (3) PAVEMENT PLACED AND UNBONDED TO END OF DOWEL.
- (4) DOWEL TURNED TO PREVENT BOND, REMOVED, FORM REMOVED AND DOWEL REINSERTED INTO SAME HOLE.
- (5) ADJACENT PAVING LANE PLACED.

(b) Sharonville test track

Figure 3.1. Dowel installations at Lockbourne and Sharonville test tracks

- Load transfer across doweled joints resulted in an edge stress reduction in excess of 25 percent.
- Load transfer efficiencies computed from deflections were greater than load transfer efficiencies computed from stresses.
- The load transfer across joints in multi-layer pavements is about the same as load transfer in single layer construction.

A review of the unpublished minutes of the All-Division Meeting on Doweled Joints held at the Ohio River Division Laboratories, September 1958, revealed that it was the opinion of the Corps' rigid pavement experts that doweled joints provided the best performance of the commonly used joint types. The available performance data up to that point revealed that the 25 percent load transfer value used in design was conservative for doweled joints. Indeed, it was a topic of discussion that the load transfer assumption should perhaps be increased for doweled joints allowing a thinner pavement to be constructed. It was the opinion of these experts that load transfer values of 35 to 40 percent might be appropriate for doweled joints. However, it is important to note that these same experts were cognizant of the importance of careful construction procedures in obtaining load transfer. The minutes of the meeting contain this statement:

We must realize that we do not, as yet, have sufficient information to accurately evaluate the amount of load transfer that is obtained from the various methods of construction [of doweled joints], therefore, for the time being, we must be conservative and continue to use the assumed 25 percent. This does not mean, however, that we can relax our construction requirements. We must insist on good dowel installations, and we must keep the dowel looseness to a minimum if we are to ever realize the benefits of the doweled joint, because performance of the joints now being constructed will pay an important role in any future work we may do along this line. Otherwise, if through looseness, we fail to obtain the better load transfer, we may as well not use the more expensive doweled joint.

After World War II aircraft loadings continued to increase. To accommodate these increasing demands on the pavement, aircraft manufacturers added more wheels to the

landing gear to achieve wheel loadings sufficient to permit usage on existing pavements.

These multiple-wheel gear loadings over an entire slab raised doubts about the adequacy of the assumptions concerning interior and edge loadings on slabs assumed to extend to infinity.

The advent of the C5-A military transport and the Boeing B-747 commercial aircraft with loads twice as heavy as their predecessors lead to Multiple-Wheel Heavy Gear Load (MWHGL) Pavement Tests conducted at the Waterways Experiment Station in the late 1960s and early 1970s (Ahlvin 1971; Burns 1971; Ledbetter 1971a, 1971b). A rigid pavement test track was trafficked as a part of the MWHGL tests. The track was constructed in two 7.6-m (25-ft) wide lanes separated by a longitudinal keyed construction joint. The keyway was formed using metal strips. All transverse joints were weakened plane contraction joints.

Four test items were constructed so that failures would occur at times varying from a few weeks to a few years under normal operating conditions and traffic volumes as follows:

<u>Item</u>	<u>Thickness</u>
1	254 mm (10 in.)
2	305 mm (12 in.)
3	356 mm (14 in.)
4	203 mm (8 in.)

The subgrade was a lean clay soil compacted to 95 percent of the modified density at optimum water content. The modulus of subgrade reaction was approximately 27.1 MPa/m (100 psi/in.).

A 12-wheel load cart, each wheel loaded to 133 kN (30,000 lb) for a total load of 1,600 kN (360,000 lb), was used to traffic the test section in such a way as to obtain edge loading along the longitudinal keyed joint.

The results of these tests raised questions about the practice of using keyed construction joints for heavy loads on low-strength subgrades. Observations made from test pits excavated after trafficking indicated that the keyed joint had failed either by shearing the key or by spalling of the bottom portion of the keyway. It was not possible to determine exactly when the keyed joint failed, but it was likely in the first 1,650 coverages, as evidenced by faulting along the joint. The failure of both the male and female portions of the keyed joints were taken as evidence of optimum geometry of the keyed joint. No inferences concerning the performance of keyed joints on a stiff subgrade could be made.

The performance of the transverse weakened-plane contraction joints was considered adequate. Little, if any, faulting was observed. An examination of the exposed faces of the joints in the test pits did not reveal excessive deterioration of the aggregate interlock.

SUMMARY

The FAA Westergaard rigid pavement structural design criteria has its origins in research conducted by the U.S. Army Corps of Engineers from 1940 to 1970. The following statements summarize the development of these criteria:

- The response model that forms the basis for the FAA structural design criteria for rigid pavements is Westergaard's 1948 edge loading model. The applicability of this model was verified by a series of full-scale and small scale experiments conducted by the Corps during the years during and just after World War II.
- The FAA structural design criteria for rigid pavements allows a reduction of Westergaard's edge load stresses by 25 percent to account for load transfer at joints. This reduction is based upon experimental evidence from full-scale and small-scale experiments as well as measurements of in-service pavements. However, it is recognized

that in reality load transfer is not a constant value but varies with a number of factors, among which are type of joint and quality of joint construction.

- The FAA structural design criteria for rigid pavements features a fatigue relationship which relates aircraft traffic, measured in coverages, to the ratio of concrete flexural strength to design stress. A series of full-scale experimental test tracks was used to develop a database of performance data for this purpose.

CHAPTER 4: CLASSICAL RESPONSE MODELS

WESTERGAARD THEORY

Professor Harald Malcolm Westergaard published a series of papers containing relationships for calculating stresses in rigid pavements based upon the theory of elasticity. His pioneering work was first published in Danish in 1923 (Westergaard 1923). However, this work was not widely read, and in 1926, he published a method in English for calculating the stresses in a rigid pavements (Westergaard 1926). He developed relationships for stresses

...by assuming the slab to act as a homogeneous, isotropic, elastic solid in equilibrium, and by assuming that the reactions of the subgrade to be vertical only and to be proportional to the deflections of the slab (Westergaard 1926).

Westergaard characterized the subgrade by the modulus of subgrade reaction (k), which is a measure of the stiffness of the subgrade and has units of force per area per unit deflection or force/length³. An important term in the Westergaard theory which quantifies the stiffness of the slab relative to that of the subgrade, called the radius of relative stiffness, is expressed by the following relationship:

$$\ell = \sqrt[4]{\frac{Eh^3}{12(1-v^2)k}} \quad (4.1)$$

where

E = modulus of elasticity of concrete

h = thickness of slab

v = Poisson's ratio of concrete

Assuming the response of the slab to be that of a plate on a Winkler foundation, Westergaard developed a closed form relationship for the dimensionless ratio oh^2/P as a function of

dimensionless ratio a/ℓ where σ is the maximum bending stress, P is the magnitude of the applied load, and a is the radius of the circular area over which the applied load acts for the following three cases:

- Wheel load close to the corner of a semi-infinite slab.
- Wheel load at the interior of an infinite slab.
- Wheel load at the edge of a semi-infinite slab.

In 1932 the Bureau of Public Roads conducted the Arlington Road Tests at Arlington, Virginia, using Westergaard's theory as a basis for planning the tests. Following these tests Westergaard modified his 1926 formulas to reflect the conditions and results of the tests (Westergaard 1933). Westergaard extended his procedures to airfield pavements in 1939. Again, Westergaard revised his formulas, this time to account for the larger contact area of aircraft tires (Westergaard 1939). Although Westergaard considered the interior, corner, and edge loading cases in his early works, he concentrated on interior loadings. Ioannides, Thompson, and Barenberg (1985) found that several of the equations ascribed to Westergaard in the literature are incorrect due to typographical errors or misapplication. They also reported that the 1926 equation for edge loading was incorrect.

It was not until 1948 that Westergaard published relationships that were valid for computation of stresses caused by edge loading of large wheel loads on large contact areas (Westergaard 1948). His revised formulas allowed the load to be characterized as an ellipse rather than being limited to a circular tire print. Ioannides, Thompson, and Barenberg (1985) recommended the use of these equations as being more accurate than the 1926 equations.

Response charts

Pickett and Ray (1951) developed a graphical solution of the Westergaard theory in the form of influence charts. These graphical solutions greatly simplified the determination of

theoretical deflections and moments caused by wheel loads on slabs. Influence charts were presented for four different load cases: interior loading assuming a bed of springs subgrade, interior loading assuming an elastic solid subgrade, edge loading assuming a bed of springs subgrade, and load placed at $\ell/2$ from an edge assuming a bed of springs subgrade. Stresses can be calculated from the moment read from the chart by dividing by the section modulus, defined as $h^2/6$. In a separate paper, Pickett et al. (1951) presented 16 additional influence charts for deflection, moment, and reactive pressures under interior, near edge, and near center loadings on slabs for springs, elastic solid, and elastic layer subgrades.

The first step in applying the influence chart involves solving for the radius of relative stiffness of the pavement section. The scale for the chart is then set according to the value of the radius of relative stiffness, and the tire print to be analyzed is subsequently drawn to this scale. The number of blocks (including partial blocks) covered by the tire print are counted and multiplied by the appropriate relationship to obtain either moment, deflection, or reactive pressure.

Because of their simplicity, the FAA, U.S. Army, and U.S. Air Force adopted the influence charts for the computation of maximum tensile stress for edge loading (Hutchinson 1966). Multiple-wheel gear assemblies can be analyzed with the charts simply by drawing them to the appropriate scale and counting the blocks covered by the tire print. However, it should be noted that the orientation of the gear must be positioned such that the maximum number of blocks is covered to calculate the maximum stress or deflection.

Computerized solutions

A few computerized solutions to the Westergaard theory have been developed, most notably the programs H-51, H51-ES, and PDILB (commonly referred to as the PCA AIRPORT program.) The H-51 program, originally developed by General Dynamics Corporation and

modified by WES, calculates the edge stress under multiple-wheel loads on a slab supported by a dense liquid foundation. The solution is essentially a computerized version of Pickett and Ray's response charts. The program allows the user to place the gear at any number of different orientations and positions to calculate the maximum stress condition. H-51 was modified by Ioannides (1984) by incorporating an elastic solid foundation in the program H51-ES. The PCA AIRPORT program is based upon Westergaard's theory for loads at the interior of an infinite slab supported by a dense liquid foundation (Packard, no date). This program also allows multiple-wheel assemblies and allows the user to orient the gear to maximize the response. Ioannides (1984) developed WESTER, a collection of Westergaard solutions in a single, user-friendly personal computer program.

Westergaard theory limitations

For nearly three quarters of a century, Westergaard's theory has been used to calculate the response of rigid pavements to wheel loads. His theory is relatively simple to apply and has been accepted as accurate. However, there are several limitations as discussed in the following paragraphs.

- All pavement layers below the slab must be represented by a single parameter, the modulus of subgrade reaction. A typical pavement may have several layers of materials including unbound or bound subbases and base courses with each overlying layer having an increase in quality and stiffness. In a typical application of Westergaard's theory to such a system, these layers are modeled by an increased modulus of subgrade reaction intended to give an equivalent response.
- The foundation is assumed to respond linear-elastically. Few subgrade, subbase, or base materials are truly linear-elastic. In fact most are nonlinear, stress-dependent,

and change with time and environment. The effect of nonlinear, stress-dependent material behavior on rigid pavement foundations is obscure.

- Westergaard assumed the slab to be in full contact with the subgrade at all points. Thus the boundary conditions are violated if a void develops due to pumping or if the slab and subgrade separate due to curling and warping.
- Westergaard assumed that the slabs were infinite (for the interior load case) or semi-infinite (for the edge and corner load case); that is, the slabs extend far enough from the loaded area that boundaries (discontinuities such as cracks or joints) have no effect on the solution. In actual practice this may not be the case, because rigid pavement slabs tend to be relatively narrow and have many cracks and joints.
- Load transfer cannot be directly modeled. For airport pavement design, load transfer is set at a constant 25 percent; thus edge stresses are reduced by that amount in calculating the design factor. These values have been related to performance in field test sections to formulate design criteria.
- The thickness of the slab must be uniform. This assumption makes it impossible to analyze slabs with thickened edges or other slabs of nonuniform thickness.

ELASTIC LAYER MODELS

The elastic layer theory was first formulated for a concentrated load and one layer by Boussinesq and later generalized by others for a uniformly distributed load acting over a circular area and to two or more layers. Manual solutions of one- or two-layer elastic systems subjected to a singular circular load are cumbersome at best. Computerized solutions have made it possible to analyze a system of many layers subjected to multiple loads. Among these programs are the BISAR, CHEVRON, and JULEA programs (Barker and Gonzalez 1991).

The basic assumptions of the elastic layer theory (Crawford and Katona 1975) are as follows:

- All materials in the system are assumed to be homogeneous, isotropic, and linear elastic; thus, each pavement layer can be represented by three parameters: thickness, modulus of elasticity, and Poisson's ratio. Each layer may have different elastic properties.
- Each layer is infinite in horizontal extent, and the bottom layer extends vertically to infinity.
- The load is static and is uniformly distributed over one or more circular areas. Most programs assume the load to be entirely vertical, although some can accommodate horizontal components.
- The layers are continuously in contact. Also, the degree of restraint between adjacent layers must be assumed. Common assumptions are that adjacent layers are fully bonded or that they are frictionless. Some programs can allow any degree of restraint between these two extremes.

In the past several years layered elastic design models for rigid pavements have been developed. The U.S. Army and Air Force have developed design guidance for elastic layered design methodologies for both rigid and flexible pavements (Departments of Army and Air Force 1988, 1989). The FAA (1995) has adopted an alternative design procedure (known as LEDFAA) based on a layered elastic theory. For rigid pavements the basic design principle is to limit the tensile stresses in the slab to a level sufficiently below the concrete flexural strength so that failure (cracking) occurs only after some significant number of load repetitions. Rigid and flexible overlays of rigid pavements can be accommodated in the design model.

Because of the assumptions of the layered elastic model, certain limitations are intrinsic:

- The model assumes each layer to be infinite in horizontal extent; therefore, joints and cracks in rigid pavements are ignored. Even the base and subbase layers in a pavement are not infinite in horizontal extent. Stabilized layers may also develop cracks which cannot be directly modeled.
- The model assumes each material to be linear elastic. This assumption may lead to inconsistencies in stress calculations in the foundation layers. For example, it is not possible for an unbound granular layer to carry significant tensile stresses; yet the layered elastic model may predict such stresses.

MODELS FOR DOWEL STRESSES

Dowels have been used as load transfer devices in jointed concrete pavements for over three-quarters of a century. Dowel bars are thought to prevent faulting, reduce pumping, and reduce corner breaks. However, the design of dowels is based mostly on experience. Most design criteria prescribe the diameter, length, and spacing of dowel bars based upon pavement thickness.

Dowels located at some distance away from the point of application of the load are not as effective in transferring load as those that are closer. The number of dowels effective in distributing the load has been debated since the early developments of rigid pavement modeling. Westergaard (1928) concluded that only the first couple of dowels on either side of the load are effective in transferring load. Based upon Westergaard's theory, Friberg (1940) noted that for loadings a considerable distance from any edge, the maximum positive moment occurs beneath the load, and the maximum negative moment occurs a distance of $1.8l$ from the point of loading. Beyond $1.8l$, sometimes referred to as the effective length (e), the

moment changes very little. Friberg concluded, therefore, that the influence of dowel shear beyond that point is negligible, stating:

The effective dowel shear decreases inversely as the distance of the dowel from the point of loading, to zero at a distance of $1.8l$. No dowels beyond that point influence the moment at the load point.

Friberg's assumption of linear decrease of transferred shear force with distance appears realistic and has been widely accepted (Ioannides and Korovesis 1992). Kushing and Fremont (1940) accepted Friberg's linear assumption, but postulated that e could be as great as πl . Finite element studies led Tabatabaie (1978) to conclude that the linear assumption of Friberg was appropriate, but that the effective length was $1.0l$. The above arguments are appropriate for a single-wheel loading only; multiple wheel gear configurations will lead to different values of the effective length. In fact, Ioannides and Korovesis (1992) have shown that e is not a constant and is not function of l alone.

It is thought that bearing stresses under the dowel are responsible for spalling and looseness of the dowels. Analytical models for determining the bearing stresses in dowel bars have been in existence since the late 1930s. Several investigators have presented formulas for calculating the concrete bearing stresses (Friberg 1940; Tabatabaie 1978; Ioannides, Lee, and Darter 1990). According to Ioannides et al. (1990), all of these formulations for bearing stress (σ_b) may be represented by the following relationship:

$$\sigma_b = A(\text{structural}) \times B(\text{load}) \quad (4.2)$$

The first term, A , is determined from the structural characteristics of the pavement system, while the second term, B , quantifies the transferred load.

Friberg (1940) presented an analysis of stresses in doweled joints based upon the work of Timoshenko and Lessels (1925). His analysis was based upon considering the dowel as a semi-infinite beam on a Winkler foundation. His basic relationship for dowel stresses was

$$\sigma_b = Ky_o \quad (4.3)$$

where

K = modulus of dowel support

y_o = deflection of the dowel with respect to the concrete at the face of the joint

Friberg's analysis of dowel bar support is shown in Figure 4.1.

Friberg's relationship for the maximum deformation of concrete under a dowel bar with a shear force P_t , is

$$y_o = \frac{P_t}{4\beta^3 E_d I_d} (2 + \beta\omega) \quad (4.4)$$

where

ω = joint opening

E_d = modulus of elasticity of the dowel

I_d = moment of inertia of dowel bar

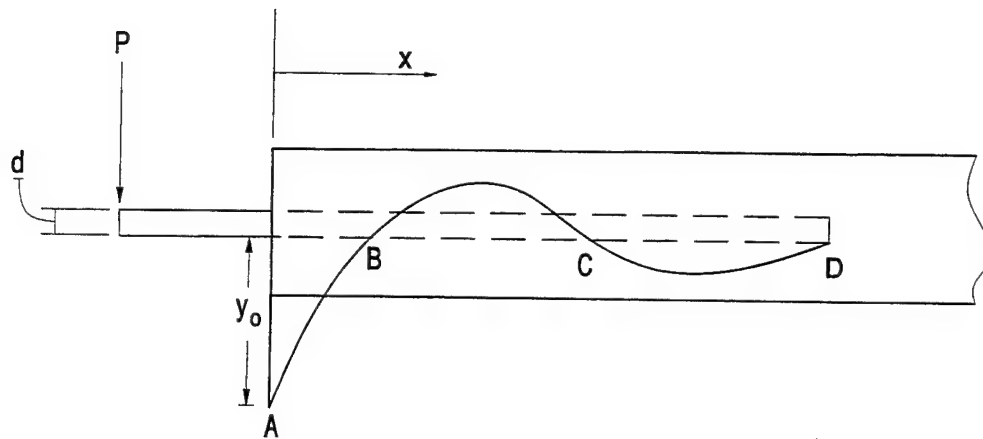
β = relative stiffness of the dowel-concrete system.

Friberg adopted Timoshenko's definition of the relative stiffness of a bar embedded in concrete as

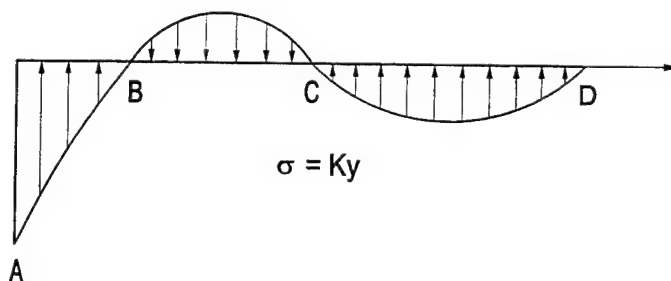
$$\beta = \sqrt[4]{\frac{Kd}{4E_d I_d}} \quad (4.5)$$

The bearing stress on the concrete at the joint face then becomes

$$\sigma_b = \frac{KP_t}{4\beta^3 E_d I_d} (2 + \beta\omega) \quad (4.6)$$



(a) Deflection diagram



(b) Stress diagram

Figure 4.1. Friberg's (1940) analysis of dowel bar support

Ioannides, Lee, and Darter (1990) retained Friberg's *A* term in Equation 4.4, but proposed an alternative *B* or loading term. Their relationship for critical bearing stress is given by:

$$\sigma_b = \frac{K(2 + \beta\omega)}{4\beta^3 E_d I_d} \times P_t \times TLE \times f_{dc} \quad (4.7)$$

where f_{dc} is a dimensionless term quantifying the portion of the load carried by the critical dowel. The critical dowel is the dowel carrying the largest shearing force. Approximations for f_{dc} are given by

$$f_{dc} = \begin{cases} \frac{s}{e} & \text{for edge load} \\ \frac{2s}{e+s} & \text{for corner load} \end{cases} \quad (4.8)$$

where

e = effective length

s = dowel spacing

TLE is given by

$$TLE = \frac{P_T}{P_t} \quad (4.9)$$

where P_T is the total load transferred across the entire length of joint.

Grinter (1931) reported that the value of K depended on the modulus of the slab concrete, the thickness of the slab, and the modulus of subgrade reaction. Reported values of K vary greatly. Tabatabaie (1978) reported finding values in the literature from 0.08×10^6 MPa/m (0.3×10^6 psi/in.) to 8.6×10^6 MPa/m (32×10^6 psi/in.). The value typically assumed is 0.41×10^6 MPa/m (1.5×10^6 psi/in.). Ioannides and Korovesis (1992) developed a procedure for backcalculating K from measured values of LTE_s obtained using the a falling weight deflectometer (FWD), Benkelman beam, etc.

Localized crushing of the concrete caused by stress concentrations at the locations of dowel bearing can cause a reduction in the dowel-concrete stiffness. Also, many cycles of loading leads to a decrease in joint efficiency due to fatigue. Channakeshava, Barzegar, and, Voyiadjis (1993) conducted an localized joint response analysis using a special-purpose, non-linear 3D finite element code to estimate the effect of localized stress concentrations. Spring

dowel supports were utilized to model the concrete-dowel interaction. These analyses indicated large concentrations of tensile stresses above the dowel and compressive stresses beneath dowel. Figure 4.2 shows the evolution of the dowel-concrete interaction spring forces where the dowel penetrates the face of the concrete slab with increasing displacement. Three different concrete strengths were used to represent the different levels of strength loss caused by fatigue. These curves are nonlinear with a decrease in stiffness with increasing load.

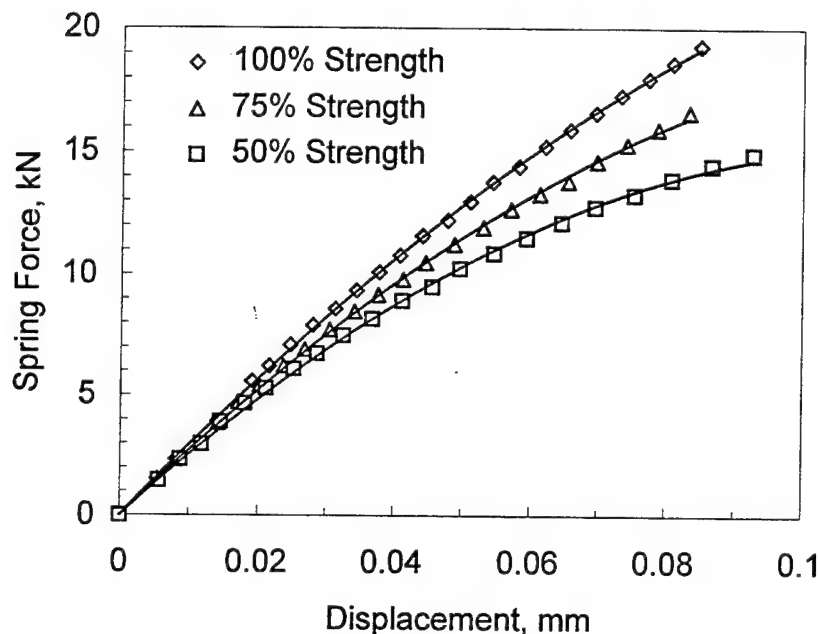


Figure 4.2. Loss of dowel-concrete interaction stiffness with increasing displacement (after Channakeshava, et al. 1993)

WESTERGAARD-TYPE SOLUTION FOR LOAD TRANSFER

Ioannides and Hammons (1996) reported the results of a study which effectively broadens the Westergaard-type solution to explicitly include load transfer. In his 1948 paper

Westergaard briefly described a solution for the edge load transfer problem. However, this work was limited by his implicit assumption that deflection load transfer and stress load transfer were identical. Model studies and full-scale tests in the 1940s and 1950s conducted by the Corps of Engineers, and more recently by finite element investigations (Ioannides and Korovesis 1990, 1992), disproved this assumption.

In 1949 Mikhail S. Skarlatos described his analytical investigations (Skarlatos 1949). He defined a dimensionless joint stiffness (f) in terms of the radius of relative stiffness, modulus of subgrade reaction, and a parameter (q) which represents the force transferred across a unit length of joint per unit differential deflection across the joint as follows:

$$f = \frac{q}{kl} \quad (4.10)$$

Using this approach, Skarlatos developed relationships involving integral equations for maximum stress and deflection on the unloaded side of the joint. Ioannides and Hammons (1996), using modern personal computers and powerful mathematical software, were able to perform these integrations for square loaded areas of various sizes, 2ϵ by 2ϵ . Following the same approach as Westergaard, closed-form equations for the maximum deflection and maximum bending stress on the unloaded side of a joint capable of load transfer were developed. When used together with Westergaard's edge loading equations, the relationships developed by Ioannides and Hammons (1996) can be used to investigate the load transfer problem.

The results of the analytical development work were consolidated into two graphs as suggested by the Ioannides and Korovesis (1990). Figures 4.3 and 4.4 illustrate the variation of the deflection load transfer efficiencies, LTE_δ , and stress load transfer efficiencies, LTE_σ , with respect to the dimensionless joint stiffness, f , and the dimensionless loaded area size,

ϵ/ℓ . Nonlinear regression was used to develop an expression for LTE_δ as a function f and ϵ/ℓ as follows:

$$LTE_\delta = \frac{1}{1 + \log^{-1} \left[\frac{0.214 - 0.183 \left(\frac{\epsilon}{\ell} \right) - \log f}{1.180} \right]} \quad (4.11)$$

Likewise, nonlinear regression was used to develop an expression for LTE_δ as a function of LTE_σ and ϵ/ℓ . The following regression formula was obtained:

$$LTE_\delta = \frac{\left[1206 \left(\frac{\epsilon}{\ell} \right) + 377 \right] LTE_\sigma^2 - 693 \left(\frac{\epsilon}{\ell} \right) LTE_\sigma^3}{1 + 689 \left(\frac{\epsilon}{\ell} \right) LTE_\sigma + \left[370 - 154 \left(\frac{\epsilon}{\ell} \right) \right] LTE_\sigma^2} \quad (4.12)$$

Nonlinear regression was used to develop an expression for LTE_σ as a function of ϵ/ℓ and LTE_δ . The resulting algorithm was obtained:

$$LTE_\sigma = \frac{\left[10.14 \left(\frac{\epsilon}{\ell} \right) + 4.00 \right] LTE_\delta - \left[4.3 \left(\frac{\epsilon}{\ell} \right) + 3.98 \right] LTE_\delta^2}{21.03 + \left[5.74 \left(\frac{\epsilon}{\ell} \right) - 20.98 \right] LTE_\delta} \quad (4.13)$$

The functional forms of these regression algorithms were arbitrary from an engineering viewpoint and were selected from among a large number of choices investigated. These relationships, based upon sound analytical principles, provide a complete solution for the load transfer problem in jointed rigid pavements in a form that is convenient for routine engineering calculations.

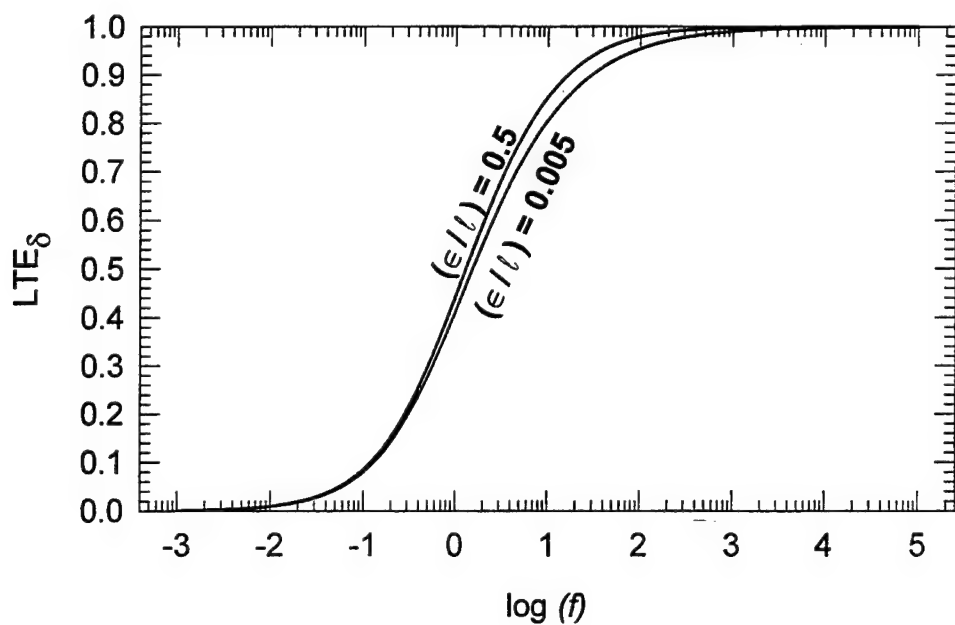


Figure 4.3. Variation of deflection load transfer efficiency with dimensionless joint stiffness and dimensionless load size ratio

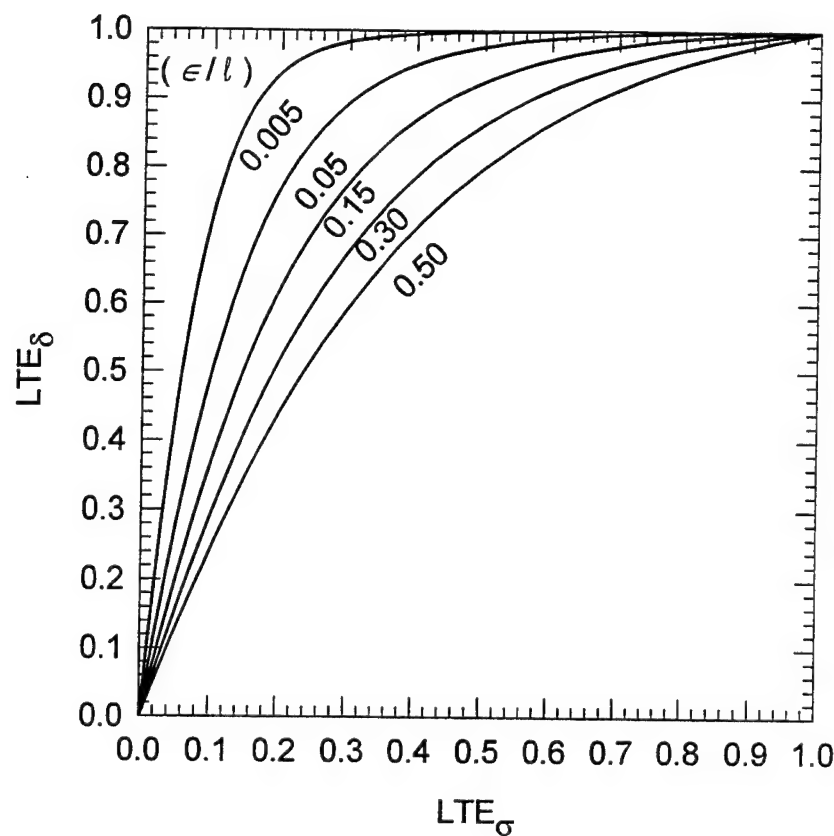


Figure 4.4. Relationship between deflection and stress load transfer efficiencies with dimensionless load size ratio

CHAPTER 5: FINITE ELEMENT RESPONSE MODELS

The finite element method is a powerful approximation technique that has been used to analyze a broad class of boundary value problems in engineering. With the development of the high-speed digital computer, finite element techniques have been applied to a variety of problems in pavement analysis. The finite element method's ability to model joint and edge discontinuities has led to its emergence as the analysis method of choice for rigid pavement research (Chatti 1992).

Table 5.1 presents an overview of certain key attributes of the more common finite element programs applied to rigid pavements as reported in the literature. These finite element programs can be characterized in two general categories by their representation of the slab model as either (a) 2D thin plate elements or (b) 3D continuum elements.

2D FINITE ELEMENT MODELS

A number of finite element programs featuring the use of a 2D thin plate model for the concrete slab have been developed and reported in the literature in recent years. These include ILLI-SLAB, JSLAB, KENSLABS, WESLIQID, FEACONS III, KENLAYER, WESLAYER, and RIGMUL. Each of the programs has similarities, yet certain key features (such as mechanics of the joint and available foundation models) vary. Some of the programs allow the user to choose the foundation model from a library of available models. Each of the programs incorporates load transfer capabilities with some differences in the philosophy and mechanics of the load transfer model. Because it is perhaps the most widely used and verified of these programs, only ILLI-SLAB will be described in detail in this dissertation.

Table 5.1
Overview of Finite Element Models for Rigid Pavements

Program Name	Slab Model	Load Transfer	Foundation Model(s)
ILLI-SLAB (Tabatabaie 1978)	2D thin plate	Linear spring, beam element on spring foundation	Dense liquid, Boussinesq, nonlinear resilient, two- and three-parameter models
JSLAB (Tayabji and Colley 1984)	2D thin plate	Linear spring, beam element on spring foundation	Dense liquid
WESLIQID (Chou 1981) and KENSLABS (Huang 1993)	2D thin plate	Linear springs	Dense liquid
WESLAYER (Chou 1981) and KENLAYER (Huang 1993)	2D thin plate	Linear springs	Layered elastic
FEACONS III (Tia et al. 1987)	2D thin plate	Linear and torsional springs	Dense liquid (linear and nonlinear springs)
GEOSYS (Ioannides et al. 1986)	3D brick element	None	3D brick elements with stress-dependent subgrade model
ABAQUS (Kuo 1994)	2D shell element 3D brick element	Linear and nonlinear springs, interface elements, gap elements, multi-point constraints, explicit models	Dense liquid, 3D brick element with linear and nonlinear elastic, plastic, and viscoelastic constitutive models, user-defined models

All of the 2D plate programs model the slab using a 2D thin plate element. A number of references describe the formulation of this element, such as Zienkiewicz and Cheung (1967) and Tabatabaie (1978). This four-noded plate bending element has dimensions of $2a$ by $2b$, as illustrated in Figure 5.1. Each node has three degrees of freedom: a displacement w in the z direction, a rotation θ_x about the x axis, and a rotation θ_y about the y axis. The following assumptions are made for this element:

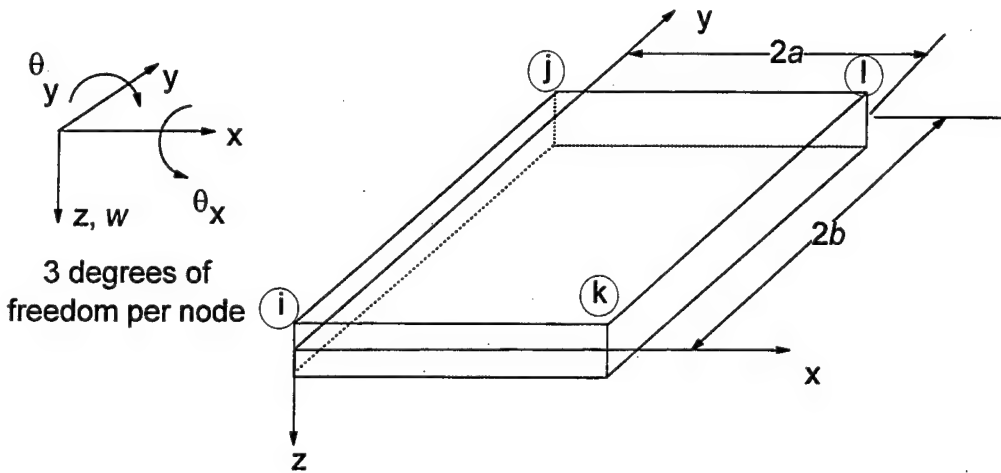


Figure 5.1. Four-node plate bending element

- The plate element is assumed to be isotropic, elastic, and homogeneous.
- Transverse loads are carried by flexure rather than by in-plane forces (membrane theory) or by transverse shear (thick plate theory).
- Lines normal to the middle surface in the undeformed plate remain straight, unstretched, and normal to the middle surface of the deformed plate.
- Each lamina parallel to the middle surface is in a state of plane stress, and no axial or in-plane shear stress develops due to loading.

ILLI-SLAB models

ILLI-SLAB is the most widely used and verified of the 2D thin plate finite element programs. Originally developed at the University of Illinois by Tabatabaie (1978), ILLI-SLAB has been enhanced by adding a variety of foundation models (Ioannides 1984, Khazanovich and Ioannides 1993) and by adding the capability to include temperature loadings (Korovesis

1990). It was extended by Chatti (1992) at the University of California at Berkeley to a new dynamic computer program called DYNA-SLAB for the analysis of jointed concrete pavements with load transfer systems at joints subjected to moving transient loads. Larralde and Chen (1985) presented a method of analysis including fatigue based on ILLI-SLAB. Majidzadeh, Ilves, and McComb (1981) coupled the slab and load transfer models in ILLI-SLAB with a three-layer elastic foundation model to formulate the finite element program RIGMUL.

The basic assumptions made by Tabatabaie (1978) in the initial development of ILLI-SLAB are as follows:

- Thin plate theory (as previously described) can be used to model the slab, overlay, or stabilized base.
- The subgrade behaves as a bed of springs.
- In case of a bonded stabilized base or overlay, there is full strain compatibility at the interface. In the case of an unbonded base or overlay, the shear stresses at the interface are neglected.
- The dowel bars at joints behave like a linear-elastic material and are located at the neutral axis of the slab.
- When an aggregate interlock or a keyway is used as the load-transfer system, the load is transferred from one slab to an adjacent one by means of shear. However, when dowel bars are used as the load transfer system, moment as well as shear may be transferred across the joints.

Figure 5.2 shows the finite element model used by Tabatabaie. The rectangular plate element was employed to model the two-layer slab system (Figure 5.2a). For the case in

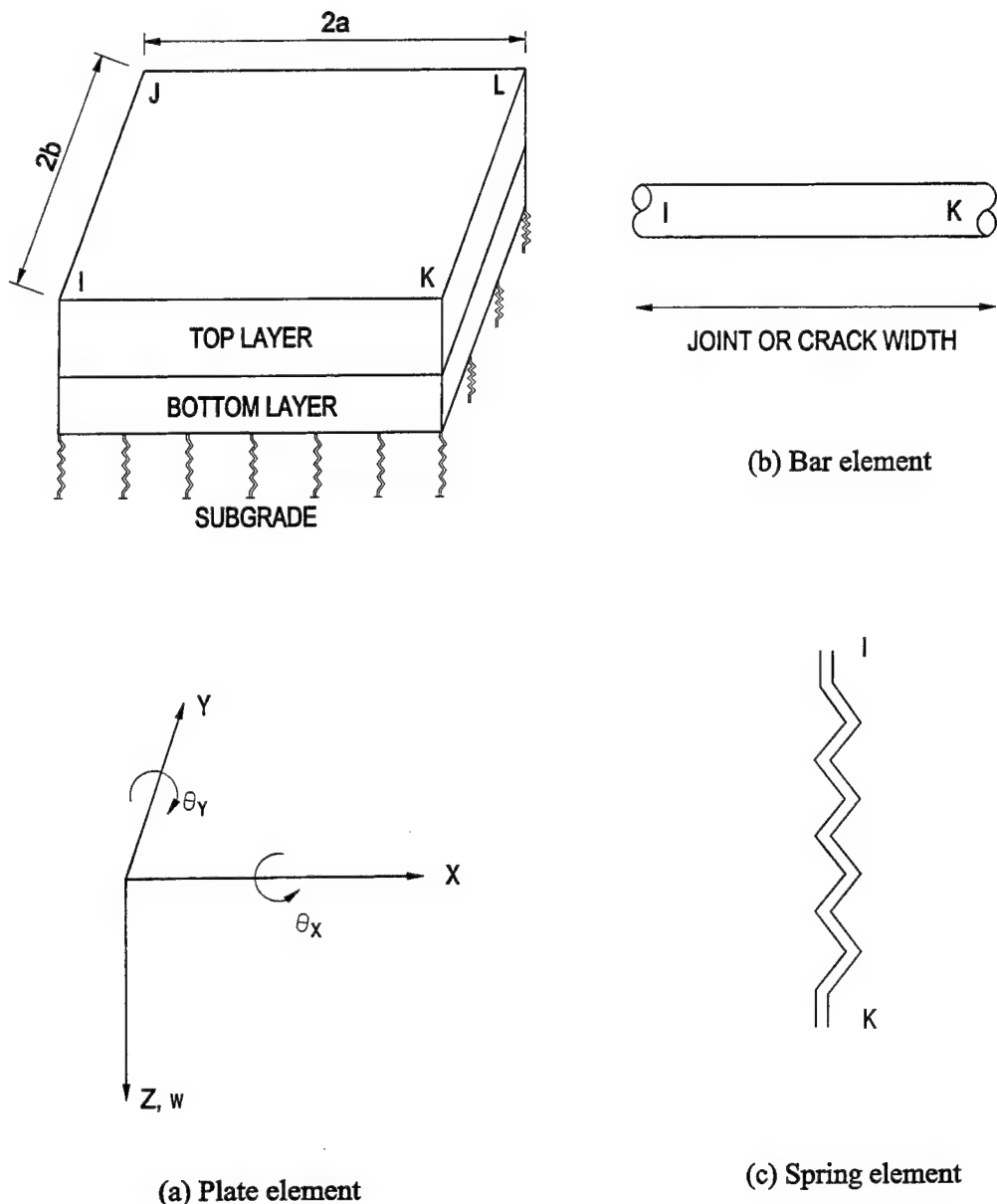


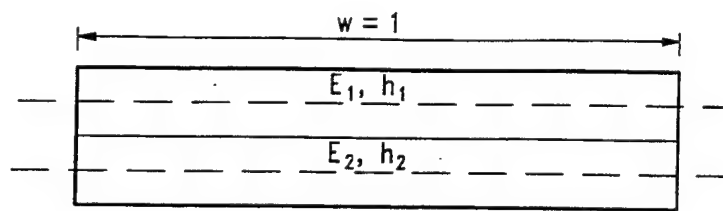
Figure 5.2. Finite element model in ILLI-SLAB (after Tabatabaie 1978)

which the two layers are bonded, the transformed section technique was used to develop an equivalent layer (Figure 5.3). The subgrade is modeled as a bed of springs characterized by the modulus of subgrade reaction (k). The value of k can be varied spatially from node to node by the user.

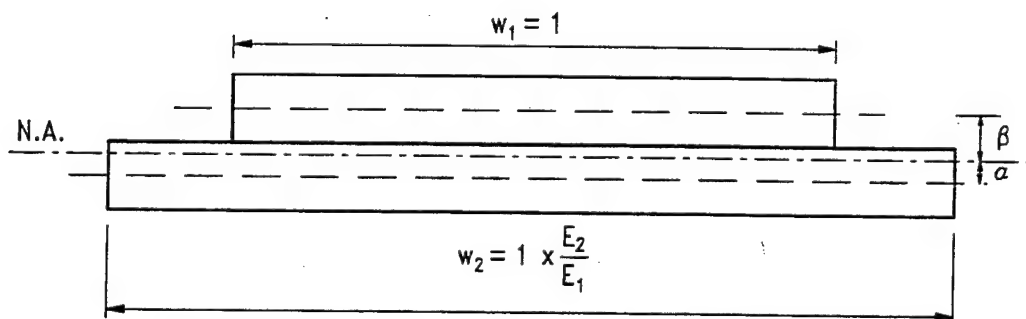
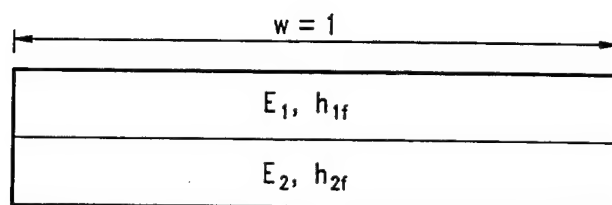
Load transfer model

Figure 5.4 shows the concept of how ILLI-SLAB models joint load transfer. A pure shear (aggregate interlock) load transfer mechanism is modeled by a linear spring element at each node along the joint face (Figure 5.2c). The spring element features one degree of freedom per node: w , the displacement in the z direction. The spring constant (called an “aggregate interlock factor,” AGG) is input by the user and is indicative of the stiffness of the joint. The value of the aggregate interlock factor can be estimated by backcalculating it from field tests. Using ILLI-SLAB, Ioannides and Korovesis (1990) developed an s-shaped curve defining a relationship between joint efficiency and a dimensionless joint stiffness ($AGG/k\ell$) shown in Figure 5.5. The points plotted in Figure 5.5 represent individual ILLI-SLAB runs used to develop the curve. This curve shows that any value of joint efficiency from zero to 100 percent can be calculated with an appropriate choice of aggregate interlock factor or vice versa. Comparison of Figure 5.5 with Figure 4.2 and Equation 4.10 reveals that the dimensionless joint stiffness proposed by Ioannides and Korovesis (1990) is identical to that employed by Skarlatos (1949) when $AGG = q$.

Dowel bars are modeled by a two-node bar element (Figure 5.2b) having three degrees of freedom per node: a displacement w in the z direction and a rotation θ_y about the y axis, and a rotation θ_x about x axis. A vertical spring element (Figure 5.2b) is employed to model the relative deformation of the dowel bar and the surrounding concrete. The spring element extends between the dowel bar and the surrounding concrete at the joint face. The dowel



(a) Two bonded layers

(b) Equivalent section of modulus E_1 

(c) Equivalent system of two unbonded layers

Figure 5.3. Equivalent sections for a two-layer system (after Korovesis 1990)

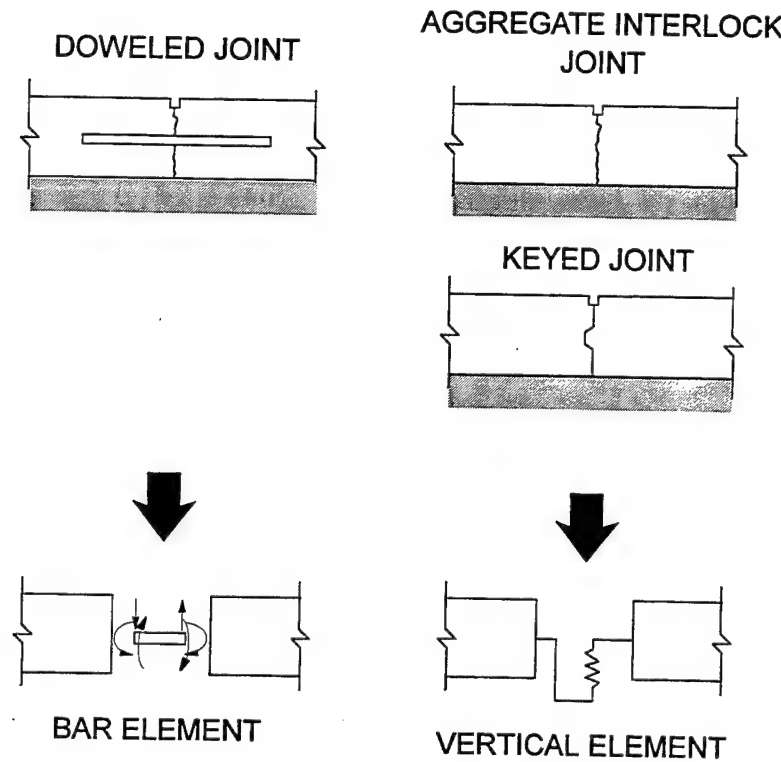


Figure 5.4. ILLI-SLAB joint models (after Larralde and Chen 1985)

bars are located at the neutral axis of the slab and are assumed to have the same deflection and slope at the joint face at the neutral axis of the slab.

Also using ILLI-SLAB, Ioannides and Korovesis (1992) developed the concept of a dimensionless joint stiffness for the doweled joint expressed by the quotient $D/sk\ell$ where s is the dowel spacing and D is the stiffness of the vertical spring element. The value of D depends upon the vertical stiffness caused by the support of the concrete, called the dowel-concrete interaction (DCI), and a vertical stiffness caused by beam bending (C). These two stiffnesses are summed as springs in series as follows:

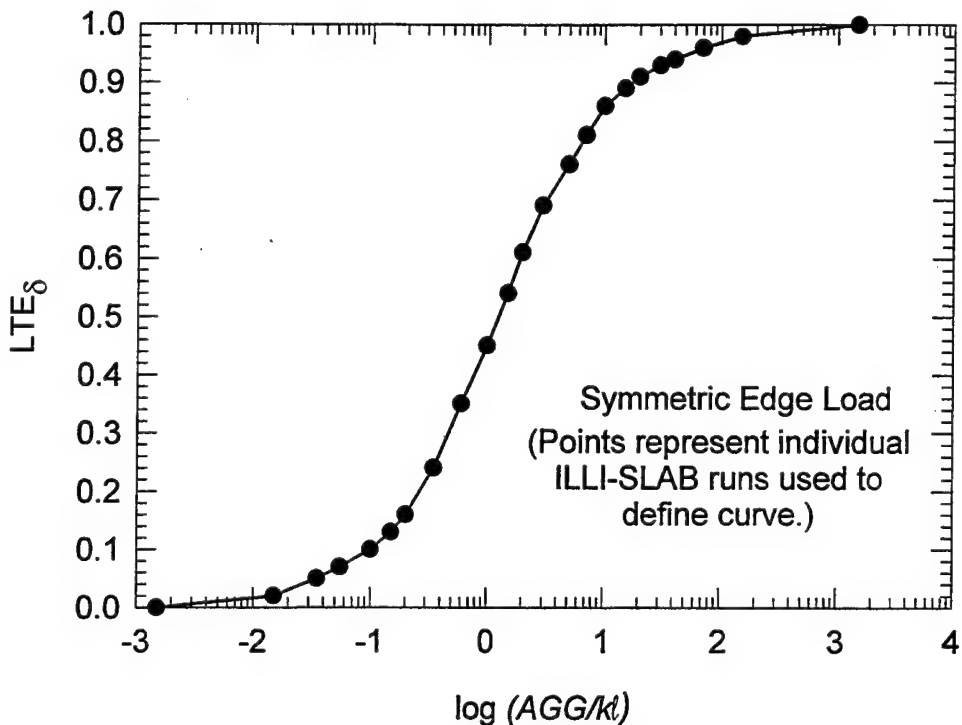


Figure 5.5. Joint efficiency as a function of dimensionless joint stiffness for aggregate interlock joint (after Ioannides and Korovesis 1990)

$$D = \frac{1}{\frac{1}{DCI} + \frac{1}{12C}} \quad (5.1)$$

The value of DCI is based on assuming the dowel to be a beam on a spring foundation (Friberg analysis) and is given by the following relationship:

$$DCI = \frac{4\beta^3}{(2+\beta\omega)} E_d I_d \quad (5.2)$$

where ω is the width of the joint opening. Comparing this relationship with Equation 4.4 reveals that DCI is identical with the ratio P_i/y_o in the Friberg analysis and has units of

force/length. The term β is identical to that used by Friberg (Equation 4.5). The term C in Equation 5.1 is defined by the relationship

$$C = \frac{E_d I_d}{\omega^3 (1 + \phi)} \quad (5.3)$$

where

$$\phi = \frac{12 E_d I_d}{G_d A_z \omega^2} \quad (5.4)$$

G_d is the shear modulus of the dowel bar as defined by

$$G_d = \frac{E_d}{2(1 + v_d)} \quad (5.5)$$

The term A_z is the effective cross-sectional area in shear and is assumed to be 0.9 times the circular area as follows:

$$A_z = 0.9 \left(\frac{\pi d^2}{4} \right) \quad (5.6)$$

A plot of joint efficiency as a function of dimensionless joint stiffness is presented in Figure 5.6. As with the aggregate interlock factor, any value of joint efficiency from zero to 100 percent can be obtained by appropriate choice of the joint stiffness. Ioannides and Korovesis' formulation of the dimensionless joint stiffness for the doweled joint is identical to that proposed by Skarlatos (1949) when $q = D/s$ (Equation 4.10).

Foundation models

The original subgrade model used by Tabatabaie was the dense liquid or Winkler foundation. Later enhancements to ILLI-SLAB have included the addition of a library of foundation models. Currently available models are discussed below.

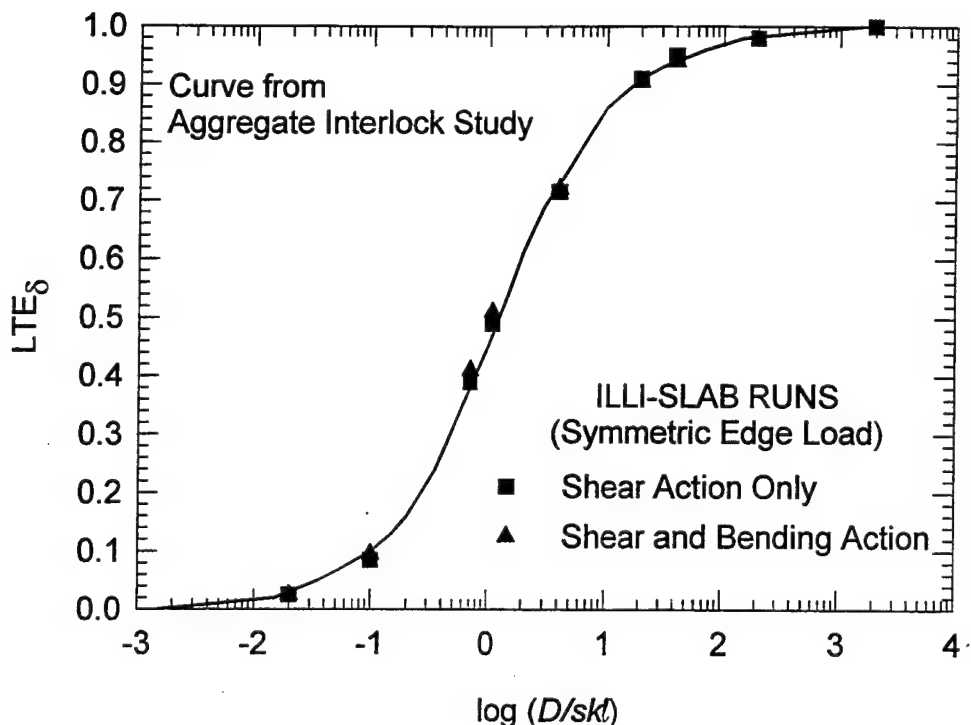


Figure 5.6. Joint efficiency as a function of dimensionless joint stiffness for doweled joint (after Ioannides and Korovesis 1992)

Bed of springs. The bed of springs (also referred to as the dense liquid or Winkler foundation) is the classical subgrade model characterized by the modulus of subgrade reaction (k) as in the Westergaard closed-form solution. This model represents the soil as a series of linear vertical springs with no shear interaction between them (Figure 5.7a).

Two dense liquid formulations are incorporated in ILLI-SLAB. The original model incorporated by Tabatabae (1978) was an equivalent mass formulation with a uniformly distributed subgrade. Later an additional dense liquid model was added featuring four concentrated springs at nodes of plate element (Ioannides 1984). The primary reason for adding this model was for direct comparison with other finite element codes which also use four concentrated springs at the nodes such as WESLIQID.

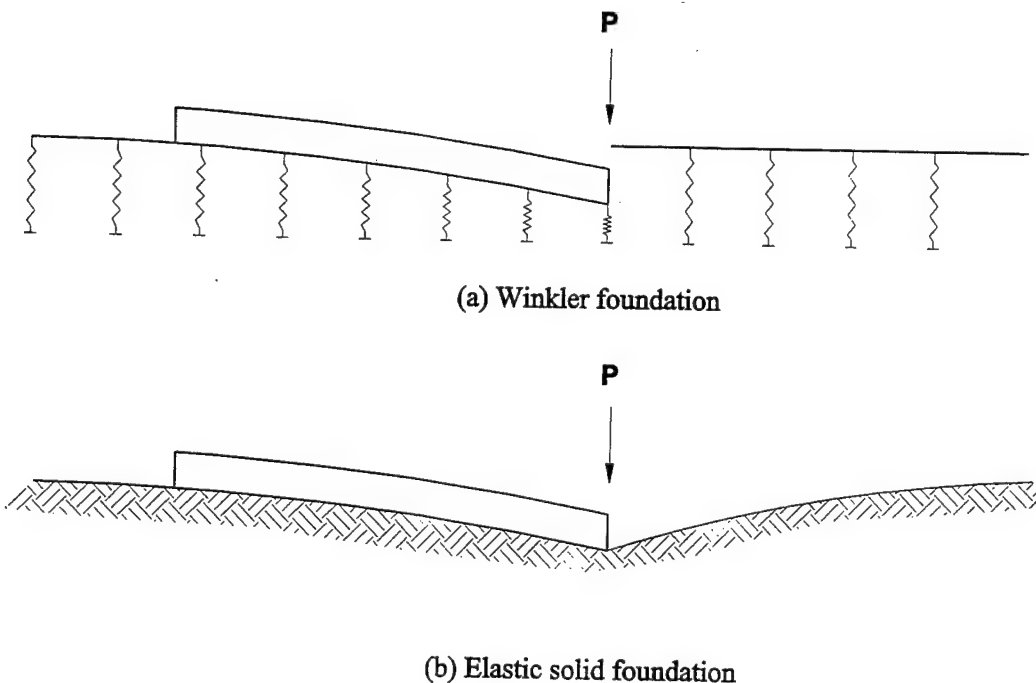


Figure 5.7. Foundation displacement under a loaded plate for Winkler and elastic solid foundations (after Majidzadeh et al. 1981)

Elastic solid subgrade. A one-layer elastic solid (Boussinesq) foundation model is available in ILLI-SLAB (Ioannides 1984). This model is a continuum model in which the deflection at a node depends not only on the forces on the node but also on forces and deflections at other nodes as well. The model is completely characterized by the two elastic parameters $E_{subgrade}$ and $v_{subgrade}$. When loaded with a plate, the elastic solid foundation predicts deflections at a point beyond the plate as shown in Figure 5.7b. This is in direct contrast with the dense liquid model which predicts zero deformations at points beyond the loaded plate (Figure 5.7a). In reality soil is a particulate material which exhibits some deformations beyond a load plate, but these will vanish faster than those predicted by the elastic solid model (Khanovich and Ioannides 1993).

The elastic solid model will allow the calculation of stresses and strains in the subgrade. However, the calculated values may not be realistic, especially in granular materials. Because of the linear elastic nature of the model, it cannot predict nonlinear, stress-dependent behavior. A second shortcoming of the elastic solid model is that it predicts infinite stresses under a free slab edge. Therefore, the use of the elastic solid subgrade to predict load transfer should be discouraged. The elastic solid foundation requires considerably more computational effort than the dense liquid formulation.

Resilient subgrade model. To introduce some degree of nonlinear behavior into the foundation model in ILLI-SLAB, the concept of the resilient modulus of subgrade reaction K_R was introduced (Ioannides 1984). The resilient modulus model does not truly model stress-dependent behavior, but introduces material nonlinearity through deformation-dependent response. Relationships between K_R and deflection w were developed in the form of a regression equation

$$K_R = \frac{1}{w} \left\{ A_1 \left[1 - \exp \left(-A_2 \left(\frac{w}{D_y} - A_3 \right) \right) \right] + A_4 \left[\frac{w}{D_y} - A_3 \right] + 2 \right\} \quad (5.7)$$

where A_1 , A_2 , A_3 , A_4 , and D_y are regression parameters determined from simulated plate load tests using the axisymmetric finite element program ILLI-PAVE. To simplify the selection of the regression parameters, ILLI-SLAB allows the user to select from four general subgrade types typical to Illinois (characterized as very soft, soft, medium, or stiff) for which the regression parameters are fixed. Alternatively, the user can enter values for the regression coefficients.

The resilient modulus foundation model is implemented in ILLI-SLAB as an iterative procedure in which the current value of K_R as determined from the calculated deflections is compared against previously assumed or calculated values. If agreement is not obtained, new

values of K_R are assigned, and the calculations are repeated. This process is continued until convergence is obtained.

Vlasov two-parameter foundation. The Vlasov or Pasternak model provides some degree of shear interaction between adjacent soil elements (Ioannides 1994, Khazanovich and Ioannides 1993, Kerr 1993). Figure 5.8 shows a representation of the Vlasov foundation. It is characterized by the subgrade reaction pressure, Q , which is a function of deflection, w , as follows:

$$Q = kw - G\nabla^2 w \quad (5.8)$$

where

k = modulus of subgrade reaction

G = coefficient describing the interaction of adjacent springs

∇ = Laplace operator

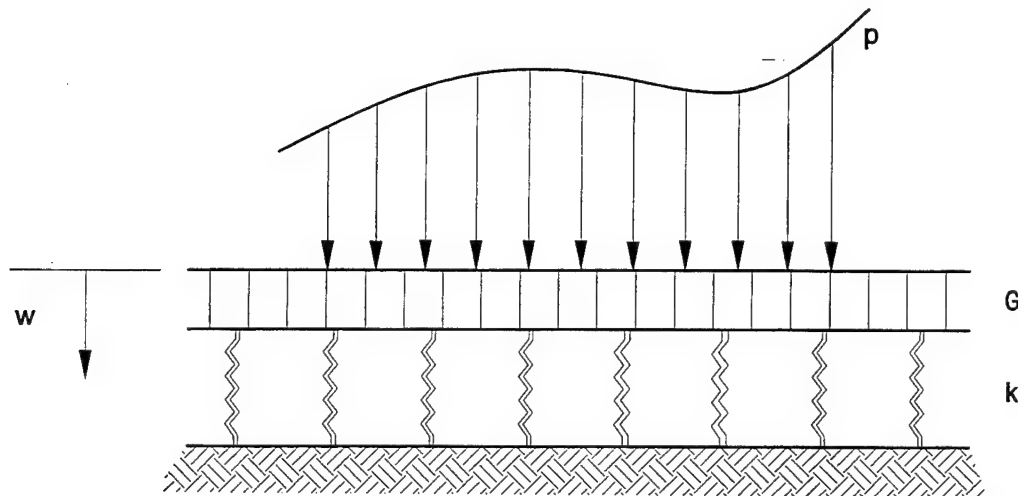


Figure 5.8. Vlasov or Plasternak foundation (after Kerr 1993)

As G approaches zero, it can be seen that the Vlasov model approaches the dense liquid foundation. To account for the influence of foundation deflections beyond the edge of the slab, ILLI-SLAB uses a strain energy approach that adds terms to the stiffness matrix to reflect the energy of soil deformation beyond the slab (Khazanovich and Ioannides 1993).

Kerr three-parameter foundation. Kerr (1964, 1965, 1993) generalized the two-parameter model by adding a third parameter k_U which describes a second, upper layer of springs as shown in Figure 5.9. In essence, the Kerr foundation is an in-series combination of the dense liquid foundation and the Vlasov two-parameter model. The upper dense liquid portion ensures that stresses in the region of a free edge will not go to infinity. Also, the lower two-parameter portion of the model allows shear interaction.

The partial differential equation which describes the response of the Kerr model is

$$\left(1 + \frac{k_L}{k_U}\right) p - \frac{G}{k_U} \nabla^2 p = kw - GV^2 w \quad (5.9)$$

The Kerr three-parameter model is implemented in ILLI-SLAB by introducing a eight-node, 24 degree-of-freedom element (Khazanovich and Ioannides 1993): four nodes are placed at the top of the upper springs, while the other four nodes are positioned at the bottom of the upper layer of springs. The additional nodes in the model formulation require additional computational effort, but the resulting stiffness matrix is banded leading to some computational benefit.

A disadvantage of the Kerr model is that it requires three parameters to calibrate the model for a subgrade material. These parameters lack the simple, convenient nature of the dense liquid k . However, it is possible to define an effective modulus of subgrade reaction (k_{eff}) analogous to the dense liquid case by considering k_U and k_L as springs in series:

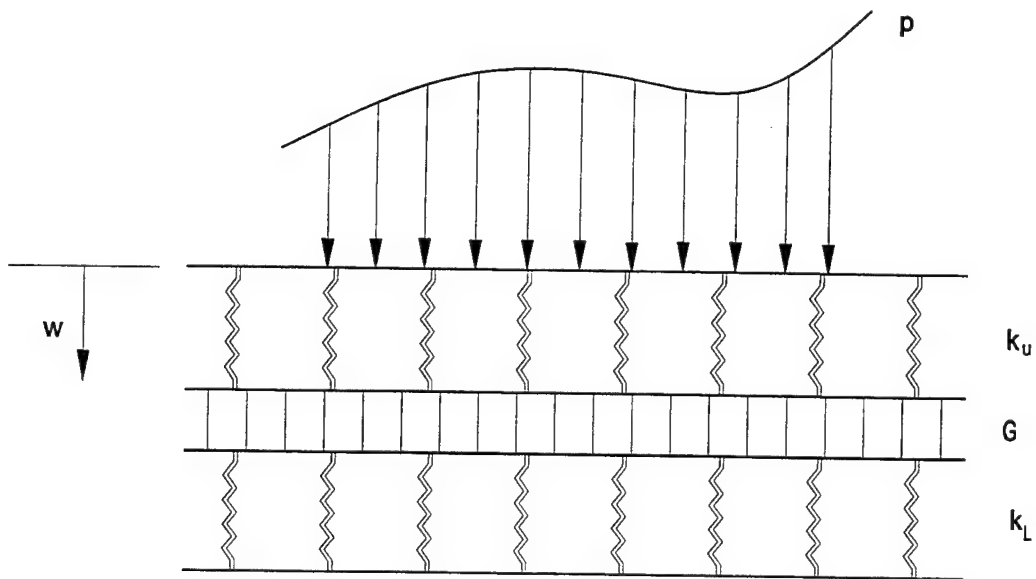


Figure 5.9. Kerr foundation model (after Kerr 1993)

$$k_{eff} = \frac{1}{\frac{1}{k_u} + \frac{1}{k_L}} \quad (5.10)$$

Zhemochkin-Sinitsyn-Shtaerman foundation. The Zhemochkin-Sinitsyn-Shtaerman model is an in-series combination of the dense liquid and elastic solid models (Khazanovich and Ioannides 1993). Like the Kerr model, it overcomes the elastic solid model's shortcoming of predicting infinite stresses at a free edge. The computational effort required for the Zhemochkin-Sinitsyn-Shtaerman model is comparable to that of the elastic solid foundation.

3D FINITE ELEMENT MODELS

GEOSYS model

Ioannides et al. (1986) developed user guidelines for a 3D finite element pavement model. GEOSYS, an existing 3D finite element program, was adopted for this study. The authors stated that their purpose was to "provide an essential guide of the effective utilization of the

three-dimensional finite element approach ... and perhaps eliminate the need for conducting such preliminary and time consuming studies again."

GEOSYS is a multipurpose, 3D, finite element program developed for geotechnical applications. It has a library of several element types including beams, rods, 2D quadrilaterals; and 3D brick and shell elements. Also, it is capable of time-dependent loading, gravity loading, and incremental excavation or construction.

For the pavement studies a 3D isoparametric brick element was used to model both the slab and foundation. The element had eight nodes with three translational degrees of freedom per node. The pavement layers were assumed to be linear elastic, isotropic, homogeneous materials.

Over 100 GEOSYS runs were executed. The effects of the finite element mesh fineness, vertical and lateral subgrade extent, boundary conditions, number of slab layers, vertical division of the subgrade were investigated. No attempt was made to model joints in this study.

The primary findings of the study were:

- A subgrade depth of about 10ℓ should be used to ensure convergence of subgrade deflections and strains.
- A lateral subgrade extent of about 7ℓ to 10ℓ should be used ensure convergence of subgrade deflections.
- The horizontal lower subgrade boundary should be on rollers to allow the subgrade elements to distribute loads by deforming. Similarly the lateral boundary conditions should also be rollers.
- Maximum responses of the slab can be modeled adequately by representing the slab as two layers of 3D brick elements. Very little increase in accuracy can be gained by increasing the number of layers in the slab to five or even six layers.

- The subgrade may be divided into three regions in the vertical direction. The upper region should extend to a depth of 1ℓ . The thickness of the finite element layers should not be greater than 0.25ℓ to 0.5ℓ . The middle region should extend from a depth of 1ℓ to 4ℓ and should be divided into at least two layers of elements. The lower region may be divided into one or more layers of elements.
- Smaller subgrade elements are required near the slab with the element size increasing near the lateral boundaries.
- The slab mesh fineness ratio, defined as the ratio of the shortest plan view length of the element to the element thickness should be less than 0.8. The element aspect ratio, defined as the ratio of the long plan view side of the element divided by the short plan view side of the element, should be less than 4.

ABAQUS models

ABAQUS is a general-purpose, nonlinear, 3D, dynamic finite element code developed by Hibbit, Karlsson, and Sorensen, Inc. (ABAQUS 1993). ABAQUS incorporates a comprehensive library of element types and material models.

Zaghoul and White (1993) used ABAQUS to perform nonlinear, dynamic analysis of rigid highway pavements. Their 3D model was very general and included such aspects as vertical friction between the pavement edge and the adjacent soil and the lateral passive pressure of the adjacent soil. The slab, subbase, and subgrade were modeled with 3D, eight-node continuum elements. The subgrade was modeled with up to five different layers. Coulomb type friction was imposed between layers with full contact between the slab and subbase assumed as an initial condition.

Joints were modeled using gap elements with an initial opening in the range of 9 to 19 mm (0.35 to 0.75 in.). Gap elements were placed between the nodes on each side of the joint to

allow for the nodes to be in contact or separated, depending upon the deformed shape of the slabs. When the nodes were in contact, friction forces were developed. Dowel bars were modeled as reinforcing bars at the mid-depth of the slabs. Bond stress on one side was assumed to be zero to allow for relative horizontal movements between slabs.

Subbase and base courses were modeled using nonlinear, stress-dependent constitutive models. The subbase and granular subgrade materials were modeled with the Drucker-Prager incremental plasticity model. This model predicted elastic material behavior at stress levels below a yield criteria and plastic behavior beyond the yield criteria. All unloading was linear elastic.

Clay subgrades were modeled with a critical state plasticity model, often referred to as the modified Cam-Clay model. This model is based upon the concept of a critical state defined as that stress state for which, upon yielding, perfectly plastic flow occurs. The loci of all critical state points forms a critical state line which effectively separates stress states for which softening behavior and hardening behavior occurs.

The load was applied in such a fashion to simulate a truck tire traveling at various velocities across the pavement. Parametric studies were conducted to investigate the effects of the load velocity, load position, load magnitude, base course, dowel bars, joint width, and slab thickness. The pavement modeled for these studies consisted of a 200 mm (7.9 in.) thick concrete slab resting directly on a sandy subgrade. The model was loaded with an 80 kN (18,000 lb) single axle load moving at a speed of 2.8 km/h (4.5 mi/hr). The results of the parameter studies were consistent with the current state of knowledge of joint behavior. The analyses indicated that dowel bars increased the joint efficiency and decreased the maximum vertical deflections. The model also predicted an increase in joint efficiency with closer

dowel spacing. The effect of a stiff subbase on joint efficiency increased the joint efficiency for both doweled and undoweled joints.

Kuo (1994) attempted to realistically model some of the more complex aspects of rigid pavement behavior with a three-dimensional model developed using ABAQUS. He used this model to study the effects of various foundation supports, base thicknesses and stiffness, interface conditions between layers, temperature and moisture gradients, and load transfer at joints. One of the major objectives of his research was to investigate factors influencing the value of the modulus of subgrade reaction, particularly for pavements with stabilized layers. The second major objective was to determine the effects of base layers on slab response.

As a part of his research Kuo conducted an investigation into the proper element types to model the slab on grade using the ABAQUS "FOUNDATION" model. The "FOUNDATION" option in ABAQUS is equivalent to the dense liquid or Winkler foundation of classical analysis. In applying the "FOUNDATION" option, the user simply applies a spring coefficient (with units force/length³) to the face of an element. Kuo found that the twenty-node isoparametric brick element with reduced integration (C3D20R) adequately approximated the theoretical Westergaard solution. This element formulation was subsequently used in more sophisticated analyses involving the modeling of the base and subgrade layers.

Kuo employed a simplistic yet effective model for aggregate interlock and doweled joints. Aggregate interlock was modeled using the ABAQUS "JOINTC" element type. The "JOINTC" element, which can be applied in both 2D and 3D analyses, is placed between nodes on either side of the joint. Translational and rotational spring constants can be used to define the joint stiffness in both translational and rotational degrees of freedom. The spring constants are specified as piecewise linear functions of the displacement in the active degree of freedom. Damping can also be specified in a dynamic analysis. Kuo compared the results

of this ABAQUS "JOINTC" model with those from an ILLI-SLAB run with the same shear interlock stiffness and found that the results compared very closely for both load transfer efficiency and maximum slab stresses.

Kuo modeled doweled bars with beam elements. To account for slip of one end of the dowel bars, he invoked the "SLIDER" option, one of the multipoint constraints available in ABAQUS. A multipoint constraint is a restriction imposed between degrees of freedom of a model. The "SLIDER" multipoint constraint allows the possibility of a node moving along a straight line defined by two other nodes and the line length of change. By invoking this restraint, Kuo was allowed one end of the dowel bar to move relative to the slab. However, Kuo did not model dowel-concrete interaction. He found that his model compared favorably with ILLI-SLAB when a very high dowel concrete interaction was assumed in ILLI-SLAB.

CHAPTER 6: SMALL-SCALE PHYSICAL MODEL STUDIES

Physical modeling techniques were used by early researchers to supplement the results obtained from analytical studies, full-scale test tracks, and observations of in-service pavement performance. Small-scale physical models were used to verify Westergaard's theory for interior and edge loading, particularly as it related to the effects of contact pressures and multiple-wheel loadings (Mellinger and Carlton 1955). Similarly, small-scale models were used extensively in developing and verifying design procedures for prestressed concrete pavements (Corps of Engineers 1962, 1963). The effects of sawkerfs and bored recesses of the load-carrying capacity of rigid pavements were investigated by Behrmann (1966). Perhaps of most importance to this dissertation was a set of yet unpublished small-scale tests on doweled joints, described in more detail later in this chapter.

SINGLE-SLAB MODELS

Test description

Physical model testing to verify Westergaard's theory for predicting maximum stresses acting at the interior and edge of rigid pavement slabs were conducted in the early to mid-1950s (Mellinger and Carlton 1955, Carlton and Behrmann 1956, Behrmann 1972). These tests involved measuring strains resulting from static loadings on Hydostone gypsum cement slabs resting on a solid, natural rubber pad. The materials and dimensions of the models were selected after considering several factors:

- A natural rubber pad was chosen to simulate a uniform subgrade and to provide continuous support.

- Hydrostone gypsum cement was chosen to provide a homogeneous and isotropic material to model a slab of constant thickness.
- The horizontal dimensions of the slab were chosen so that distant edge effects were minimal.
- The thickness of the rubber pad was chosen so that the bottom effects were minimal.
- The size of the loaded area and the thickness of the slab were of such relative dimensions that the ordinary theory of bending of thin plates is applicable.
- Applied loads in the tests were small to ensure that stresses in the model did not exceed the elastic limit of the slab and subgrade.

The material properties that were of concern were:

slab modulus of elasticity, E_s

slab Poisson's ratio, ν_s , and

modulus of subgrade reaction, k .

The basic similitude relationship between the model and prototype was

$$\frac{a_{model}}{\ell_{model}} = \frac{a_{prototype}}{\ell_{prototype}} \quad (6.1)$$

where ℓ is the radius of relative stiffness as defined by Equation 4.1 and a is the radius of the circular loaded area.

The slab dimensions were approximately 380 mm (15 in.) by 380 mm (15 in.) by 3 mm (0.125 in.) thick. The slabs were constructed by placing gypsum cement mortar in a steel form between two plates of glass to insure a uniform thickness. The rubber pad had dimensions of 610 mm (24 in.) by 610 mm (24 in.) by 305 mm (12 in.) thick, and was supported by a rigid concrete table and confined on its sides by a rigid box.

After a 7-day curing period, 6.3-mm- (0.25-in.)-long resistance wire strain gages were bonded to the slab. Up to 17 gages were installed on a single slab. Experience with corresponding gages bonded opposite each other on the top and bottom of the slab had shown that strain measurements were identical within the precision of the gages. Thus the strain gages were typically placed on the top of the slab for convenience. The slab was subsequently placed directly on the rubber subgrade. A layer of 19-mm (0.75-in.) lead cubes was uniformly distributed over the top surface of the slab to insure intimate contact between the slab and subgrade. Static loads were applied through a circular rubber pad cemented to a rigid die. The static load was applied by means of a reaction beam as shown in Figure 6.1.

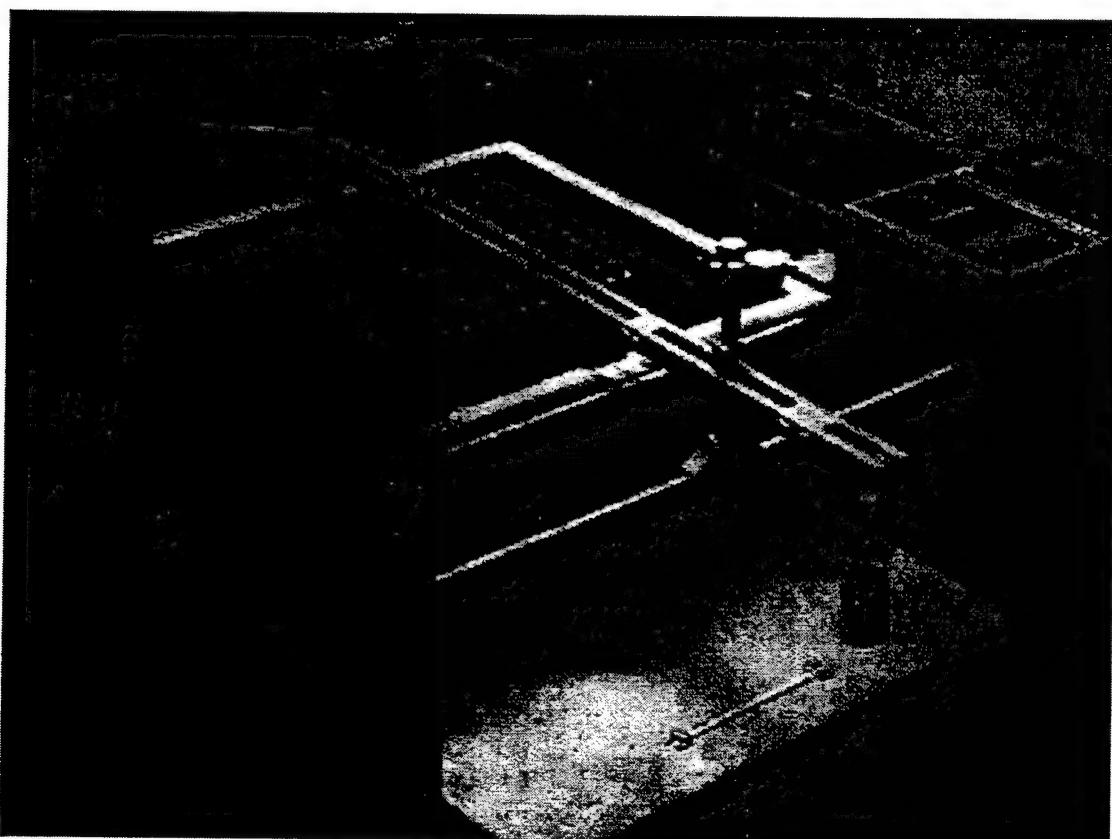


Figure 6.1 Photograph of small-scale physical models test setup

The measured elastic properties of the cured gypsum cement were $E_s = 20,700 \text{ MPa}$ (3,000,000 psi) and $\nu_s = 0.25$. The flexural strength was 17 MPa (2,500 psi). The modulus of subgrade reaction of the natural rubber subgrade was determined by measuring the volumetric displacement of the subgrade within the limits of the slab as 9.6 MPa/m (35 psi/in.) for interior loading and 17.8 MPa/m (65 psi/in.) for edge loading. Based upon the physical constants of the model, the model had a radius of relative stiffness of approximately 43 mm (1.7 in.).

Test results and analysis

Figure 6.2 shows a contour plot of deflections for a typical test under edge loading conditions (Carlton and Behrman 1956). Figure 6.3 shows the deflection basin profile from the test shown in Figure 6.2 along with profiles obtained from finite element solutions from ILLI-SLAB. The experimental basin was obtained by carefully scaling the deflections along the edge from Figure 6.2. The lower ILLI-SLAB deflection basin was obtained using the reported values of $E_s = 20,700 \text{ MPa}$ (3,000,000 psi), $\nu_s = 0.25$, and $k = 17.8 \text{ MPa/m}$ (65 psi/in.). Obviously, the calculated response using these values does not approximate that of the experiment. Therefore, an iterative backcalculation procedure was used to determine the combination of E_s and k (holding $\nu_s = 0.25$) which would produce a deflection basin profile matching that of the experiment. The best match curve is shown as the upper ILLI-SLAB curve in Figure 6.3. These backcalculated material characterization values were as follows:

$$E_s = 24,340 \text{ MPa} (3,530,000 \text{ psi})$$

$$\nu_s = 0.25$$

$$k = 44.11 \text{ MPa/m} (162.5 \text{ psi/in.})$$

These values will be used in analyses of data from scaled dowel joint models.

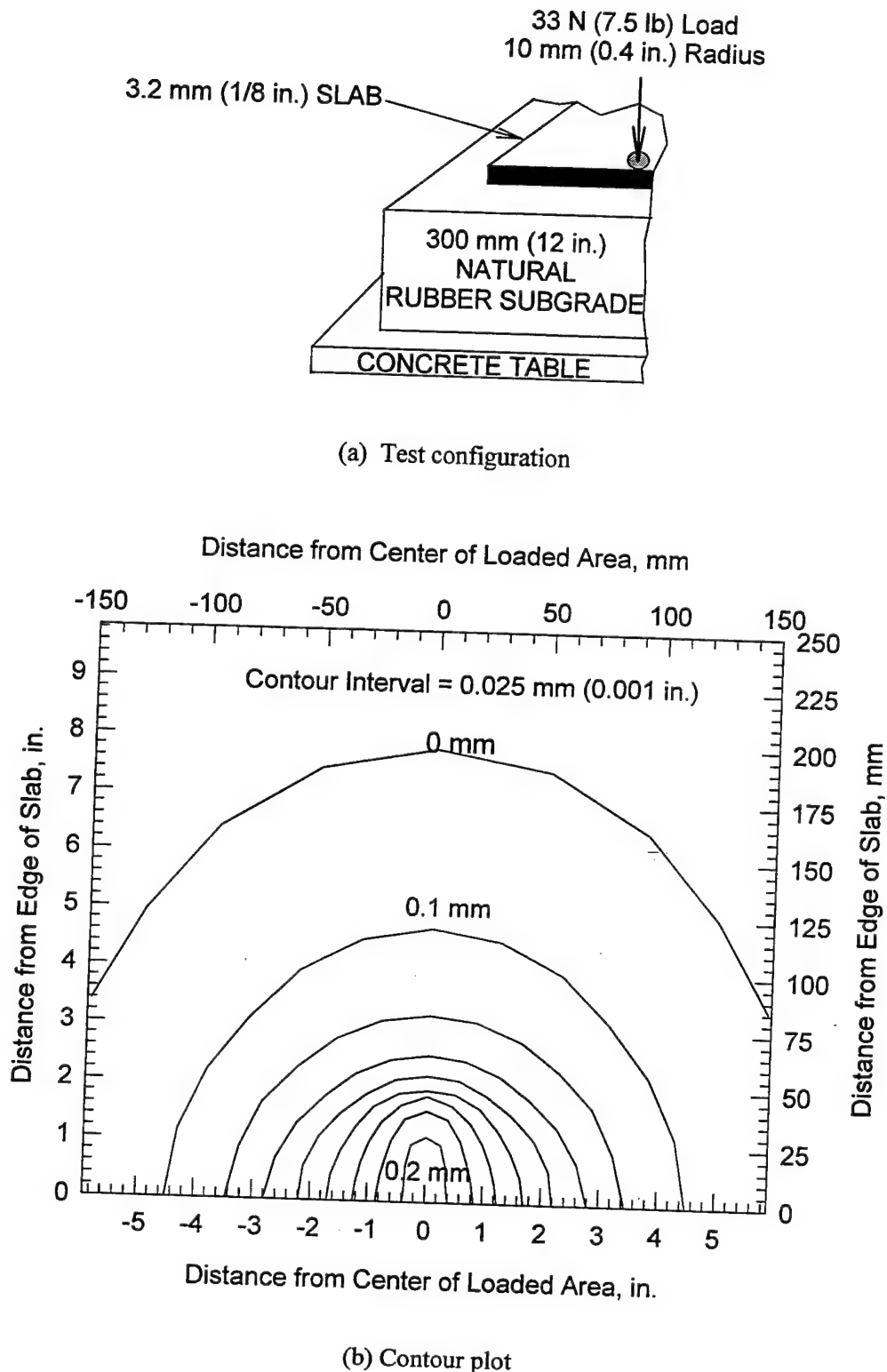


Figure 6.2. Edge loading deflection contours from small-scale model study
(after Carlton and Behrman 1956)

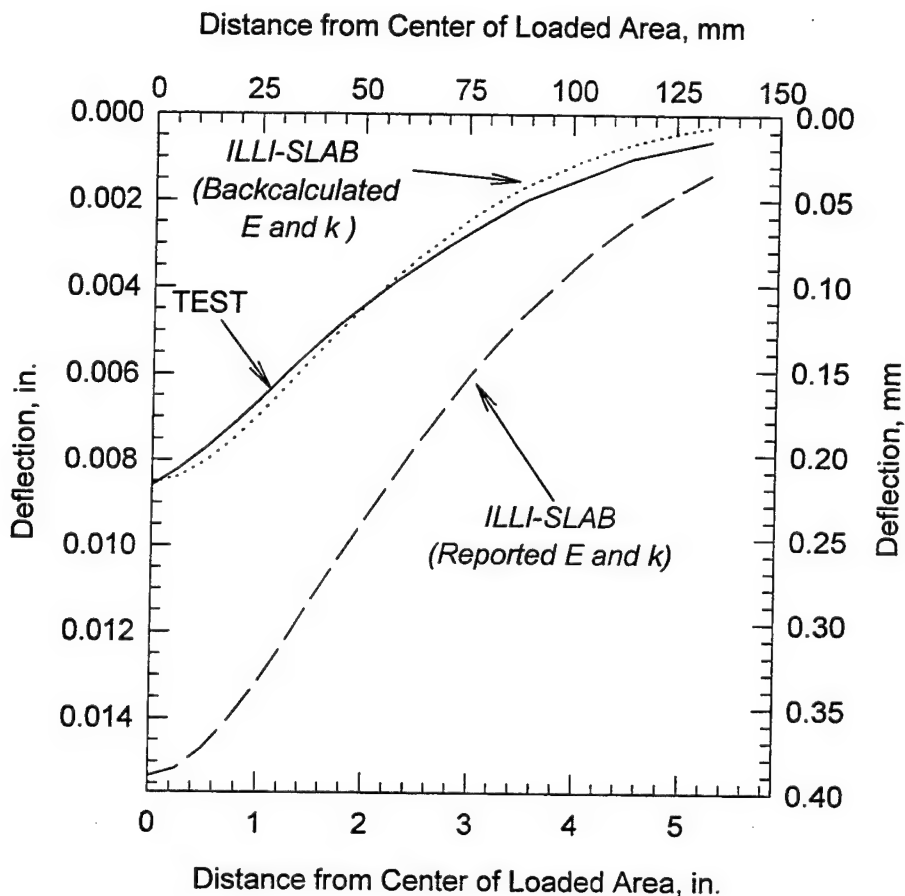


Figure 6.3. Comparison of edge loading deflection basins from experiment and ILLI-SLAB

The results of these model studies indicated that models were excellent analog devices for investigating a wide variety of problems related to rigid pavement design. Model studies can be used to study conditions for which a theoretical solution has not been developed or to verify the applicability of new theory. In fact, these small-scale models were referred to as an "analog computer," and were a very significant part of the Corps' investigational program.

DOWELED JOINT MODELS

Test description

By the early 1950s certain Corps researchers thought that the thickness requirements for heavily-loaded pavements had reached such proportions that the formulation of a definitive method of design for doweled joints was imperative. These objectives were never fully achieved. In an attempt to obtain basic information about the behavior of doweled joints under various loading conditions, a study using small-scale physical models was undertaken by the Ohio River Division Laboratories in 1954. The stated objective was to use these behavior data to develop criteria for use in a rational method for design of doweled joints. The techniques of model construction and data collection described for single slabs above were used to study various combinations of doweled joint designs and loading conditions.

Hydrostone gypsum cement slabs approximately 5.08 mm (0.2 in.) thick were fabricated. A single joint simulating a longitudinal construction joint divided the slabs into two halves each approximately 213 mm (8.38 in.) by 425 mm (16.75 in.). Dowels were simulated by music wire located at mid-depth. The joint design was varied by combining different dowel diameters and dowel spacings. The music wire had been straightened by passing an electrical current through the wire while it was under tension.

The subgrade was simulated by a 610-mm (24-in.) square by 305-mm (12-in.) thick pad of natural rubber identical to the one described above for testing of single slabs. The radius of relative stiffness (ℓ) of the models was approximately 51 mm (2 in.). Loads were applied through a single circular footprint whose radii (a) were set at 19.0 mm (0.75 in.), 12.7 mm (0.50 in.), 7.6 mm (0.30 in.), and 5.1 mm (0.20 in.); additional test variables were dowel bar diameter (d), dowel spacing (s), and joint openings (ω). The testing program followed a matrix in which several dimensionless ratios, listed in Table 6.1, were formed among the

variables. For each of the three values of d/h in Table 6.1, slabs were constructed at the three dowel spacings indicated by s/h . Finally, for each combination of d/h , s/h , and w/h , the loading radii were varied among the values indicated by the four a/ℓ ratios.

Table 6.1
Small-Scale Doweled Joint Model Test Parameters

a/ℓ	d/h	s/h	w/h
0.098	0.05	1.5	0
0.156	0.07	2.5	0.025
0.244	0.10	4.5	0.10
0.366			

Each half of the model was cast separately in molds constructed from glass plates and brass bars. One of the brass bars was fitted with holes at the selected dowel spacing. The dowels were cleaned and secured in these holes prior to casting. Dowels in this half were referred to as being bonded. The second half of the model was cast in a similar form arrangement, except the first half was used to form the joint. Dowel surfaces were treated to prevent bonding; dowels in this half were referred to as being unbonded. The slabs were allowed to set for 45 min before the forms were removed and to cure for 7 days before testing.

The two slabs were placed directly on the rubber pad. Two layers of 19-mm (0.75-in.) lead cubes were distributed uniformly over the surface of each slab to ensure continuous contact between the slab and the rubber. Tests were conducted with the load placed directly over a dowel and with the load placed midway between dowels. The loadings were conducted on either side of the joint, referred to as loading on the bonded-dowel side of the joint or loading on the unbonded-dowel side of the joint. Strains were measured at the surface of the slab

immediately above dowels and midway between dowels using resistance wire strain gages bonded to the slab. A typical slab layout showing approximate locations of strain gages is shown in Figure 6.4.

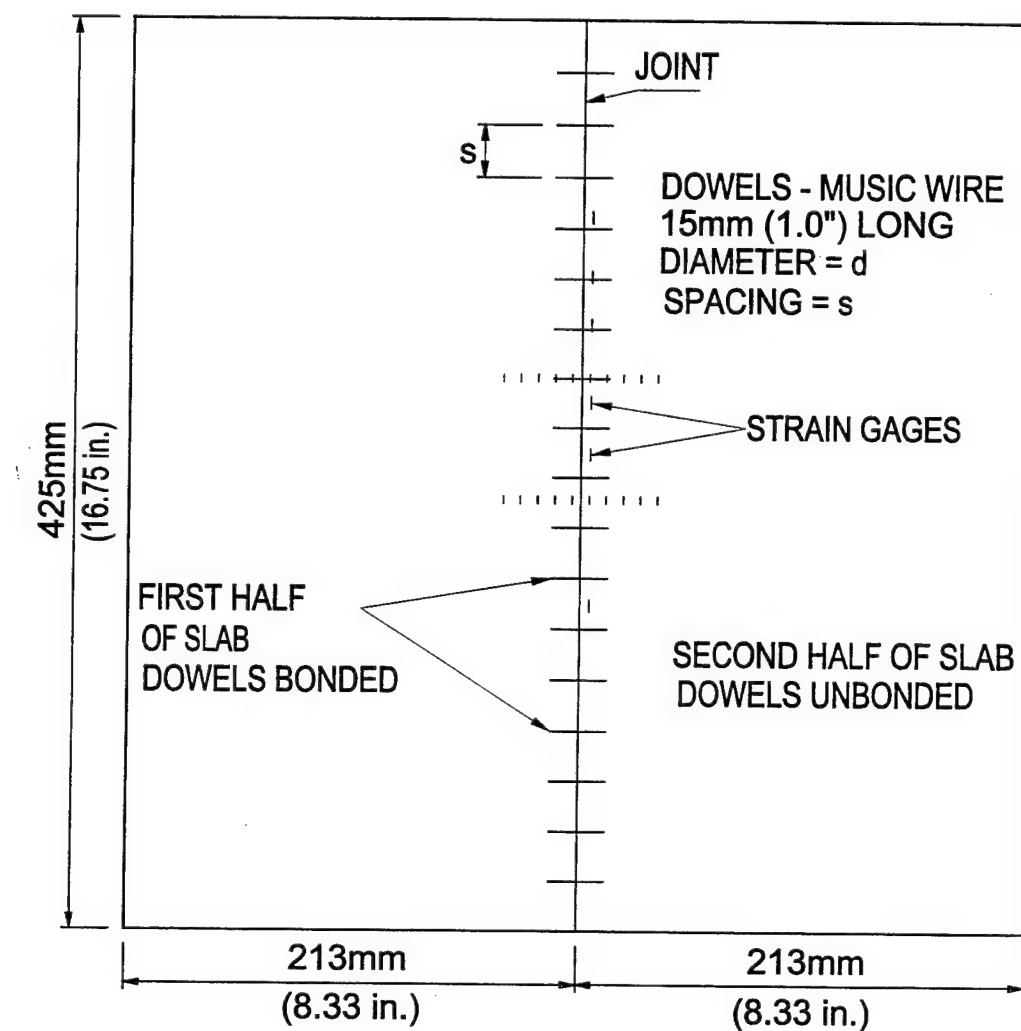


Figure 6.4. Typical small-scale dowel joint test slab showing approximate strain gage positions

Test results

Experimental strain curves are presented in Appendix A. The values of strain measured on either side of the joint were used to estimate load transfer using the following approximation:

$$LT (\%) = \frac{\epsilon_u}{\epsilon_f} \times 100 \quad (6.2)$$

where ϵ_u and ϵ_f are the experimentally obtained edge strains on the unloaded slab and a slab loaded at a free edge, respectively. This approximation differs from an exact measurement of LT , because it neglects Poisson's effects; however, the error in the approximation is small. The estimates of LT are tabulated in Appendix B. These values confirm that load transfer depends on the size of the dowel, spacing of the dowel, joint opening, and radius of the loaded area. For the various combinations of joint parameters tested, the load transfer values obtained in the experiments were mostly greater than 25 percent, supporting data obtained from full-scale experimental slabs.

Analysis

The data were analyzed to backcalculate the joint response parameters necessary to estimate the dimensionless doweled joint stiffness $D/sk\ell$ and the modulus of dowel reaction K . First, the basic material characterizations were assumed to be the same as those backcalculated from the experiments of Carlton and Behrmann (1956); that is,

$$E_s = 24,340 \text{ MPa (3,530,000 psi)}$$

$$\nu_s = 0.25$$

$$k = 44.11 \text{ MPa/m (162.5 psi/in.)}$$

The modulus of elasticity of the dowels were set at $E_d = 207,000 \text{ MPa}$ ($30,000,000 \text{ psi}$) and a Poission's ratio of $\nu_d = 0.25$, values typical of steel. For each combination of test parameters, LTE_δ was estimated from LTE_o using Equation 4.13.

Table 6.2 summarizes the backcalculated values of the modulus of dowel reaction and doweled joint stiffnesses. These data are plotted in Figures 6.5 and 6.6. In Figure 6.5 values of K have been normalized by forming the dimensionless ratio of $K(h - d)/E$ suggested by Nishizawa et al. (1989). Backcalculated values of dimensionless joint stiffness ranged from a low of 3.7 to a high of 996.2, a range of three orders of magnitude. In almost every case, the backcalculated values of dimensionless joint stiffness decrease as the joint opening increases and increase as the dowel diameter increases, which follows with intuition. However, modulus of dowel reaction does not appear to be as well behaved as the dimensionless joint stiffness. Backcalculated values of K varied from $0.3 \times 10^6 \text{ MPa/m}$ ($1.0 \times 10^6 \text{ psi/in.}$) to $598 \times 10^6 \text{ MPa/m}$ ($2,220 \times 10^6 \text{ psi/in.}$). These values range from approximately equal to those values commonly reported in the literature to some two orders of magnitude greater than those commonly reported. The reasons for these discrepancies are not immediately apparent. However, it is possible that there exists a significant size effect, similar to that observed as the size of the circular plate is varied in the plate bearing test method for determining the modulus of subgrade reaction. It should be noted that K is not an intrinsic material property, but rather a system parameter. Thus, K , like the modulus of subgrade reaction, is a useful tool for calculating system response, but can be difficult to measure even in carefully controlled experiments, and even more difficult to estimate *a priori* for design purposes. Despite the limitations exhibited by the modulus of dowel reaction, the experimental data confirm the usefulness of the dimensionless joint stiffness as a means of characterizing the response of the doweled joint.

Table 6.2
Backcalculated Doweled Joint Response Parameters

Test Name	s/h	d/h	ω/h	$K 10^6$ psi/in.	$K 10^6$ MPa/m	D/skℓ
8-DJ	1.5	0.05	0	14.6	4.0	18.3
			0.025	10.3	2.8	12.8
			0.100	5.1	1.4	6.1
5-DJ	2.5	0.05	0	47.4	12.9	27.1
			0.025	14.4	3.9	10.0
			0.100	8.8	2.4	5.3
14-DJ	4.5	0.05	0	30.4	8.2	10.6
			0.025	22.3	6.0	7.5
			0.100	12.6	3.4	3.7
7-DJ	1.5	0.07	0	6.8	1.8	18.6
			0.025	4.6	1.2	13.0
			0.100	3.3	0.9	8.8
3-DJ	2.5	0.07	0	34.7	9.4	38.0
			0.025	11.8	3.2	15.6
			0.100	7.4	2.0	9.16
13-DJ	4.5	0.07	0	327	88.7	116.4
			0.025	52.5	14.3	26.1
			0.100	50.6	13.7	17.7
6-DJ	1.5	0.10	0	31.1	8.4	110.4
			0.025	9.7	2.6	43.3
			0.100	5.2	1.4	24.0
4-DJ	2.5	0.10	0	231	62.6	297.6
			0.025	94.3	25.6	134.4
			0.100	43.6	11.8	59.5
12-DJ	4.5	0.10	0	1.0	0.3	996.2
			0.025	2,220	598	554.3
			0.100	52.3	14.2	37.1

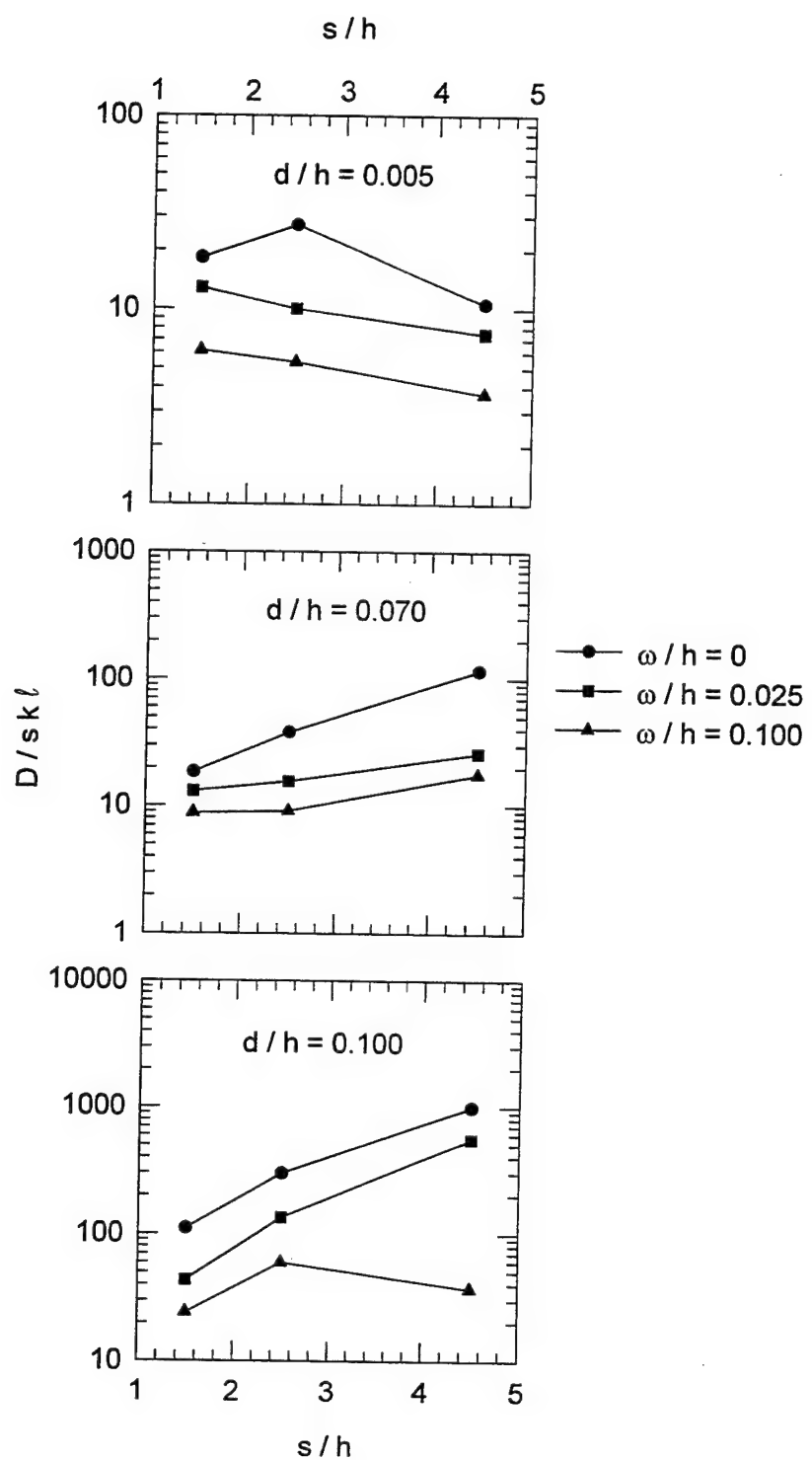


Figure 6.5. Backcalculated dimensionless joint stiffness from small-scale model tests

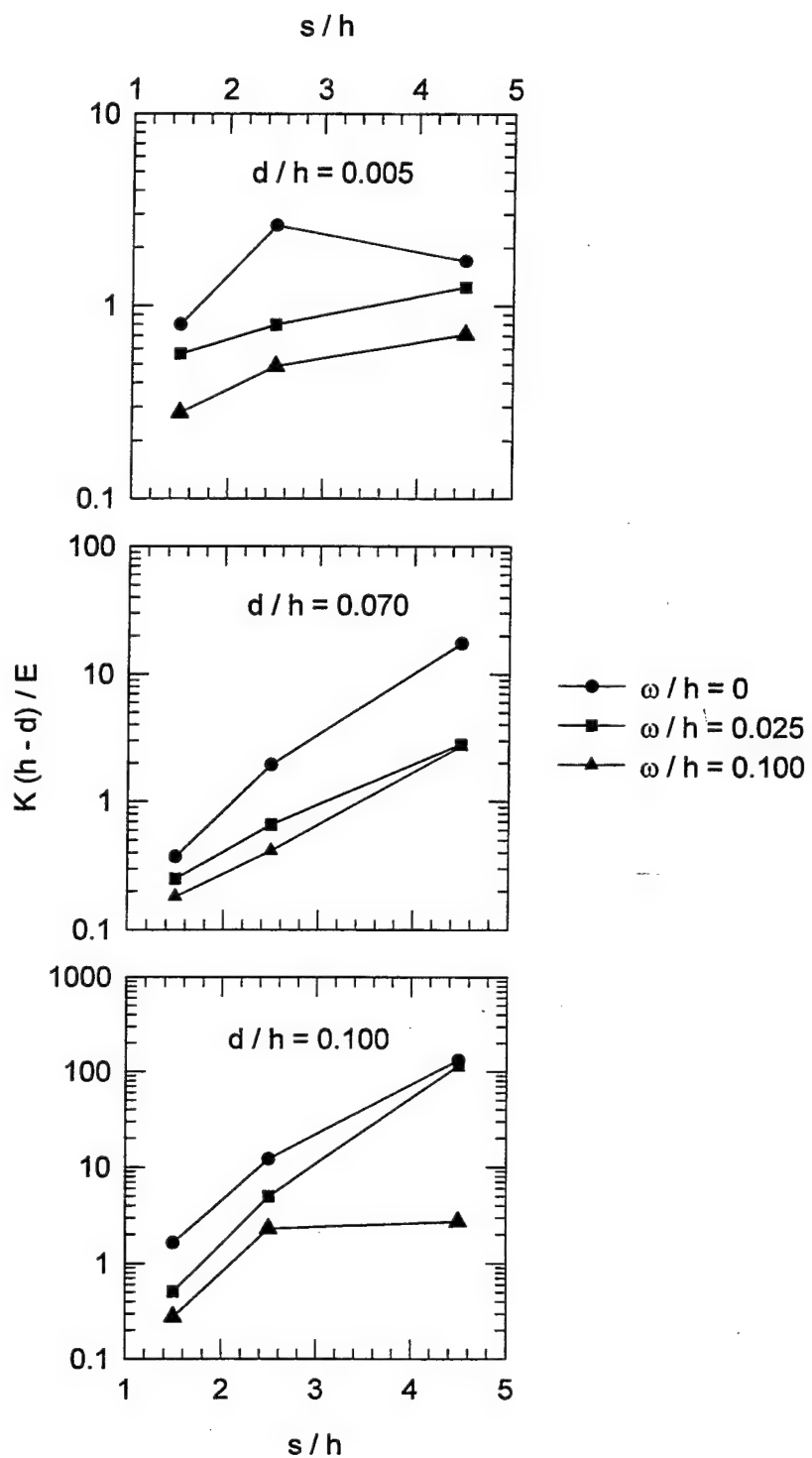


Figure 6.6. Backcalculated modulus of dowel reaction from small-scale model tests

CHAPTER 7: FINITE ELEMENT RESPONSE AND SENSITIVITY STUDIES

BACKGROUND

This chapter contains a discussion of response and sensitivity studies conducted with the finite element code ABAQUS. The finite element method is a numerical procedure for obtaining approximate solutions to many types of problems in structural analysis and mechanics, heat transfer, fluid flow, and other disciplines of engineering. It makes use of an approach referred to as "going from part to whole," i.e., instead of solving the problem for an entire body in one operation, the solution is approximated for discrete elements and then combined to obtain the solution for the whole (Desai and Abel 1972). As such, the solution for the whole is, at best, no better than the approximations used for the discrete elements.

Purpose of sensitivity studies

The purpose of these sensitivity studies was primarily to select the refinement of the discretization (referred to as the mesh fineness) and the approximations within the elements (choice of element type) for the 3D rigid pavement problem. This process involved producing a number of finite element models with varying mesh fineness and element types, executing those models to obtain approximate solutions, and observing the convergence trends for key response parameters such as bending stress, shear stress, and deflection. Where possible, these responses were compared to analytical solutions and experimental results. All discussions presented in this chapter are relevant to ABAQUS, but would likely hold for any finite element code with identical element types and solution schemes.

First, a well-accepted analytical solution was chosen to check the accuracy of the approximations made by the various finite element models produced during the sensitivity studies. Because of the widespread acceptance and verification of Westergaard's theory, it was chosen for this study. For the sensitivity studies to be valid, the finite element models generated must be compatible with Westergaard's assumptions. Thus, all sensitivity studies for this research were conducted for the general problem of an elastic plate resting on a bed of springs foundation considering interior or edge loading conditions. Solutions to Westergaard's theory include Westergaard's equations, Pickett and Ray response charts, and computerized solutions such as WESTER, a computerized compendium of Westergaard solutions developed by Ioannides (1984). ILLI-SLAB is perhaps the most widely used and verified 2D plate theory finite element solution for the rigid pavement problem. Thus, where possible, all finite element solutions were compared against a Westergaard theory solution obtained from WESTER. Also, an ILLI-SLAB solution, developed considering the user guidance given by Ioannides (1984), was used as a benchmark.

Description of ABAQUS

ABAQUS is a general-purpose finite element program developed and marketed by Hibbit, Karlsson, and Sorensen, Inc. of Pawtucket, Rhode Island. ABAQUS is written in transportable FORTRAN, although the input/output routines are optimized for specific computer systems. The source code for ABAQUS, not available to the user, contains about 300,000 executable statements.

One of the salient features of ABAQUS is its use of the library concept to create different models by combining different solution procedures, element types, and material models. The analysis module consists of an element library, a material library, a procedure library, and a loading library. Selections from each of these libraries can be mixed and matched in any

reasonable way to create a finite element model. Among the element families in the element library are the following which are of specific interest for this research:

- First- and second-order continuum elements in one, two, and three dimensions.
- First- and second-order axisymmetric and general shell elements.
- Contact elements and surfaces for determining normal and shear stresses transmitted at the point of contact between two bodies.
- Special purpose stress elements such as springs, dashpots, and flexible joints.

The material library includes linear and nonlinear elasticity models as well as plasticity and viscoplasticity formulations. The analysis procedure library includes static stress analysis, steady-state and transient dynamic analysis, and a number of other specialized procedures.

All ABAQUS computations were conducted on Cray Y-MP or Cray C-90 supercomputers. Finite element model development for ABAQUS was accomplished interactively on engineering workstations using The MacNeal-Schwendler Corporation's PATRAN software incorporating an ABAQUS application interface. PATRAN was also utilized to post-process many of the results from ABAQUS.

Isoparametric element considerations

All of the ABAQUS continuum finite elements considered for this study were modern, isoparametric element formulations. Isoparametric elements are elements for which the geometry and displacement formulations are of the same order. Stated more precisely, the interpolation of the element coordinates and element displacements use the same interpolation functions, which are defined in a natural coordinate system (Bathe 1982). A natural coordinate system is a local coordinate system which specifies the location of any point within the element by a set of dimensionless numbers whose magnitudes never exceed unity (Desai and

Able 1972). An interpolation function N_i must be formulated such that its value in the natural coordinate system is unity at node i and zero at all other nodes. The full development of isoparametric elements is documented in many finite element texts and will not be discussed here.

Isoparametric elements satisfy the following necessary and sufficient conditions for completeness and compatibility (Desai and Abel 1972):

- The displacement models must be continuous within the elements, and the displacements must be compatible between adjacent nodes.
- The displacement modes must include the rigid body displacements of the elements.
- The displacement models must include the constant strain states of the element.

The isoparametric concept is a powerful generalized technique for constructing complete and conforming elements of any order (Desai and Abel 1972). In the first-order or linear element, the interpolation functions of the elements are linear with respect to the natural coordinates. Similarly, for a quadratic or second-order element, the interpolation functions are quadratic with respect to the natural coordinates.

A second-order element which has interpolation function based solely upon nodes at the corners and mid-sides of the element is commonly referred to as a serendipity element, while those elements that feature an internal node and use full product forms of the LaGrange polynomials are referred to as Lagrangian elements. In one dimension (1D), an nth-order Lagrange polynomial is defined as

$$L_k^n(x) = \prod_{\substack{i=1 \\ i \neq k}}^{n+1} \frac{x - x_i}{(x_k - x_i)} \quad (7.1)$$

where the element has $n+1$ nodes defined by the nodal coordinate vector

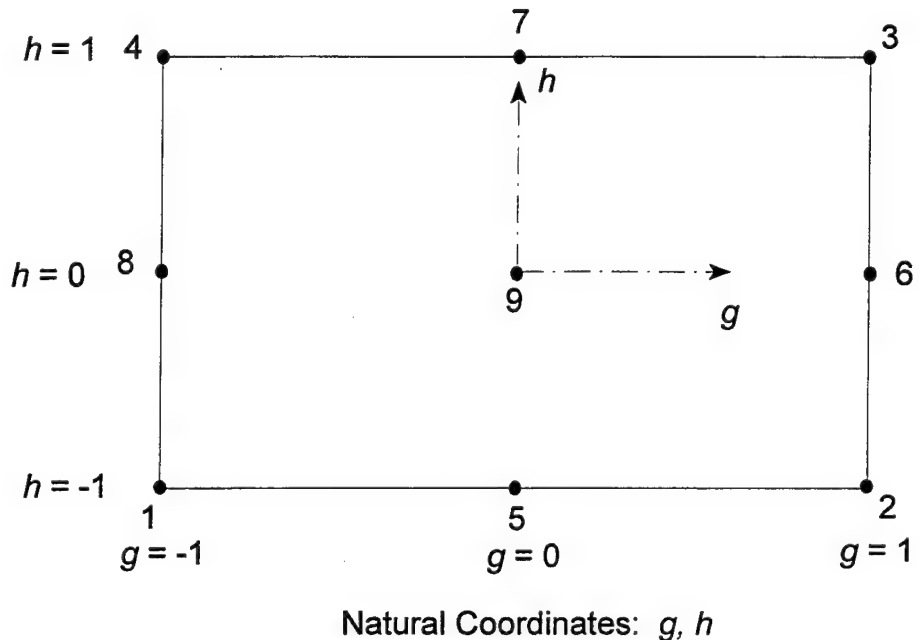
$$\{x\} = \begin{Bmatrix} x_1 \\ x_2 \\ \cdot \\ \cdot \\ \cdot \\ x_{n+1} \end{Bmatrix} \quad (7.2)$$

In 2D and 3D the Lagrange polynomials are made up of products of the 1D Lagrange polynomials.

Figures 7.1 and 7.2 illustrate the Lagrangian and serendipity element interpolation functions, respectively, in 2D for quadrilateral elements. Each of these elements is a second order (quadratic) element. The interpolation functions for the nine-noded element in Figure 7.1 are made up of exclusively of products of Lagrangian polynomials. However, the eight-noded or serendipity element in Figure 7.2 requires additional terms other than products of Lagrangian polynomials to force the value of N_i to be unity at node i and zero at the other seven nodes.

These concepts can be readily extended to 3D continuum elements. The Lagrangian hexahedral element has 27 nodes and 27 interpolation functions which are quadratic products of the Lagrangian polynomials of the three natural coordinates shown here as g , h , and r . The serendipity hexahedral element is characterized by 20 nodes (one at each of the eight corners of the element and one located along each of the twelve lines forming the edges of the element) with twenty corresponding quadratic interpolation functions.

All of the isoparametric elements are integrated numerically. For many element types, the user has the option of selecting elements with full integration or reduced integration. The choice of order of integration is important, because it can have a significant affect on cost of the analysis and on the accuracy of the solution (Bathe 1982). Full integration means that the



Interpolation Functions:

$$N_1 = \frac{gh}{4}(g - 1)(h - 1) \quad N_2 = \frac{gh}{4}(g + 1)(h - 1)$$

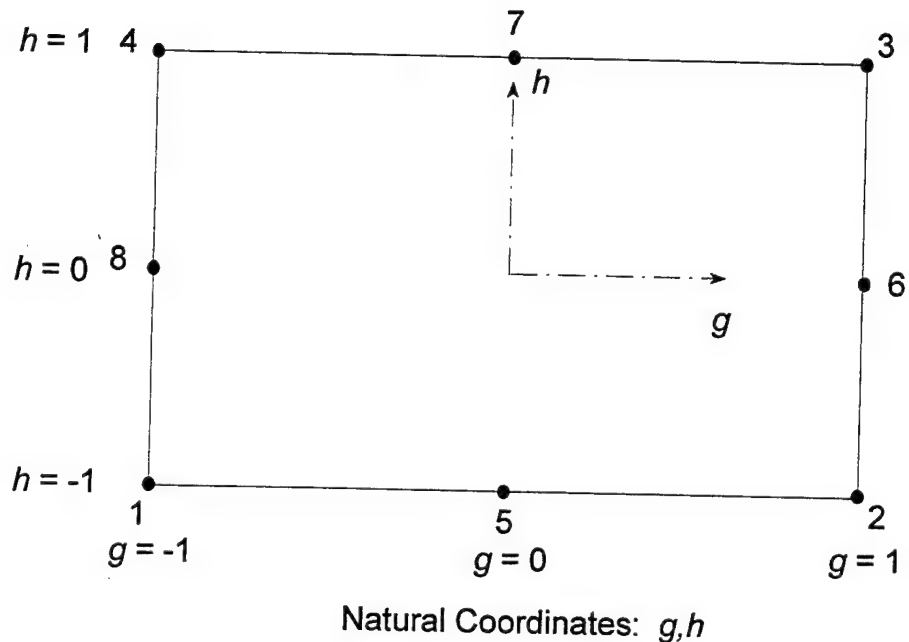
$$N_3 = \frac{gh}{4}(g + 1)(h + 1) \quad N_4 = \frac{gh}{4}(g - 1)(h + 1)$$

$$N_5 = -\frac{h}{2}(h - 1)(g^2 - 1) \quad N_6 = -\frac{g}{2}(g + 1)(h^2 - 1)$$

$$N_7 = -\frac{h}{2}(h + 1)(g^2 - 1) \quad N_8 = -\frac{g}{2}(g - 1)(h^2 - 1)$$

$$N_9 = (g^2 - 1)(h^2 - 1)$$

Figure 7.1. Interpolation functions, 2D Lagrangian isoparametric element



Interpolation Functions:

$$N_1 = -\frac{1}{4}(1-g)(1-h)(1+g+h) \quad N_2 = \frac{1}{4}(1+g)(1-h)(g-h-1)$$

$$N_3 = \frac{1}{4}(1+g)(1+h)(g+h-1) \quad N_4 = -\frac{1}{4}(1-g)(1+h)(g-h+1)$$

$$N_5 = \frac{1}{2}(1-g^2)(1-h) \quad N_6 = \frac{1}{2}(1-h^2)(1+g)$$

$$N_7 = \frac{1}{2}(1-g^2)(1+h) \quad N_8 = \frac{1}{2}(1-h^2)(1-g)$$

Figure 7.2. Interpolation functions, 2D serendipity isoparametric element

Gaussian integration employed will integrate the element stiffness matrix exactly if the determinant of the Jacobian matrix is constant over the element, i.e., if opposing sides for 2D elements or opposing faces for 3D elements are parallel. For reduced integration the integration scheme is one order less than that required to fully integrate the element stiffness matrix. Solution times may be significantly less with reduced integration resulting in considerable savings for large 3D models.

In problems where the predominant response mode is bending, fully integrated first-order elements may "lock"; i.e., the stiffness may be several orders of magnitude too great. Spurious shear stresses known as parasitic shear stresses are present. In these cases a reduction in order of the numerical integration can lead to improved results. The finite element displacement formulation overestimates the stiffness of the system; thus, by not evaluating the element stiffness matrices exactly, better results may be obtained if the error in the numerical integration compensates for the overestimation of the system stiffness. However, a possibility with reduced integration is a type of mesh instability known as hourgassing. For 2D and 3D reduced integration elements, the element stiffness matrix is rank deficient, causing problems with the solution if the element is not provided with sufficient stiffness restraint in the global assemblage of elements. When this occurs, the global stiffness matrix becomes ill-conditioned and, in some cases, singular. An hourglass mode does not result in strain (and therefore does not contribute to the energy integral) leading to spurious zero-energy displacement modes which behave like a rigid-body mode.

Hourglass modes for the first-order reduced integration quadrilateral and hexahedral elements can propagate through the mesh, and hourgassing can become a serious problem. ABAQUS employs hourglass control for these elements in an attempt to suppress hourgassing. In effect, additional stiffness is artificially added to the system to restrain the

hourgassing modes. Default hourglass stiffness values are based upon the elastic properties of the system. Values for these stiffnesses other than the default values may be specified by the user. The artificial energy associated with the hourglass control stiffnesses must be much less than the total strain energy of the system. First-order reduced integration elements with hourglass control may perform satisfactorily for very fine meshes, but can be inaccurate for coarse meshes.

ELEMENT DESCRIPTIONS

The ABAQUS element library contains a vast selection of element types and formulations. A basic understanding of the type of element and assumptions made in the formulation of the element is required before selecting a element for use in a finite element model. The following paragraphs contain brief descriptions of the 2D and 3D elements considered in this response and sensitivity study.

2D element description

Even though the purpose of this research was to develop a 3D finite element model for the rigid pavement system, it was instructive to conduct certain sensitivity studies in 2D. These 2D sensitivity studies were conducted using elements from the ABAQUS element library. The ABAQUS element library contains a large library of general shell elements for analysis of curved shell, plate bending, and membrane problems. For a flat plate subjected to both in-plane and transverse loads, the bending and membrane effects are uncoupled; thus the total response can be obtained by superimposing the bending and membrane responses. In general this is not true of the shell element. The shell element is similar to a plate element, except that the mid-surface of a general shell element can be curved. In this case the bending and membrane stresses are coupled, and it is no longer possible to superimpose the two conditions (Fagan 1992).

The basic assumption for thin plate bending and shell elements is that the thickness, h , is small compared to the minimum in-plane dimension of the structure, L . Thus, the stress perpendicular to the mid-surface of the plate or shell is zero, and material particles originally on a straight line perpendicular to the mid-surface will remain on a strain line as the structure deforms. In the thin plate (or Kirchhoff) theory, transverse shear deformations are neglected, and the cross-section remains plane and perpendicular to the mid-surface during deformations. The rule of thumb is that for values of $L/h > 10$, the Kirchhoff assumptions hold. For case where the transverse shear deformations cannot be neglected, it can be shown that the transverse shear stresses τ_{xz} and τ_{yz} are distributed parabolically across the thickness of the plate or shell with the maximum value occurring at the mid-surface (Timoshenko and Woinowsky-Krieger 1959).

Table 7.1 gives a description of the ABAQUS shell elements considered in this sensitivity study. These elements include first- and second-order finite elements with five or six degrees of freedom per node. All shell elements in ABAQUS employ a reduced integration scheme. Each of the elements with five degrees of freedom per node explicitly impose the Kirchhoff shear constraints (i.e., transverse shear deformation is not allowed). Elements with six degrees of freedom per node, known as “shear flexible” elements, allow transverse shear deformations. When these elements are used for thin shell applications, the default transverse shear stiffness (G_z) imposes the Kirchhoff constraints approximately so that, in many cases, the results are not significantly different from the results from the thin shell elements. Thus, ABAQUS calculates the default transverse shear stiffness as

$$G_z = \frac{5}{6} Gh = \frac{5}{6} \left[\frac{Eh}{2(1+v)} \right] \quad (7.3)$$

Table 7.1
Description of ABAQUS 2D Shell Elements Used in Sensitivity Study

Element Type	General Description	Number of Nodes	Degrees of Freedom per Node	Interpolation	No. of Gauss Points	Notes on Usage
S4R	Isoparametric shell element, reduced integration	4	6 ($u, v, w, \theta_x, \theta_y, \theta_z$)	Linear	1	Subject to hourgassing, intended for thick shell applications
S4R5	Isoparametric shell element, reduced integration	4	5 ($u, v, w, \theta_x, \theta_y$)	Linear	1	Subject to hourgassing, recommended for thin shell applications
S8R	Isoparametric brick element, reduced integration	8	6 ($u, v, w, \theta_x, \theta_y, \theta_z$)	Serendipity quadratic	4	Intended for thick shell applications
S8R5	Isoparametric shell element, reduced integration	8	5 ($u, v, w, \theta_x, \theta_y$)	Serendipity quadratic	4	Recommended for thin shell applications
S9R5	Isoparametric shell element, reduced integration	8	5 ($u, v, w, \theta_x, \theta_y$)	LaGrangian quadratic	4	Recommended for thin shell applications

where

G = shear modulus of shell

h = thickness of shell

E = modulus of elasticity of shell

ν = Poisson's ratio of shell.

Elements S4R and S8R are especially susceptible to hourglass displacement modes in the displacement components perpendicular to the shell surface. In general, the 8-node serendipity element is considered a good basic element for most shell problems. When reduced integration is employed (as is the case for all of the ABAQUS shell elements used in this study), shear locking is of no consequence. Although the reduced integration element can exhibit hourgassing, it, too, is nonconsequential because hourglass modes cannot propagate throughout the mesh (Schnobrich 1990).

3D element description

Table 7.2 contains a listing of the 3D hexahedral elements from the ABAQUS library considered in this study. Element types considered included both linear and quadratic elements, employing both full integration and reduced integration. Furthermore, both Lagrangian and serendipity formulations were considered for the quadratic elements. Each element type features three translational degrees of freedom per node. The C3D27 and C3D27R elements are variable node elements; that is, the number of nodes can be reduced from 27 nodes per element down to 21 nodes per element (or any number between) by removing the interior node from each of the faces of the element as desired.

As is the case with 2D shell elements, fully-integrated elements can exhibit locking where bending is the primary response mode. This is particularly true of the linear element. Reduced integration provides relief from locking but may lead to problems with hourgassing.

Table 7.2
Description of ABAQUS 3D Hexahedral Elements Used in Sensitivity Study

Element Type	General Description	Number of Nodes	Degrees of Freedom per Nodes	Interpolation	No. of Gauss Points	Notes on Usage
C3D8	Isoparametric brick element	8	3 (u, v, w)	Linear	8	Subject to parasitic shear stresses
C3D8R	Isoparametric brick element, reduced integration	8	3 (u, v, w)	Linear	8	Subject to hourglassing
C3D20	Isoparametric brick element, reduced integration	20	3 (u, v, w)	Serendipity quadratic	27	May exhibit locking when used to analyzed bending
C3D20R	Isoparametric brick element, reduced integration	20	3 (u, v, w)	Serendipity quadratic	8	Subject to hourglassing, although rarely problematic
C3D27	Isoparametric brick element	21 - 27	3 (u, v, w)	LaGrangian quadratic	27	May exhibit locking when used to analyzed bending
C3D27R	Isoparametric brick element, reduced integration	21 - 27	3 (u, v, w)	LaGrangian quadratic	14	Subject to hourglassing, although rarely problematic

However, for the quadratic elements, hourgassing is typically nonconsequential, because hourglass modes do not propagate throughout the mesh.

Solution times and the corresponding costs for 3D problems are considerable greater than for their 2D counterparts. This is due to the dramatic increase in the bandwidth and well as the increase in the time required to formulate the element stiffness matrices because of the time required to integrate in the third dimension (Schnobrich 1990).

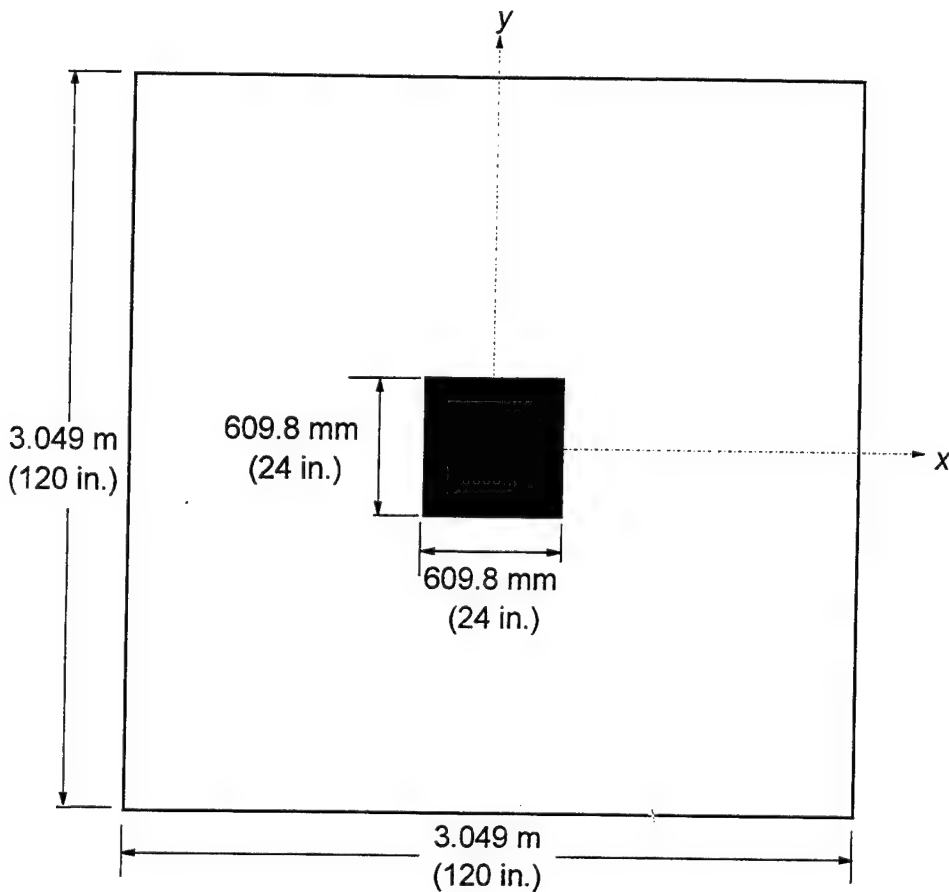
EXAMPLE PROBLEMS FOR SENSITIVITY STUDIES

A set of example problems was selected for performing the sensitivity studies. These problems included three interior load cases and two edge load cases. Each case consisted of an 203.3-mm (8-in.) thick elastic slab resting on a dense liquid foundation with a modulus of subgrade reaction $k = 81.43 \text{ MPa/m}$ (300 psi/in.). The elastic slab had a modulus of elasticity of $E_s = 20,700 \text{ MPa}$ (3,000,000 psi) and a Poisson's ratio of $\nu_s = 0.15$. These values yield a radius of relative stiffness $\ell = 653.1 \text{ mm}$ (25.70 in.).

Interior Load Case I

Figure 7.3 shows the configuration for Interior Load Case I. The slab was square with the length of the sides set at $L = 3.054 \text{ m}$ (120 in.). The center of the slab was loaded with a uniform pressure of $p = 6.895 \text{ MPa}$ (100 psi) over a square area, the length of the sides of the loaded area being 609.8 mm (24 in.). An equivalent circular load would have a radius of $a = 344.0 \text{ mm}$ (13.54 in.); thus the dimensionless load size ratio is $a/\ell = 0.527$. The total applied load was 256.2 kN (57,600 lb).

The personal computer program WESTER was used to obtain a Westergaard solution. Due to the very large size of the load, the Westergaard-type solution for Interior Load Case I may not be entirely accurate. For this case, the maximum interior bending stress predicted



$$\begin{aligned}
 p &= 6.895 \text{ MPa (100 psi)} \\
 k &= 81.43 \text{ MPa/m (300 psi/in.)} \\
 E &= 20,700 \text{ MPa (3,000,000 psi)} \\
 v &= 0.15 \\
 h &= 203.3 \text{ mm (8 in.)} \\
 \ell &= 653.1 \text{ mm (25.7 in.)}
 \end{aligned}$$

Figure 7.3. System configuration, Interior Load Case I

by Westergaard's theory, which occurs beneath the centroid of the loaded area, is 4.434 MPa (643.2 psi); thus the maximum normalized bending stress can be expressed as

$$\left(\frac{\sigma h^2}{P} \right)_{\text{Interior Case I}} = \frac{4.434 \text{ MPa} \times (0.2033 \text{ m})^2}{0.2562 \text{ MN}} = 0.715 \quad (7.4)$$

The maximum deflection from the Westergaard theory, which also occurs beneath the centroid of the loaded area, is 0.8398 mm (0.00331 in.). The maximum deflection, expressed as a dimensionless quotient, is the following:

$$\left(\frac{wkl^2}{P} \right)_{\text{Interior Case I}} = \frac{0.0008398m \times 81.43 \text{ MPa/m} \times (0.6531m)^2}{0.2562 \text{ MN}} = 0.114 \quad (7.5)$$

Interior Load Case II

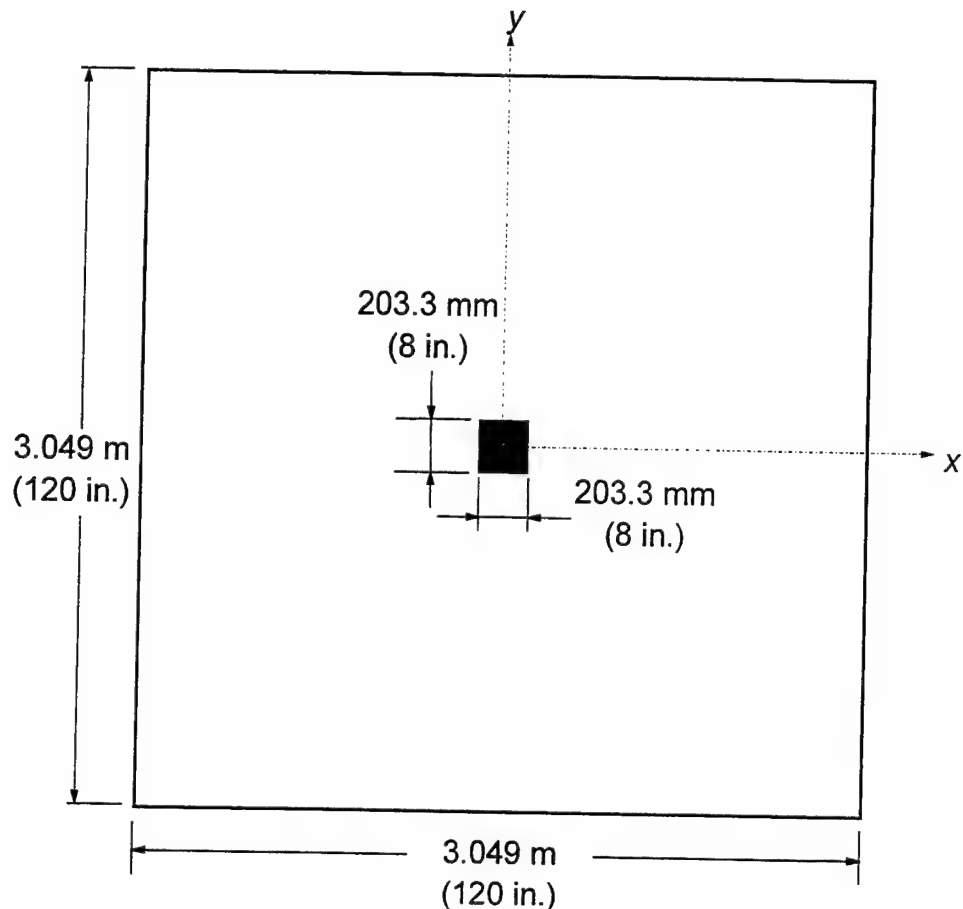
A second interior load case, shown in Figure 7.4, was investigated. This load case was identical to Interior Load Case I, except that the size of the square loaded area decreased to 203.3 mm (8 in.) on a side. Thus, the magnitude of the load was total load was 28.47 kN (6400 lb) for Interior Load Case II. The equivalent radius for circular loaded area is $a = 114.7 \text{ mm (4.51 in.)}$, yielding a dimensionless load size ratio of $a/l = 0.175$.

Again, WESTER was used to obtain the Westergaard solution for Interior Load Case II. For this case, the maximum bending stress is 0.8898 MPa (129.1 psi), yielding a maximum dimensionless bending stress of

$$\left(\frac{\sigma h^2}{P} \right)_{\text{Interior Case II}} = \frac{0.8898 \text{ MPa} \times (0.2033m)^2}{0.02847 \text{ MN}} = 1.29 \quad (7.6)$$

The maximum deflection predicted by Westergaard theory is 0.1010 mm (0.00397 in.), which, expressed as a dimensionless quotient, is

$$\left(\frac{wkl^2}{P} \right)_{\text{Interior Case II}} = \frac{0.0001010m \times 81.43 \text{ MPa/m} \times (0.6531m)^2}{0.02847 \text{ MN}} = 0.123 \quad (7.7)$$

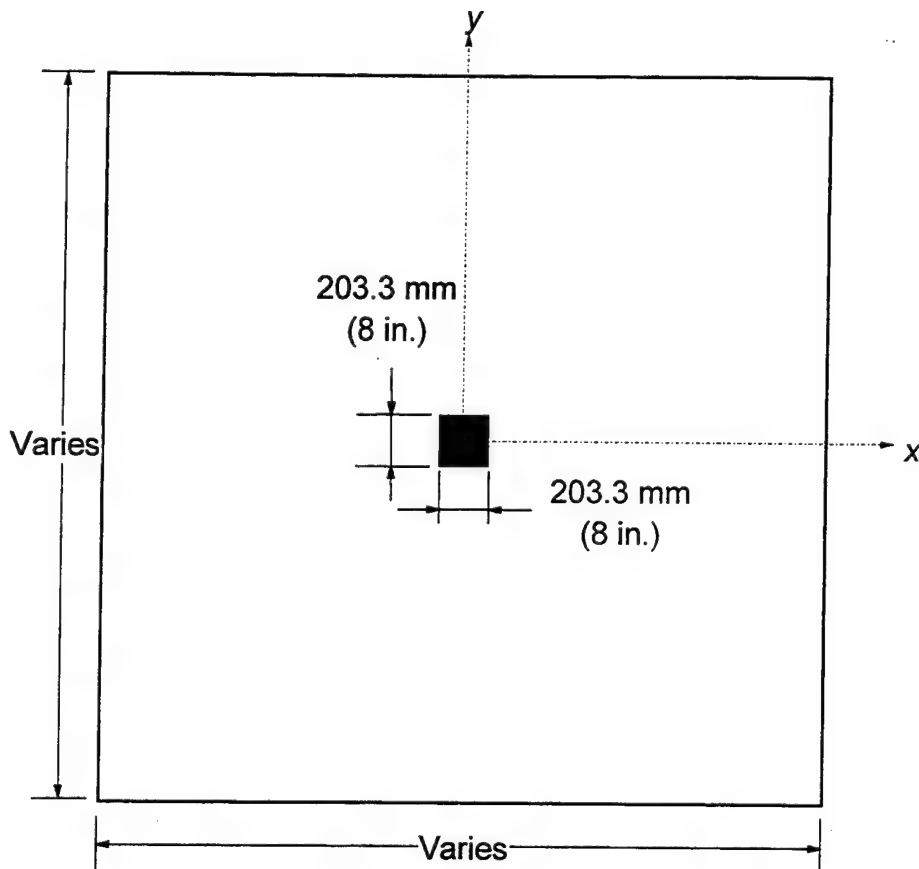


$$\begin{aligned}
 p &= 6.895 \text{ MPa (100 psi)} \\
 k &= 81.43 \text{ MPa/m (300 psi/in.)} \\
 E &= 20,700 \text{ MPa (3,000,000 psi)} \\
 v &= 0.15 \\
 h &= 203.3 \text{ mm (8 in.)} \\
 \ell &= 653.1 \text{ mm (25.7 in.)}
 \end{aligned}$$

Figure 7.4. System configuration, Interior Load Case II

Interior Load Case III

A third interior load case, shown in Figure 7.5, was studied. All slab parameters from Interior Load Case II were retained with the exception of the horizontal extent of the slab,



$$\begin{aligned}
 p &= 6.895 \text{ MPa (100 psi)} \\
 k &= 81.43 \text{ MPa/m (300 psi/in.)} \\
 E &= 20,700 \text{ MPa (3,000,000 psi)} \\
 v &= 0.15 \\
 h &= 203.3 \text{ mm (8 in.)} \\
 \ell &= 653.1 \text{ mm (25.7 in.)}
 \end{aligned}$$

Figure 7.5. System configuration, Interior Load Case III

which was varied from 2ℓ to 10ℓ . In all cases, the slab remained a perfect square. Therefore, the maximum bending stress and deflection as predicted by Westergaard's theory are identical to those of Interior Load Case II.

Edge Load Case I

The edge load case considered in the sensitivity studies is illustrated in Figure 7.6. The slab was rectangular with the maximum dimension of 3.049 m (120 in.) and the minimum dimension of 2.541 m (100 in.). A uniform pressure of $p = 6.895 \text{ MPa}$ (100 psi) was applied at the center of one edge of the slab over a square area, the length of the sides of the loaded area being 203.3 mm (8 in.). An equivalent circular load would have a radius of $a = 114.7 \text{ mm}$ (4.51 in.), yielding a dimensionless load size ratio of $a/\ell = 0.175$. The magnitude of the load was total load was 28.47 kN (6400 lb).

WESTER was used to obtain a Westergaard solution for the edge loading problem. The maximum bending stress, which occurs at the edge of the slab underneath the along the centroidal axis of the loaded area, is 1.719 MPa (249.3 psi) which can be expressed as the dimensionless quotient.

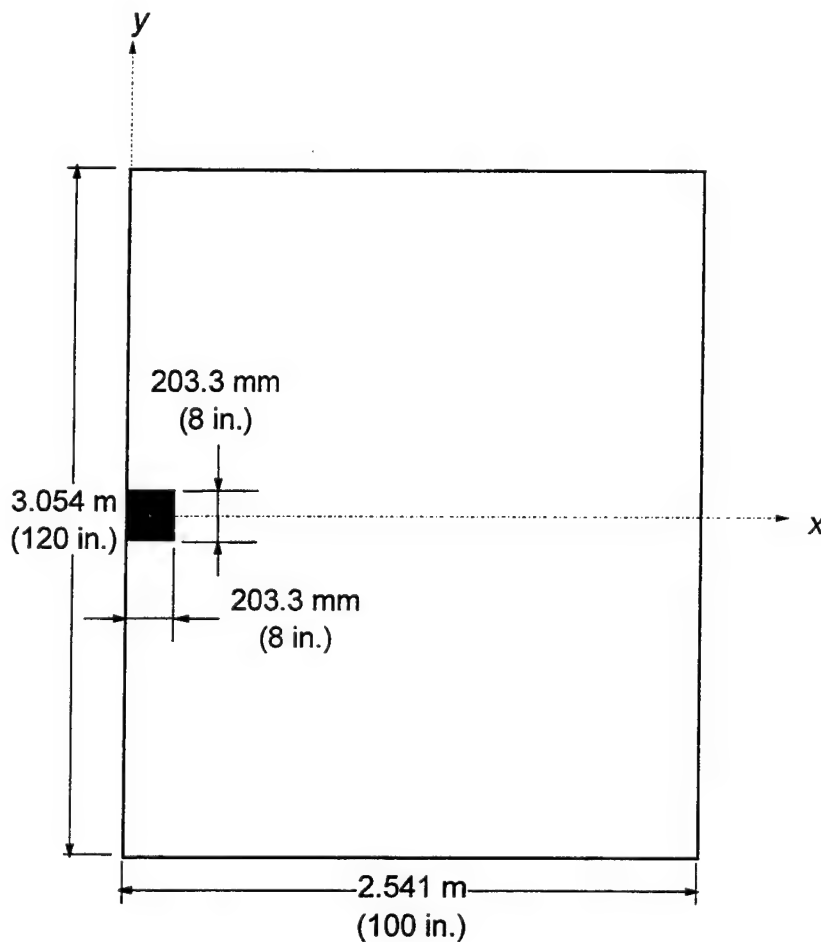
$$\left(\frac{\sigma h^2}{P} \right)_{\text{Edge Case I}} = \frac{1.719 \text{ MPa} \times (0.2033 \text{ m})^2}{0.02847 \text{ MN}} = 2.49 \quad (7.8)$$

The maximum deflection predicted by Westergaard is 302.8 mm (0.01192 in.). The dimensionless deflection is

$$\left(\frac{w k \ell^2}{P} \right)_{\text{Edge Case I}} = \frac{0.0003028 \text{ m} \times 81.43 \text{ MPa/m} \times (0.6531 \text{ m})^2}{0.02847 \text{ MN}} = 0.369 \quad (7.9)$$

Edge Load Case II

A plot of the system configuration for Edge Load Case II is shown in Figure 7.7. The lengths of the sides of the square slab were varied from 2ℓ to 10ℓ . The load, slab thickness, slab elastic properties, and modulus of subgrade reaction were identical to that of Edge Load Case I; thus, the radius of relative stiffness of the system was identical and the expected bending stress and deflection remained unchanged from Edge Load Case I.



$$p = 6.895 \text{ MPa (100 psi)}$$

$$k = 81.43 \text{ MPa/m (300 psi/in.)}$$

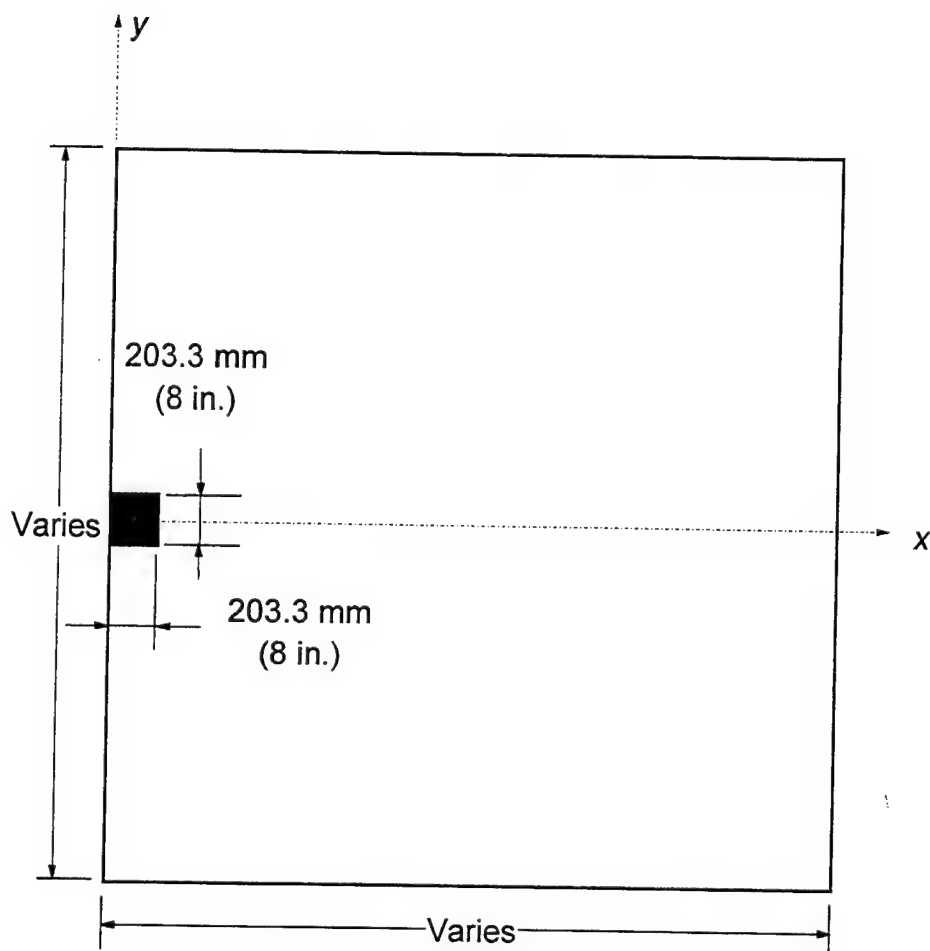
$$E = 20,700 \text{ MPa (3,000,000 psi)}$$

$$\nu = 0.15$$

$$h = 203.3 \text{ mm (8 in.)}$$

$$\ell = 653.1 \text{ mm (25.7 in.)}$$

Figure 7.6. System configuration, Edge Load Case I



$p = 6.895 \text{ MPa (100 psi)}$
 $k = 81.43 \text{ MPa/m (300 psi/in.)}$
 $E = 20,700 \text{ MPa (3,000,000 psi)}$
 $\nu = 0.15$
 $h = 203.3 \text{ mm (8 in.)}$
 $\ell = 653.1 \text{ mm (25.7 in.)}$

Figure 7.7. System configuration, Edge Load Case II

RESPONSE AND SENSITIVITY STUDY RESULTS

Some of the questions to be answered by the response and sensitivity study include the following:

- What 3D hexahedron element is appropriate for the slab-on-grade problem?
- What mesh fineness is required in the plane of the slab surface?
- What mesh fineness is required in the plane of the slab thickness?
- Should the analyst be concerned about transverse shear deformations for interior and edge load cases for rigid pavements?
- What is the minimum slab dimension in the plane of the slab surface required to meet Westergaard's assumption of a semi-infinite or infinite slab? How significant is this boundary effect for finite element modeling?

These issues are addressed in the remainder of this chapter.

Interior Load Case I

Interior Load Case I was the most general load case studied and was primarily intended to study mesh fineness and element selection issues. Studies were conducted in both 2D and 3D. These studies are described and summarized below.

2D convergence studies

Four finite element meshes representing different degrees of mesh refinement were generated. Table 7.3 is a summary of the results of these calculations. The degree of mesh refinement is characterized by the dimensionless ratio $h/2a$ where h is the thickness of the slab and $2a$ is the minimum length of the side of an element. Figure 7.8(a) shows a diagram of the lengths of the sides of the 2D shell elements. Each of the finite element meshes are shown in Figure 7.9.

Table 7.3
Results of 2D Convergence Study, Interior Load Case I

$h/2a$	Mesh Fineness	ILLI-SLAB	ABAQUS					
			S4R	S4R5	S8R5	S8R (Default G_z)	S8R (100 x Default G_z)	S9R5
Dimensionless maximum interior bending stress, $\sigma h^2/P$								
0.67	Coarse	0.804	0.575	0.575	0.804	0.805	0.802	0.716
1.33		0.751	0.695	0.694	0.748	0.748	0.751	0.727
2.67		0.739	0.722	0.722	0.735	0.735	0.739	0.730
4.00		0.736	0.727	0.727	0.733	0.733	0.736	0.733
Dimensionless maximum interior deflection, $wk\ell^2/P$								
0.67	Coarse	0.129	0.130	0.130	0.132	0.132	0.131	0.132
1.33		0.129	0.132	0.132	0.132	0.132	0.139	0.132
2.67		0.129	0.132	0.132	0.132	0.132	0.129	0.132
4.00		0.128	0.132	0.132	0.132	0.132	0.129	0.132

For each mesh the slab was modeled using double symmetry, i.e., both the x-axis and the y-axis were axes of symmetry, thus reducing the memory requirements and computing time. The elements were all square and uniform throughout each mesh. Identical meshes were used for ILLI-SLAB and ABAQUS, with the exception that mid-side nodes were required for the quadratic shell elements in ABAQUS. For the nine-noded ABAQUS shell element, an additional node was required at the centroid of each element.

The Westergaard solution for this problem predicts a greater stress and a lesser deflection as compared to the ILLI-SLAB solution. This is due to the quite large load size ratio ($a/\ell > 0.5$) for this problem. In this case, the ILLI-SLAB solution is more accurate and should be used as the baseline calculation for this load case.

It is immediately apparent from Table 7.3 that for both ILLI-SLAB and ABAQUS deflections converge much faster than stresses. The linear shell elements (S4R and S4R5) performed poorly for the coarser meshes, while the quadratic shell elements (S8R5, S8R, and

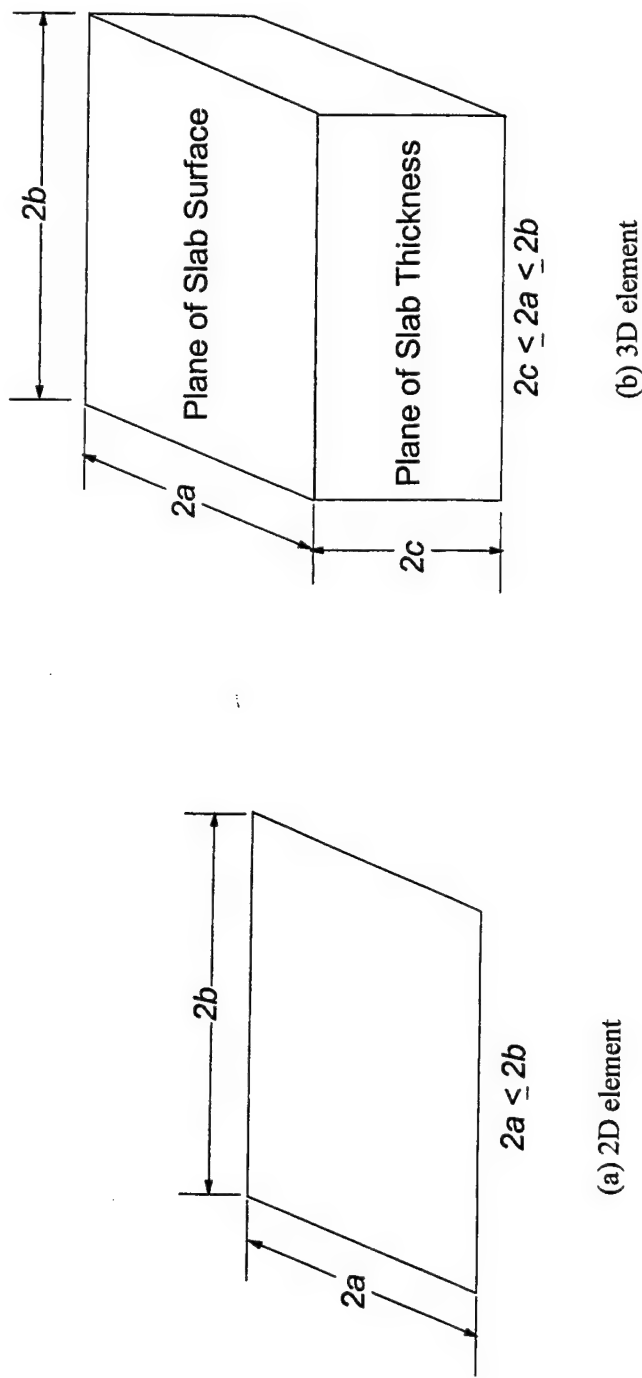


Figure 7.8. Definition of element dimensions for determining mesh fineness

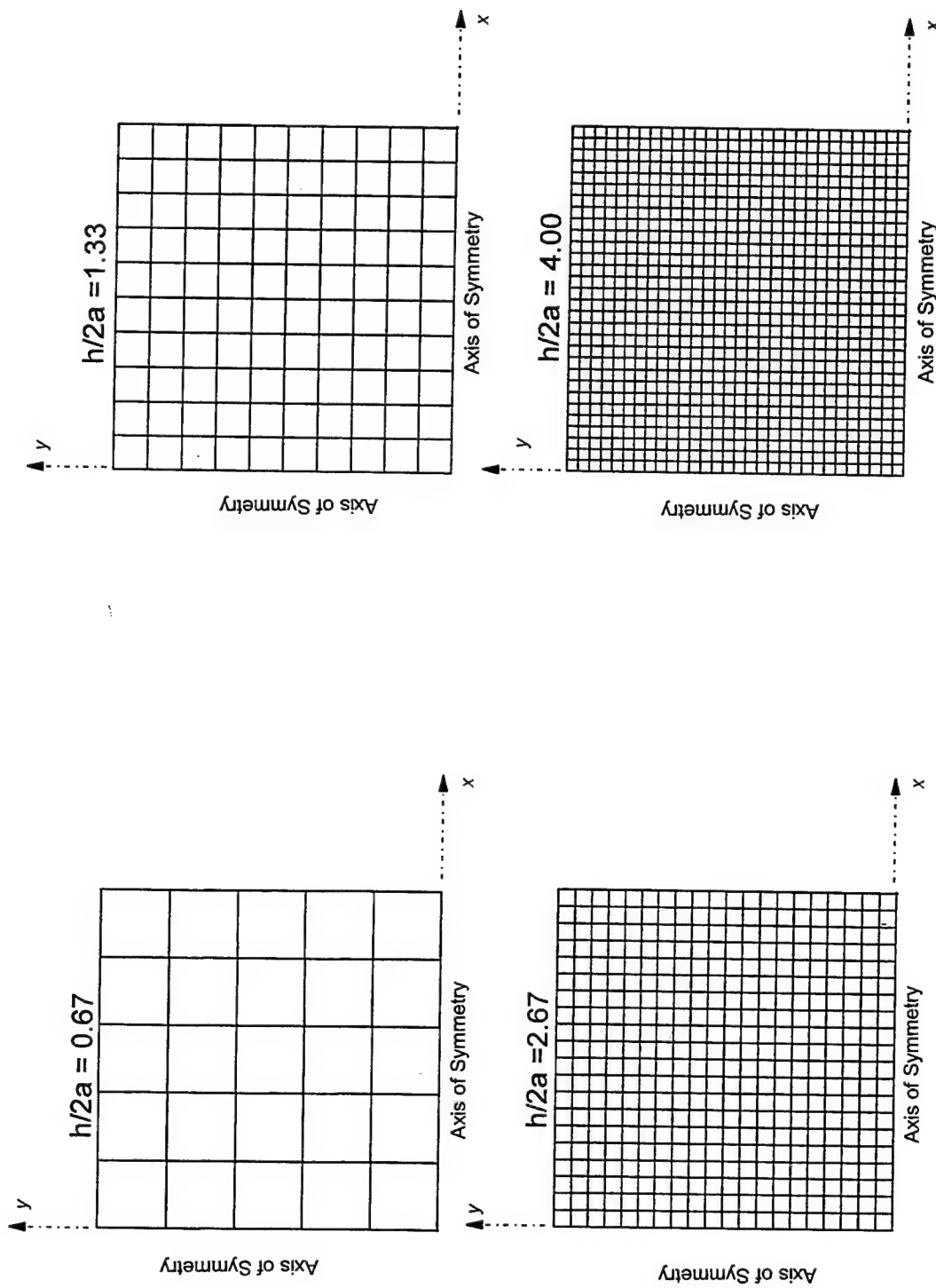


Figure 7.9. Finite element meshes in plane of slab surface, Interior Load Case I

S9R5) performed much better. The differences observed between the ABAQUS shell elements with six degrees of freedom per node (S4R and S8R) and their conjugate element with five degrees of freedom per node (S4R5 and S8R5, respectively) were small.

3D convergence studies

A partial matrix of convergence studies was conducted in 3D for Interior Load Case I. The results of these studies are summarized in Table 7.4. This load case was used to study the choice of element types for 3D modeling, the mesh fineness in the plane of the pavement surface, and the mesh fineness across the depth of the slab. As in the case of the 2D shell elements, the fineness of the mesh in the plane of the slab is characterized by the element aspect ratio in that plane defined by $h/2a$ where $2a$ is the length of the smallest side of the element in the horizontal plane. Likewise, in the plane of the slab thickness, the fineness of the mesh is characterized by the aspect ratio $h/2c$, where $2c$ is the length of the smallest side of the element in the vertical plane. These dimensions are indicated in Figure 7.8(b). In plan view the meshes were composed of square elements whose aspect ratios were identical to those shown in Figure 7.9. Figure 7.10 shows a diagram of selected 3D meshes through the thickness of the slab.

The results tabulated in Table 7.4 indicate that the linear hexahedral elements, both fully-integrated (C3D8) and under-integrated (C3D8R) are much too stiff for the rigid pavement problem. This is due to locking of the element. However, the responses of the quadratic elements (C3D20, C3D20R, C3D27, and C3D27R) are much better than those of the linear elements. Each of the serendipity formulation elements (C3D20 and C3D20R) and the Lagrangian elements (C3D27 and C3D27R) performed quite well. The convergence trends for dimensionless bending stress and dimensionless deflection are shown in Figures 7.11 and 7.12, respectively. One of the primary distinctions between the serendipity and Lagrangian

Table 7.4

Results of 3D Convergence Study, Interior Load Case I

$h/2a$	ILLI-SLAB (2D)	$h/2c$	ABAQUS					
			C3D8	C3D8R	C3D20	C3D20R	C3D27	C3D27R
Dimensionless Stress at Center of Loaded Area ($\sigma_w h^2/P$)								
0.67	0.751	1.0	0.414	0.431	0.754	0.751	0.753	0.750
		1.5	0.476	0.505	0.754	0.755	0.752	0.751
		2.0	0.509	0.545	0.753	0.757	0.752	0.752
1.33	0.739	1.0	--	--	--	--	--	--
		1.5	--	--	--	--	--	--
		2.0	0.582	0.571	0.746	0.744	0.746	0.745
2.00	0.736	1.0	--	--	0.745	--	--	--
		1.5	--	--	0.745	--	--	--
		2.0	0.597	0.575	0.745	0.742	0.745	0.743
Dimensionless Deflection at Center of Loaded Area ($wk\ell^2/P$)								
0.67	0.129	1.0	0.128	0.146	0.131	0.131	0.131	0.131
		1.5	0.124	0.137	0.131	0.131	0.131	0.131
		2.0	0.123	0.134	0.131	0.131	0.131	0.131
1.33	0.129	1.0	--	--	--	--	--	--
		1.5	--	--	--	--	--	--
		2.0	0.130	0.135	0.131	0.131	0.131	0.131
2.00	0.128	1.0	--	--	0.131	--	--	--
		1.5	--	--	0.131	--	--	--
		2.0	0.132	0.135	0.131	0.131	0.131	0.131
CPU Time on CRAY Y-MP Computer, sec								
0.67	--	1.0	8.6	7.4	25.1	20.9	28.4	32.6
		1.5	12.8	11.0	38.3	32.1	57.3	50.4
		2.0	17.0	14.7	52.7	44.2	81.2	54.0
1.33	--	1.0	--	--	--	--	--	--
		1.5	--	--	--	--	--	--
		2.0	57.6	60.4	180.2	225.3	298.8	268.7
2.00	--	1.0	--	--	202.2	--	--	--
		1.5	--	--	325.9	--	--	--
		2.0	165.7	144.3	773.4	695.3	1636.6	1560.6

Table entries of "--" indicate that this computation was not performed or is not applicable.

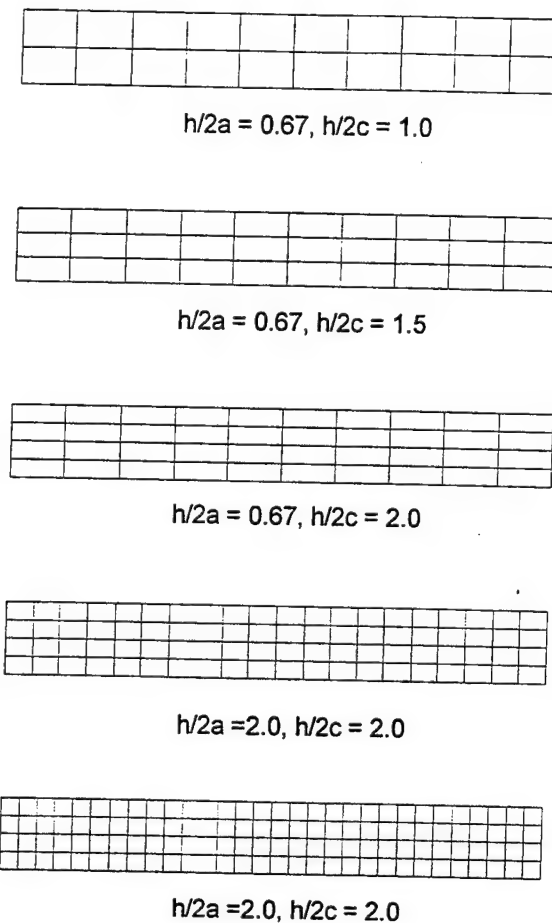


Figure 7.10 Finite element meshes in plane of slab thickness, Interior Load Case I

elements is in the amount of CPU time required to perform the calculations as illustrated in Figure 7.13. The solution time for the C3D27 element is over two times that required for the C3D20 element. For both the C3D20R and C3D27R, use of reduced integration results in a reduction of CPU time by about 10 percent over its fully-integrated counterpart.

The results in Table 7.4 show that increasing the mesh fineness in the plane of the slab thickness from $h/2c = 0.67$ (in this case, two elements through the slab thickness) to

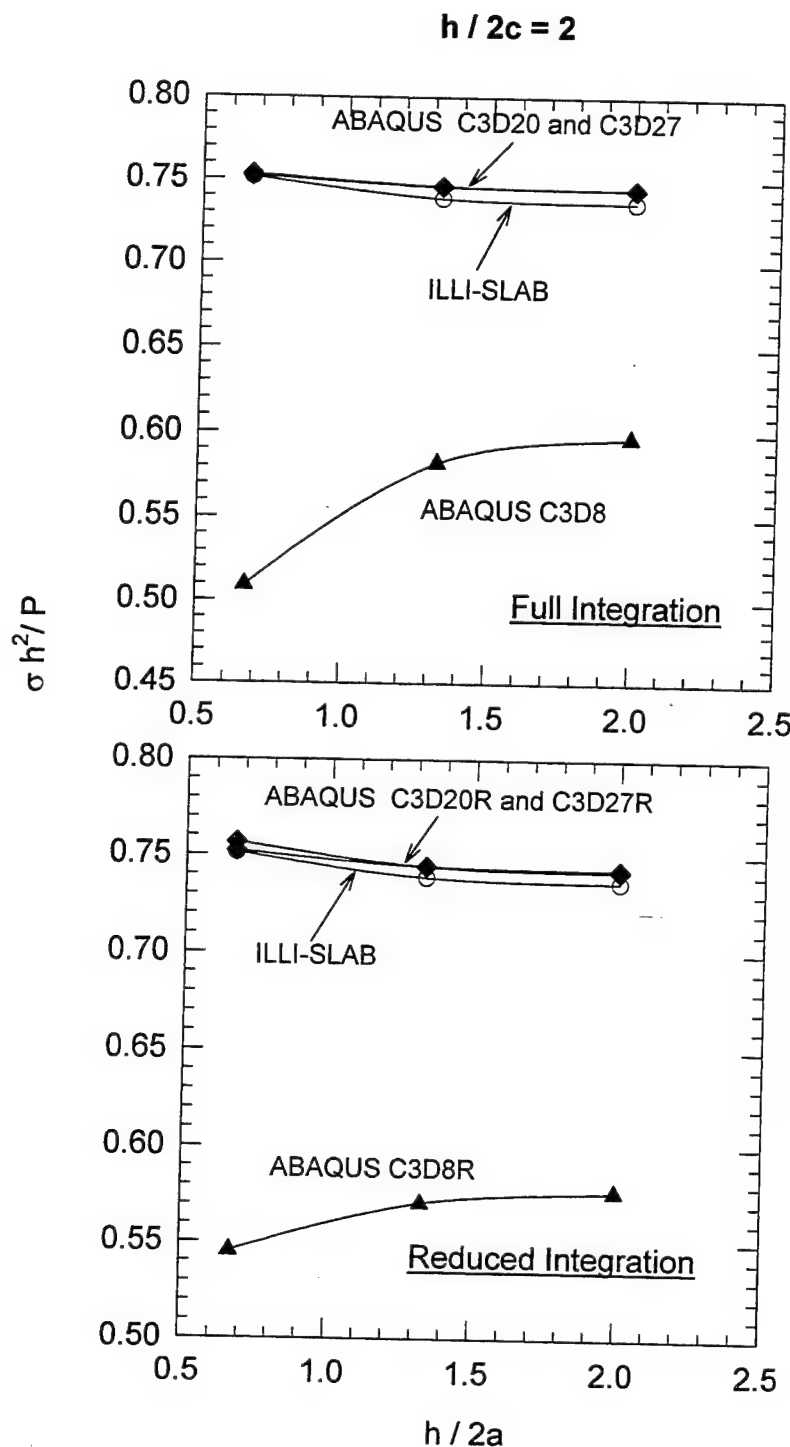


Figure 7.11. Dimensionless bending stress, Interior Load Case I

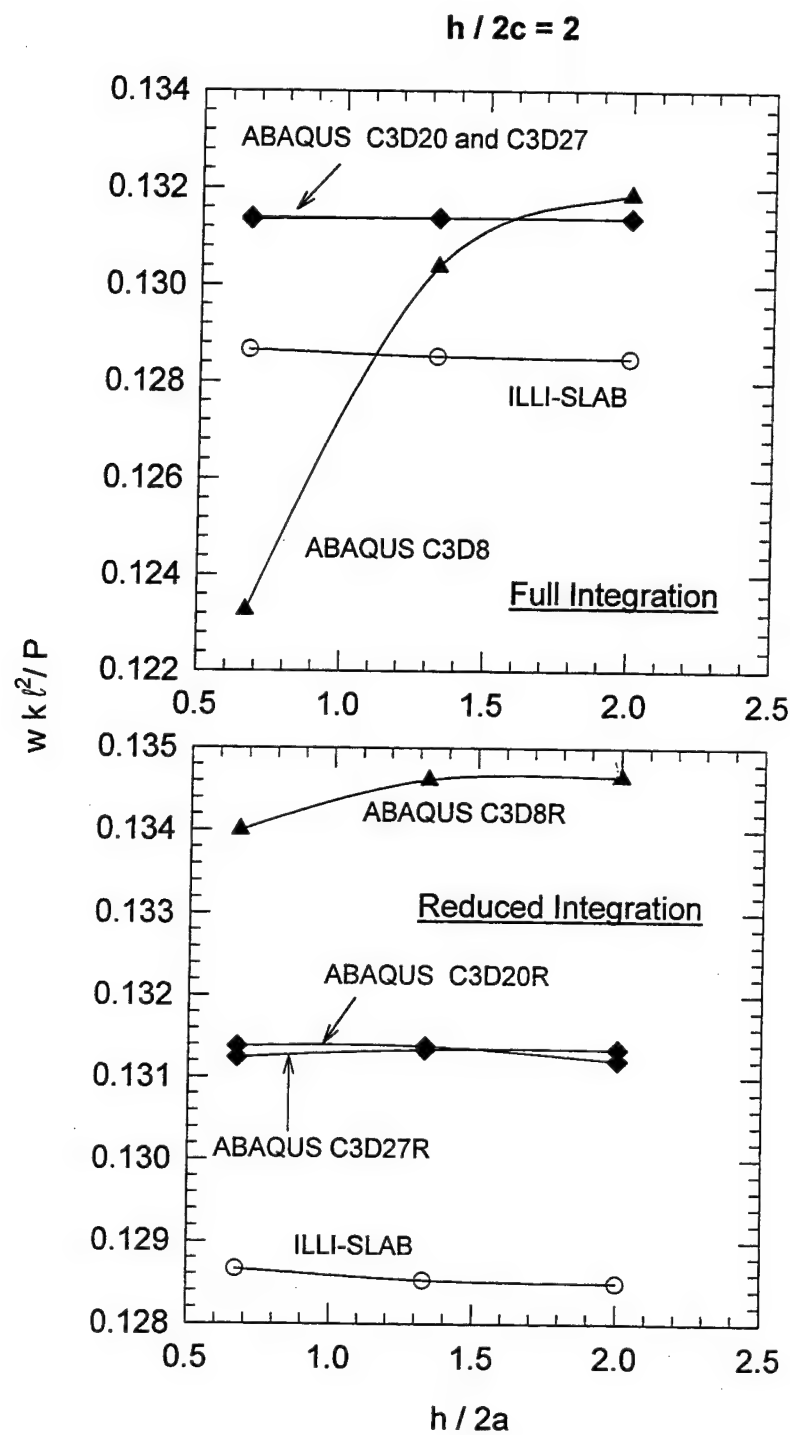


Figure 7.12. Dimensionless deflection, Interior Load Case I

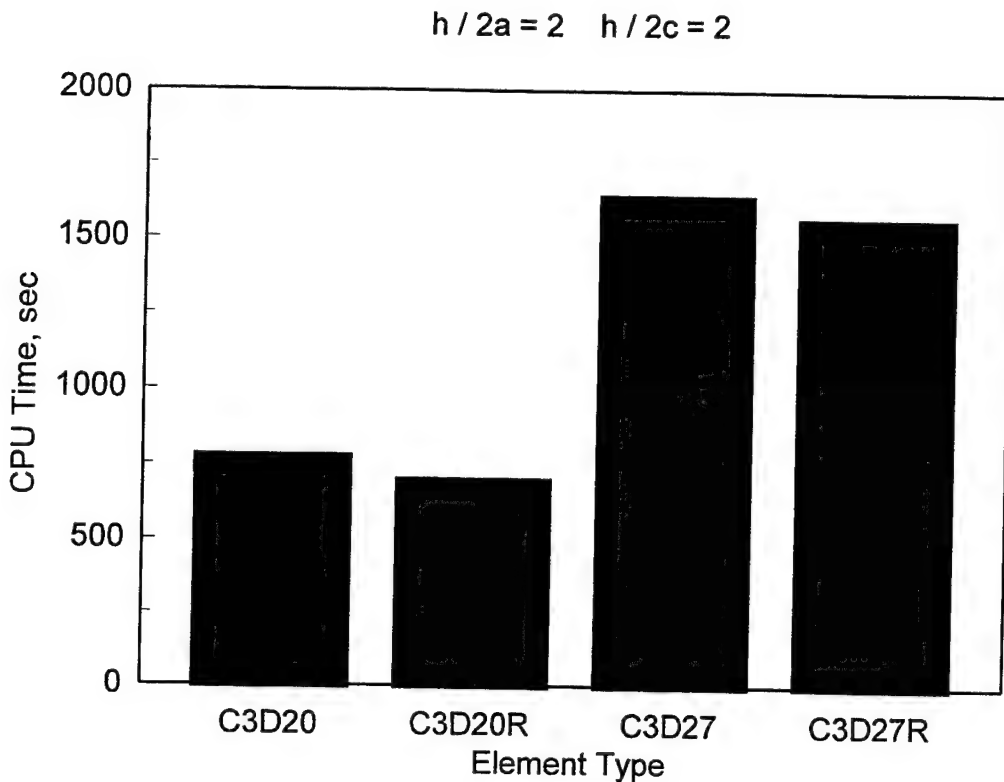


Figure 7.13. CPU time, selected 3D runs, Interior Load Case I

$h/2c = 2$ (four elements through the slab thickness) has a negligible affect on the accuracy of the solution for the quadratic hexahedron elements.

Summary

Figure 7.14 shows a comparison of dimensionless bending stress between ILLI-SLAB and the ABAQUS S8R (with both the default transverse shear stiffness and 100 times the default transverse shear stiffness) and C3D27R elements as a function of mesh fineness as measured by $h/2a$. It is apparent from this plot that the response of the S8R element most nearly matches that of ILLI-SLAB when the transverse shear stiffness is increased over that of the default value. The data in this plot also indicate that the C3D27R element predicts slightly

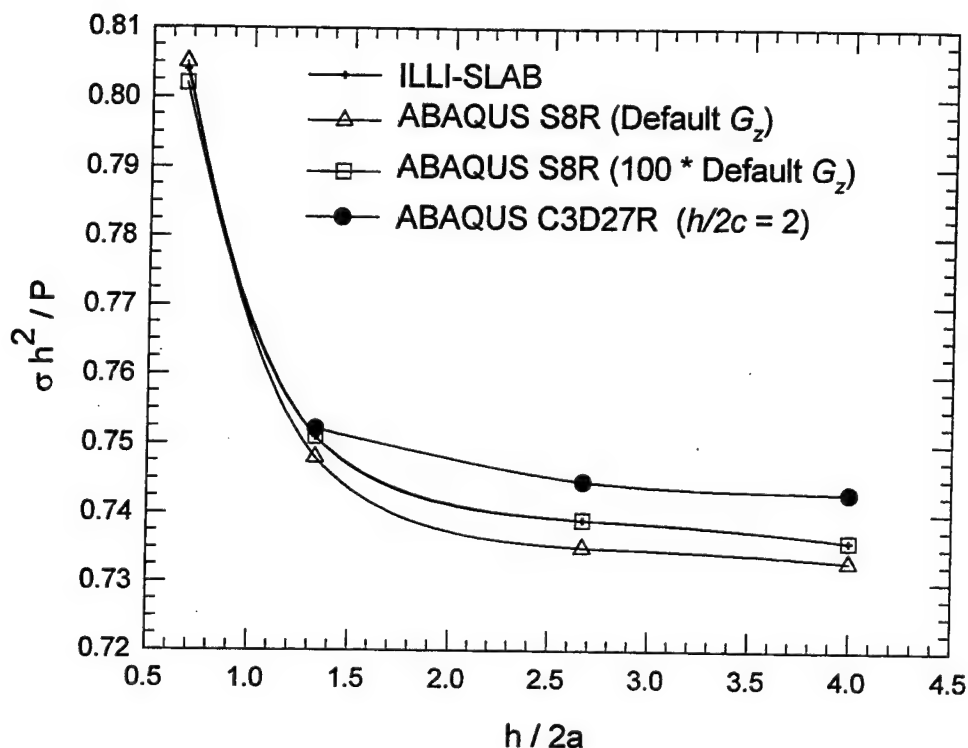


Figure 7.14. Dimensionless bending stress summary, Interior Load Case I

greater stresses than either of the two ABAQUS models and ILLI-SLAB. Figure 7.15 shows a similar plot for dimensionless deflection. These data show that the deflection convergence curves for ABAQUS are completely flat, indicating that additional mesh fineness does not increase accuracy. It is of interest to note that the deflection of the C3D27R element lies between the two indicated curves for the S8R element. Thus, it would appear that any of the quadratic hexahedron elements would perform satisfactorily in a general, 3D model of the rigid pavement system. Strictly based upon indicated solution times, the C3D20R would appear to be the optimum element for this problem. However, other concerns (such as compatibility with contact surfaces and joint elements) make the C3D27R a more pragmatic choice for further model development.

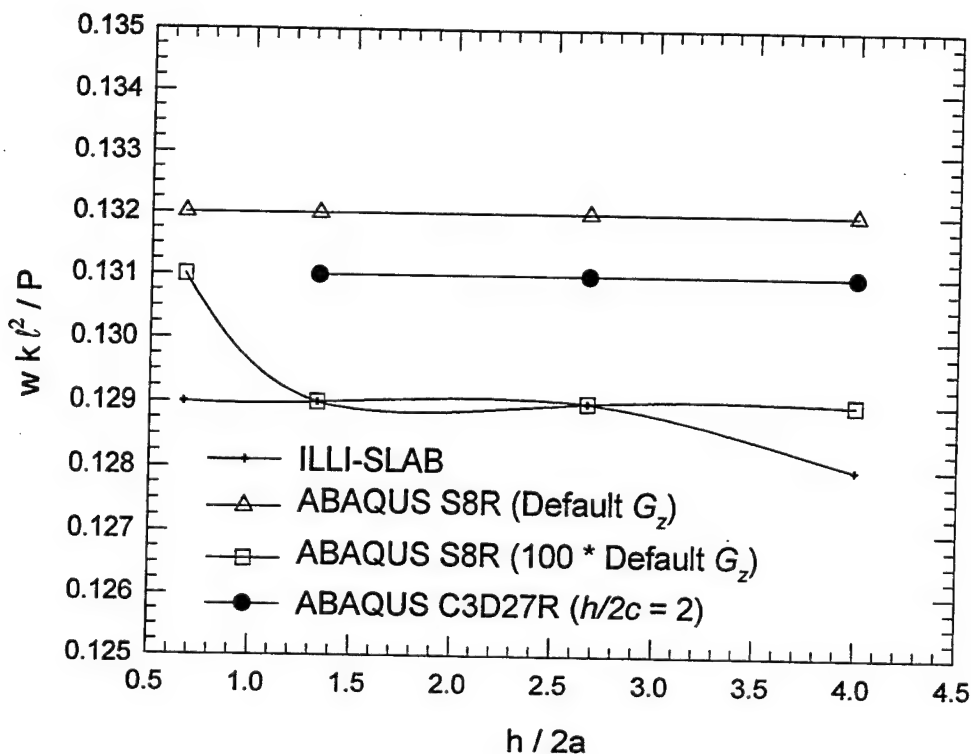


Figure 7.15. Dimensionless deflection summary, Interior Load Case I

Interior Load Case II

Interior Load Case II was studied to obtain a more direct comparison of the finite element solutions to the Westergaard interior load case. The finite element meshes used for Interior Load Case II are shown in Figure 7.16. Three models were used with $h/2a$ ratios of 2, 4, and 8, respectively. For each case a quarter-slab model was used, taking advantage of symmetric boundary conditions along both the x and y axes to enforce the interior loading condition. For the C3D27R model the aspect ratio in the plane of the slab thickness was set at $h/2c = 2$. The results of these analyses are summarized in Table 7.5.

These data indicate that the finite element models considered tend to predict maximum interior bending stresses that are in reasonable agreement with those predicted by

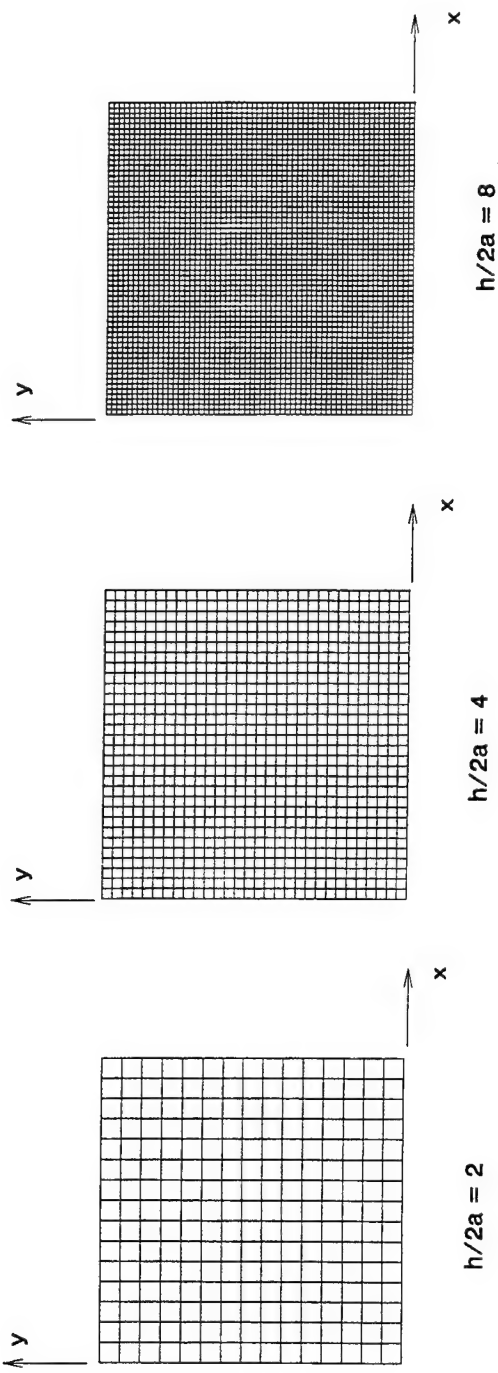


Figure 7.16. Finite element meshes in plane of slab surface, Interior Load Case II

Table 7.5
Results of Convergence Study, Interior Load Case II

Westergaard	$h/2a$	ILLI-SLAB	ABAQUS			
			S8R5	S8R (Default G_z)	S8R (100*Default G_z)	C3D27R ($h/2c = 2$)
Dimensionless Bending Stress ($\sigma h^2/P$)						
1.295	2	1.405	1.403	1.405	1.407	1.354
	4	1.347	1.342	1.342	1.346	1.330
	8	1.330	1.323	1.328	1.327	1.322
Dimensionless Deflection ($wk\ell^2/P$)						
0.123	2	0.139	0.146	0.146	0.138	0.143
	4	0.138	0.146	0.146	0.138	0.143
	8	0.138	0.146	0.146	0.138	0.143

Westergaard when the mesh fineness in the plane of the slab surface is given by $h/2a \geq 4$.

For deflections the results are virtually insensitive to mesh fineness over the ranges considered in this study. However, it should be noted that the deflections calculated from the finite element analyses are approximately 15 percent greater than those predicted by Westergaard.

Interior Load Case III

The lengths of the sides of the square slab were varied from 2ℓ to 10ℓ to investigate the effects of the slab dimensions on Westergaard's assumption of an infinite slab using the S8R element with the ABAQUS default transverse shear stiffness. The finite element meshes used for Interior Load Case III are shown in Figure 7.17. A quarter-slab model was used, taking advantage of symmetric boundary conditions along both the x and y axes to enforce the interior loading condition. Figure 7.18 summarizes the results of these calculations expressed as the ratios of the maximum stress calculated from the finite element method (σ_{FEM}) to the maximum Westergaard interior stress ($\sigma_{Westergaard}$). Based upon these calculations, one can conclude that the minimum slab dimensions required to approximate an infinite slab for the

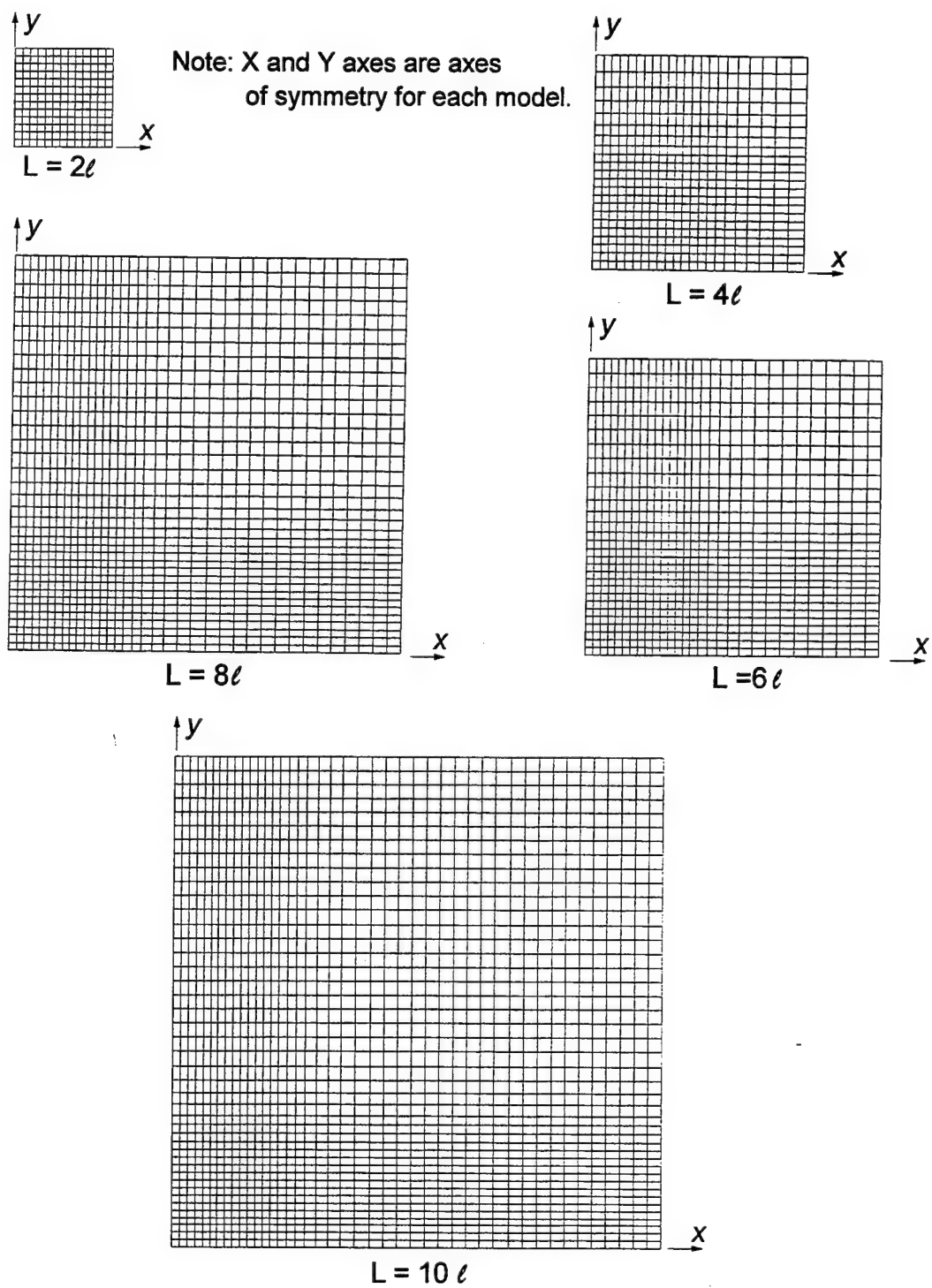


Figure 7.17. Finite element meshes in plane of slab surface, Interior Load Case III

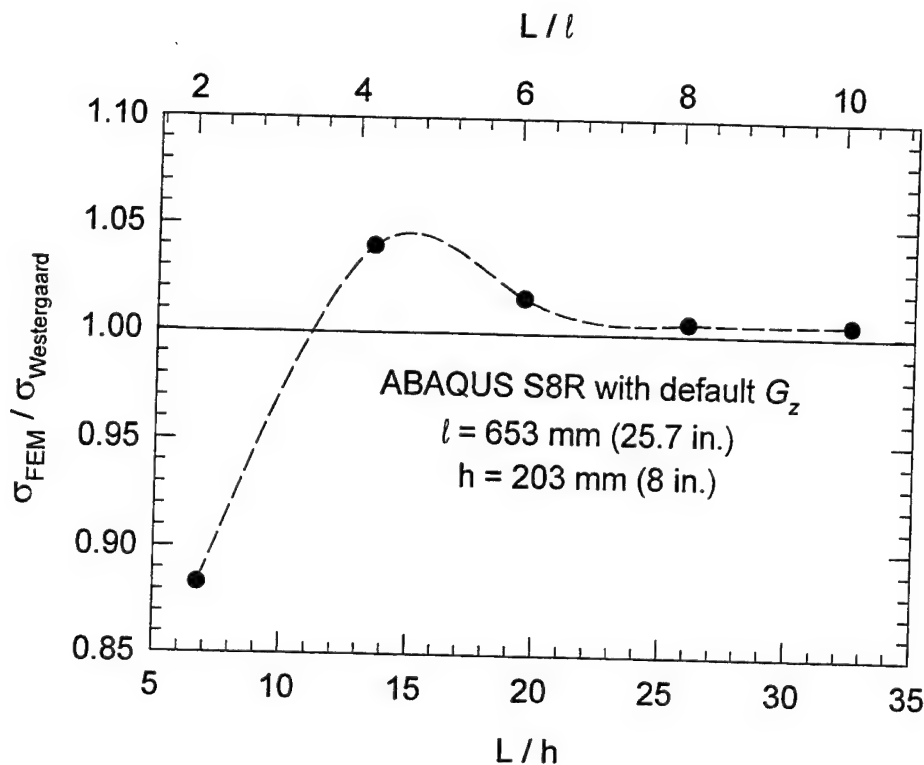


Figure 7.18. Stress ratio, Interior Load Case III

interior loading case is approximately $L/\ell = 6$. Also, the commonly held rule-of-thumb for the transition between thin and thick plate theory of $L/h \approx 20$ appears to be borne out by these calculations. Figure 7.19 shows a plot of the maximum deflection calculated from the finite element method (w_{FEM}) to the maximum Westergaard interior deflection ($w_{Westergaard}$). Similar conclusions can be drawn from this plot.

Edge Load Case I

Edge Load Case I was developed to study the response of the finite element model for the edge load case. As with the interior load cases, ILLI-SLAB runs were made using identical meshes for purposes of comparison. Based upon the results of the previously described interior load cases, the only ABAQUS 2D element considered for this load case was the S8R.

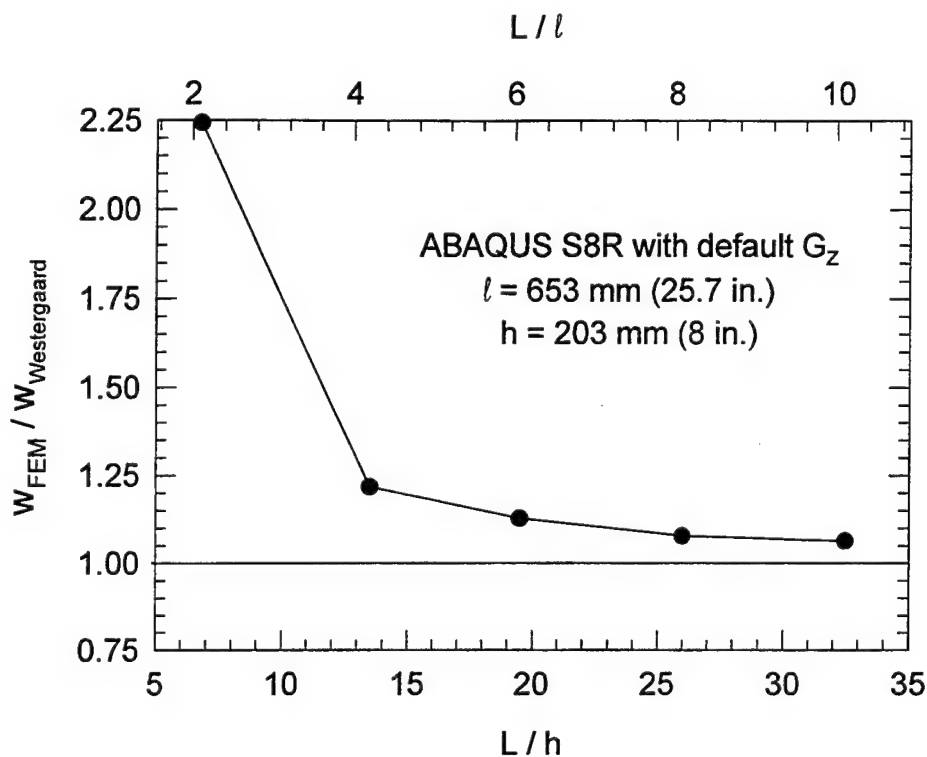


Figure 7.19. Deflection ratio, Interior Load Case III

However, the transverse shear stiffness of the element was varied to study its influence on the response of the model. A half-slab model was employed, taking advantage of symmetric boundary conditions along the x axis to enforce the edge loading condition. Figure 7.20 shows the finite element model developed for this purpose. The model consisted of square elements with an $h/2a$ ratio of 4.

Figure 7.21 shows dimensionless bending stresses from ABAQUS and ILLI-SLAB for Edge Load Case I plotted versus distance from the edge of the slab as a function of the radius of relative stiffness. These data show a perplexing result from ABAQUS: the stresses do not increase monotonically to the edge of the slab but decrease near the edge. This finding disagrees with the ILLI-SLAB solution, which increases monotonically to the edge of the

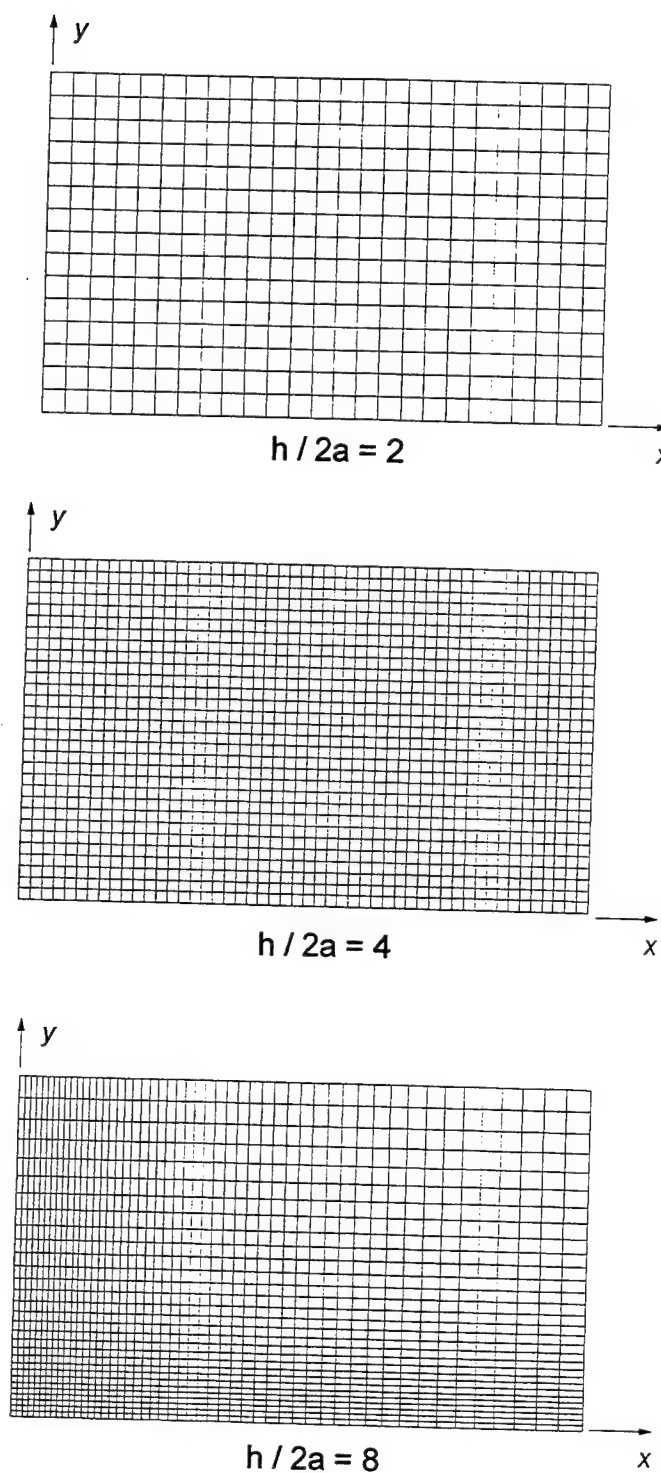


Figure 7.20. Finite element meshes in plane of slab surface, Edge Load Case I

slab. Away from the edge of the slab, ILLI-SLAB and ABAQUS S8R agree quite well. In fact, as the transverse shear stiffness of the S8R element is increased, the response approaches that of ILLI-SLAB, until at a transverse shear stiffness of 100 times the default, the ABAQUS S8R response approximates the ILLI-SLAB response.

A 3D model was developed using the ABAQUS C3D27R element with three elements through the thickness of the slab ($h/2c = 1.67$). In the plane of the slab surface, the mesh was identical to that shown in Figure 7.20. Figure 7.22 shows a plot of dimensionless bending stresses from ABAQUS and ILLI-SLAB plotted versus distance from the edge of the slab as a function of the radius of relative stiffness including the ABAQUS C3D27R model. Also shown in the plot are the responses predicted by the ABAQUS S8R element for three values of transverse shear stiffness: one, two and 100 times the ABAQUS default values. Interestingly enough, the ABAQUS C3D27R response more nearly matches the response of the S8R element with the default transverse shear stiffness than the ILLI-SLAB response. In fact, the 3D model matches very closely the response from the S8R model when the default transverse shear stiffness is twice the default value.

The above observations leads to a very significant and perhaps far-reaching conclusion: the classical Kirchhoff assumptions of thin plate theory, adopted by Westergaard, are not strictly valid for the edge loading case in rigid pavements. It is interesting to note that Timoshenko and Woinsowsky-Krieger (1959) in their now classical treatise on plates and shells made the following observation:

The disregard of the deformation due to the transverse stress component obviously is equivalent to the assumption of a shear modulus $G_z = \infty$; proceeding in this way we replace the actual material of the plate, supposed to be isotropic, by a hypothetical material of no perfect isotropy.

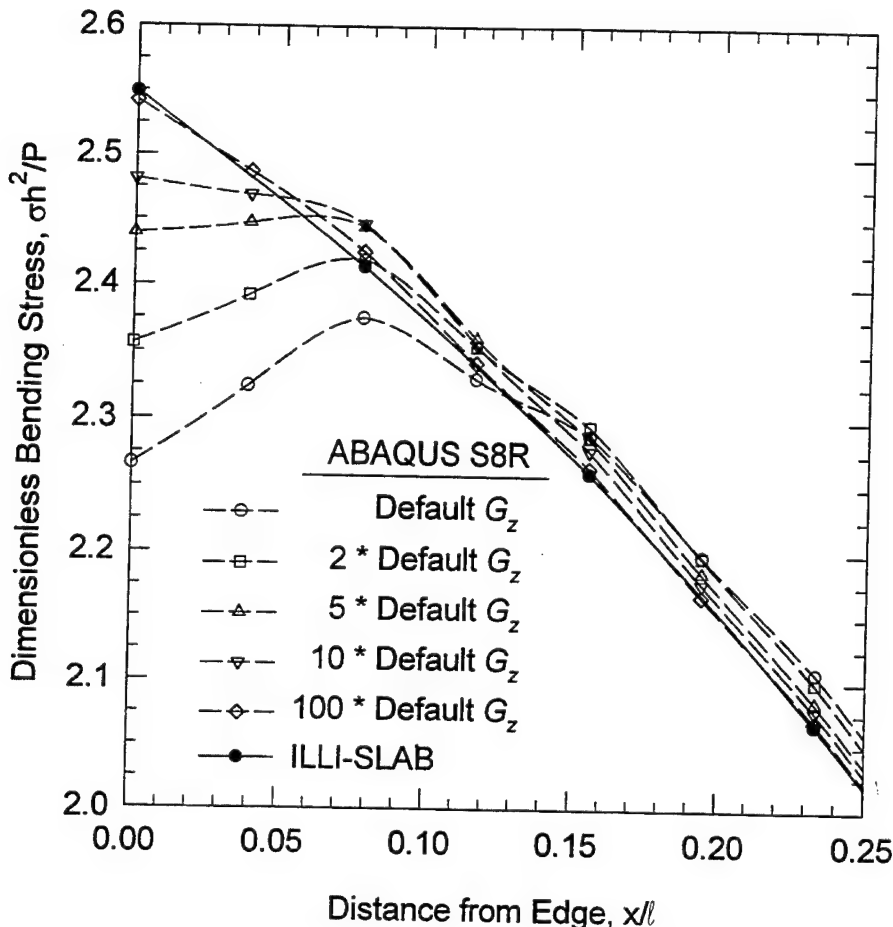


Figure 7.21. Dimensionless bending stress, Edge Load Case I

They go on to draw the following conclusion:

On the other hand, in attributing some purely hypothetical properties to the material of the plate we cannot expect complete agreement of the theoretical stress distribution with the actual one. The inaccuracy of the customary thin-plate theory becomes of practical interest in the edge zones of plates and around holes that have a diameter which is not large in comparison with the thickness of the plate.

Edge Load Case II

Additional insight into the effect of the Kirchhoff assumptions on the response for a load near the edge of a slab-on-grade was obtained from Edge Load Case II. As was the case with

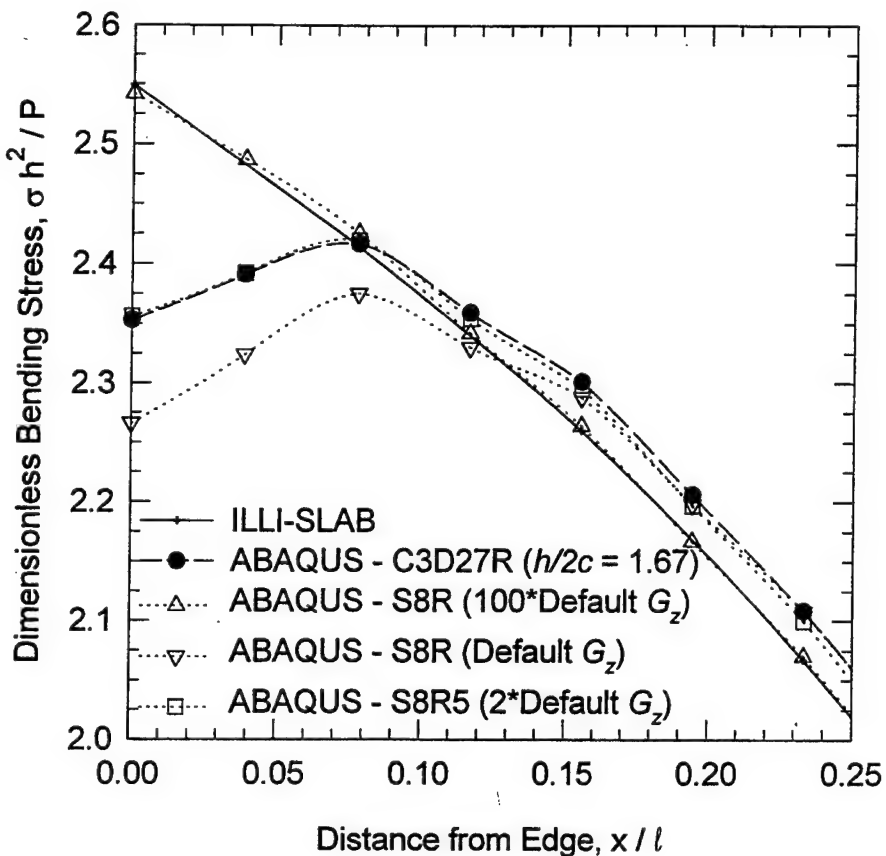


Figure 7.22. Summary of 2D and 3D runs, dimensionless bending stress, Edge Load Case I

Interior Load Case III, the lengths of the sides of the square slab were varied from 2ℓ to 10ℓ to investigate the effects of the slab dimensions on Westergaard's assumption of an infinite slab using the S8R element with two values of the transverse shear stiffness: the default G_z and 100 times the default G_z . The finite element meshes used for Edge Load Case II are shown in Figure 7.23. A half-slab model was used, taking advantage of symmetric boundary conditions along the x axis to enforce the edge loading condition.

The results of these analyses are shown in Figures 7.24 and 7.25 as plots of dimensionless bending stress versus distance from the edge of the joint expressed as a function of the radius of relative stiffness. In Figure 7.24 the S8R transverse shear stiffness was set to the

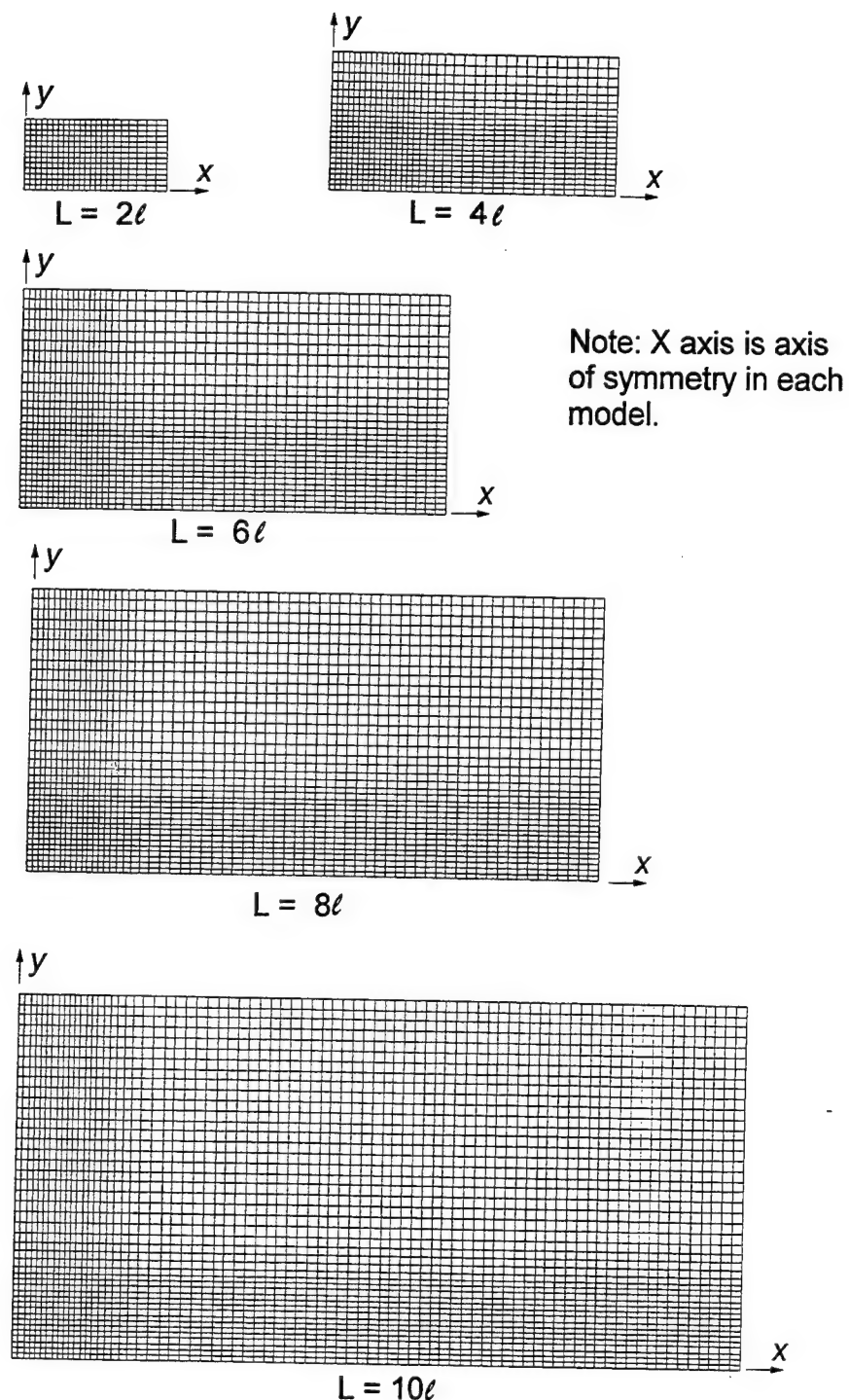


Figure 7.23. Finite element meshes in plane of slab surface, Edge Load Case II

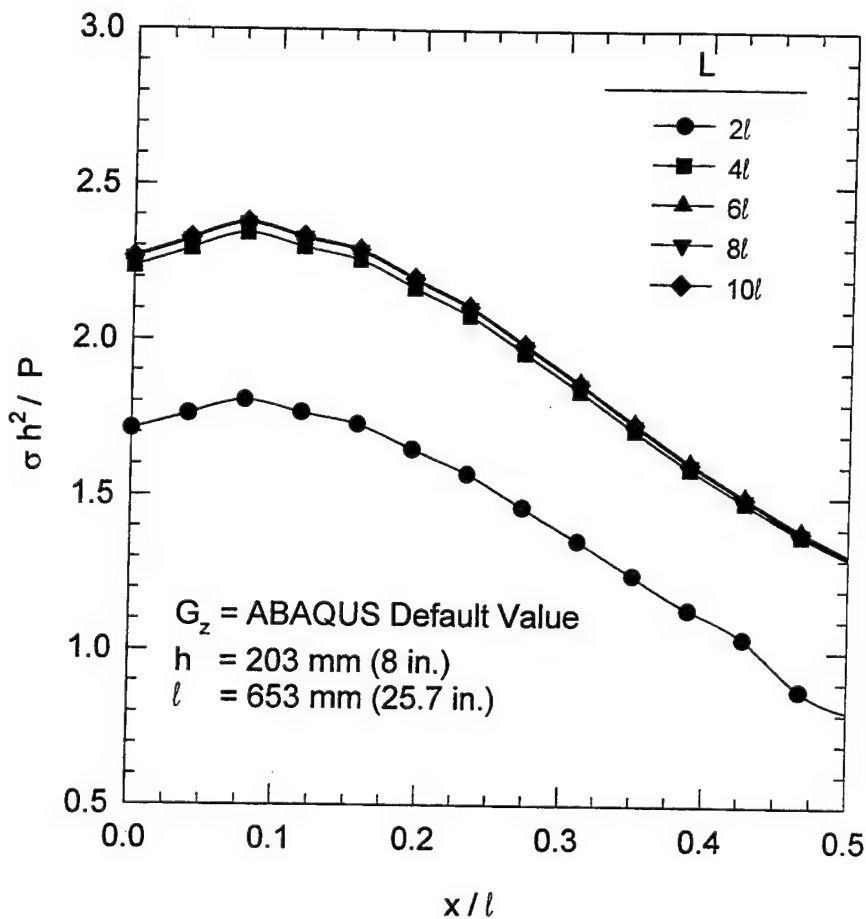


Figure 7.24. Dimensionless bending stress, default transverse shear stiffness, Edge Load Case II

ABAQUS default value. Clearly, the maximum stress occurs at a distance of about $0.1l$ from the edge of the slab for all values of L . Only for the case where $L = 2l$ is the response significantly different. Figure 7.25 is a similar plot for the case where the transverse shear stiffness was set to 100 times the default G_z . In this case each of the response curves monotonically increase to the edge of the slab as predicted by Westergaard and thin-plate finite element programs such as ILLI-SLAB. Again, the response is significantly different for the case where $L = 2l$.

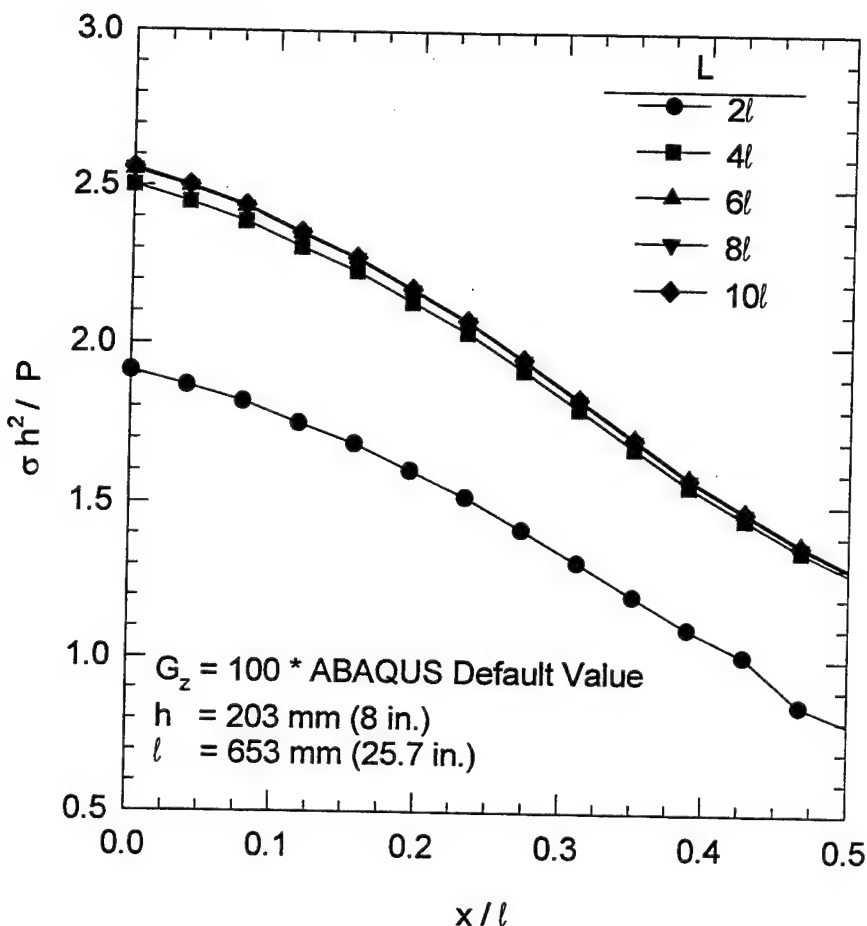


Figure 7.25. Dimensionless bending stress, 100 times default transverse shear stiffness, Edge Load Case II

Figures 7.26 and 7.27 show similar curves for dimensionless deflection versus distance from the edge of the slab for the two values of transverse shear stiffness investigated. These curves indicate that deflections are not significantly influenced by the choice of transverse shear stiffness. Also, it can be observed that the deflection response is essentially the same for all curves were $L/l \geq 6$.

Based upon these observations it can be stated that, like the interior load case, the ratio of the minimum slab dimension to the radius of relative stiffness of at least six is required to

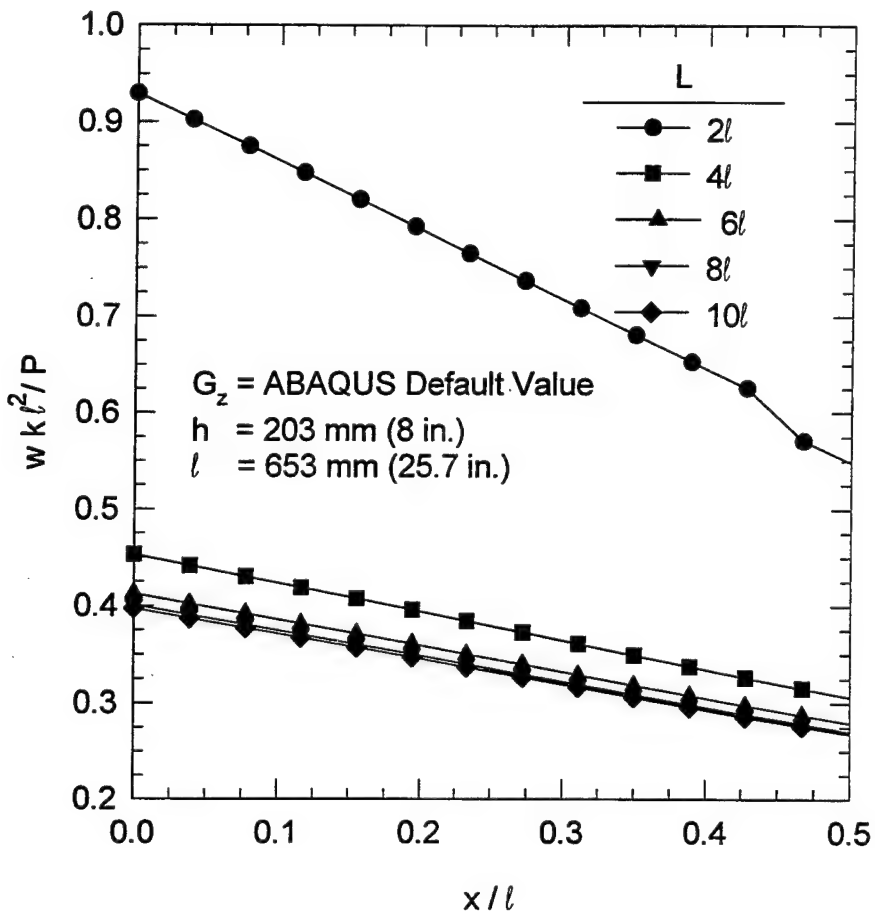


Figure 7.26. Dimensionless deflection, default transverse shear stiffness, Edge Load Case II

model a semi-infinite slab. It can also be concluded that the magnitude and distribution of bending stresses near the edge of a slab are strongly dependent upon the transverse shear stiffness of the slab while deflections are not sensitive to this parameter.

To develop further insight into effect of the transverse shear stiffness on the edge loading response, a set of finite element calculations were performed to determine the limiting value of L/h for which thin plate theory was acceptable for the edge load case. Figure 7.28 shows the result of these analyses. From these data it appears that for $L/h > 100$, the effects of

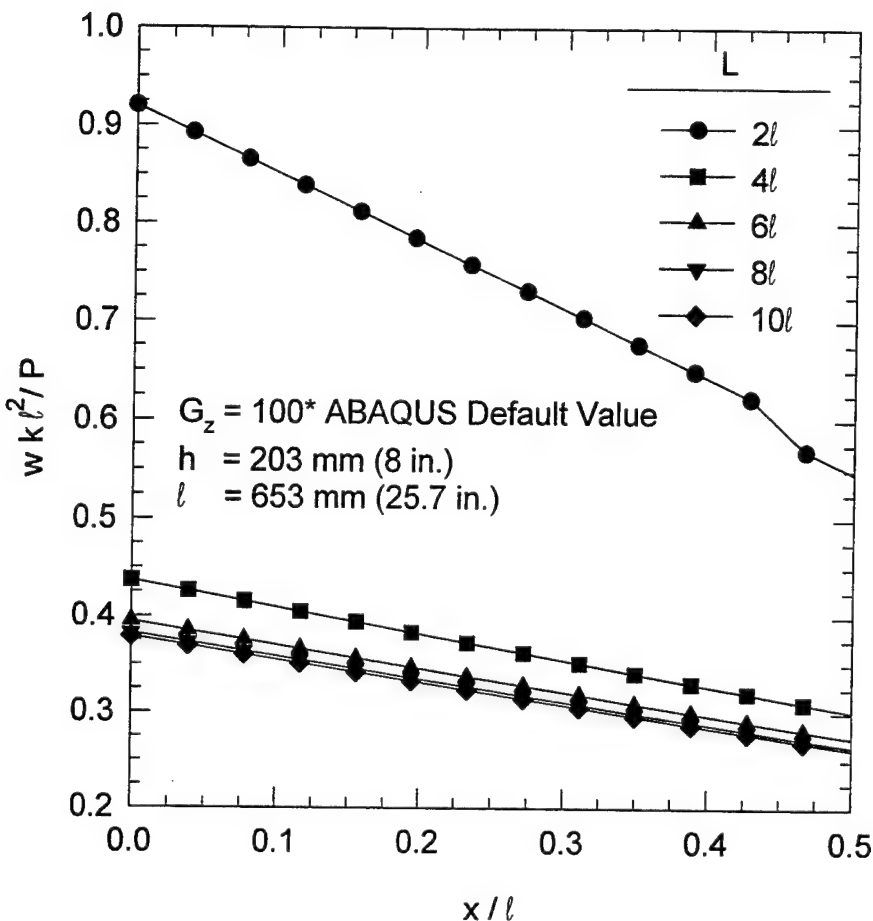


Figure 7.27. Dimensionless deflection, 100 times default transverse shear stiffness, Edge Load Case II

transverse shear stiffness on the edge loading response is negligible. Thus, for any practical rigid pavement the edge stress is influenced by the assumption of the Kirchhoff plate theory.

A special 3D finite element calculation was conducted to study the distribution of transverse shear stresses throughout the slab. The mesh in the plan of the slab surface was identical to that used in Edge Load Case I with $h/2a$ ratio set to 4. Four elements were used across the thickness of the slab so that the slab's mid-surface would be located at an element boundary. The load was identical to that described for Edge Load Cases I and II.

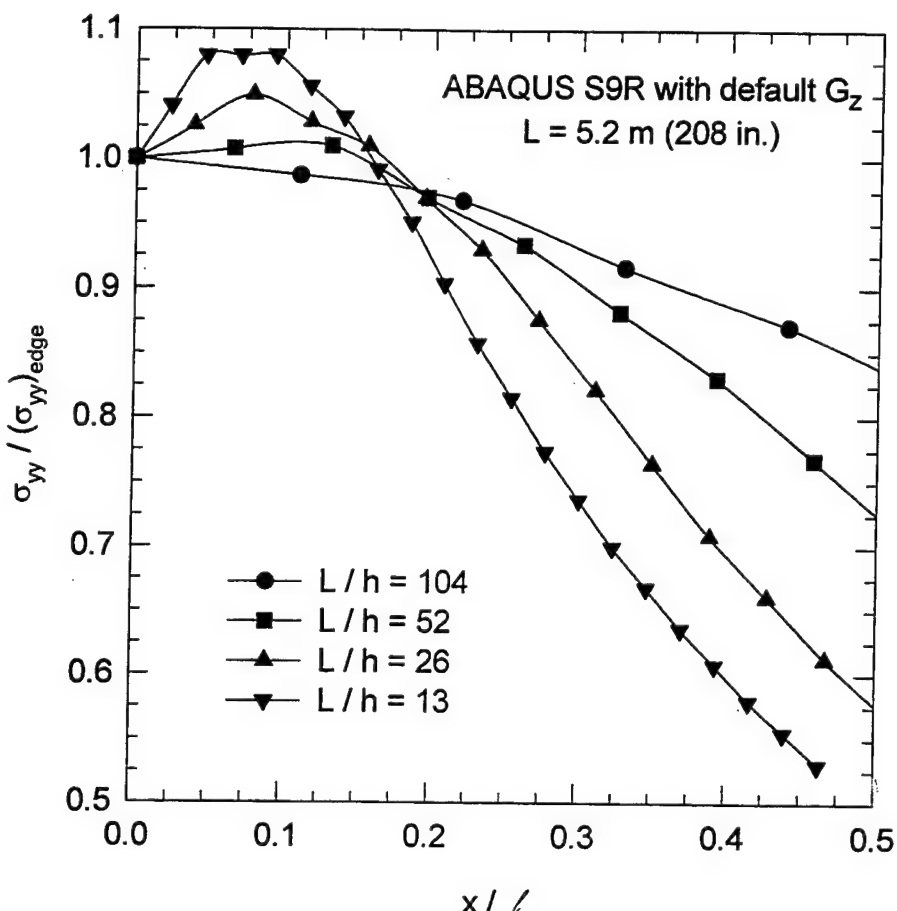


Figure 7.28. Effect of slab width to depth ratio on edge stresses

These results indicate the magnitude of the maximum value of τ_{xz} is approximately 20 percent of the magnitude of the maximum edge stress in the slab. The maximum value occurs just to the right edge of the loaded area near the centerline of the slab. The magnitude of the maximum value of τ_{yz} is approximately 30 percent of the magnitude of the maximum edge stress in the slab. The maximum value occurs near the free edge of the slab in the vicinity of the loaded area.

Figure 7.29 shows a cross-section of the distribution of $\tau_{yz}h^2/P$ through the thickness of the slab near where its maximum value occurs. These data show that the transverse shear stress is distributed in a manner that is very nearly parabolic with the maximum value occurring at the slab's mid-surface. Thus, the finite element solution agrees with the theorized distribution of transverse shearing stresses across the slab.

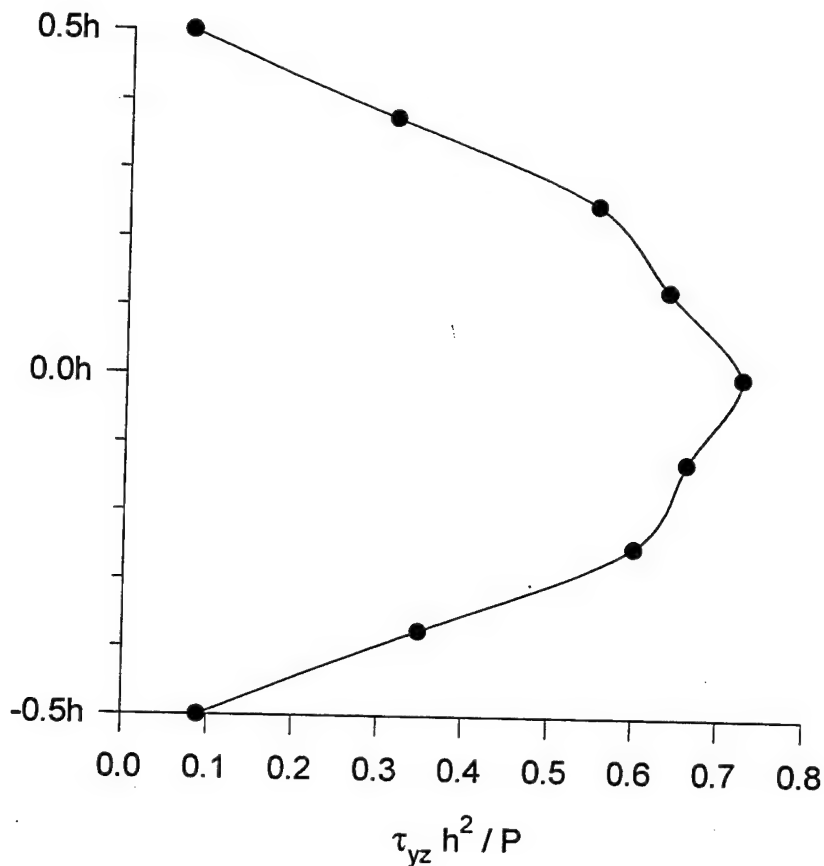


Figure 7.29. Finite element distribution of $\tau_{xz}h^2/p$ through slab thickness

Experimental data to confirm the above observations are inconclusive. Full-scale accelerated test tracks as well as small-scale model tests conducted by the Corps of Engineers have indicated that the Westergaard analytical model overestimates the stresses and strains experienced in the pavement (Rollings and Pittman 1992). Similar trends are indicated by small-scale model tests conducted by the Corps in the 1950s. Figure 7.30 shows results from small-scale model tests conducted by the Corps of Engineers (1954). These data indicate that the Westergaard theory solution is conservative for both edge and interior load cases. In Figure 7.31 the ratio of the Westergaard theory stresses to the experimental stresses is shown for both interior and edge loads over a range of a/l . For these experiments the discrepancy between theoretical and experimental stresses for the edge load case was less than that for the interior load case. However, two factors may have led to some errors in this data:

- Stresses were not directly measured. Strains were measured by resistance strain gages bonded to the slab. For the edge load case the strain gages were located at some finite distance from the edge, and the strains were extrapolated to the edge. This is effectively equivalent to assuming that the Kirchhoff theory applies.
- The modulus of subgrade reaction of the rubber foundation used in these tests was estimated from the volume of the deflection basin produced by an edge loading and an interior loading. This method, at best, gives a composite estimate of the modulus of subgrade reaction but may lead to errors in the calculation of theoretical stresses.

JOINTED RIGID PAVEMENT MODELS

To extend the concepts established for single-slab models, 2D and 3D jointed rigid pavement models were developed. First, a two-slab jointed rigid pavement model with 2D shell elements was developed to establish baseline response data for development of 3D jointed pavement models and to further explore the effect of transverse shear stiffness on stresses at

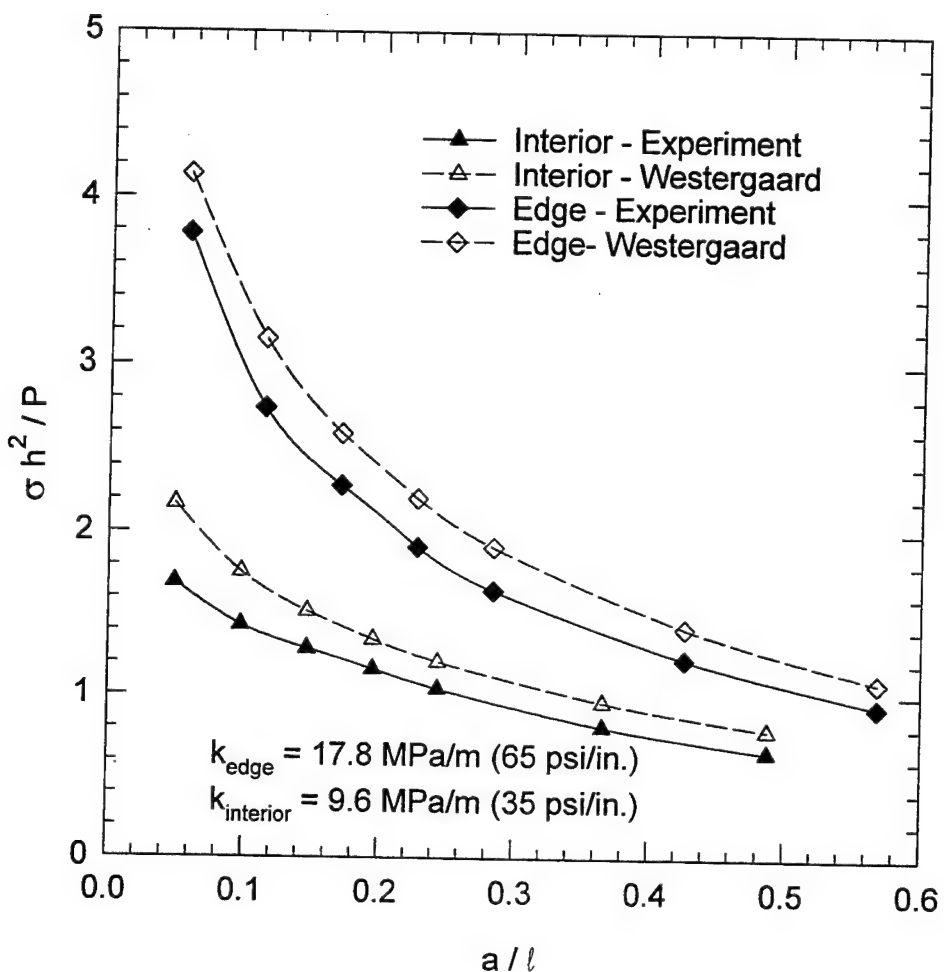


Figure 7.30. Theoretical and experimental dimensionless bending stress from small-scale model studies

the edge of slabs. Subsequently a two-slab 3D finite element model with a joint was developed to demonstrate techniques of specifying the stiffness of the joint in 3D and for comparison of the response parameters with 2D analytical models. The results of both the 2D and 3D finite element models were compared to the closed-form Westergaard-type solution developed by Skarlatos (1949) as presented by Hammons and Ioannides (1996).

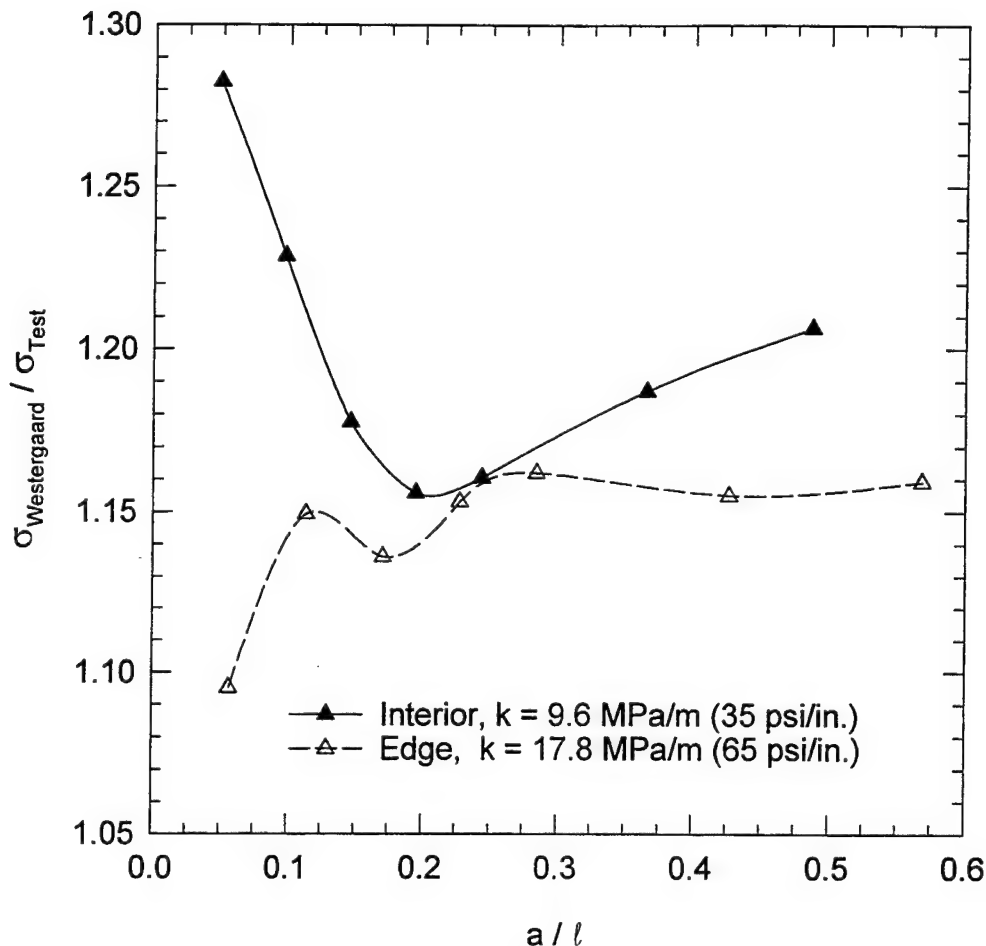


Figure 7.31. Ratio of theoretical to experimental bending stress from small-scale model studies

Representation of the joint stiffness

The analytical work of Ioannides and Korvesis (1992) using ILLI-SLAB led them to conclude that the response of both aggregate interlock and doweled joints can be represented by the concepts of dimensionless joint stiffness. This conclusion, verified experimentally by small-scale model studies conducted by the Corps of Engineers in the 1950s as reanalyzed in this study, eliminates the need to explicitly model dowels in finite element models. Coupled

with the analytical developments of Skarlatos (1949) as presented by Ioannides and Hammons (1996) a powerful, yet simple, way of characterizing the dimensionless joint stiffness for finite element modeling emerges.

Selection of an appropriate ABAQUS finite element spring model for use modeling the interaction of nodes across a joint was required. The ABAQUS element library contains a collection of three simple spring models, each having its own unique properties. The SPRINGA element is an axial spring between two nodes whose line of action is the line joining the two nodes. The SPRING2 element allows the user more control over the line of action of the spring than the SPRINGA element by acting only a user-specified direction. The third simple spring element, the SPRING1 element, is a spring between a node and ground (a fixed, unmoveable fictitious node) which acts in a user-specified direction.

For each of these element types, the force-displacement relationship may be linear or nonlinear. For a linear force-displacement relationship, the user simply inputs the spring constant. For a nonlinear spring the user must input a table containing ordered pairs of force-displacement data. ABAQUS then linearly interpolates between the input values to obtain a complete nonlinear description of the force-displacement relation of the spring.

ABAQUS also includes a more general spring and dashpot element called the JOINTC element. The JOINTC element, more formally known as flexible joint element, models the interaction between two nodes which may have internal stiffness or damping. The stiffness and damping properties, which may be linear or nonlinear, are defined by the user in three orthogonal directions. In a static analysis damping is of no consequence and may be ignored; therefore, the JOINTC element reduces to a general spring element which may have a user-defined stiffness value in three orthogonal directions. Nonlinear force-displacement

relationships for the JOINTC element are input by the user in a manner identical to that for the simple spring elements.

The stiffness of the joint in most finite element codes for rigid pavement analysis (such as ILLI-SLAB) consists of springs which have stiffness in the vertical direction only. Following this pattern, the interaction between nodes across a joint in ABAQUS could be modeled using the SPRING2 element. In the simplest case the stiffness of the JOINTC element could be specified to be in the vertical direction only reducing its effect to that of the SPRING2 element. However, the additional capabilities of the truly general 3D JOINTC element render it an attractive alternative to the more limited SPRING1 element. For example for future research studies in which dynamic analysis may be considered, or for environmental analysis in which temperature and moisture gradients are important, the JOINTC element offers some attractive capabilities. Based upon these considerations the JOINTC element was selected for use in this study. However, where the stiffness of the JOINTC element is limited to only a single direction and damping is ignored, the simpler SPRING2 element would give identical results.

The dimensionless joint stiffness, as defined by Skarlatos (1949), is given by Equation 4.10. For an aggregate interlock load transfer mechanism, the joint stiffness is prescribed by the parameter q , which defines the force transmitted per unit length along the joint per unit differential deflection across the joint. This term is identical to the AGG term defined in ILLI-SLAB. For the dowel load transfer mechanism, q is defined as

$$q = \frac{D}{s} \quad (7.10)$$

where D is defined by Equation 5.1 and s is the dowel spacing.

Once q has been established, it is necessary to distribute the stiffness to the nodes along the joint in a rational manner. One method of allocating the stiffness to the nodes is by using

the concept of contributing area, which is commonly used in structural analysis. In this method the stiffness values assigned to each node, κ , are determined based upon the length (in 2D) or area (in 3D) that contributes to the stiffness of the node. For equally spaced nodes in a 2D model, the nodes along a joint may be categorized into one of two types: interior nodes and edge nodes. Edge nodes are those which occupy the ends of the joint, while all other nodes are interior nodes. Based upon the concepts of contributing area, the stiffness of the interior nodes must be twice that of the edge nodes. If the length of the joint is given by λ , and the number of nodes along the joint (for a 2D model) is given by N , then

$$\bar{\kappa} = \frac{q\lambda}{2(N - 1)} \quad (7.11)$$

and

$$\begin{aligned} \kappa_{interior} &= 2\bar{\kappa} \\ \kappa_{edge} &= \bar{\kappa} \end{aligned} \quad (7.12)$$

For 3D finite element models, the nodes along the face of the solid model at a joint must be categorized into three types: corner, edge, and interior nodes. Corner nodes are those nodes which occupy the four corners of the face, while edge nodes are all other nodes on the edge of the face. Interior nodes make up the remainder of the nodes. If the spacing of the nodes on the face of the joint is uniform, the unit stiffness value is given by

$$\bar{\kappa} = \frac{q\lambda}{4(N_R - 1)(N_C - 1)} \quad (7.13)$$

where

N_R = the number of rows of nodes on the face of the joint

N_C = number of columns of nodes on the face of the joint

The complete development of Equation 7.13 is given in Appendix C. Using the concept of contributing areas, the following stiffness can be assigned to each type of node:

$$\begin{aligned}
 \kappa_{corner} &= \bar{\kappa} \\
 \kappa_{edge} &= 2\bar{\kappa} \\
 \kappa_{interior} &= 4\bar{\kappa}
 \end{aligned} \tag{7.14}$$

A simply supported beam with a uniformly distributed load (Figure 7.32) was used to investigate the behavior of the JOINTC element. The material properties chosen for the beam were $E = 27,600$ MPa (4,000,000 psi) and $\nu = 0.18$. The maximum deflection from beam theory is 0.906 m (35.7 in.).

The beam was modeled with C3D27R elements. Three cases were explored. First, the beam was modeled as a monolithic elastic solid. For this case ABAQUS predicted a maximum deflection (δ_{ES}) of 0.913 m (35.9 in.).

For the second case the beam was split in two parts at its centerline, and the nodes across the joint were joined with JOINTC elements, as indicated in the inset labeled "DETAIL A" in Figure 7.32. Values of q ranging from 10^3 to 10^7 MN/m/m (1.45×10^5 to 1.45×10^9 lb/in./in.) were selected, and the individual spring constants, κ , were calculated using Equations 7.13 and 7.14. Because it was desired to transfer both shear and bending moments across the joint, the JOINTC elements were assigned identical stiffnesses in all three degrees of freedom. The models were submitted as ABAQUS runs, and the maximum deflections were extracted from the output files. The results of these computations, presented in Figure 7.33, indicate that as q approaches infinity, the deflection (δ_{JOINTC}) approaches that calculated for the case in which the beam was monolithic. This could be true only if the JOINTC elements were effective in transferring shear and bending moments across a joint.

In the third and final case investigated for this beam problem, the JOINTC elements were replaced with a type of kinematic restraint known in ABAQUS as multi-point constraints (MPC). MPCs are used to specify constraints between nodes. These constraints may be

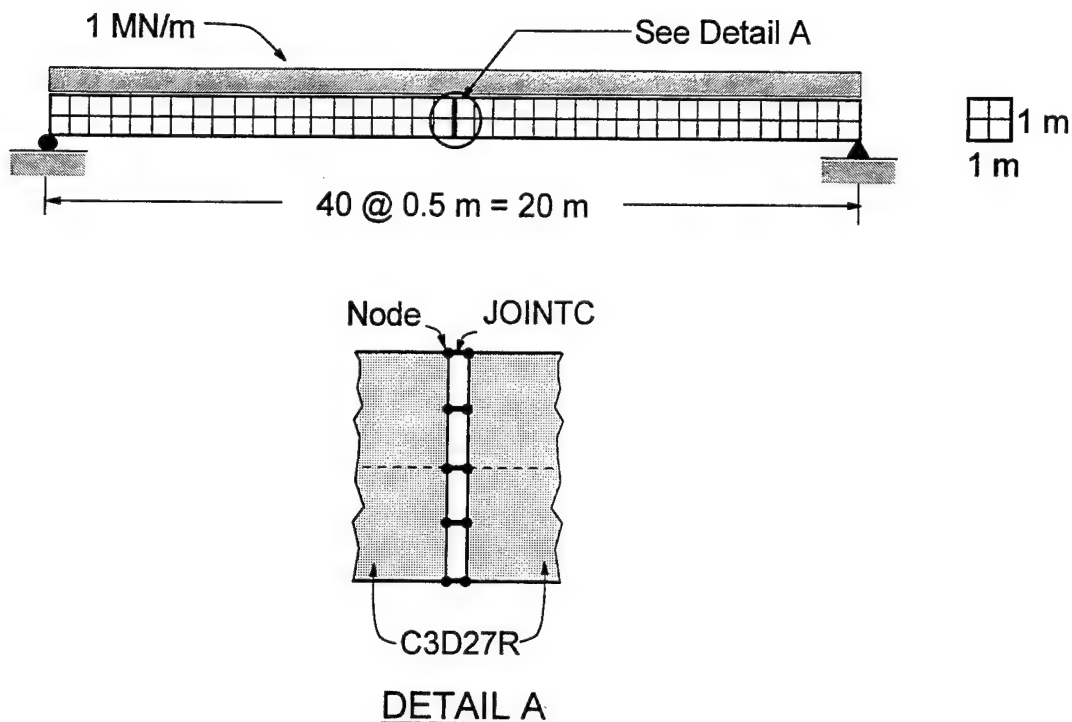


Figure 7.32. Simply-supported beam problem to test JOINTC element

quite general, and a full description is not warranted here. The type of MPC option chosen for the beam problem is referred to as a "TIE"; that is, all active degrees of freedom are set equal at two nodes. It is intended to be used to join two parts of a mesh when corresponding nodes are to be fully connected. The results from this analysis, as expected, indicated that the maximum deflection was 0.913 m (35.9 in.), identical to that from the monolithic elastic solid beam. Thus, MPCs with the "TIE" option invoked may be used to rigidly connect two bonded elastic bodies.

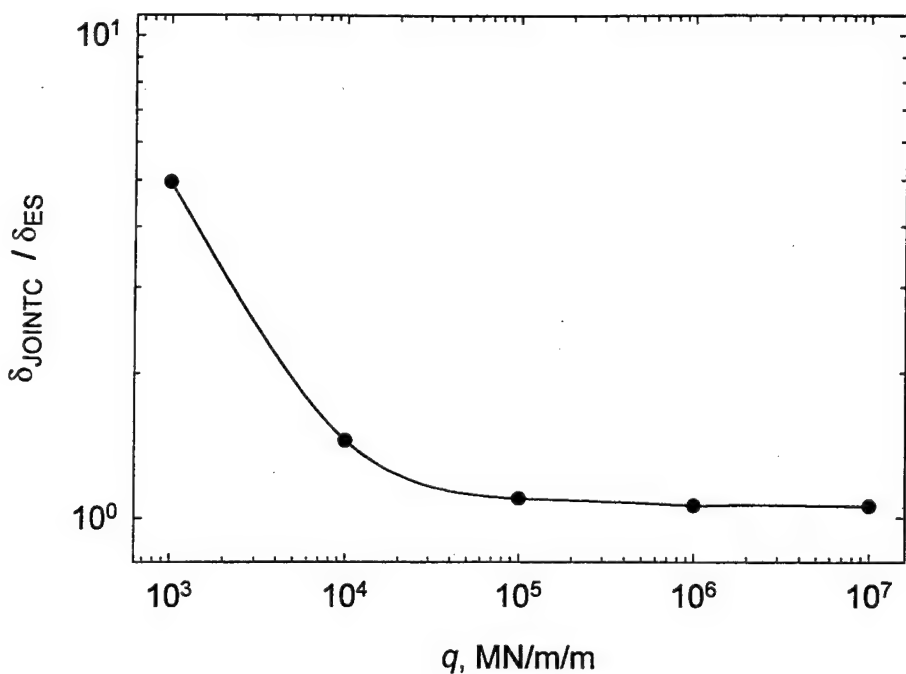


Figure 7.33. Results from simply-supported beam with JOINTC elements

Example problem

An example jointed slabs-on-grade problem was developed to verify the usefulness of the proposed ABAQUS model. The structural response obtained from the finite element solutions was compared with the closed-form, Westergaard-type solution for load transfer developed by Ioannides and Hammons (1996). The concepts of the dimensionless joint stiffness developed by Ioannides and Korovesis (1992), as described in Chapter 5, were used to determine the structural parameters for the joint.

Two 6-m (20-ft) square slabs-on-grade separated by a doweled joint were chosen for the example problem. Table 7.6 contains of summary of the material and structural parameters for this problem. Where applicable, the equation numbers from Chapters 2, 4, and 5 have

Table 7.6

Material and Structural Parameters, Jointed Slabs-on-Grade Example Problem

Parameter	Equation No.	Dimensions	Value
Slabs-on-Grade Material Parameters			
E_s	--	F/L^2	27,600 MPa (4,000,000 psi)
v_s	--	--	0.15
k	--	F/L^3	115 MPa/m (425 psi/in.)
Slabs-on-Grade Structural Parameters			
h	--	L	0.432 m (17 in.)
ℓ	4.1	L	1.133 m (44.6 in.)
a	--	L	0.138 m (5.4 in.)
ϵ	--	L	0.123 m (4.8 in.)
ϵ/ℓ	--	--	0.108
Joint Material Parameters			
E_d	--	F/L^2	200,000 MPa (29,000,000 psi)
v_d	--	--	0.30
K	--	F/L^3	407,000 MPa/m (1,500,000 psi/in.)
Joint Structural Parameters			
s	--	L	0.457 m (18 in.)
d	--	L	0.0508 m (2 in.)
I_d	--	L^4	$0.327 \times 10^{-6} \text{ m}^4$ (0.785 in. ⁴)
A_z	5.6	L^2	$1.82 \times 10^{-3} \text{ m}^2$ (2.83 in. ²)
G_d	5.5	F/L^2	76,900 MPa (1,115,000 psi)
ω	--	L	0.00254 m (0.1 in.)
ϕ	5.4	--	867
C	5.3	F/L	4600 MN/m (26,300,000 lb/in.)
β	4.5	L^{-1}	16.8 m^{-1} (0.427 in. ⁻¹)
DCI	5.2	F/L	604 MN/m (3,450,000 lb/in.)
D	5.1	F/L	597 MN/m (3,410,000 lb/in.)
$f = D/sk\ell$	--	--	10.0
$q = D/s$	--	F/L^2	1300 MN/m/m (190,000 psi/in.)
Structural Response Parameters			
LTE_δ	4.11	--	0.828
LTE_α	4.13	--	0.281
LT	2.7	--	0.220

been listed in the table. The material parameters assumed in this problem were typical of those commonly used in analysis. Similarly, the joint structural parameters were selected to be representative of those which might be expected in airport pavements. The load consisted of a uniform pressure of ($p = 2.5 \text{ MPa (360 psi)}$) distributed over an area of 0.06 m^2 (93 in.^2). The structural response calculated from the Westergaard-type solution is also tabulated in Table 7.6.

2D shell element model

A 2D shell element model of the example problem was developed to obtain response parameters for comparison with 3D models and to study the effect of the Kirchoff assumptions on load transfer at a joint. Figure 7.34 shows a plot of the finite element mesh used for this problem along with the material and structural properties assumed in the analysis. The ABAQUS shell element used in this model was the S8R element. The shell elements were supported on a bed of springs using the ABAQUS "FOUNDATION" option. Because calculations using this element are relatively inexpensive on the Cray computer, a fine mesh was employed to mitigate any effects from mesh fineness concerns.

Analyses were conducted using several multiples of the default transverse shear stiffness to investigate the effect this parameter might be having on load transfer. Figure 7.35 shows plots of dimensionless bending stress versus distance from the joint. The loaded slab was to the left of the joint. This plot shows that transverse shear stiffness has the same effect near a joint as near a free edge. For values of transverse shear stiffness less than approximately 100 times the ABAQUS default value, the maximum transverse bending stress values were predicted to be at some finite distance from the joint. This phenomenon is evident on both the loaded and unloaded sides of the joint.

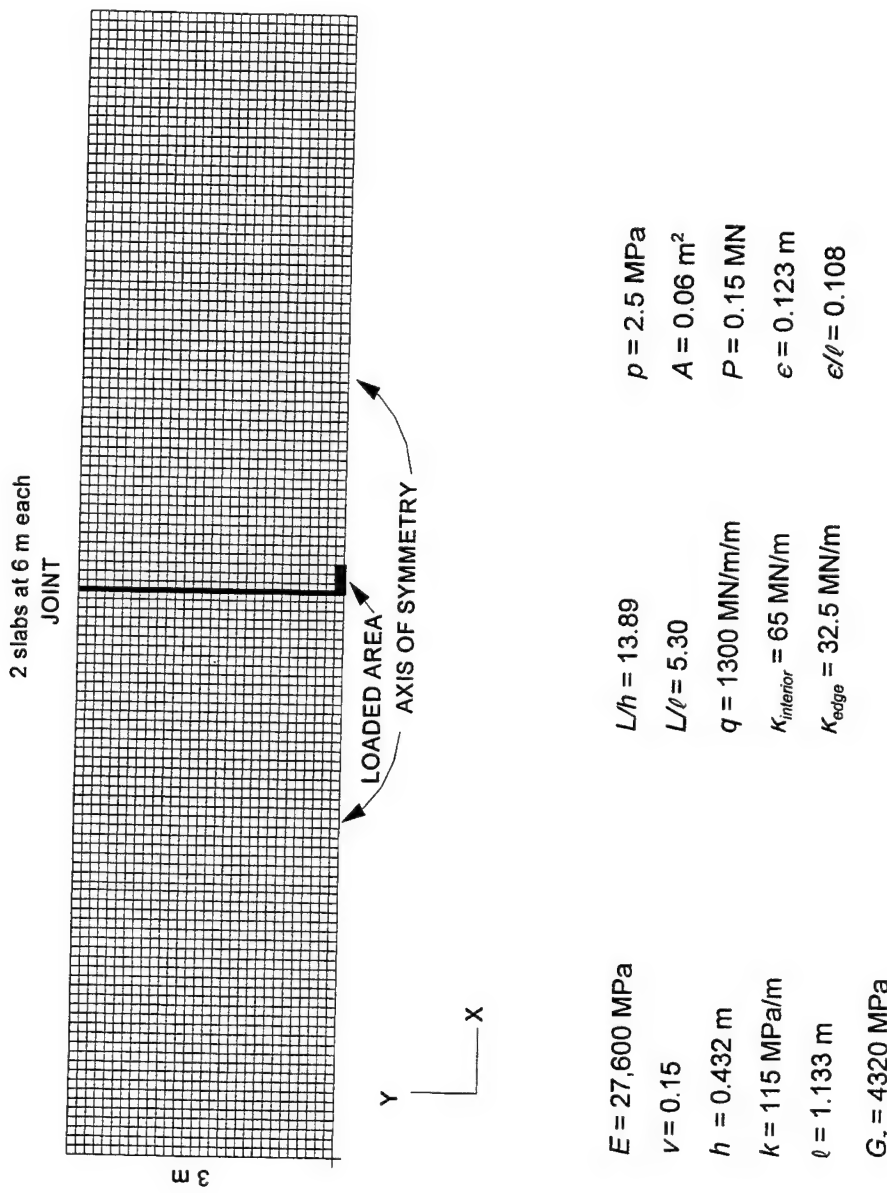


Figure 7.34. Finite element mesh for 2D jointed rigid pavement model

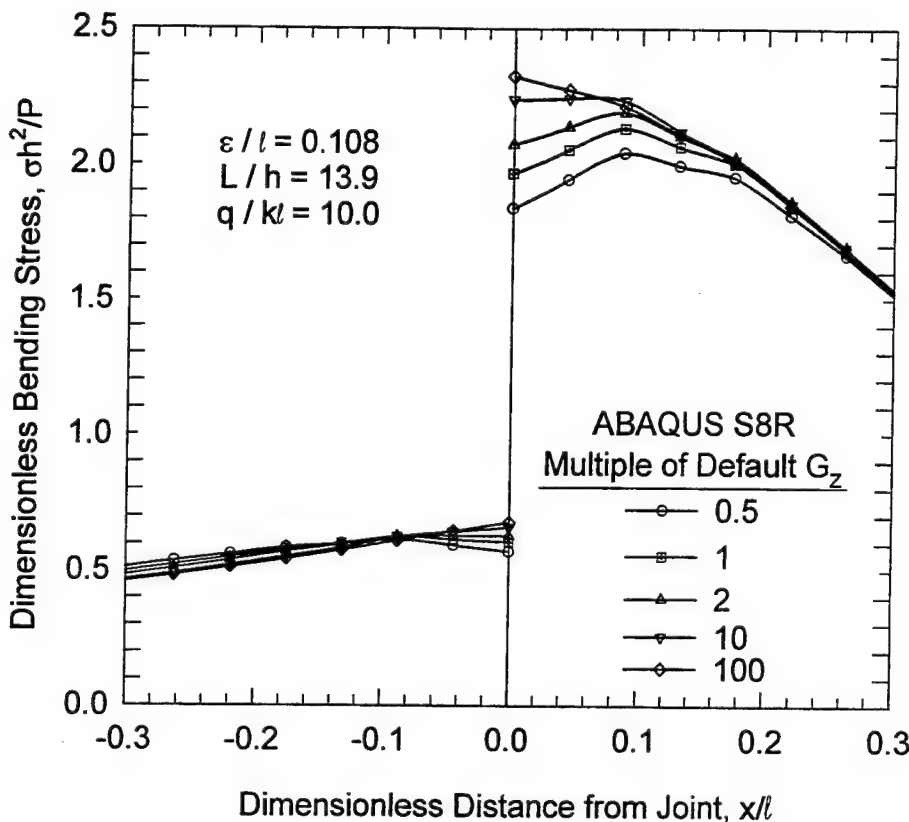


Figure 7.35. Bending stresses predicted by 2D finite element model of a jointed pavement

The influence of the transverse shear stiffness on the commonly used measures of joint response is indicated in Figure 7.36. Load transfer efficiencies were calculated by forming the ratios of the slab responses (deflection or stress) at the joint, not at the peak values. Also shown on these plots are the Skarlatos solutions. It can be seen in Figure 7.36 that LTE_s converges to the Skarlatos solution from below as transverse shear stiffness increases, while LTE_o and LT converge from above. It should be recognized that the Skarlatos solution is based upon Westergaard's theory and implicitly assumes that the slab can be modeled as a thin plate. Deflection load transfer efficiency for values of default transverse shear stiffness

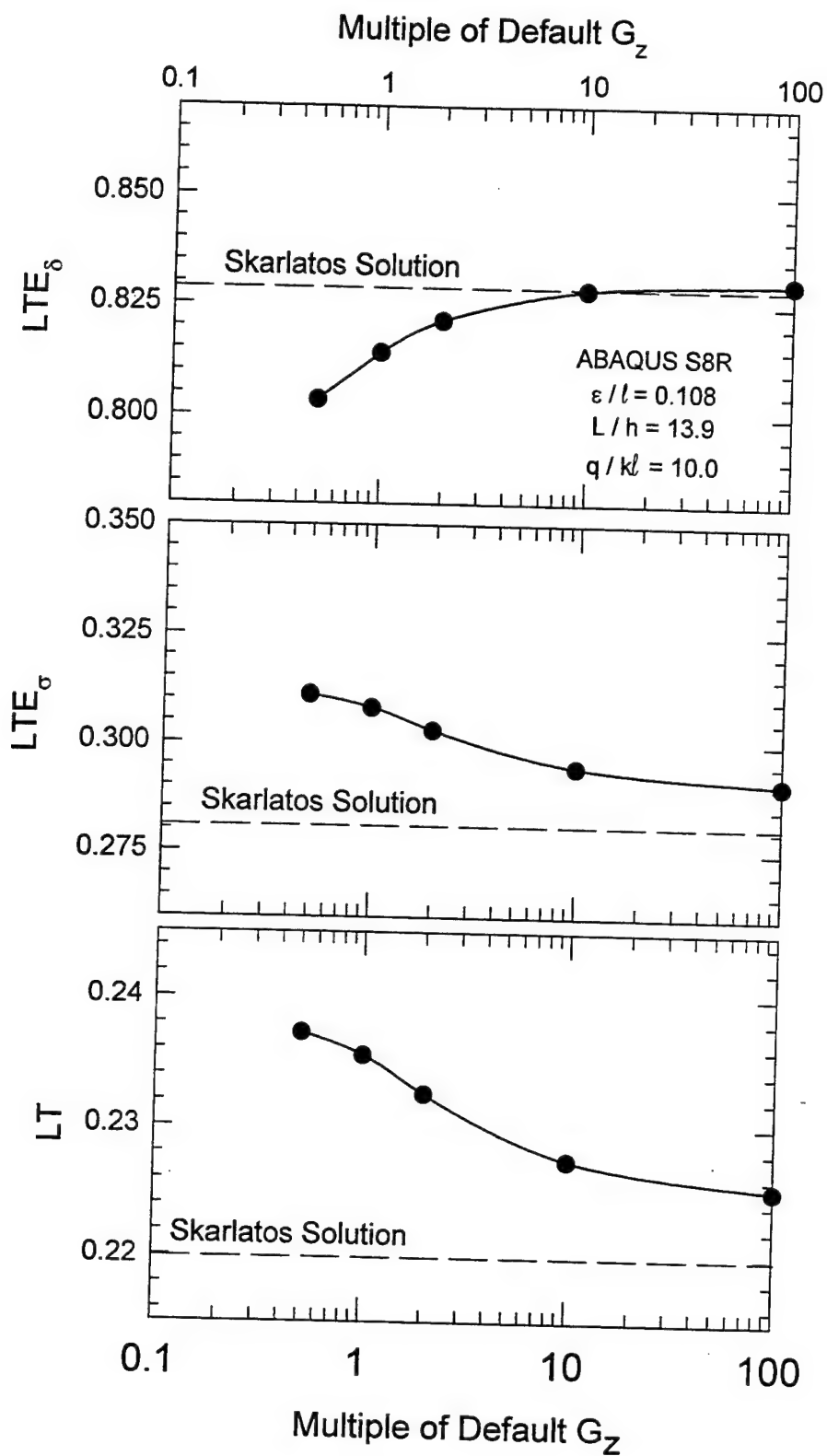


Figure 7.36. Comparison of joint response parameters, 2D finite element model

greater than approximately 10 times the ABAQUS default values agrees well with the Skarlatos solution. However, load transfer and stress load transfer efficiencies predicted by the finite element model are consistently greater than those predicted by Skarlatos.

3D model

A 3D finite element model using ABAQUS C3D27R elements was created and executed. The model was identical in plan view to the 2D shell element model shown in Figure 7.34. Four elements were used through the depth of the model. The lowest layer of elements were supported on a bed of springs using the ABAQUS "FOUNDATION" option. All material and structural parameters were the same as those used for the 2D shell element model (as described in Figure 7.34). However, one exception should be noted. In 3D the individual spring constants were assigned according to Equations 7.13 and 7.14 as follows

$$\begin{aligned}\kappa_{corner} &= 2.031 \text{ MN/m (11,600 lb/in.)} \\ \kappa_{edge} &= 4.063 \text{ MN/m (23,200 lb/in.)} \\ \kappa_{interior} &= 8.125 \text{ MN/m (46,400 lb/in.)}\end{aligned}\quad (7.15)$$

Figure 7.37 shows the a plot of the dimensionless bending stress from the 3D model along with selected data from the 2D shell element model. On the loaded side of the joint, the 3D model predicted lower stress than the 2D models. As was the case for a free edge, the 3D model predicts that the maximum stress does not occur at the joint but some small distance away from the joint. The higher bending stresses predicted by the 2D model were believed to be an artifact of the 2D shell element formulation, and the 3D bending stresses are likely more accurate.

The 3D finite element model was repeatedly executed, varying the value of q to get a range of responses. These data were then plotted against results from the relationships developed by Ioannides and Hammons (1996) from the Skarlatos model. The results of these

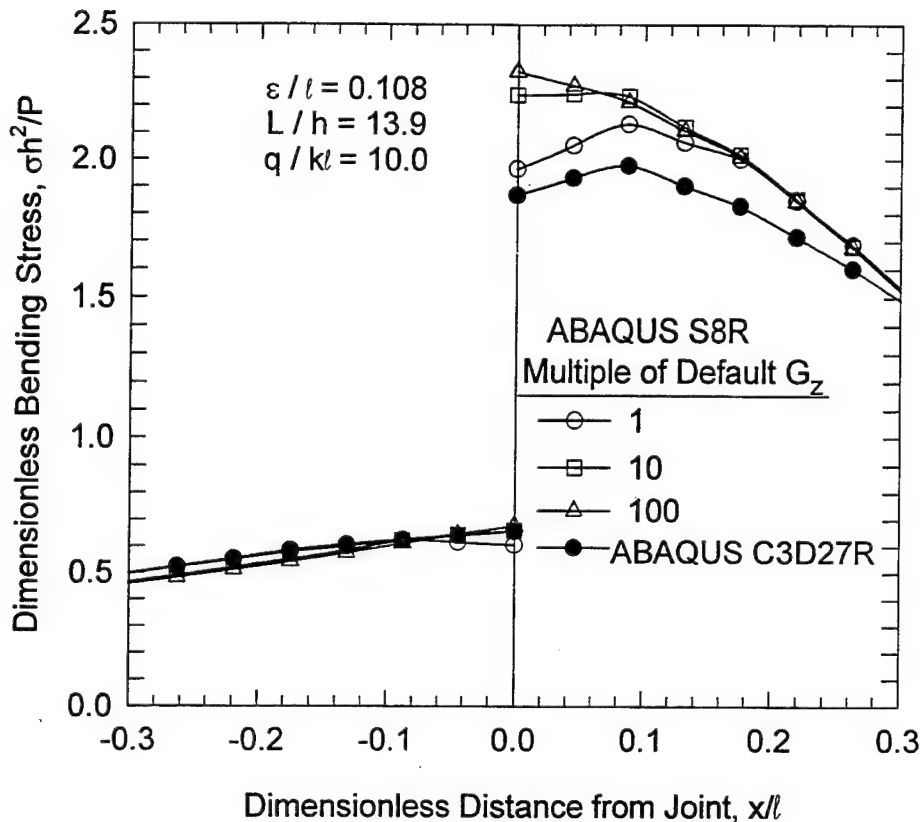


Figure 7.37. Comparison of bending stresses predicted by 2D and 3D finite element models of a jointed pavement

comparisons are presented in Figures 7.38 and 7.39. The ABAQUS 3D example problem is indicated in each plot. These figures indicate that over a wide range of values of joint stiffnesses and load transfer efficiencies, the trends predicted by the 3D finite element models are in agreement with those predicted by the closed-form solution. From Figure 7.39, it can be observed that the Skarlatos model predicts lower values of stress load transfer efficiencies over a range of deflection load transfer efficiencies from 0.6 to 0.9, the range commonly encountered in airport pavements. Thus, the Skarlatos closed-form solution is more

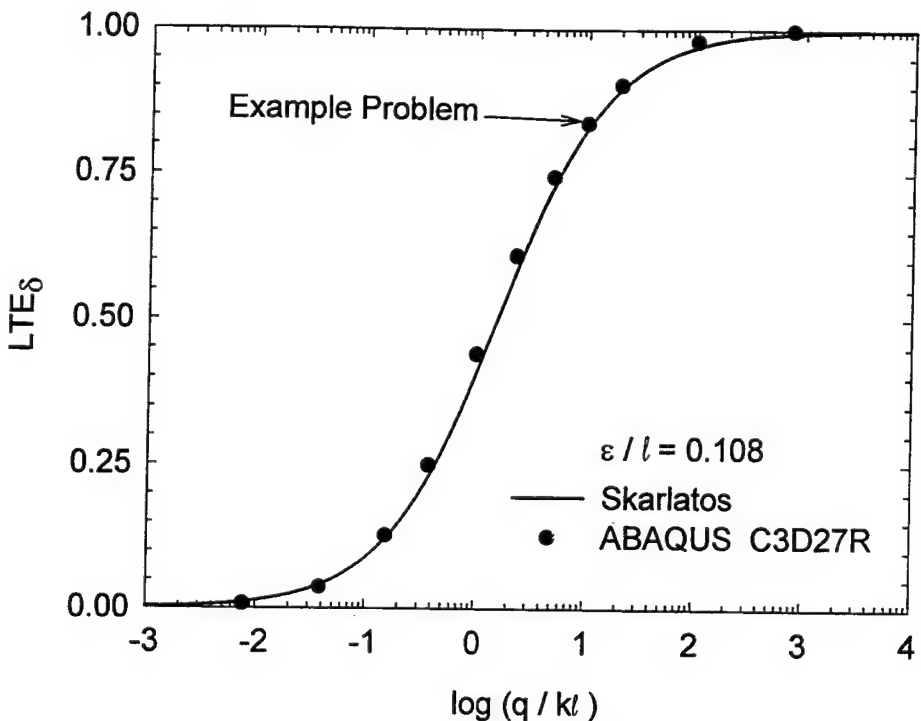


Figure 7.38. Comparison of 3D finite element model with closed-form solution, dimensionless joint stiffness versus deflection load transfer efficiency

conservative than the finite element solutions over this range of values. This conclusion is also confirmed by the results from the example problem as shown in Figure 7.36. However for many, if not all, heavily-loaded rigid airport pavement slabs, the slab thickness is great enough that thin plate theory is not strictly valid. For these slabs load transfer is greater than that predicted by thin plate theory.

CONTACT SURFACES

In a rigid pavement structure the interface between the slab and base course may be bonded, debonded, or perhaps some condition in between. In the debonded case movement

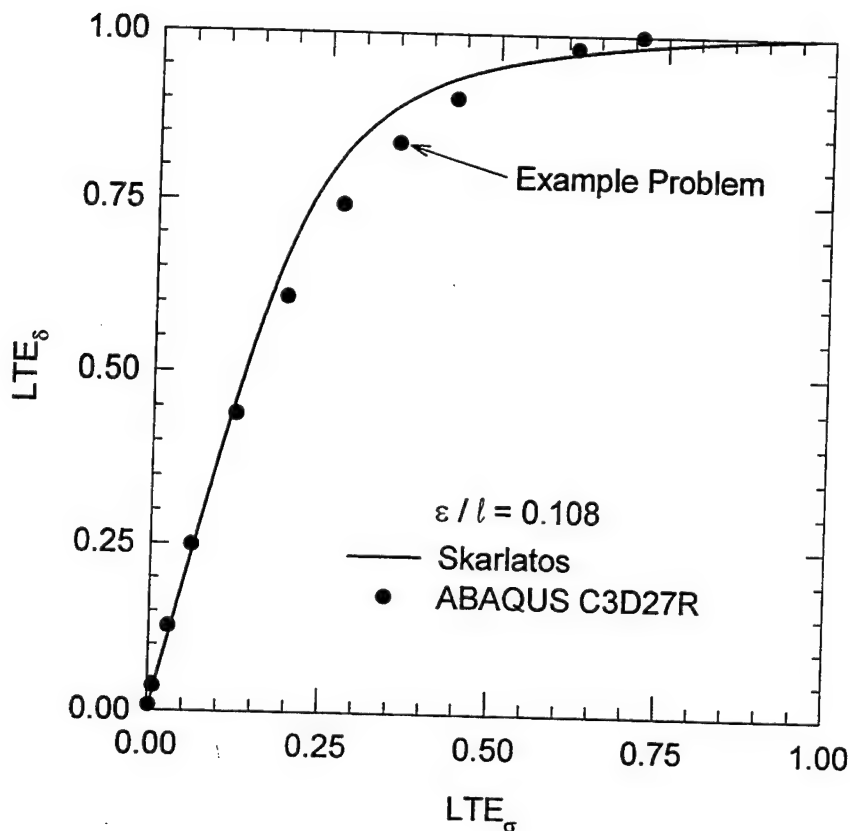


Figure 7.39. Comparison of 3D finite element model with closed-form solution, stress load transfer efficiency versus deflection load transfer efficiency

along the interface between the two bodies may be resisted by friction. If the slab and base are truly debonded, gaps may open up, particularly in the vicinity of a loaded joint. These type of contact interaction problems pose a challenge for the finite element modeler. This section discusses some contact and friction modeling options available in ABAQUS.

When two solid bodies touch, a contact stress will be transmitted across the common surface. If there is friction between the two surfaces, a shear stress will also be present. The

contact areas must be determined, and then the normal and shearing stresses transmitted through the contact area must be calculated. This gives rise to a nonlinear problem which requires an iterative solution procedure.

Two methods of modeling the mechanical interaction between element faces in ABAQUS are germane to the rigid pavement problem. The first of these methods involves the use of interface elements, referred to in ABAQUS as "INTER" elements, for contact and friction analysis. These elements are formulated to calculate the contact direction, contact area; and the normal and shear stresses transmitted across the contact surface. For 3D problems three INTER elements are available in the ABAQUS element library: the INTER4 element, intended for used with 8-node hexahedral elements and 4-node shell elements; the INTER8 element, intended for used with 20-node hexahedral elements and 8-node shell elements; and the INTER9 element, intended for used with 21- to 27 node hexahedral elements and 9-node shell elements. Use of the INTER8 element is discouraged, because uniform pressure on the 8-node surface produces negative contact forces at the corner nodes. The use of INTER elements is tedious, since they require the creation of zero-thickness elements along the contact interface.

The second method of modeling the contact and friction between two bodies is the ABAQUS contact interaction option. This option, recently added to ABAQUS, is more convenient than the INTER element, because creation of additional elements is not required. The two surfaces which may be in contact are defined by the user along with a choice of several friction models. Because of negative contact forces which arise at the corners of elements with 8 nodes on a face, the use of contact interaction for 20-nodes hexahedral elements is not recommended. For purposes of this research a simple Coulomb friction model was adopted.

For both the INTER elements and the contact interaction option, the selection of boundary conditions at the interface is important to avoid certain numerical solver problems. Over constraint of the model results in “zero pivot” and “numerical singularity” warning messages from the solver, and in most cases, leads to a crash of the finite element run. Because the contact interaction provides a kinematic constraint, these errors occur when two nodes on either side of a contact surface are constrained with redundant kinematic boundary conditions.

Figure 7.40 shows examples of an overconstrained and a nonoverconstrained contact surface problem.

Figure 7.41 shows a simply-supported beam problem investigated using the friction and contact capabilities in ABAQUS. The beam was loaded with a uniformly distributed load of 1 MN/m (5,710 lb/in.) and was assigned the elastic constants $E = 27,600 \text{ MPa}$ (4,000,000 psi) and $\nu = 0.18$. The symmetry of the problem was used to model only half of the beam. The beam was split into two parts along its neutral axis, and various friction values were assigned to the contact surface along the neutral axis. The beam was modeled using C3D27R elements, while both the INTER9 elements and the contact interaction element were used (in separate analyses) to model the contact and friction at the neutral axis. The maximum deflection of this beam (if it were monolithic) predicted by beam theory is 0.906 m (35.7 in.).

Results from these analyses are plotted in Figure 7.42. For both of the investigated methods of modeling contact, deflections calculated by the finite element method approach that predicted by beam theory as the coefficient of friction becomes large. The results also indicate that the contact interaction option predicts deflections closer to the theoretical deflection for values of the coefficient of static friction greater than approximately 10. Because the contact interaction method is easier to use than interface elements, and because the contact

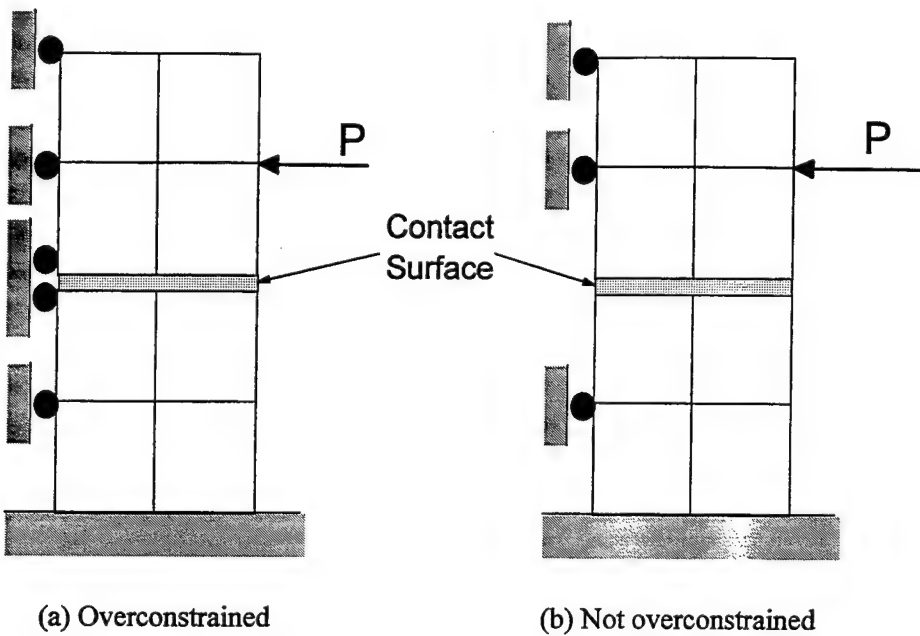


Figure 7.40. Example of over constraint for contact problem

interaction method appears to be slightly more accurate than the interface element method, it is recommended that the contact interaction method should be used to model contact and friction where required.

SUMMARY

The following conclusions can be reached from the finite element response and sensitivity studies conducted using ABAQUS:

- For slabs where L/h is less than 100, classical Kirchhoff assumptions, adopted by Westergaard, lead to errors in predicting edge stresses. The maximum edge stress is in fact less than that predicted by Westergaard. Furthermore, the maximum edge stress does not occur at the edge of the slab but at some finite distance from the edge. For most practical rigid pavement systems, the maximum edge stress will occur

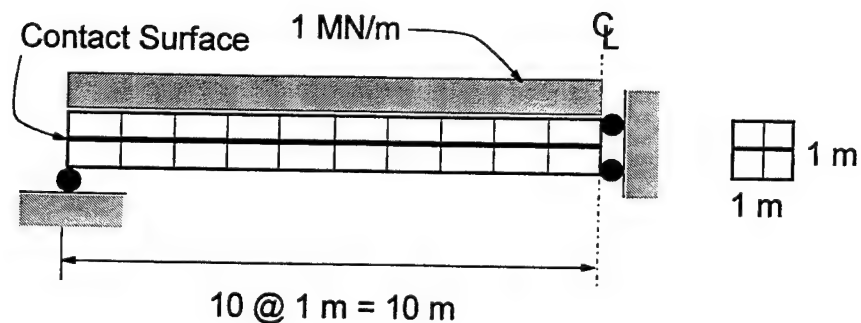


Figure 7.41. Simply-supported beam problem to test contact interaction features of ABAQUS

within 0.1ℓ of the edge of the slab and will be approximately 10 percent less than that predicted by the Westergaard theory. Experimental studies done by the Corps of Engineers have shown that edge and interior stresses predicted by the Westergaard theory are conservative, but direct experimental evidence of the above conclusion could not be located in the literature.

- The phenomenon described above is also present on the loaded and unloaded sides of a joint in analysis of jointed pavements. Thus, the Kirchoff assumptions have an effect on the calculated values of load transfer. However, most airport rigid pavement slabs are thick enough that the Kirchoff thin plate assumptions are not strictly valid. Based upon the analytical results from this chapter, it appears that load transfer values for slabs in which transverse shear deformations cannot be ignored are greater than those predicted by thin plate theory. Therefore, the classical

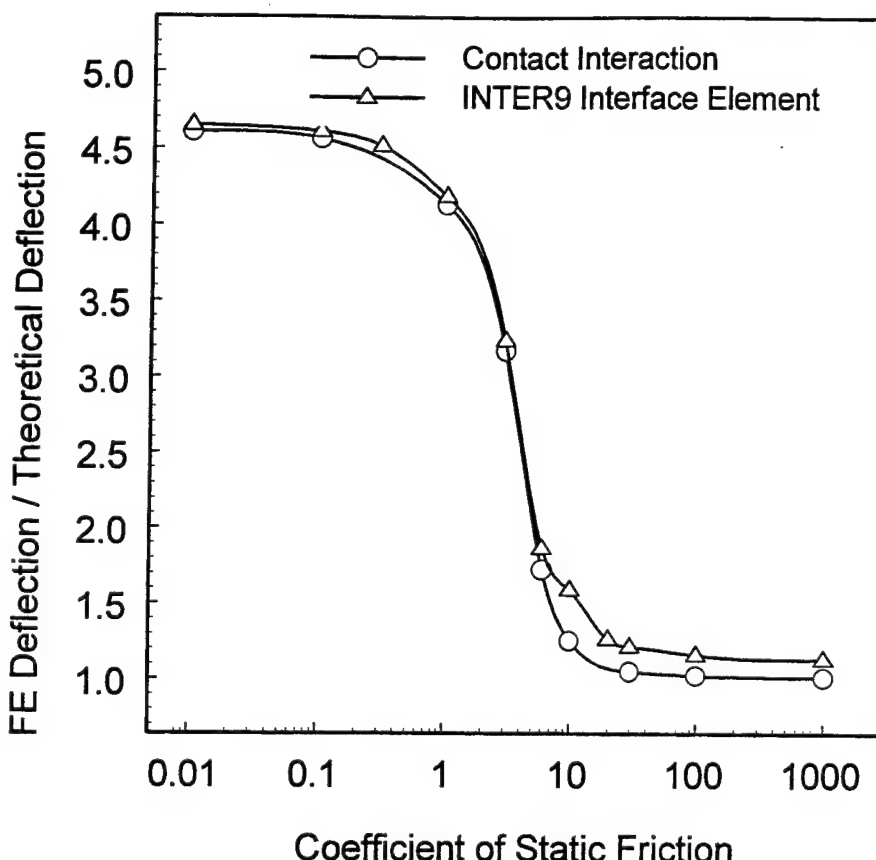


Figure 7.42. Results from simply-supported beam with contact and friction

assumptions used in developing the FAA design criteria have a fortuitous intrinsic margin of safety which previously had gone unrecognized.

- A method for allocating the joint stiffness to the nodes along the joint was developed based upon the concept of contributing area. Furthermore, the ABAQUS JOINTC element was chosen for the connecting nodes at the joint due to its capabilities and versatility.
- The ABAQUS C3D27R element was chosen for development of the general rigid pavement model. The primary advantages and disadvantages of this element were the following:

- (1) Accuracy. This Lagrangian quadratic element with reduced integration is not subject to locking when the primary response mode is bending. Furthermore, spurious, zero-energy displacement modes (hourgassing) cannot propagate through the mesh; thus, hourgassing is not problematic.
 - (2) Compatibility with contact interaction model. The C3D27R element is compatible with both the INTER9 interface element and the contact surface method of modeling contact interaction. Use of the C3D20R element leads to numerical instability due to negative contact forces at the corner nodes.
 - (3) Computational efficiency. The primary disadvantage of the C3D27R element lies in the fact that more computer time is required than for the corresponding serendipity quadratic element (ABAQUS C3D20R).
- The multi-point kinematic constraint capability in ABAQUS (known as the MPC with the "TIE" option envoked) can be used to rigidly connect two bonded elastic bodies.
 - Example 3D finite element calculations conducted for jointed slabs-on-grade indicated that the finite element solution compares favorable with the closed-form Westergaard-type solution of Skarlatos. Therefore, it is reasonable to extend the techniques developed in this chapter to the more challenging problem of slabs resting on stabilized bases.
 - The ABAQUS contact interaction method is recommended in lieu of interface elements for further use where contact and friction modeling is required.

CHAPTER 8: EXPERIMENTS ON LABORATORY-SCALE PAVEMENT MODELS

INTRODUCTION

Laboratory-scale experiments were conducted on jointed rigid pavement models to supplement the data from the small-scale model studies conducted in the 1950's (described in Chapter 3). Specifically, the objectives of these experiments were to:

- Observe the qualitative response of the rigid pavement slab-joint-base system at the phenomenological level.
- Obtain quantitative data to verify certain aspects of the analytical models developed in this study.

This chapter includes a description of the experimental test plan and materials used to construct the models as well as the results of the experiments are presented and discussed.

EXPERIMENTAL PLAN

Experiments were conducted on five laboratory-scale jointed rigid pavement models. A matrix describing the parameters of each experiment is given in Table 8.1. Each rigid pavement model consisted of two portland cement concrete slabs, 915 mm (36 in.) by 1,220 mm (48 in.) by 51-mm (2-in.) thick, separated by a joint. In each experiment the subgrade was modeled by a 1,800 mm (72 in.) by 1,200 mm (48 in.) by 300 mm (12 in.) thick rubber block. This block, purchased by the Waterways Experiment Station about 1968 from the Goodyear Tire and Rubber Company, was composed of styrene butadiene (automobile tire) rubber.

The response of the joint was expected to depend upon the presence of discontinuities in the base and the degree of bonding between the base course and the slabs. The slabs were

Table 8.1**Laboratory-Scale Experiment Matrix**

Experiment	Load Transfer Device	Foundation	Loading
LSM-1	None	Rubber Block	Edge and Corner
LSM-2	Doweled Joint	Rubber Block	Corner
LSM-3	Doweled Joint	Monolithic Cement- Stabilized over Rubber Block	Corner
LSM-4	Doweled Joint	Induced-Crack, Cement- Stabilized over Rubber Block	Corner
LSM-5	Doweled Joint	Monolithic Cement-Stabilized over Rubber Block with Bond Breaker	Corner

Note: Experiment LSM-3 was flawed due to technical difficulties. This experiment was repeated as LSM-3R.

founded either directly on the rubber block or on one of three different configurations of

38-mm (1-1/2-in.) thick cement-stabilized base constructed directly on the rubber block:

- A monolithic cement-stabilized base.
- A cement-stabilized base with a discontinuity beneath the joint.
- A cement-stabilized base with the bond between the base course and slabs intentionally broken.

To develop baseline data, an experiment was also conducted in which the jointed slabs were founded directly on the rubber block without a base course. Because the cement-stabilized base course was relatively thin, the resulting composite modulus of subgrade reaction of the foundation with the base course was not expected to be significantly different from that of the rubber block alone.

Studies by Ioannides and Korovesis (1992) have shown that the response of both the aggregate interlock and dowel load transfer mechanisms can be described by a single relationship involving a dimensionless joint stiffness. Therefore, only one type of load transfer

mechanism, the doweled construction joint, was studied. The doweled construction joint was selected because the joint stiffness can be more easily duplicated from one model to another than is possible with a contraction joint even under controlled laboratory conditions. The response of the plain contraction joint could be inferred analytically using the methods pioneered by Ioannides and Korovesis (1992).

Configurations for each experiment are shown in Figure 8.1. Experiment LSM-1 was constructed to give no load transfer in order to obtain data required to estimate the modulus of subgrade reaction of the rubber block. A 1.58-mm (1/16-in.) thick piece of Teflon was placed between the two slabs to simulate a fixed joint opening and to minimize the possibility of additional load transfer caused by aggregate interlock between the slabs. All other models were constructed with uniformly spaced dowels.

The rigid pavement slab-joint-foundation models were constructed and tested in a steel reaction box. One vertical face of the box featured a transparent window allowing the cross-section of the model in the region of the joint to be observed during loading. The ends of the slabs were restrained to prevent rotation thereby increasing their effective length. Loads were provided by a closed-loop, servo-hydraulic structural testing system.

MATERIALS

The materials used in the experimental program were selected to meet three criteria:

- They must, to the extent practical, be representative of materials used to construct airport pavement facilities.
- They must be capable of being produced in the laboratory without large variations in material properties from model to model.
- They must be selected to expedite the testing schedule to meet the milestones set forth in the Interagency Agreement between WES and the FAA.

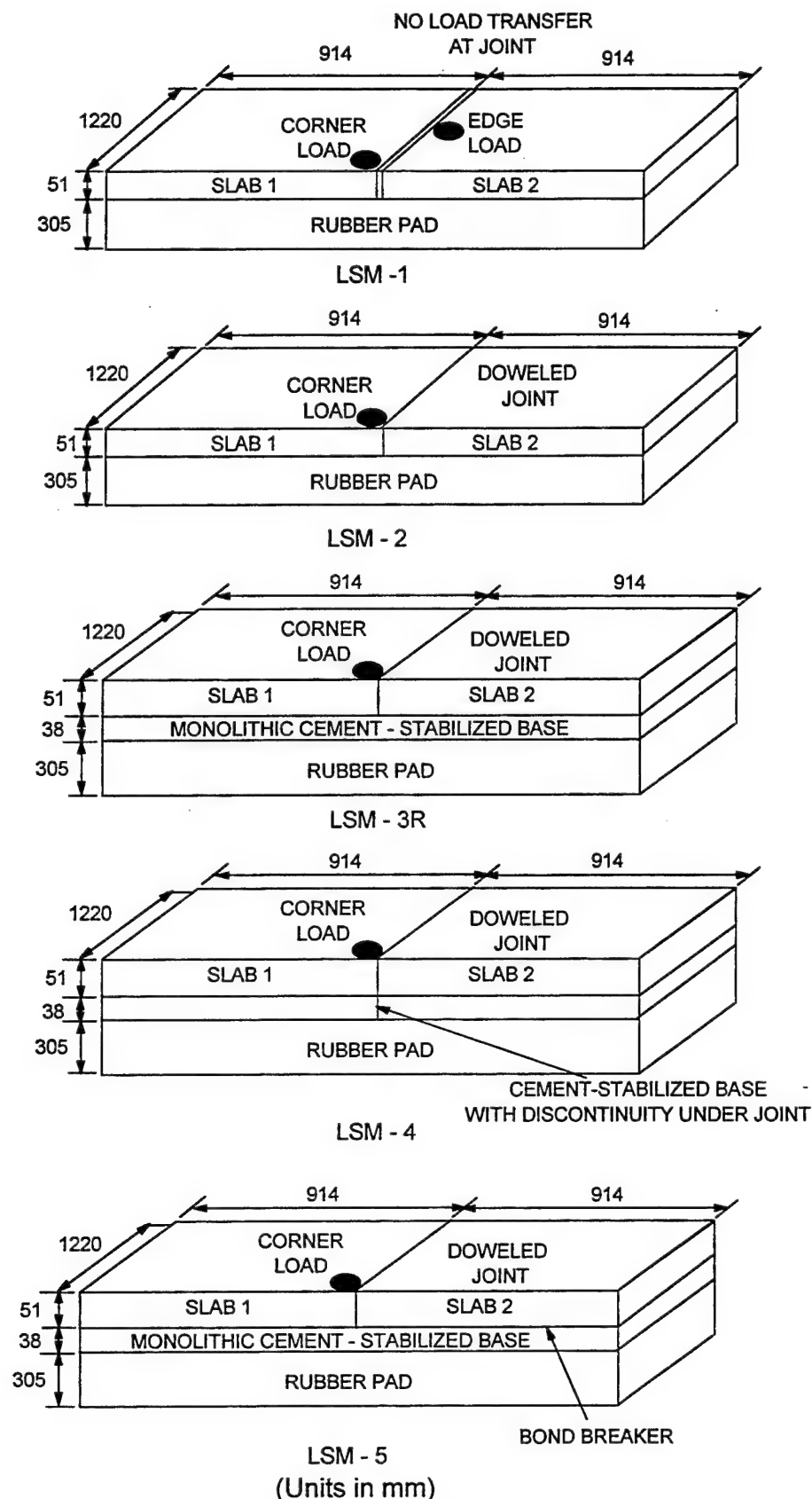


Figure 8.1. Test configurations for laboratory scale models

A discussion of the selection of the concrete materials for the slabs, cement-stabilized material for the base, and steel for the dowels follows.

Concrete materials

All slabs were portland cement concrete with 9.5-mm (3/8-in.) nominal maximum size aggregate. The mixture was proportioned to obtain a compressive strength of approximately 27.6 MPa (4,000 psi) and an elastic modulus of approximately 27,600 MPa (4,000,000 psi) at seven days with accelerated curing. To achieve these properties, a blend of ASTM C 150, Type I and Type III, cements, in equal proportions, was used along with an ASTM C 494, Type C, accelerating admixture. The fine and coarse aggregates chosen for this study were from natural (uncrushed) river deposits, consisting primarily of rounded, dense chert and silica particles.

The concrete mixture used for the slabs was selected from four trial concrete mixtures prepared in the laboratory. Water-cement ratios (by mass) varied from 0.60 to 0.70. A set of six 152 mm (6 in.) by 305 mm (12 in.) cylindrical concrete specimens was prepared from each mixture. To expedite the testing schedule for the pavement models, accelerated curing was investigated. Two curing regimens were evaluated:

- Continuous moist-curing at room temperature.
- Accelerated curing defined as two days moist-curing at room temperature, followed by two days curing in an environmental chamber at 60°C (140°F), followed by moist-curing at room temperature until time of testing.

The final concrete mixture proportions selected for the model along with a listing of the sources of the materials are shown in Table 8.2. This mixture had a water-cement ratio of 0.64 by mass. Results of tests to determine compressive strength (per ASTM C 39) and modulus of elasticity (per ASTM C 469) are presented in Table 8.3. Accelerated curing

resulted in an almost 10 percent increase in compressive strength and elastic modulus at 7 days over curing at room temperature.

Table 8.2
Concrete Mixture Proportions

Constituent	Manufacturer/Source	SI Units	U.S. Customary Units
Cement, ASTM C 150, Type I	Capital Cement San Antonio, Texas	148 kg/m ³	250 lb/yd ³
Cement, ASTM C 150, Type III	Capital Cement San Antonio, Texas	148 kg/m ³	250 lb/yd ³
Natural Sand Fine Aggregate	C. J. Horner Hot Springs, Arkansas	891 kg/m ³	1,502 lb/yd ³
Natural Coarse Aggregate	Mississippi Materials Vicksburg, Mississippi	891 kg/m ³	1,485 lb/yd ³
Pozztec 20 Admixture, ASTM C 4 94, Type C	MasterBuilders Cleveland, Ohio	2.32 l/m ³	60 fl oz/yd ³
Water	Municipal Water Supply Vicksburg, Mississippi	191 kg/m ³	322 lb/yd ³

Table 8.3
Concrete Mixture Evaluation

Test Age days	No. of Specimens	No. Of Days at 60°C (140°F)	Mean Compressive Strength MPa (psi)	Modulus of Elasticity MPa (10 ⁶ psi)
7	2	0	23.9 (3470)	25,000 (3.60)
7	2	2	25.7 (3730)	27,000 (3.90)
14	2	2	28.1 (4080)	Not Available

Cement-stabilized base materials

Cement-stabilized bases were composed of ASTM C 150, Type I, portland concrete and a silty-sand aggregate. The cement was obtained from Quikcrete of Jackson, Mississippi. The aggregate consisted primarily of a rather uniformly graded natural siliceous sand purchased

from Mississippi Materials, Vicksburg, Mississippi. Additional fines in the form of silica flour, passing a 75 μm (No. 200) sieve, manufactured by Haliburton Services of Duncan, Oklahoma, were blended with the sand in the ratio of 10 percent silica flour to 90 percent sand. A particle size analysis was conducted on the blend using the methods prescribed in AASHTO T 88. The gradation is shown in Figure 8.2.

General guidance for the cement-stabilized base was provided by FAA Advisory Circular 150/5370-10A, Item P-304 (FAA 1989). Based upon the recommendations in ACI 230.1R-90, "State-of-the-Art Report on Soil Cement" (American Concrete Institute 1994), cement contents of 7.5 and 10 percent (by mass) were selected for evaluation. The protocol in ASTM D 558 was used to determine moisture-density relationships for the silty-sand/cement blend. Moisture-density curves for both cement contents are shown in Figure 8.3. Maximum dry density for both mixtures occurred at a water content of approximately eight percent. The mixture containing 10 percent cement had a dry density approximately two percent greater than the mixture containing 7.5 percent cement. Three curing treatments of these mixtures were evaluated:

- Curing at room temperature for seven days.
- Curing at room temperature for 14 days.
- Curing at room temperature for three days followed by curing at 60°C (140°F) oven for two days, followed by curing at room temperature until a total of seven days had elapsed.

Compressive strength tests (three replicates per treatment) were conducted on 51-mm (2-in.) by 102-mm (4-in.) cylinders for the two cement contents. Specimens were prepared at a water content of eight percent and compacted to maximum density. The results of these tests are presented graphically in Figure 8.4. The bar graphs present the mean value of the

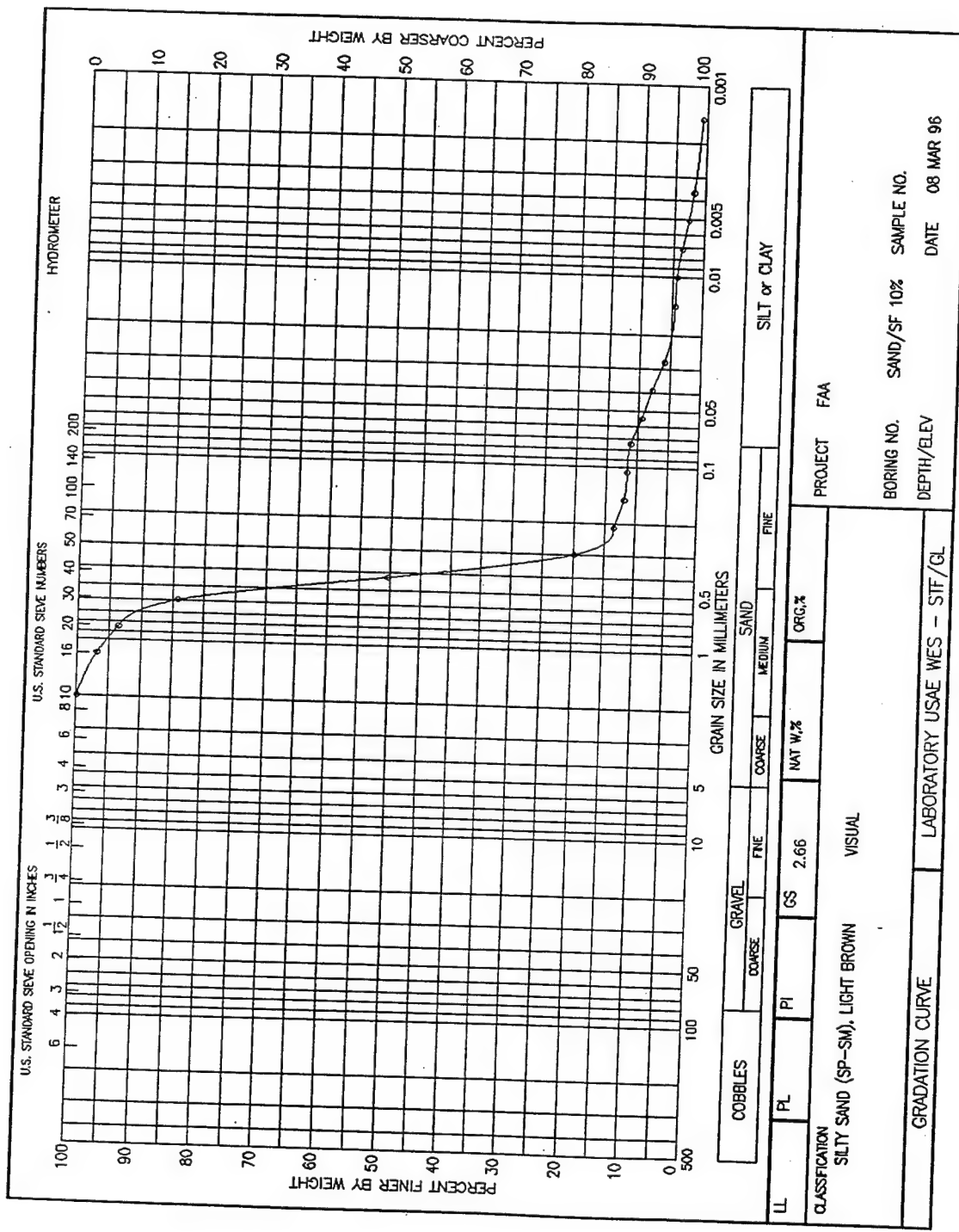


Figure 8.2. Grain size distribution of sand/silica flour blend

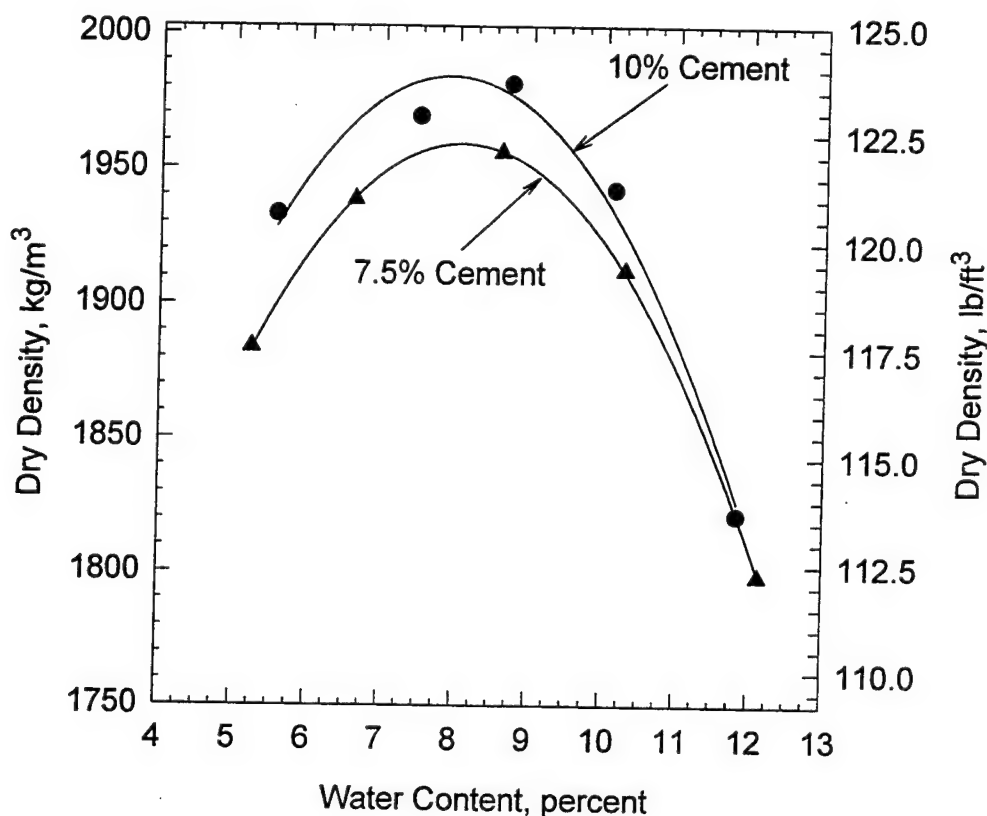


Figure 8.3. Moisture-density curves for cement-stabilized sand/silica flour blend

three replicates, while the error bars represent one standard deviation from the mean. For each treatment the compressive strengths for the mixture containing 10 percent cement are approximately 40 percent greater than the compressive strengths for the mixture containing 7.5 percent cement. For both cement contents the mean strengths at seven days cured at room temperature were approximately 65 percent of those for specimens cured 14 days at room temperature. Curing at elevated temperature increased the compressive strengths at

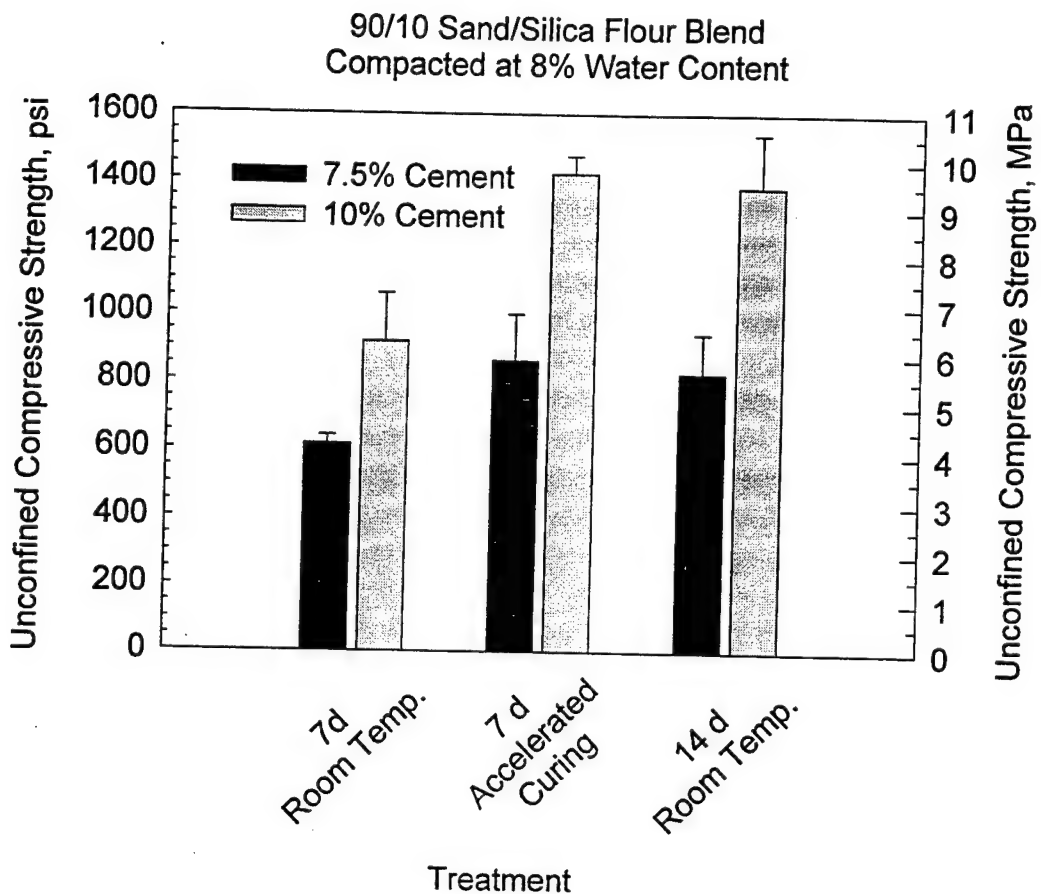


Figure 8.4. Compressive strength test results on cement-stabilized sand/silica flour blend compacted to maximum density

seven days by 30 to 35 percent to levels slightly greater than that of the specimens cured at room temperature for 14 days. Based upon these considerations, the mixture with 7.5 percent cement with accelerated curing was selected for use in the models.

Dowels

All dowels were smooth steel bars, round in cross-section, with a diameter of 6 mm (0.25 in.). The dowel bars were 434 mm (15.5 in.) long, and were spaced at 102 mm (4 in.) center to center (Figure 8.5).

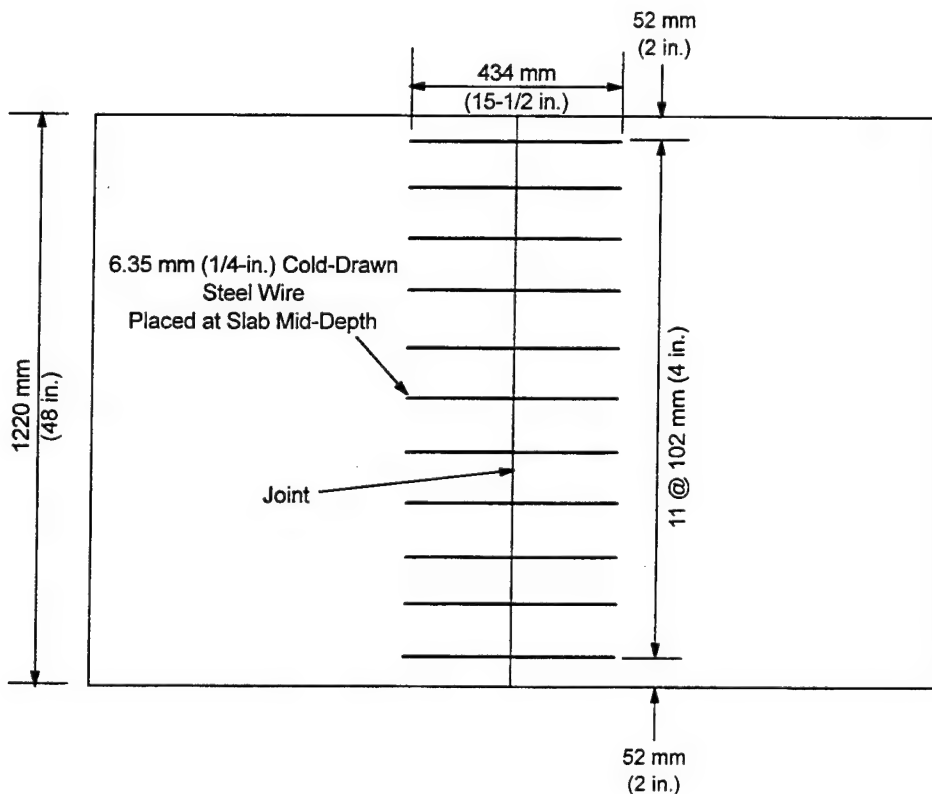


Figure 8.5. Dowel locations

MODEL CONSTRUCTION

A steel box was fabricated at the Waterways Experiment Station to house the pavement models during construction and testing. The side walls of the box were constructed of 12.7-mm (0.5-in.) thick structural steel plate, while the floor of the box was 19.1-mm (0.75-in.) thick structural steel plate. Structural steel angles were welded to the side and bottom plates. These angles were drilled and tapped so that the sides could be bolted together. Similarly, the bottom plate was constructed so that the vertical walls could be secured with bolts. The interior dimensions of the box were 1,830 mm (72 in.) by 1,220 mm (48 in.) by 762 mm (30 in.) deep. One wall of the box featured a 610 mm (24 in.) square cut-out for

insertion of a transparent pane of plexiglass to allow observation of the model during testing.

Three 102 mm (4 in.) square structural steel tubes were tack-welded underneath the box's floor so that the assembled box could be transported about the laboratory by forklift. After the reaction box was painted, the rubber block was placed on the floor of the reaction box, and the vertical walls were assembled around the box and attached with bolts. Figure 8.6 shows a photograph of the completed reaction box.

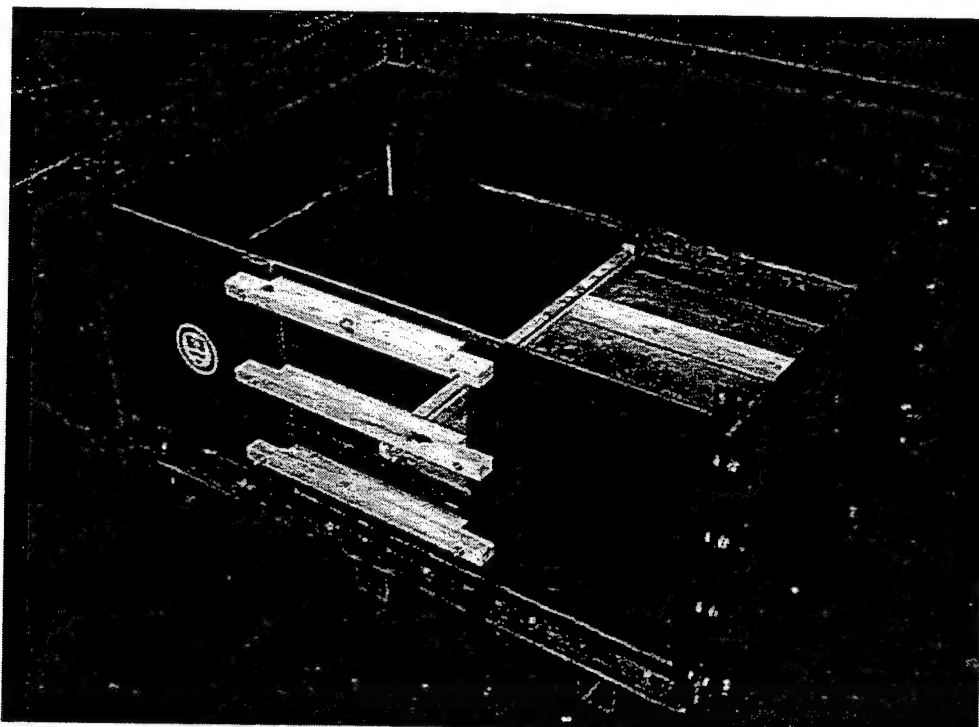


Figure 8.6. Photograph of completed reaction box

The testing proceeded along a two-week turnaround schedule as shown in Table 8.4. This expedited schedule was made possible by the use of high-early-strength cement and an accelerating admixture along with curing at elevated temperature. The concrete reached a level of maturity sufficient to produce the target strength and modulus of elasticity within approximately one week of placement.

Table 8.4
Typical Physical Model Construction Schedule

Week	Day of Week	Activity
Week 1	Monday	Prepare materials for model construction
	Tuesday	Place base course
	Wednesday	Place first slab
	Thursday	Place second slab
	Friday	3:00 p.m. Place reaction box in environmental chamber at 60°C (140°F) over weekend
Week 2	Monday	9:00 a.m. Remove from environmental chamber and allow to cool
	Tuesday	Instrument model
	Wednesday	Conduct experiment
	Thursday	Reduce data and conduct posttest photography
	Friday	Remove model and prepare reaction box for construction of next model

The physical models were constructed using the reaction box as a mold. The rubber block and the walls of the reaction box were coated with a form release agent to insure that bonding did not occur between the model and either the reaction box or rubber block.

Base course construction

The materials for the cement stabilized bases were mixed in the laboratory in a 0.17 m³ (6 ft³) portable mortar mixer. The volume and maximum wet density of the compacted base was used to calculate the mass of base material required to achieve the target density in the reaction box. An oversize batch (approximately 0.085 m³ (3 ft³)) was prepared for each placement and weighed on a scale in the laboratory. Material in excess of that required to yield the target compacted density was removed and set aside for preparation of compressive strength cylinders and flexural strength beams. The required mass of material was placed in

the box, screeded to a uniform thickness, and compacted to the target volume with a specially-fabricated compaction device (Figure 8.7).

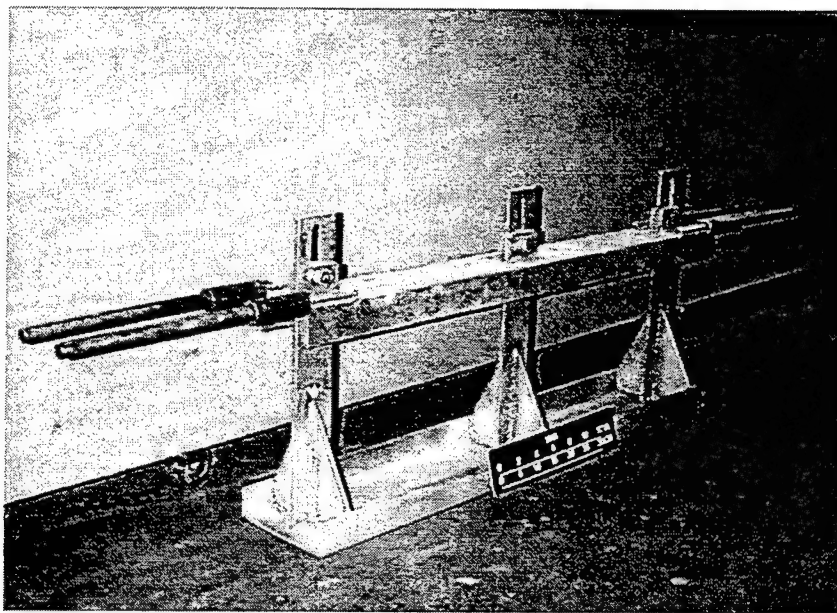


Figure 8.7. Photograph of adjustable screed/compaction device

In the case of a monolithic base, two batches of cement treated base material were prepared separately but placed and compacted simultaneously. For the model in which a discontinuity was required in the base, a cold joint was formed directly beneath the location of the joint in the slabs. This cold joint was constructed by placing the two halves of the base on consecutive days. A 38-mm (1.5-in.) deep wooden form board was placed across the reaction box as a mold for the placement of the first half of the base. The first half of the base was then placed against the mold, and the following day the mold was removed. Subsequently, the remaining half of the base was placed and compacted against first half with no other measures taken to affect the bonding between the two halves.

Three 51-mm (2-in.) diameter by 102-mm (4-in.)-high cylinders were prepared from each batch of cement-treated base. The cylinders were prepared by compacting the base material

into heavy, brass molds with a small, hand-held tamper. Also, three 76-mm (3-in.) wide by 76-mm (3-in.) deep by 286-mm (11-1/4-in.) long beams were prepared from one batch of cement-treated base per model. The base material was compacted into steel molds using a hand-held tamper featuring a square footprint. These cylinders and beams were cured under the same conditions as the models and were tested on the date the corresponding experiment was conducted to determine the compressive strength, flexural strength, and modulus of elasticity of the cement-treated base.

The bond breaker for Experiment LSM-5 was constructed of two layers of 0.152-mm (6-mil) polyethylene sheets separated by a thin layer of uniformly graded fine silica sand. Prior to casting the concrete slabs, the first sheet of polyethylene was carefully cut and fitted on top of the base as shown in the photograph in Figure 8.8. Next, a thin layer of uniform sand was spread on top of the polyethylene sheet (Figure 8.9), and a second sheet covering the entire surface was placed on top of the sand layer. Then, the slabs were placed on top the bond-breaking layer. Figure 8.10 is a photograph of the reaction box just prior to placement of the loaded slab.

Slab construction

The two concrete slabs for each experiment were placed on consecutive days. The first slab was placed against a 51-mm (2-in.) deep wooden mold faced with a 1.59-mm (1/16-in.) thick sheet of Teflon. The dowels were inserted in 6 mm (0.25 in.) diameter holes which had been predrilled through the mold and Teflon. Prior to their placement in the mold, a light coating of rust scale was removed from the dowels. The position of the dowels in the mold was adjusted to insure that equal lengths of dowel bars would be present in both slabs. A clamping device composed of pieces of wood cut to the proper dimensions and held together with screws was used to insure that the dowels were held orthogonal to the mold. The

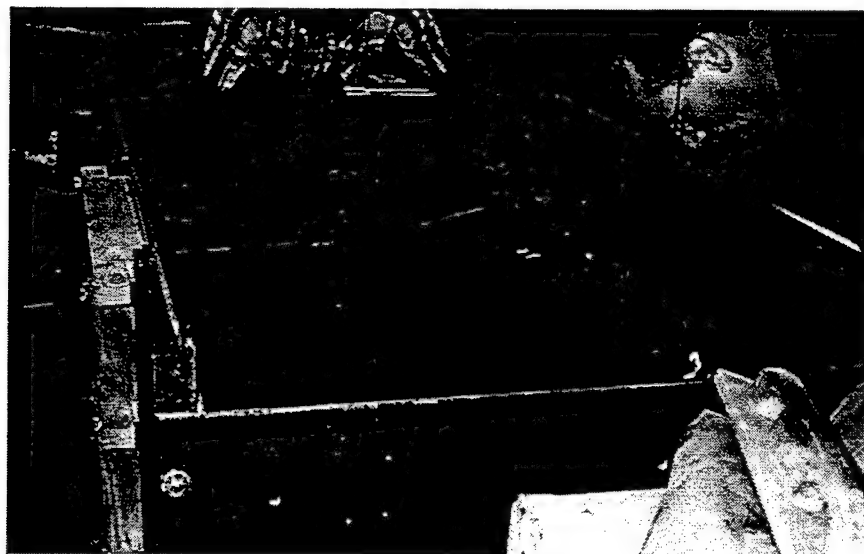


Figure 8.8. Installation of polyethylene film in reaction box

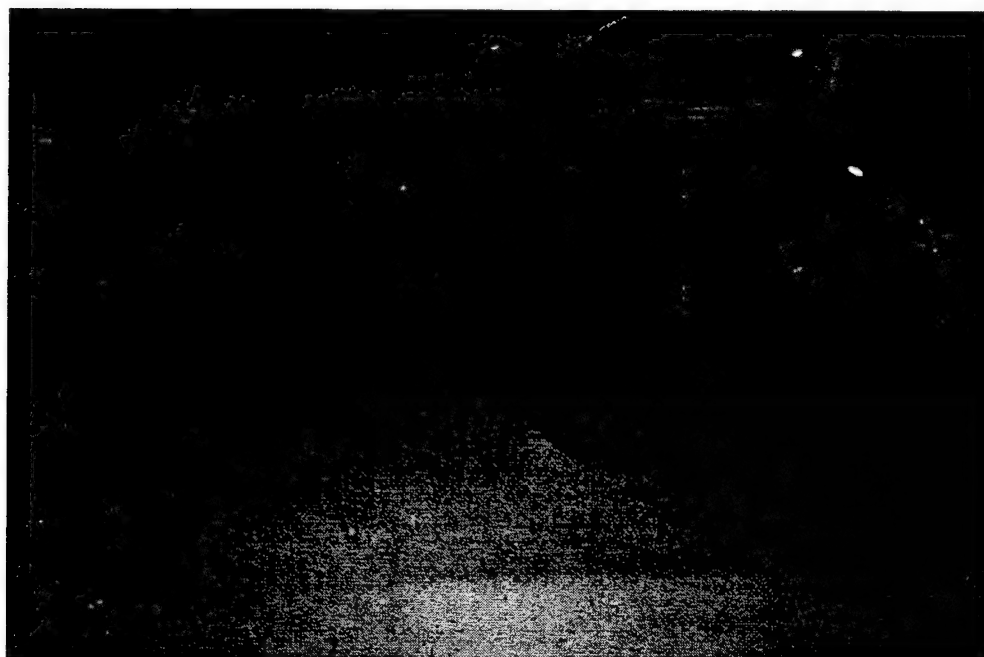


Figure 8.9. Placement of thin sand layer

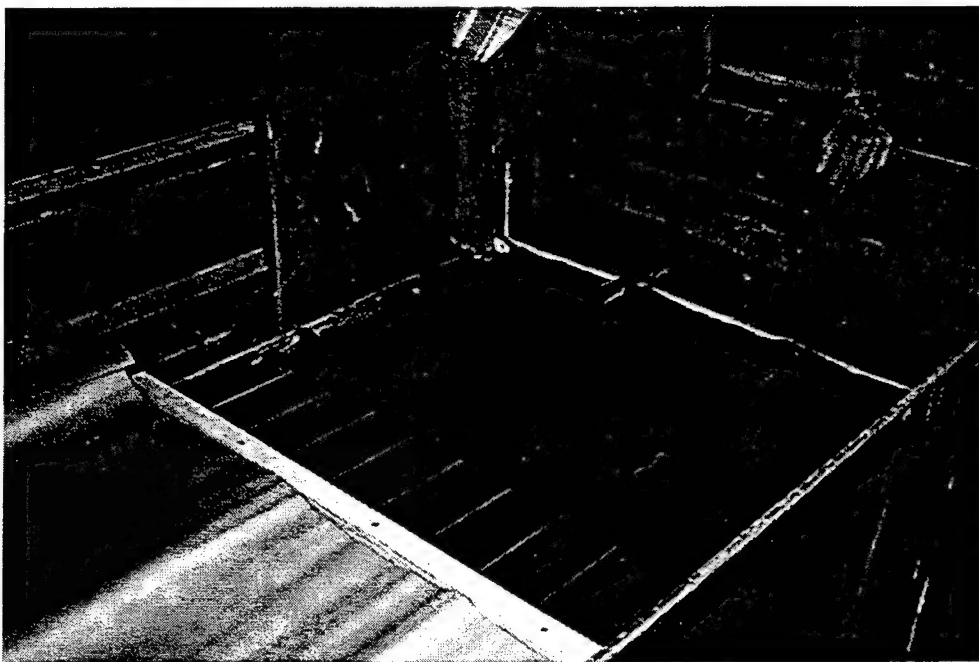


Figure 8.10. Bond breaker and doweled joint just prior to concrete placement

bonded end of the dowel was in the first slab placed; therefore, care was taken to insure that no form release agent, grease, or oil was present on the dowels.

The concrete was batched and mixed in the laboratory, carefully placed in the reaction box, and consolidated with an external spud-type concrete vibrator. The surface was floated and finished by hand, and the concrete was allowed to set for approximately 24 hrs.

After 24 hours the transverse mold along the joint was carefully removed. The free ends of the dowels (unbonded ends) were greased with an automotive-type grease. To further insure that no bond could be developed between the dowel bars and the slab, plastic drinking straws with an inside diameter of 6 mm (0.25 in.) were slipped over the greased dowels. The second slab was then placed, consolidated, and finished.

The ends of the slabs were constrained by 76 mm (3 in.) equal leg structural steel angles, 9.5 mm (3/8 in.) thick. One leg of the angle was embedded in the fresh concrete just after

placement, and the other leg was bolted to the side of the reaction box with 12.7 mm (0.5 in.) diameter steel bolts. The bolts were later torqued to near yield to maximize the clamping force on the angles.

The slabs were moist cured using wet burlap and plastic sheeting at room temperature until they were placed in the environmental chamber at 60°C (140°F) over the weekend for accelerated curing. After being removed from the environmental chamber, the slabs were allowed to cool in the laboratory to room temperature with no additional wet curing.

Three 152-mm (6-in.) diameter by 305-mm (12-in.)-high cylinders were cast from each batch of concrete used to fabricate the model slabs. Also, a single 152-mm (6-in.) wide by 152-mm (6-in.) deep by 508-mm (20-in.) long beam was cast from one batch of concrete for each model. These cylinders and beam were cured under the same accelerated curing conditions as the model slabs and were tested on the date the corresponding experiment was conducted to determine the compressive and flexural strengths, modulus of elasticity, and Poisson's ratio of the slabs.

LOADING

All experiments were conducted on the structural test floor at the Concrete and Materials Division, Structures Laboratory, Waterways Experiment Station. Loads were applied to the physical model by a closed-loop, servo-hydraulic materials testing system through a thin circular rubber pad. The radius of the loaded area was 57 mm (2-1/4 in.). The testing system was controlled by an MTS LoadStar digital controller which could be programmed through a graphical user interface to output the desired control signals to the system. So that post-peak response could be captured, the load was applied in displacement control at a rate of 0.25 mm/min (0.01 in/min).

The testing frame consisted of four vertical steel columns bolted to attachment points in the structural test floor. A stiff, deep steel beam spanned the opening between the columns. A 222-kN (50,000-lbs) capacity actuator attached to this beam provided the loading for the experiment.

INSTRUMENTATION

Instrumentation for the physical model experiments consisted of the following:

- Applied load, measured by a load cell.
- Surface strains, measured by surface-applied, foil resistance strain gages.
- Displacement, measured by linear variable displacement transducers (LVDTs).

All strain and deformation measurements were made on the top surface of the slabs. The load cell was located between the testing machine actuator and the slab. The maximum range of the load cell was ± 222 kN (50,000 lb).

Strain gages employed for these experimental studies had an electrical resistance of 350 ohms and a gage length of 25 mm (1 in.). When the gage was strained, it experienced a change in electrical resistance. These very small changes in resistance were measured by placing the gage in one leg of a Wheatstone bridge circuit, which is sensitive to small resistance changes. The maximum range of the strain gages was $\pm 50,000$ microstrains.

The locations for the strain gages were prepared by first applying a thin coat of Epicast, a low-modulus, white epoxy. This epoxy coat served two primary functions: to provide a moisture barrier to prevent water in the concrete from affecting the strain gage and to provide a smooth, uniform surface to which the strain gage could be bonded. After a 24 hour setting period, the Epicast was sanded to a uniform thickness, and the strain gages were bonded using Super Glue.

The LVDT is a transformer-type device that translates straight-line mechanical motion into an alternating current (AC) analog voltage. Each LVDT contained a movable magnetic core which rested on the surface of the concrete. As the surface of the concrete was displaced, the movement of the core caused an electromagnetic imbalance in the transformer which, in turn, output a proportional AC voltage. As calibrated for these experiments, the maximum range of the LVDTs was approximately 2.5 mm (0.1 in). All LVDTs were mounted to one or more steel angles which spanned the reaction box. The ends of these angles were rigidly attached to the reaction box using machine screws.

All data from these instruments were acquired in real time using a MEGADAC data acquisition system manufactured by Optim Electronics Corporation of Germantown, Maryland. The MEGADAC system is programmed and controlled by a Pentium personal computer running Optim's Test Control Software, which converts the analog signals to digital data using the appropriate gage calibration factors and saves the digital data to disk.

A Kodak DC 40 digital still image camera was positioned approximately 200 mm (8 in.) from the transparent window on the side of the box. This camera was set to record digital images of the slab-joint-base region.

EXPERIMENTAL RESULTS

Experiments LSM-1 through LSM-5 were conducted during the period from March 27, 1996, to May 22, 1996. However, Experiment LSM-3 was not considered to be a valid test due to problems encountered during the conduct of the experiment. An error was made in programming the loading function into the MTS TestStar controller, and the loading was not carried out as planned. Therefore, the results from LSM-3 were thrown out, and a repeat of the experiment (LSM-3R) was conducted on June 19, 1996. The results of quality control

tests conducted on the construction materials as well as data from Experiments LSM-1, LSM-2, LSM-3R, LSM-4, and LSM-5 are presented and discussed in this section.

Materials

Cement-stabilized base

The results of the quality control tests on the cement stabilized bases are summarized in Table 8.5. Compressive strength tests were conducted on 51 mm (2 in.) by 102 mm (4 in.) cylindrical specimens. These results indicate that the compressive strengths were at or below that expected from the seven day accelerated curing tests conducted during the initial materials investigation (Figure 8.4). It is believed that the lower strengths can be attributed to drying out of the cement/silty-sand material between batching and preparation of the test specimens. The material to be used to make the specimens was set aside while the bases were placed and compacted in the reaction box. Typically, more than one but less than two hours elapsed between the batching of the base materials and preparation of the quality control specimens. It is likely that some of the moisture evaporated during this period resulting in lower densities and strengths in the quality control specimens.

The modulus of elasticity of the cement-stabilized base was determined from the compressive strength tests on the cylinders. The modulus of elasticity (in compression), as calculated from the tangent to the steepest portion of the compressive stress-strain curve, is tabulated in Table 8.5. These data indicate that as the compressive strength increases, the compressive modulus of elasticity increases. The modulus of elasticity of the cement-stabilized base was approximately 5 percent of the target modulus of elasticity of the portland cement concrete slabs.

Table 8.5
Results of Tests on Cement-Stabilized Base

Experiment	Location	Compression Tests				Flexural Tests		
		Compressive Strength MPa (psi)		Modulus of Elasticity MPa (10^6 psi)		Replicates	Mean	Std. Dev.
		Mean	Std. Dev.	Mean	Std. Dev.			
LSM-3R	Top Lift	3	6.59 (826)	1.35 (196)	1,520 (0.220)	662 (0.096)	3	1.23 (179) 0.05 (8)
	Bottom Lift	3	6.24 (904)	0.48 (69)	1,822 (0.264)	693 (0.100)	No Tests Conducted	
LSM-4	Right Half	3	4.50 (653)	0.51 (73)	1,220 (0.177)	645 (0.093)	3	1.18 (171) 0.04 (5)
	Left Half	3	4.49 (652)	0.76 (110)	1,390 (0.202)	248 (0.036)	No Tests Conducted	
LSM-5	Top Lift	3	5.92 (858)	0.29 (41)	1,440 (0.208)	395 (0.057)	3	1.20 (174) 0.05 (8)
	Bottom Lift	3	4.45 (645)	0.99 (144)	1,070 (0.155)	383 (0.056)	No Tests Conducted	

The modulus of rupture (flexural strength) of the cement stabilized base was determined from tests on 76 mm (3 in.) by 76 mm (3 in.) by 286 mm (11-1/4 in.) beams loaded at the third points. These data are also reported in Table 8.5.

Statistical techniques were employed to determine if the observed variations in the material properties from batch to batch within an experiment and between experiments were statistically significant at the 0.05 significance level. Student's t-tests were conducted on the compressive strength and modulus of elasticity data from the two batches of base material within each experiment. For each of the Experiments LSM-3R, LSM-4, and LSM-5, the differences in the mean values of compressive strength and modulus of elasticity between batches were not great enough to exclude the possibility that the differences were due to random sampling variability. Therefore, it can be concluded that there was no statistically significant difference in compressive strength and elastic modulus between batches in any given experiment at the 0.05 significance level.

One-way analysis of the variance (ANOVA) procedures were used to test for statistically-significant differences in material properties between experiments. The results of these analyses indicated that for the case of compressive strength, the differences in the mean values of compressive strength between experiments were greater than would be expected by chance at the 0.05 significance level. A pairwise multiple comparison test indicated that the compressive strength values from Experiment LSM-3R were statistically different from those of LSM-4 and LSM-5. However, for the cases of modulus of elasticity and flexural strength, the differences in the mean values between experiments was not great enough to exclude the possibility that the difference was due to random sampling variability; therefore, no statistically significant differences in these two parameters were detected at the 0.05 significance level.

Portland cement concrete

The properties of the fresh portland cement concrete used to construct the slabs for the laboratory-scale model experiments are tabulated in Table 8.6. Tests conducted on the fresh concrete included slump (per ASTM C 143-90a) and unit weight (per ASTM C 131-92). The theoretical air content was calculated from the measured unit weight. The results of tests on hardened concrete cylinders and beams are reported in Table 8.7. Tests on 152 mm (6 in.) by 305 mm (12 in.) concrete cylinders included compressive strength (per ASTM C 39-93) and modulus of elasticity and Poisson's ratio (per ASTM C 469-94). Flexural strength (modulus of rupture) tests were conducted on 152 mm (6 in.) by 152 mm (6 in.) by 305 mm (12 in.) prismatic beams loaded at the third points per ASTM C 78-94. As noted in Table 8.7, all hardened concrete tests results for Experiment LSM-2 were lost due to failure of the concrete testing machine on the day of the tests.

**Table 8.6
Results of Tests on Fresh Portland Cement Concrete**

Experiment	Casting Date	Batch Placement Location	Slump mm (in.)	Unit Weight kg/m ³ (pcf)	Air Content Percent
LSM-1	3/20/96	Left Slab	70 (2¾)	2,268 (141.6)	1.8
	3/21/96	Right Slab	51 (2)	2,243 (140.0)	2.8
LSM-2	4/3/96	Left Slab	70 (2¾)	2,236 (139.6)	3.1
	4/4/96	Right Slab	64 (2½)	2,230 (139.2)	3.5
LSM-3R	6/12/96	Left Slab	51 (2)	2,252 (140.6)	2.5
	6/13/96	Right Slab	64 (2½)	2,243 (140.0)	2.8
LSM-4	5/1/96	Left Slab	70 (2¾)	2,256 (140.8)	2.3
	5/2/96	Right Slab	102 (4)	2,246 (140.2)	2.7
LSM-5	5/14/96	Left Slab	76 (3)	2,236 (139.6)	3.2
	5/16/96	Right Slab	127 (5)	2,217 (138.4)	4.0

Table 8.7
Results of Tests on Hardened Portland Cement Concrete

Experiment	Casting Date	Testing Date	Compressive Strength Tests			Elastic Modulus and Poisson's Ratio Tests			Flexural Tests		
			Replicates	Mean MPa (psi)	Std. Dev. MPa (psi)	Replicates	Modulus of Elasticity MPa (10^6 psi)	Poisson's Ratio	Replicates	Modulus of Rupture MPa (psi)	Replicates
LSM-1	3/20/96	3/27/96	3	29.0 (4200)	0.51 (75)						
	3/21/96		3	27.5 (3990)	0.38 (55)	1	26,800 (3.90)	Not Available	1	3.07 (445)	
LSM-2	4/3/96	4/10/96									
	4/4/96										
LSM-3R	6/12/96	6/19/96	3	27.1 (3930)	0.14 (20)						
	6/13/96		3	26.3 (3820)	0.72 (105)	1	28,300 (4.10)	0.18	1	2.90 (420)	
LSM-4	5/1/96	5/8/96	3	26.1 (3790)	0.62 (90)						
	5/2/96		3	26.1 (3780)	2.21 (320)	1	29,000 (4.21)	0.17	1	3.28 (475)	
LSM-5	5/14/96	5/22/96	3	25.6 (3710)	0.41 (60)						
	5/16/96		3	25.7 (3720)	0.17 (25)	1	28,700 (4.17)	0.19	1	3.21 (465)	

No data available due to failure of test machine.

The slump of the fresh concrete varied from 51 mm (2 in.) to 127 mm (5 in.), with the majority of the measurements between 51 mm (2 in.) and 76 mm (3 in.). Models LSM-1, LSM-2, and the left slab of LSM-4 were all fabricated from the same lot of Type III cement, while models LSM-3R, LSM-5, and the right slab of LSM-4 were fabricated from a different lot of Type III cement from the same manufacturer. The higher slump values noted for models LSM-4 (Right Slab) and LSM-5 were attributed to the changes in the cement between the two lots. The second lot had less water demand than the first resulting in an increase in the slump of the fresh concrete. This effect was mitigated for Experiment LSM-3R by reducing the mix water 6 percent (by mass) thus bringing the slump back in line with the models fabricated from the first lot of cement. Unit weights of the fresh concrete varied from 2,217 kg/m³ (138.4pcf) to 2,268 kg/m³ (141.6pcf), while air contents ranged from 1.8 to 4.0 percent.

The mean concrete compressive strengths ranged from a low of 25.6 MPa (3,710 psi) to a high of 29.0 MPa (4,200 psi). The modulus of elasticity ranged from 26,800 MPa (3.9×10^6 psi) to 29,000 MPa (4.2×10^6 psi), while Poission's ratio ranged from 0.17 to 0.19. The modulus of rupture varied from a minimum of 2.90 MPa (420 psi) to a maximum of 3.28 MPa (475 psi).

For FAA rigid pavement structural design, the concrete material strength parameter used to determine pavement thickness is 90-day modulus of rupture. A normal range of flexural strength at an age of 90 days is from 3.45 MPa (500 psi) to 6.20 MPa (900 psi). Therefore, the flexural strength of the slabs used in this experimental study were slightly lower than those which would be expected in the field.

Statistical techniques were employed to determine if the observed variations in the compressive strengths from slab to slab within an experiment and between experiments were

statistically significant at the 0.05 significance level. Student's t-tests were conducted on the compressive strength from the two slabs within each experiment. For each of Experiments LSM-3R, LSM-4, and LSM-5, the differences in the mean values of compressive strength between slabs were not great enough to exclude the possibility that the differences were due to random sampling variability. Therefore, it can be concluded that there was no statistically significant difference in compressive strength between batches for these experiments at the 0.05 significance level. However, for Experiments LSM-1A and LSM-1B the differences in the mean values of compressive strength were greater than would be expected by chance. Therefore, the t-test results indicate that there is likely a statistically-significant difference in the compressive strength values between LSM-1A and LSM-1B. It is difficult, however, to ascertain the impact of this difference on the experimental results.

One-way ANOVA procedures were used to test for statistically-significant differences in concrete compressive strength between experiments at the 0.05 significance level. Because the results of the previously reported t-tests had indicated that the compressive strengths from Experiments LSM-1A and LSM-1B were likely statistically different, they were treated as separate experiments in the ANOVA. The results of the ANOVA indicated that the differences in mean values of compressive strengths were greater than would be expected by chance at the 0.05 significance level. A pairwise multiple comparison analysis of the data revealed that the compressive strength of Experiment LSM-1A was statistically different from the remainder of the experiments at the 0.05 significance level, while the compressive strengths for the remainder of the experiments were not statistically different from each other.

Rubber block

A plate bearing test was conducted on the rubber block in the reaction box to determine its modulus of subgrade reaction under loading from a standard 762-mm (30-in.) diameter

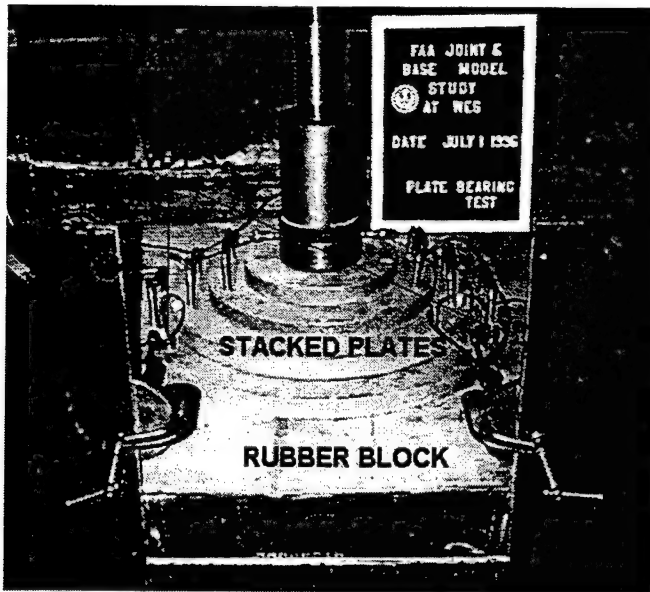


Figure 8.11. Test setup for plate bearing test on rubber pad

circular plate and to observe any nonlinear response of the rubber under compressive loading. A nest of stacked, concentric plates (Figure 8.11) was employed in conducting the tests; the diameters of the plates from bottom to top were 762 mm (30 in.), 610 mm (24 in.), and 457 mm (18 in.). Each plate was fabricated from 38-mm (1-1/2-in.) thick aluminum.

The load for the plate bearing test was applied by the same servo-controlled hydraulic structural testing system employed to test the model pavements. Deflection was measured by an array of three LVDTs equally spaced at 120° increments around the perimeter of the bottom plate. A MEGADAC digital data acquisition system was used to record and store the measured loads and deflections in real time.

Two loading regimes were followed for this testing. The first was conducted in load control following the applicable procedures specified in Section XII, FM 5-530 (Department of the Army, 1987). A seating load of 6.8 kPa (1 psi) was applied to the plate. This was considered to be the zero point of the test. An additional load increment was then applied to bring the plate bearing stress to 68.9 kPa (10 psi), where the load was held for several

minutes until the rate of deformation was less than 0.005 mm/min (0.0002 in./min). Subsequently, an additional increment of load was applied to bring the plate bearing stress to 103 kPa (15 psi), where the load was again held until the rate of deformation was less than 0.005 mm/min (0.0002 in./min). This procedure was repeated at increments of plate bearing stress of 34.4 kPa (5 psi) up to a maximum stress of 207 kPa (30 psi). Finally, the load was decreased slowly until the applied stress was zero. A plot of plate bearing stress versus plate displacement is presented in Figure 8.12. It is apparent from this plot that the rubber pad

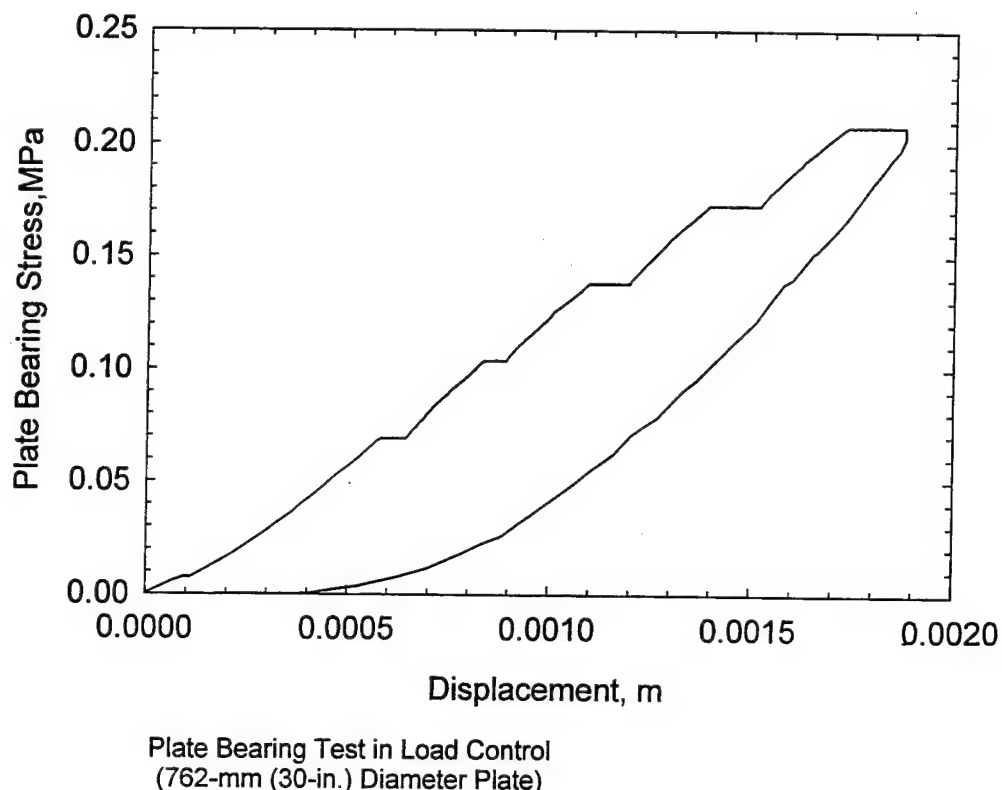


Figure 8.12. Bearing stress-displacement data from plate bearing test on rubber block in load control

crept during the portions of the tests where the plate bearing stress was held constant. It can also be seen that the amount of creep deformation which occurs until the rate of creep deformation falls below 0.005 mm/min (0.0002 in./min) increases with increasing plate bearing stress. The accumulated creep deformation at the end of the loading was approximately 0.4 mm (0.016 in.). The data from this test were used to determine the modulus of subgrade reaction, k , for the rubber block for the standard 762-mm (30-in.) diameter plate. Figure 8.13 shows a plot of corrected plate bearing stress versus displacement as prescribed by FM 5-530 (Department of the Army, 1987). Each of the data points denoted by the triangles represents the deflection and stress at the end of each increment of applied stress, adjusted for the 6.8 kPa (1 psi) initial seating load. These data were then corrected, using the procedures described in FM 5-530 (Department of the Army 1987), to account for bending of the plates. From the slope of the corrected curve, the modulus of subgrade reaction was determined to be 111 MPa/m (409 psi/in.). This value is high for a subgrade material, and would be more representative of the modulus of subgrade reaction for a dense, well-graded gravel.

The second loading regime was conducted in displacement control at a load rate of 0.25 mm/min (0.01 in./min) to mimic the loading conditions during testing of a pavement model. The bearing plate was displaced continuously and monotonically until a maximum bearing stress of 0.1 MPa (14.5 psi) was reached, at which point the displacement was reversed continuously and monotonically until the bearing stress was reduced to zero. A plot of bearing stress versus deformation is shown in Figure 8.14. In the range in which the bearing stress was less than 0.01 MPa (1.5 psi), the response was relatively soft. For bearing stresses greater than approximately 0.1 MPa (1.5 psi) the response was stiffer. Upon unloading, the response was characterized by a hysteresis loop typical of viscoelastic materials.

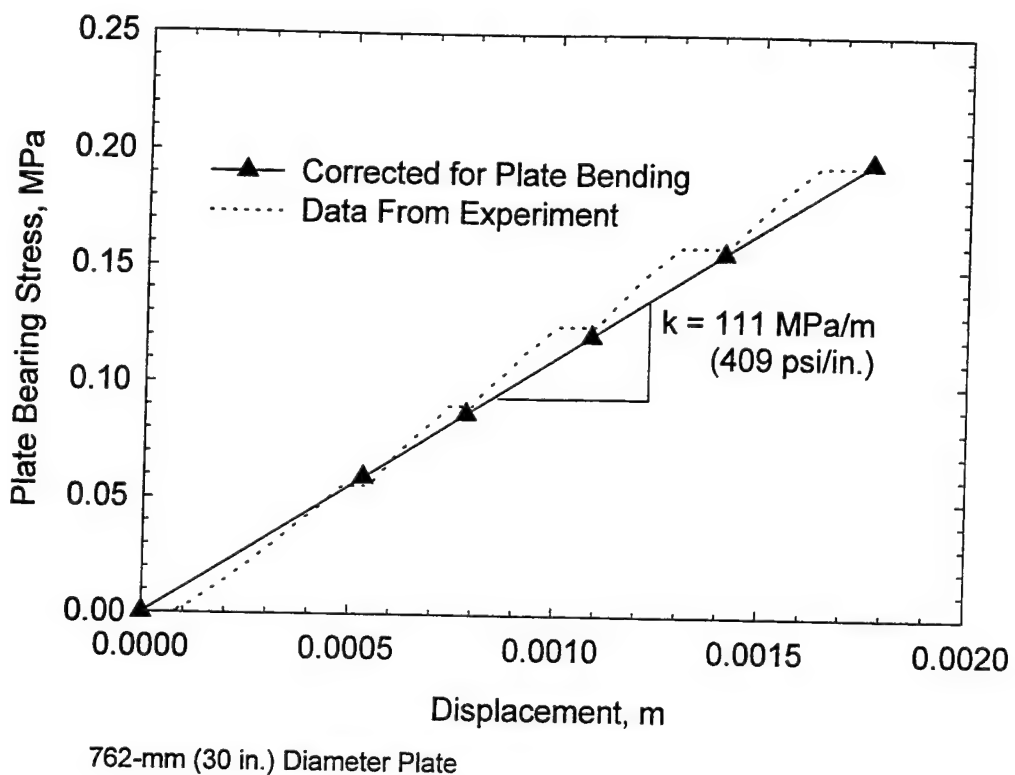


Figure 8.13. Corrected plate bearing stress

Thus, it can be concluded that the response of the rubber block in the reaction box was nonlinear viscoelastic over the range of loading expected during testing of a pavement model. These nonlinear responses of the rubber block are considerably different from those assumed for the bed-of-springs foundation in Westergaard's theory. The influence of the nonlinear viscoelastic response on the pavement model is not known.

Experiment LSM-1

Experiment LSM-1 consisted of two 51-mm (2-in.) thick slabs founded directly on the rubber subgrade. The right- and left-hand slabs were constructed with no load transfer capabilities from either dowel bars or aggregate interlock. A 5 mm (3/16 in.) gap separated the

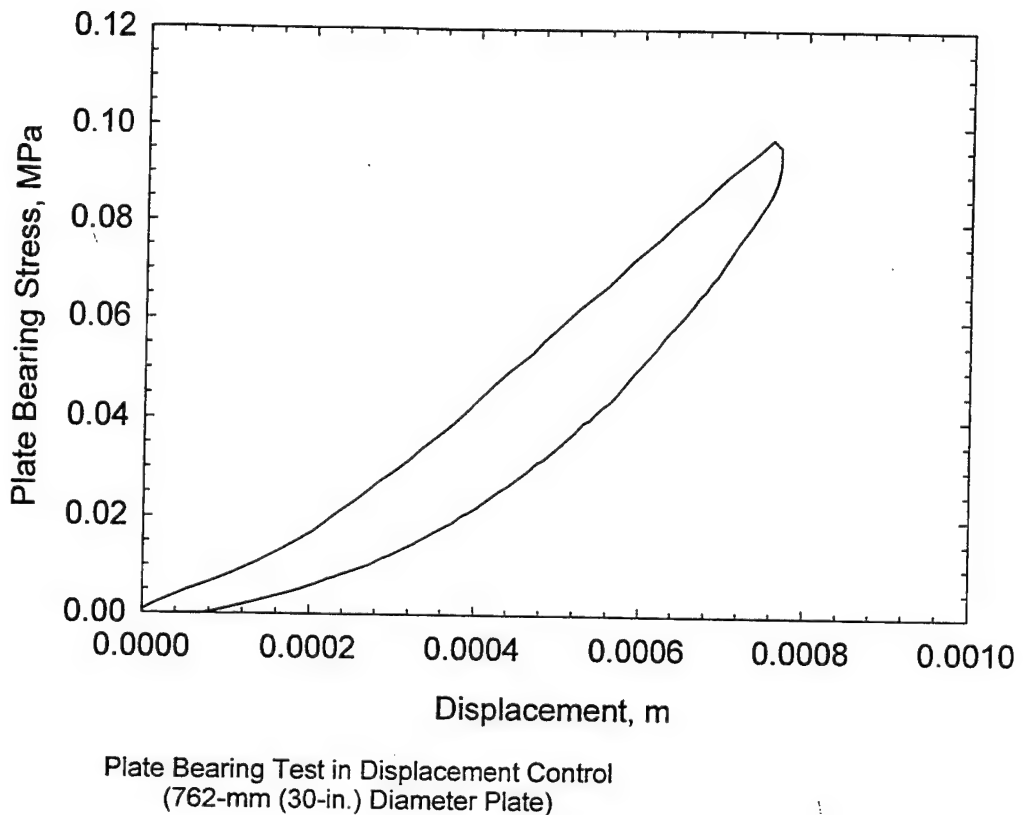


Figure 8.14. Bearing stress-displacement data from plate bearing test on rubber block in displacement control

slabs to insure that no incidental contact could occur between the slabs during testing. The experiment consisted of two separate loadings: an edge loading near the center of the right-hand slab, referred to as LSM-1A, and a corner loading near the transparent window pane on the left-hand slab, referred to as LSM-1B. The results from both of these experiments are presented and discussed in this section.

Experiment LSM-1A

The instrumentation locations for LSM-1A are presented in Figure 8.15. The LVDT locations were selected to give two deflection basin profiles: one perpendicular to the free

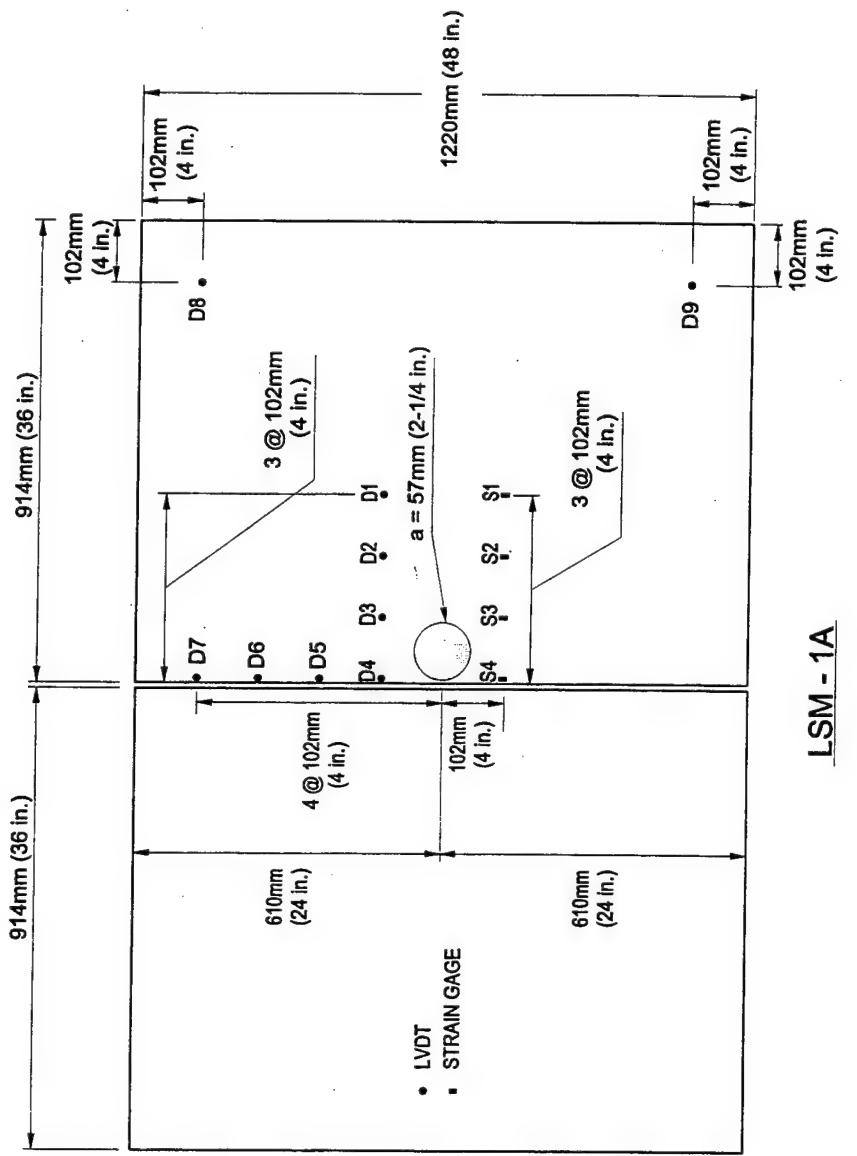


Figure 8.15. Instrumentation plan, Experiment LSM-1A

edge and one parallel to the free edge. The strain gage array was set to give only one strain profile perpendicular to the free edge.

Figure 8.16 is a plot of the load-time history of the test. The test was conducted by applying ten pre-loading cycles of 1.78 kN (400 lb) triangular pulses. The purpose of these pulses was to precondition the model to so that any potential restrictions to deformation that might be present as a result of the model construction would be overcome before actual loading began. These preconditioning cycles were followed by cycles of increasing loading intensity until the testing was stopped. This required the application of four additional cycles of loading until the test was stopped at a maximum load of approximately 26 kN (5,850 lbs).

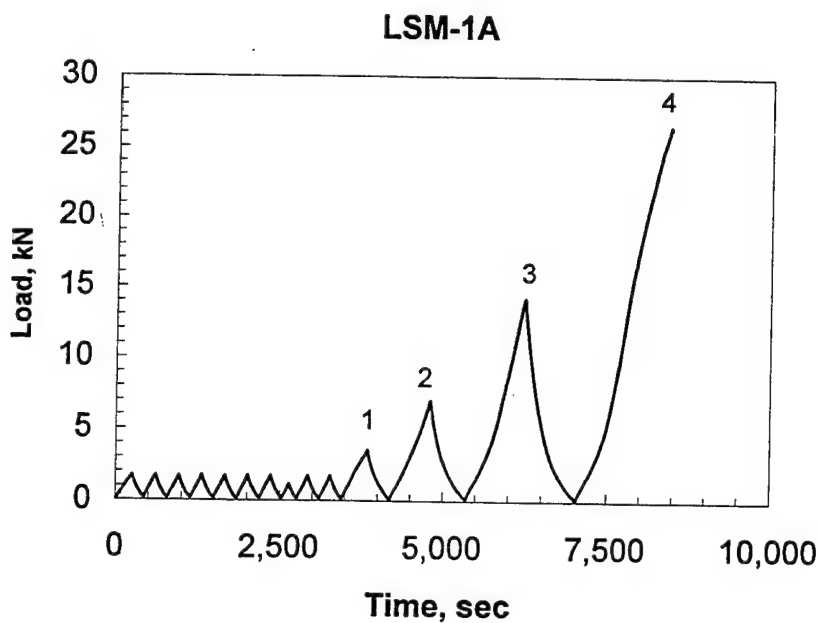


Figure 8.16. Loading history, Experiment LSM-1A

Figure 8.17 is a posttest photograph of the slabs after both Experiments LSM-1A and LSM-1B. Failure of the slab in Experiment LSM-1A, loaded near the edge, was characterized by a semi-circular crack highlighted in the photograph. Visible cracks were first observed with the naked eye at a load of approximately 17.3 kN (3,900 lb).

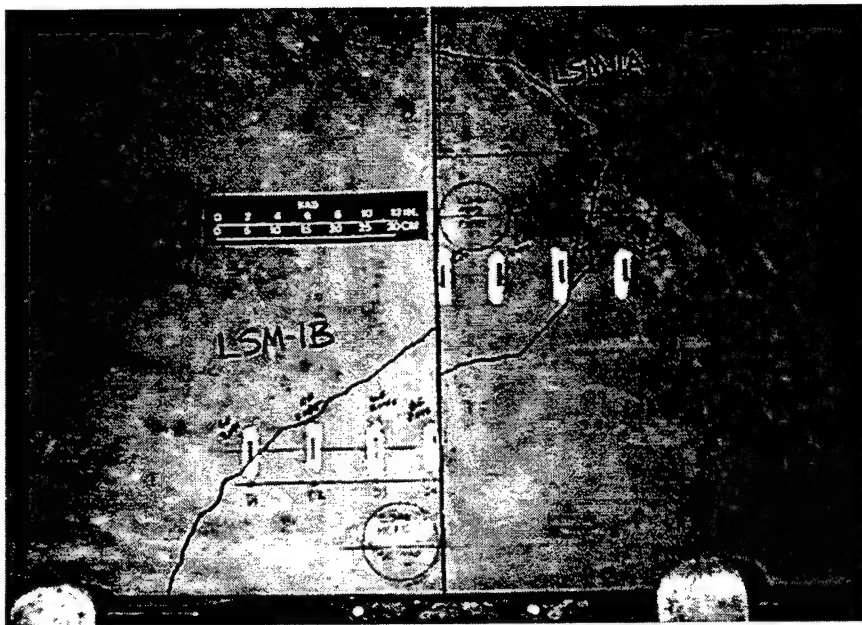


Figure 8.17. Posttest photograph, Experiments LSM-1A and LSM-1B

Data traces from the LVDTs on the surface of the slab are contained in Appendix D. The traces from the ten preconditioning cycles have been removed for clarity. For all LVDT measurements a downward displacement is considered to be positive while an upward movement is negative. Gage D4 over-ranged at a displacement of approximately 2.5 mm (0.1 in.). One obvious observation is that the overall shape of the load-displacement curves was similar to that recorded during the plate bearing test in displacement control. The slope of the curves changed at a load of approximately 5 kN (1,125 lb), as was observed in the plate bearing tests. Therefore, it was concluded that this change in stiffness can be attributed to the rubber block foundation and not to the portland cement concrete slab. Hysteresis loops and the attendant viscous deformations can be seen with each unloading cycle.

Data traces from the strain gages on the surface of the slab are found in Appendix D. For strain gage measurements tensile strains are positive, and compressive strains are negative. The strains are compressive at loads less than approximately 7 kN (1,575 lb). Beyond first

cracking the gages nearest the edge of the slab (S4 and S3) reverse directions and go into the tensile regime possibly indicating localized cracking.

In order to compare the data from this experiment with linear elastic calculations made with a finite element code, it was desirable to correct the load-displacement data to remove the nonlinear response of the rubber block. A technique similar to that used to correct for nonlinear response in the plate bearing test was used to perform this correction. Figures 8.18 and 8.19 show the raw and corrected load-displacement curves for the third cycle of loading for the LVDTs along a line perpendicular and parallel to the edge, respectively. The slopes of the linear portions of the load-deflection curves (that portion of the curve above approximately 5 kN (1,125 lb)) were determined numerically. The load-deflection curves were then shifted to the right such that the extension of the linear portion of the curve would pass through the origin as shown in Figures 8.18 and 8.19.

Deflection basins from the corrected load-deflection curves were then compared with linear elastic finite element calculations made with ABAQUS using the S8R5 reduced integration, second-order shell element. Initial calculations were made with the foundation modulus of subgrade reaction set at $k = 27, 54, 82$, and 109 MPa/m ($100, 200, 300$, and 400 psi/in.). The ABAQUS deflection profiles at points identical to the locations of the LVDTs along lines parallel and perpendicular to the edge were compared with the experimental deflection basin profiles.

Figure 8.20 shows a log-log plot obtained analytically of the modulus of subgrade reaction versus deflection (w) at gage location D4 for a load of 6 kN (1,350 lb) from the ABAQUS finite element calculations. This magnitude of load was chosen because it is midway between the value at which the change in slope occurs in the response of the rubber foundation at 5 kN (1,125 lb) and the load at which the onset of possible cracking occurred at 7 kN (1,575 lb).

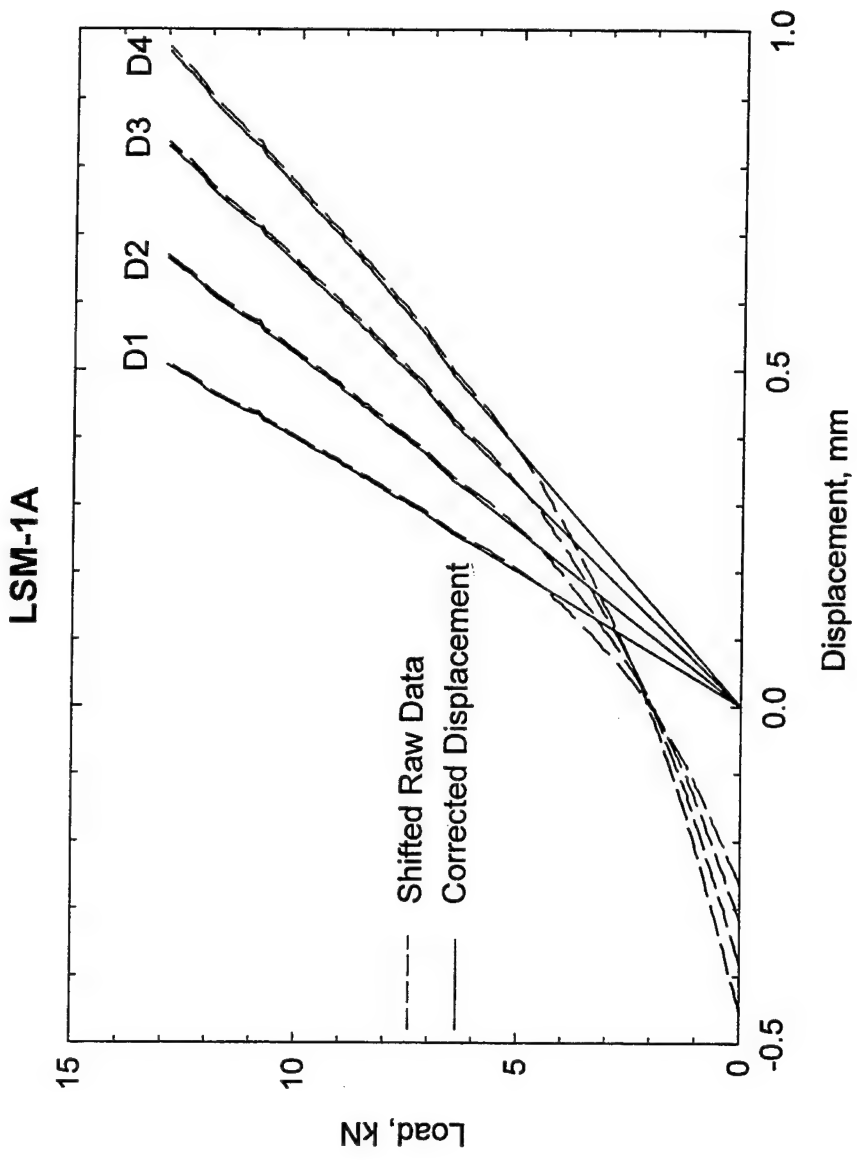


Figure 8.18. Raw and corrected displacement data from LVDTs positioned perpendicular to edge,
Experiment LSM-1A

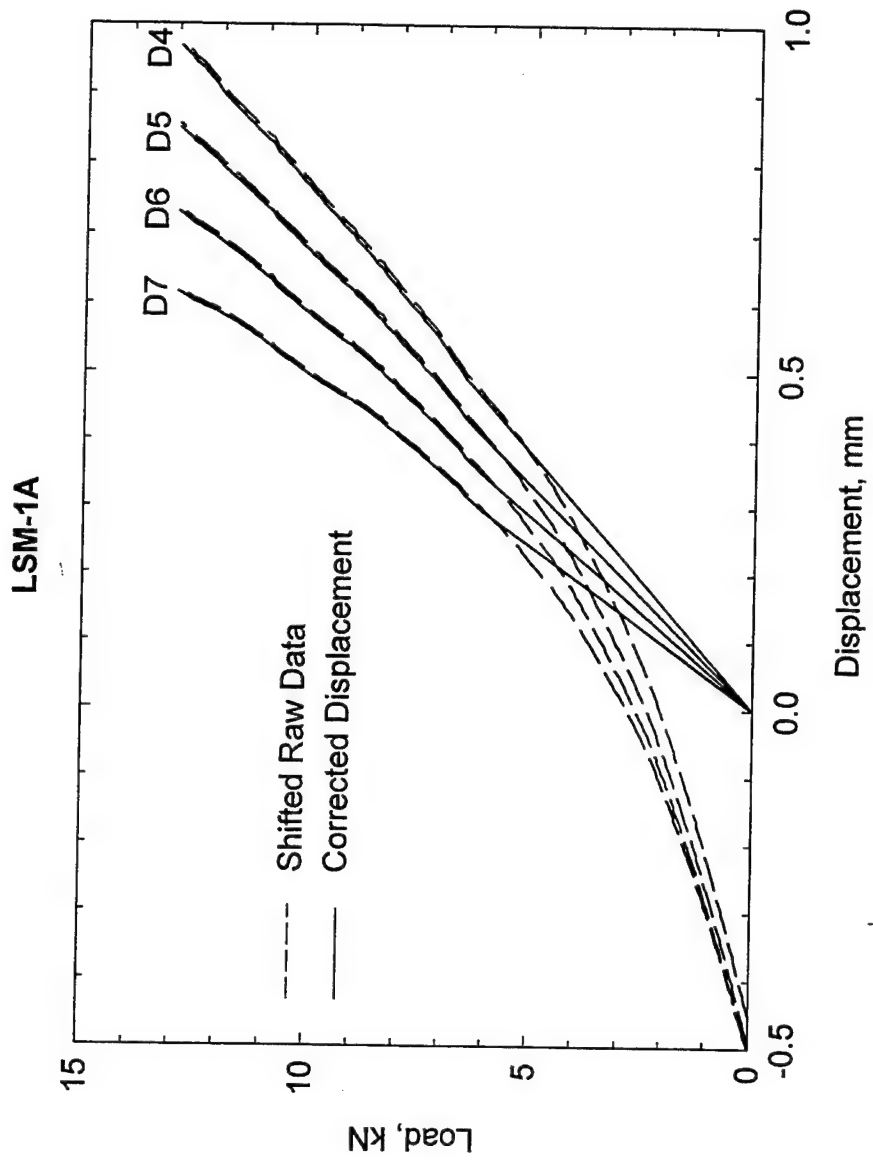


Figure 8.19. Raw and corrected displacement data from LVDTs positioned parallel to edge,
Experiment LSM-1A

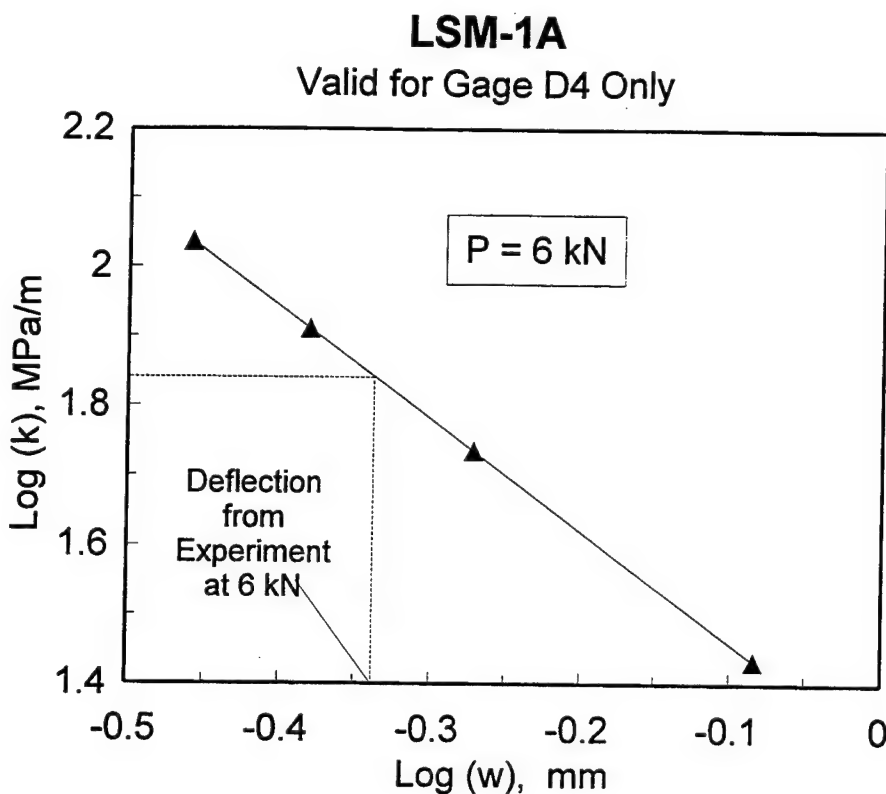


Figure 8.20. Analytical relationship between modulus of subgrade reaction and deflection from ABAQUS models, Experiment LSM-1A

Upon entering this plot with the experimental deflection obtained from gage D4 at $P = 6 \text{ kN}$ (1,350 lb), the value of k for the corner loading case can be estimated as about 70 MPa/m (258 psi/in.). An additional ABAQUS calculation was made using this value of k . The deflection basin profiles along the lines of LVDTs are shown in Figure 8.21 and 8.22. These figures show excellent agreement between the ABAQUS runs and experiment at the location of gage D4. However, the agreement deteriorates for gages distant from D4, particularly for the basin perpendicular to the edge. This disagreement was expected, because it is well known that backcalculated values of k vary as one moves away from the edge of a rigid pavement slab.

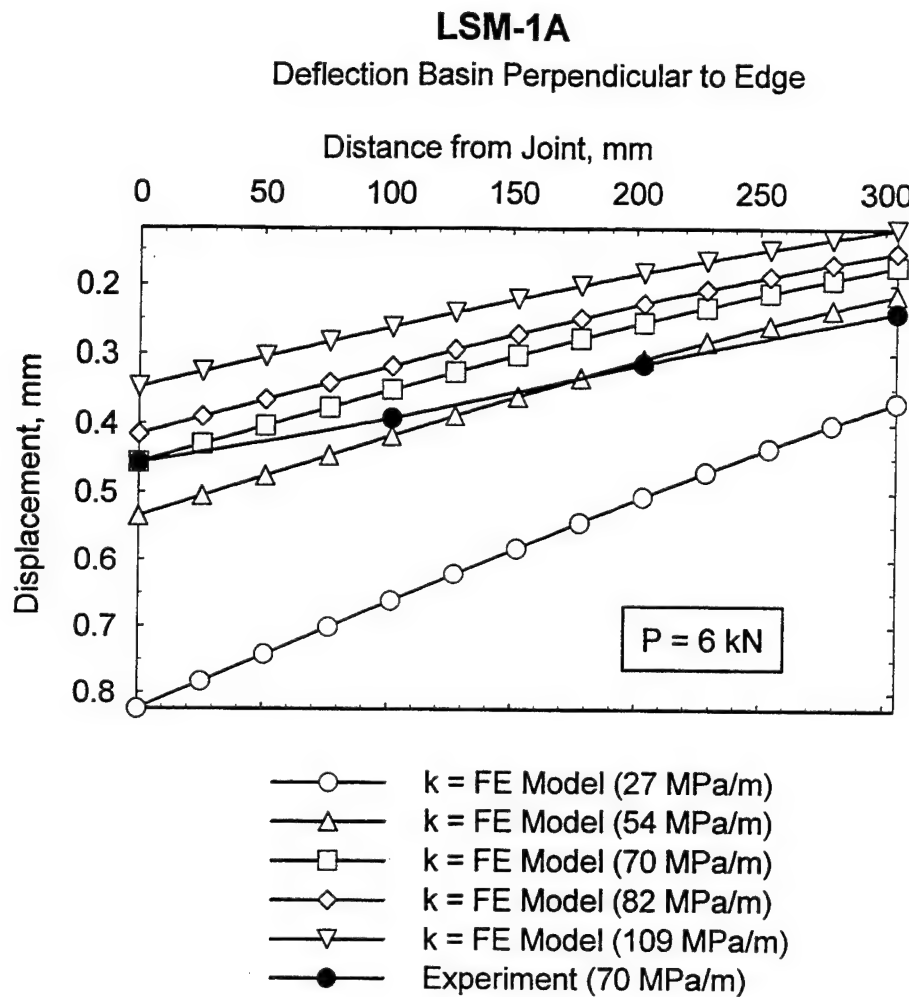


Figure 8.21. Comparison of experimental and analytical deflection basin profiles perpendicular to edge, Experiment LSM-1A

The backcalculated modulus of subgrade reaction for the rubber block in the reaction box differs significantly from that obtained from the plate bearing test. Again, this was not surprising, because it has been known at least since the 1940s that modulus of subgrade reaction is not an intrinsic material property, but rather the value of k is dependent upon the conditions of the test run to estimate it.

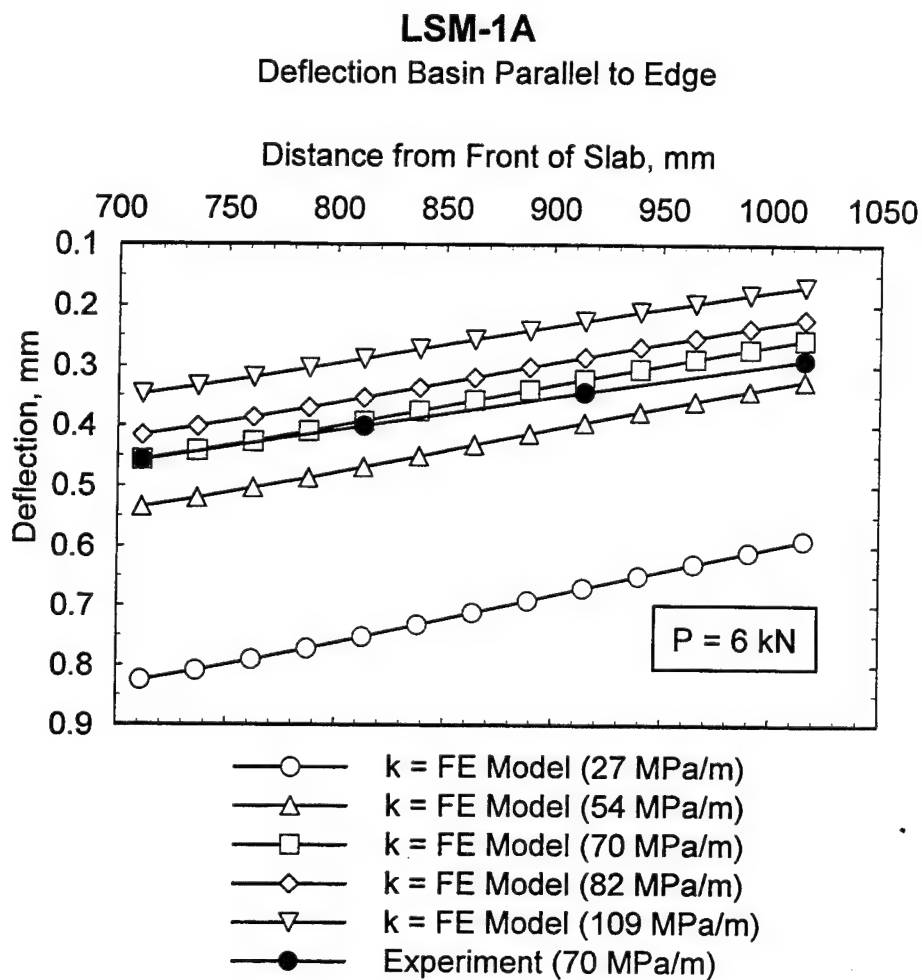


Figure 8.22. Comparison of experimental and analytical deflection basin profiles parallel to edge, Experiment LSM-1A

Experiment LSM-1B

The instrument locations for test LSM-1B are indicated in Figure 8.23. A single array of LVDTs were placed along a line perpendicular to the free edge of the left-hand slab near the loaded area. Similarly, a line of foil strain gages were placed on the surface of the left-hand slab along a line perpendicular to the edge. The left-hand slab in Figure 8.17 shows the

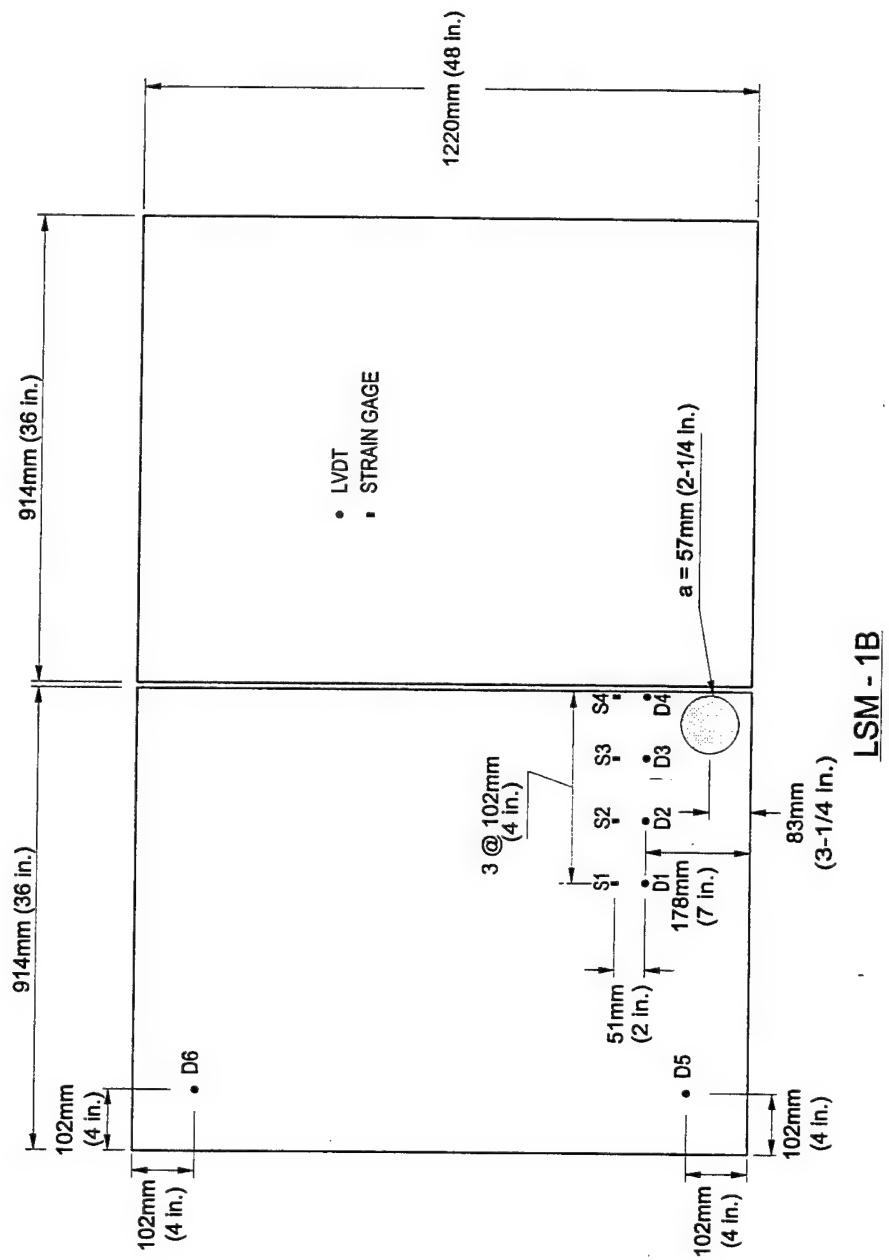


Figure 8.23. Instrumentation plan, Experiment LSM-1B

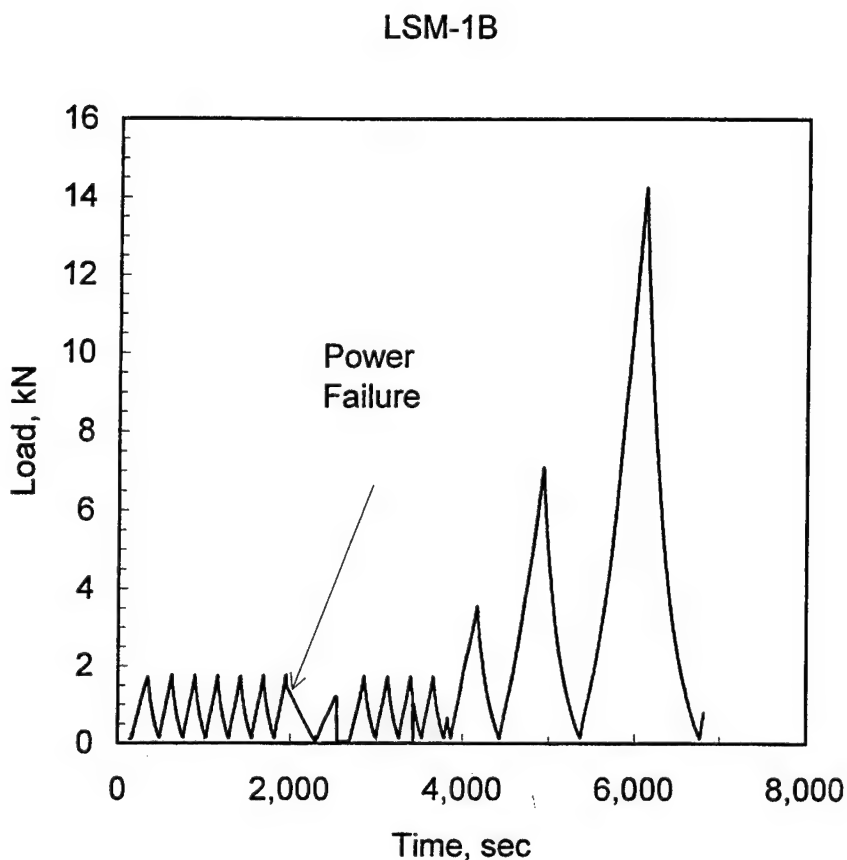


Figure 8.24. Loading history, Experiment LSM-1B

cracking patterns observed after the test was completed. Visible cracking was first observed with the unaided eye at a load of approximately 16.9 kN (3,800 lb).

The loading plan followed in Experiment LSM-1B was identical to that followed in Experiment LSM-1A. Figure 8.24 shows the loading history for Experiment LSM-1B. A brief electrical power outage lasting a few seconds occurred during the 10 preconditioning cycles. The MTS LoadStar control system and MEGADAC data acquisition systems were powered by uninterruptible power supplies during the power outage and thus were not affected. However, the hydraulic system of the loader was briefly without power, and the load dropped

off until power was restored. At this point the control system reassumed control of the loader, and the test was continued.

The load-deflection traces from the LVDTs are presented in Appendix D. The trends observed in these traces are similar to those discussed for Experiment LSM-1A.

The plots from the strain gages are also presented in Appendix D. These data traces show that the strain gages on the top surface of the slab registered tensile strains. Even though the crack passed close to Gage S1, the occurrence of the cracking cannot be discerned in the strain gage traces.

The load-deflection curves from LSM-1B were corrected for the nonlinear response of the rubber foundation in the manner described for Experiment LSM-1A. The shifted raw data traces along with the corrected data are presented in Figure 8.25. Deflection basins from the corrected load-deflection curves were then compared with linear elastic finite element calculations made with ABAQUS using the S8R5 reduced integration, second-order shell elements. Again, initial calculations were made with the modulus of subgrade reaction set at $k = 27, 54, 82$, and 109 MPa/m ($100, 200, 300$, and 400 psi/in.). The ABAQUS deflection profiles at points identical to the locations of the LVDTs along were compared with the experimental deflection basin profile.

Figure 8.26 shows a log-log plot obtained analytically of the modulus of subgrade reaction versus deflection (w) at gage location D4 for a load of 6.1 kN ($1,370 \text{ lb}$) from the ABAQUS finite element calculations. Entering this plot with the experimental deflection obtained from gage D4 at $P = 6.1 \text{ kN}$ ($1,370 \text{ lb}$), the value of k can be estimated as about 90 MPa/m (330 psi/in.). An additional ABAQUS calculation was made using this value of k . The deflection basin profiles along the line of LVDTs are shown in Figure 8.27. As was the case

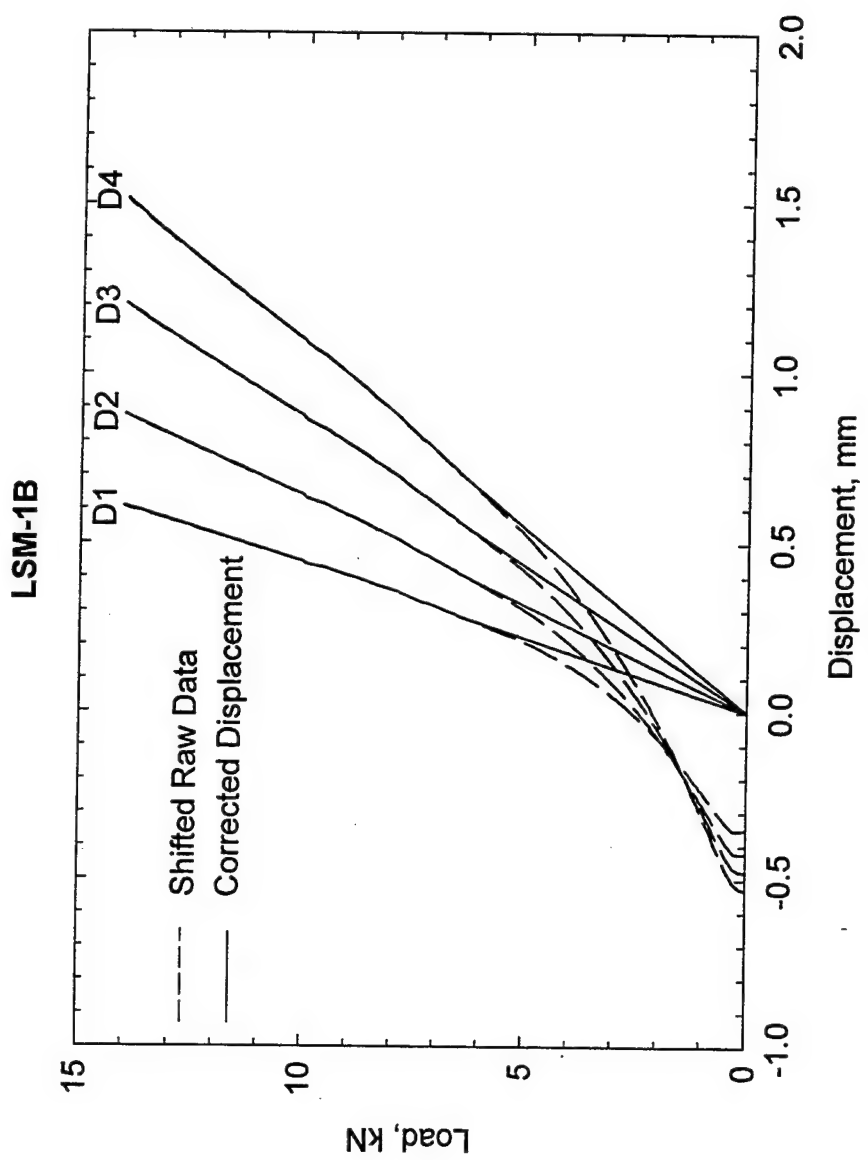


Figure 8.25. Raw and corrected displacement data from LVDTs, Experiment LSM-1B

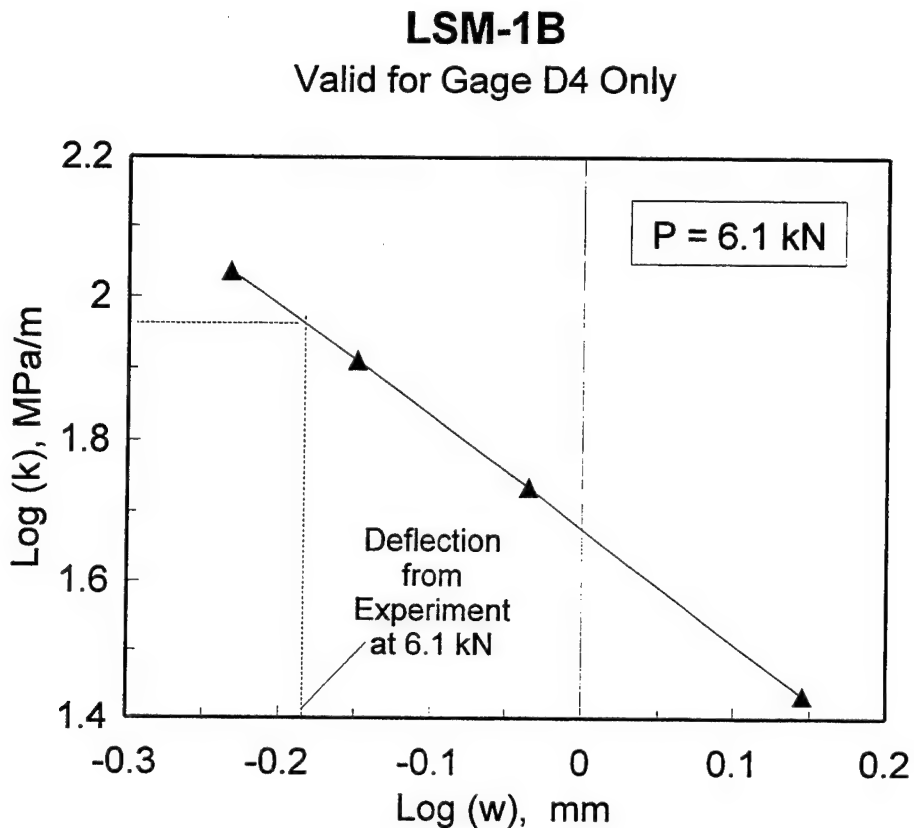


Figure 8.26. Analytical relationship between modulus of subgrade reaction and deflection from ABAQUS models, Experiment LSM-1B

for Experiment LSM-1A, excellent agreement between the ABAQUS runs and experiment at the location of gage D4 was obtained.

Summary

Experiments LSM-1A and LSM-1B demonstrated that meaningful deflection basin profile data and strain data could be obtained using the techniques set forth in the plan of test. The data indicated that the nonlinear, viscoelastic response of the rubber block foundation observed during the plate bearing was also present in the testing of slabs placed on top of the rubber slabs. The apparent modulus of subgrade reaction of the rubber block in reaction box

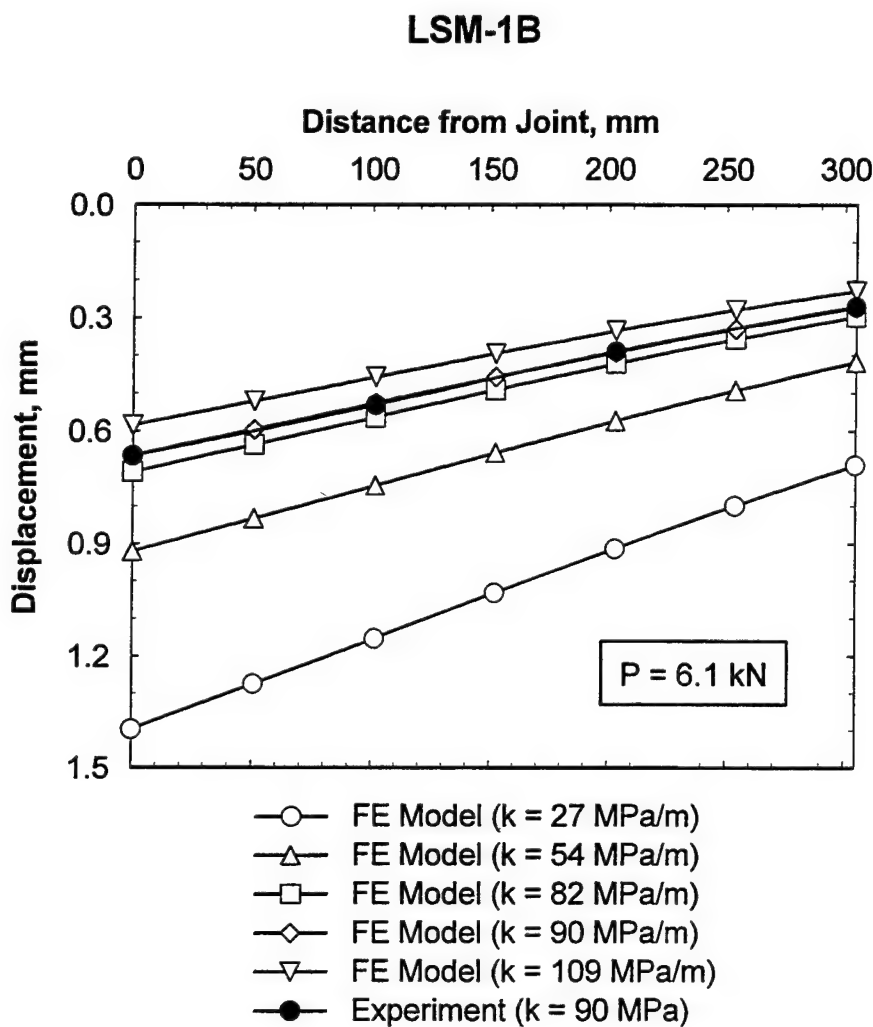


Figure 8.27. Comparison of experimental and analytical deflection basin profiles, Experiment LSM-1B

under the prevalent test conditions is 90 MPa/m (330 psi/in.) for corner loading, and 70 MPa/m (258 psi/in.) for edge loading. Based upon the quality control tests previously reported in this chapter, the mean value of the elastic modulus of the concrete is approximately 27,600 MPa (4×10^6 psi) and the mean value of Poisson's ratio is approximately 0.18; thus the radius of relative stiffness of the pavement system is 259 mm (10.2 in.) for

edge loading and 243 mm (9.55 in.) for corner loading. These values are important parameters in the analytical investigations reported in Chapter 9.

Experiment LSM-2

Experiment LSM-2 consisted of two 51-mm (2-in.) thick slabs, founded directly on a rubber foundation, separated by a doweled joint. The joint opening was fixed at 1.58 mm (1/16 in.) by a Teflon sheet inserted between the two slabs. The load was applied to the corner of the left-hand slab, which contained the bonded end of the dowels. The location and spacing of the dowels was as shown in Figure 8.5.

The loading history for Experiment LSM-2 is shown in Figure 8.28. As in Experiments LSM-1A and LSM-1B, ten preconditioning triangular pulses of magnitude 1.78 kN (400 lb) were applied. However, LSM-2 deviated from the previous test in that after the preconditioning cycles were applied, the deformation was increased monotonically until the testing was halted. After the application of the final preconditioning pulse; however, the testing was

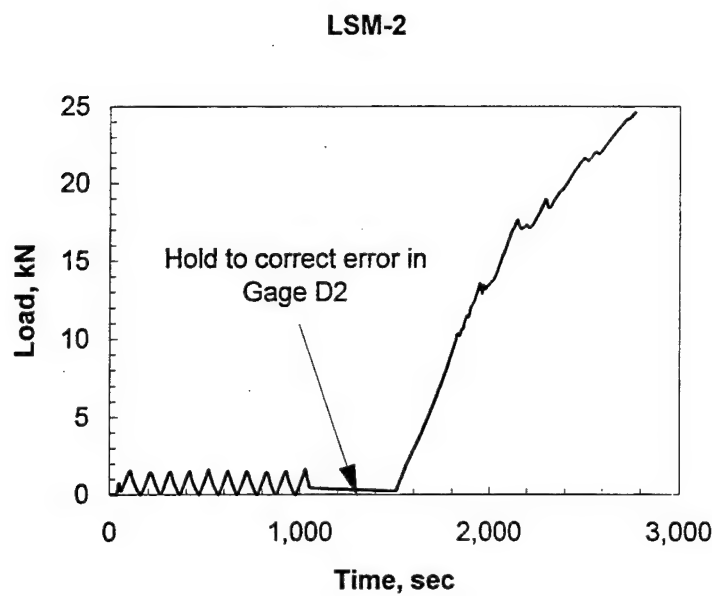


Figure 8.28. Loading history, Experiment LSM-2

paused briefly to correct an error in one of the LVDTs. After this error was corrected, the testing was resumed.

The instrumentation plan for Experiment LSM-2 is presented in Figure 8.29. This is the instrumentation plan which would be adhered to for the remainder of the experimental program. A line of LVDTs spanned across the joint to capture the deflection basin profile. Also, a line of strain gages were placed on the top surface of the slabs.

A posttest photograph of the top surface of the slabs is shown in Figure 8.30. The cracking highlighted on the left (loaded) slab was first observed at a load of approximately 17 kN (3,800 lb); while the cracking on the unloaded side was first observed at a load of approximately 19.1 kN (4,300 lb). A series of three photographs taken through the transparent window in the side of the reaction box is shown in Figure 8.31. The faint grids in the foreground of the photographs are spaced at 12.7 mm ($\frac{1}{2}$ in.). As the load is increased from zero to 13.3 kN (3,000 lb), the deflection of the top surface of the slabs is evident. Also note that no visible cracking can be noted in sides of the slabs at 13.3 kN (3,000 lb). However, once the load had increased to 17.8 kN (4,000 lb), a vertical crack was clearly visible directly beneath the loaded area in the left slab. Also, a crack which runs more or less horizontally from the joint is visible in the right (unloaded) slab. A posttest examination of the crack revealed that it originated at the dowel directly opposite the center of the loaded area and ran out and down toward the edge and base of the right slab.

The load-displacement traces from the array of LVDTs are presented in Appendix D. As noted in the figure, Gage D4 was over-ranged at a load of approximately 23 kN (5,000 lb). These traces indicate clear evidence of cracking at loads greater than approximately 10 kN (2,350 lb). Selected deflection basin profiles are plotted in Figure 8.32. Highly nonlinear

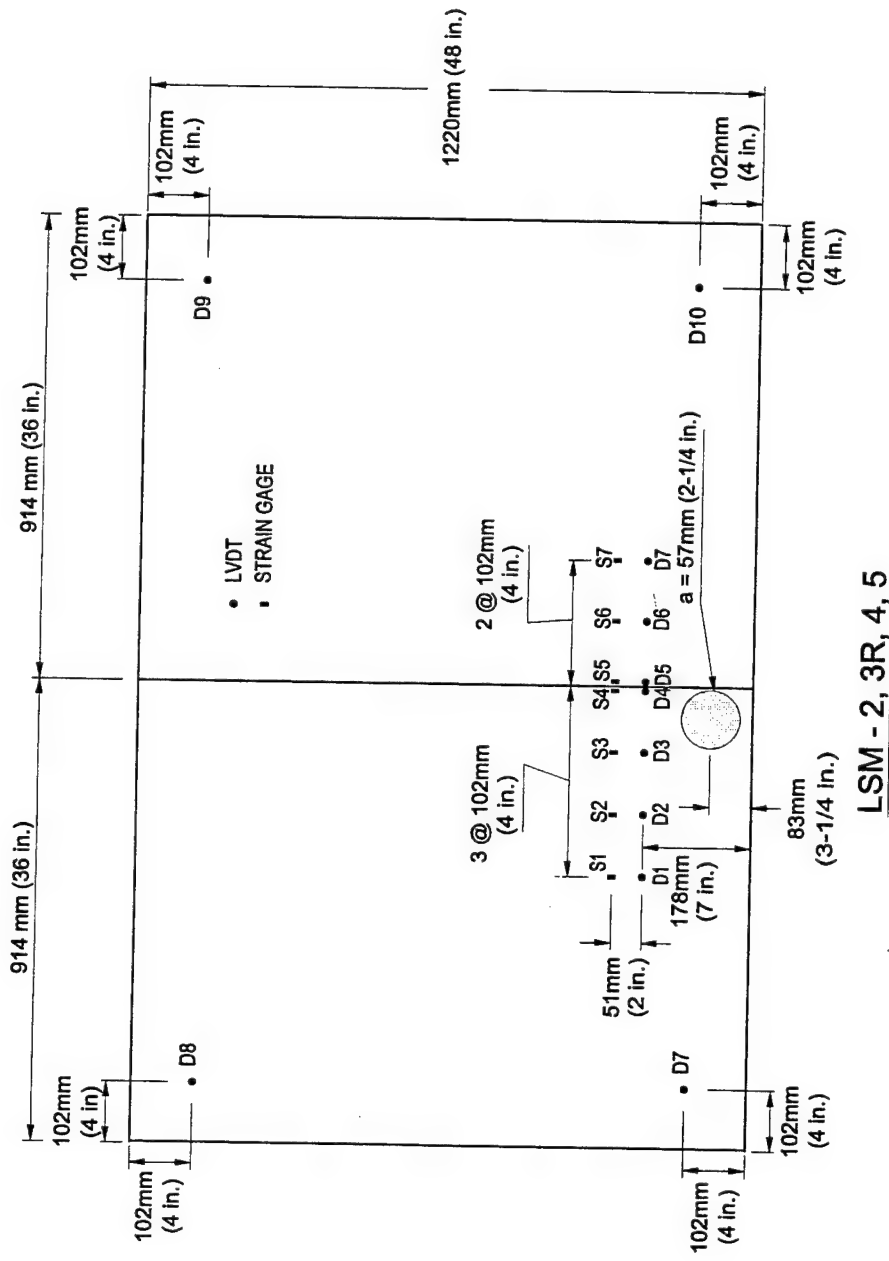


Figure 8.29. Instrumentation plan, Experiments LSM-2, -3R, -4, and -5

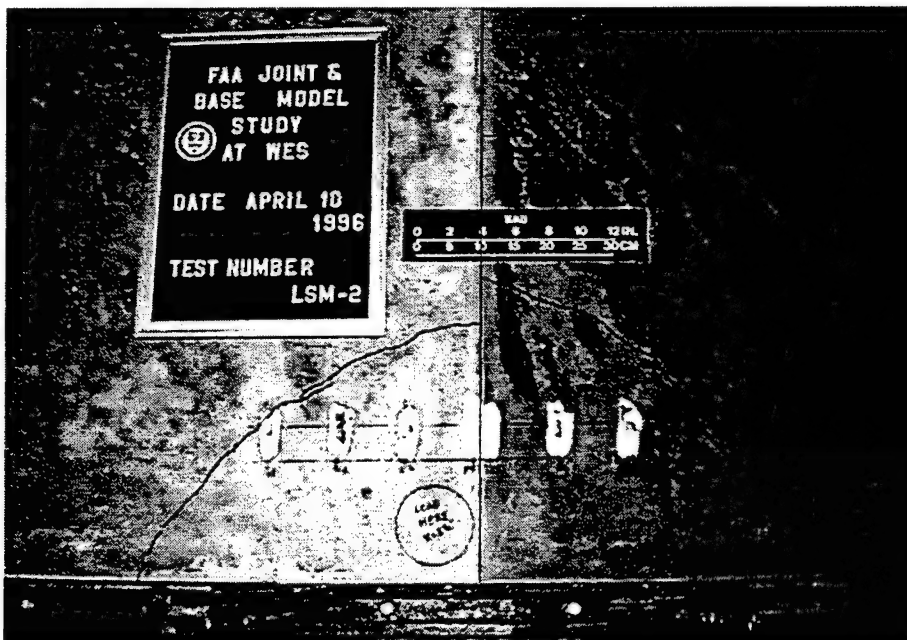


Figure 8.30. Posttest photograph of slab top surface, Experiment LSM-2

response indicating severe cracking near the loaded area is evident for the deflection basins at 20 kN (4,500 lb) and 24 kN (5,500 lb).

The traces from the strain gages bonded to the surface of the slabs are found in Appendix D. These data clearly show the formation of the cracking visible on the top surface of the slab: on the left (loaded) slab at approximately 17 kN (3,800 lb) and on the right (unloaded) slab at 19.1 kN (4,300 lb).

Experiment LSM-3R

Experiment LSM-3 was scrapped because of an operator error in programming the loading function into the MTS Test Star loader. Therefore, a second model was fabricated and tested with the designation of LSM-3R. The model consisted of two 51-mm (2-in.) thick slabs (separated by a doweled joint) founded on a monolithic 38.1-mm (1-1/2 in.) thick cement-stabilized base. The base was placed directly on the rubber block subgrade model. A Teflon sheet inserted between the two slabs maintained the joint opening at 1.58 mm (1/16 in.). A

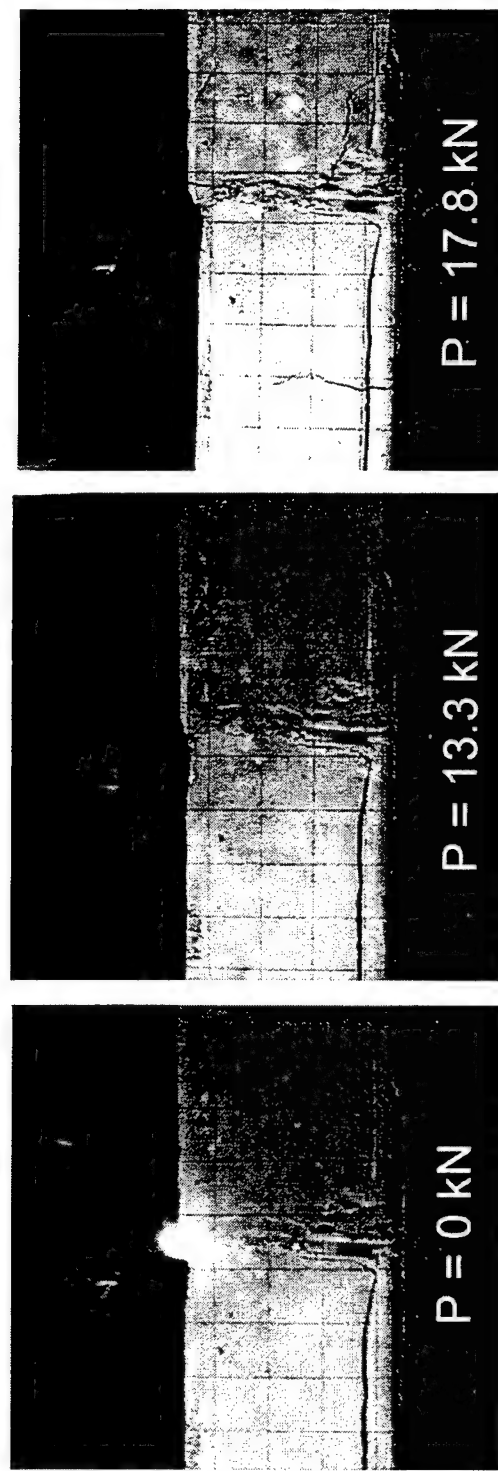


Figure 8.31. Series of photographs in vicinity of joint, Experiment LSM-2

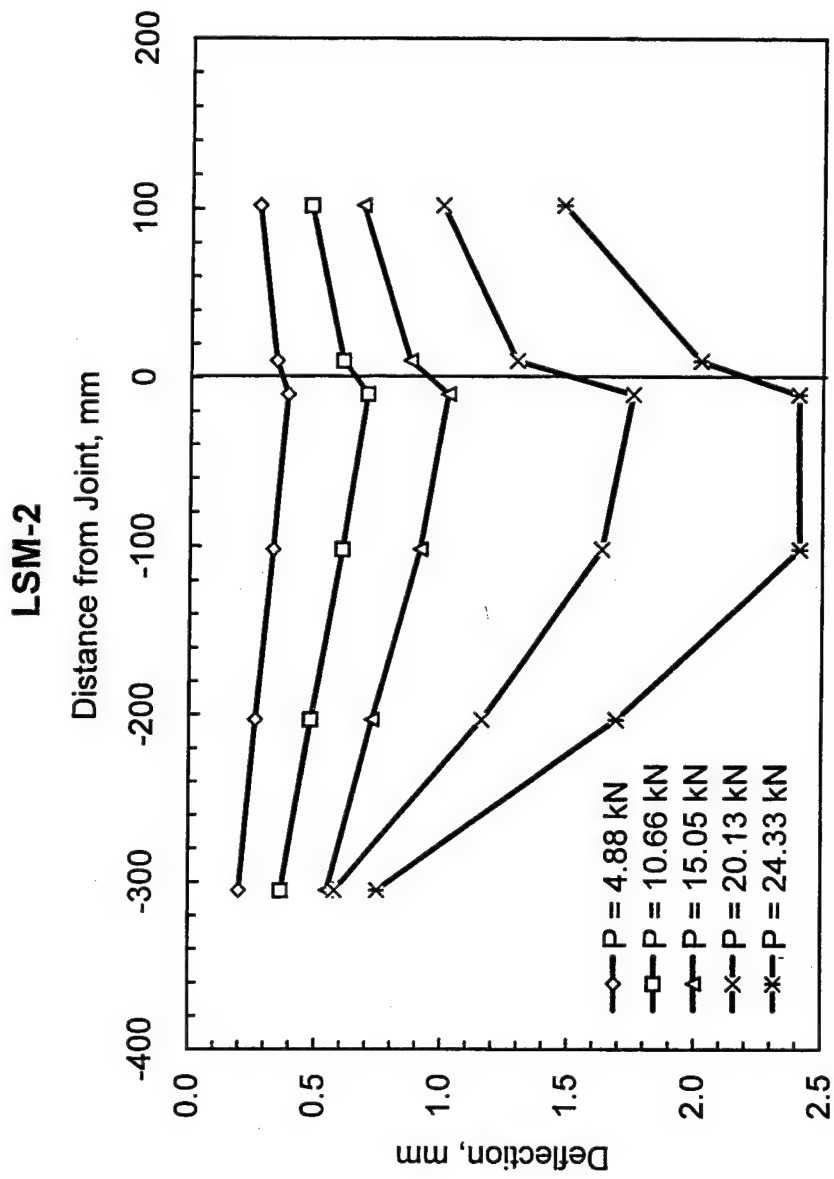


Figure 8.32. Selected deflection basin profiles, Experiment LSM-2

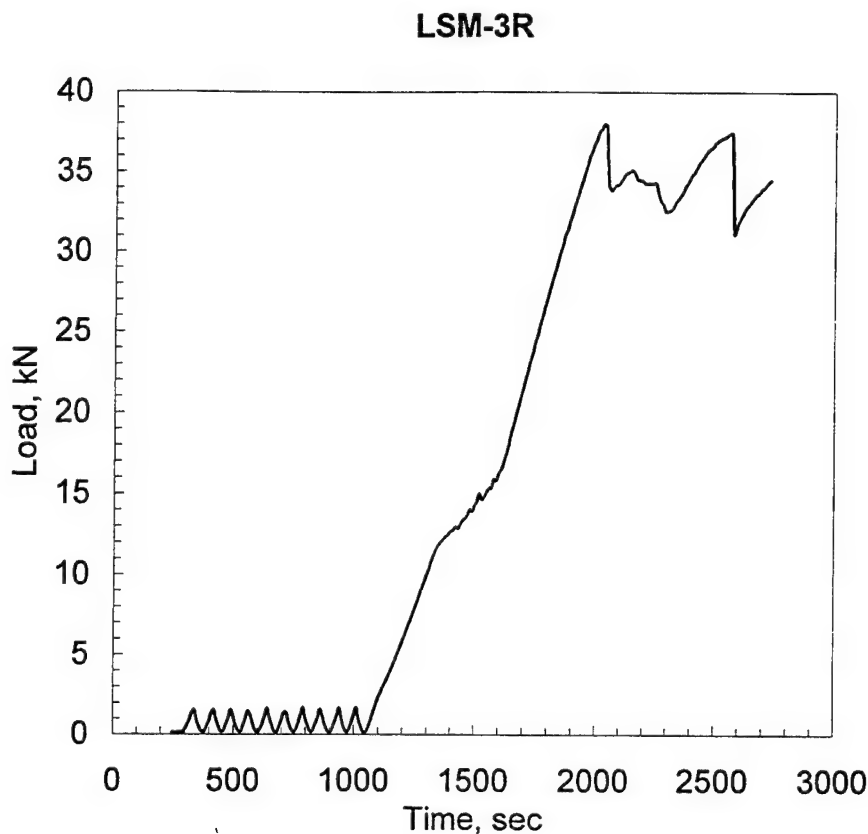


Figure 8.33. Loading history, Experiment LSM-3R

circular load was applied near the corner of the left-hand slab, which contained the bonded end of the dowels. The location and spacing of the dowels is shown in Figure 8.5. Instrumentation type and locations for LSM-3R were identical to that for LSM-2 (Figure 8.29).

The loading history for LSM-3R (Figure 8.33) indicates that the load underwent several cycles of unloading and reloading near the peak load as cracks formed and the stresses were redistributed in the model. A transient reduction in stiffness of the pavement model was evident between approximately 12 kN (2,700 lb) and 16 kN (3,600 lb). Figure 8.34 is a post-test photograph of the top surface of the model. Several corner breaks are evident on the surface of the left-hand or loaded slab. The occurrence of the outermost corner break

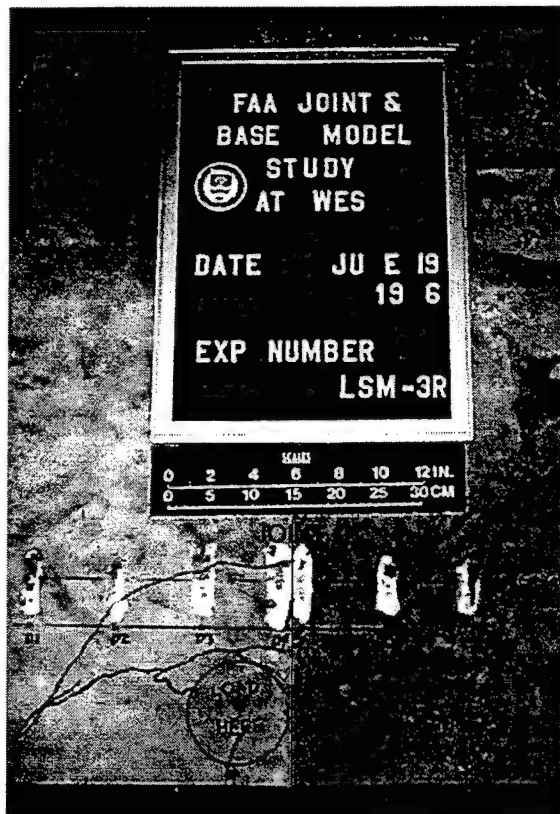


Figure 8.34. Posttest photograph of top surface of slabs, Experiment LSM-3R

corresponded with the first peak in the loading history plot at approximately 38 kN (8,550 lb), while the inner break corresponded with the second major peak at approximately 37 kN (8,300 lb). Posttest observations indicated that these cracks in the slab propagated through the stabilized base as well. No debonding of the base from the slabs at their interface was observed. Considerable crushing or punching shear deformations were noted in and around the circular loaded area.

Figure 8.35 contains selected photographs of the joint region taken through the transparent window in the side of the reaction box as the experiment was underway. A vertical crack in the cement-stabilized base was clearly visible to the unaided eye by a load of 8.9 kN (2,000 lb). The lower left photograph was taken at a load of 37.8 kN (8,500 lb), which is

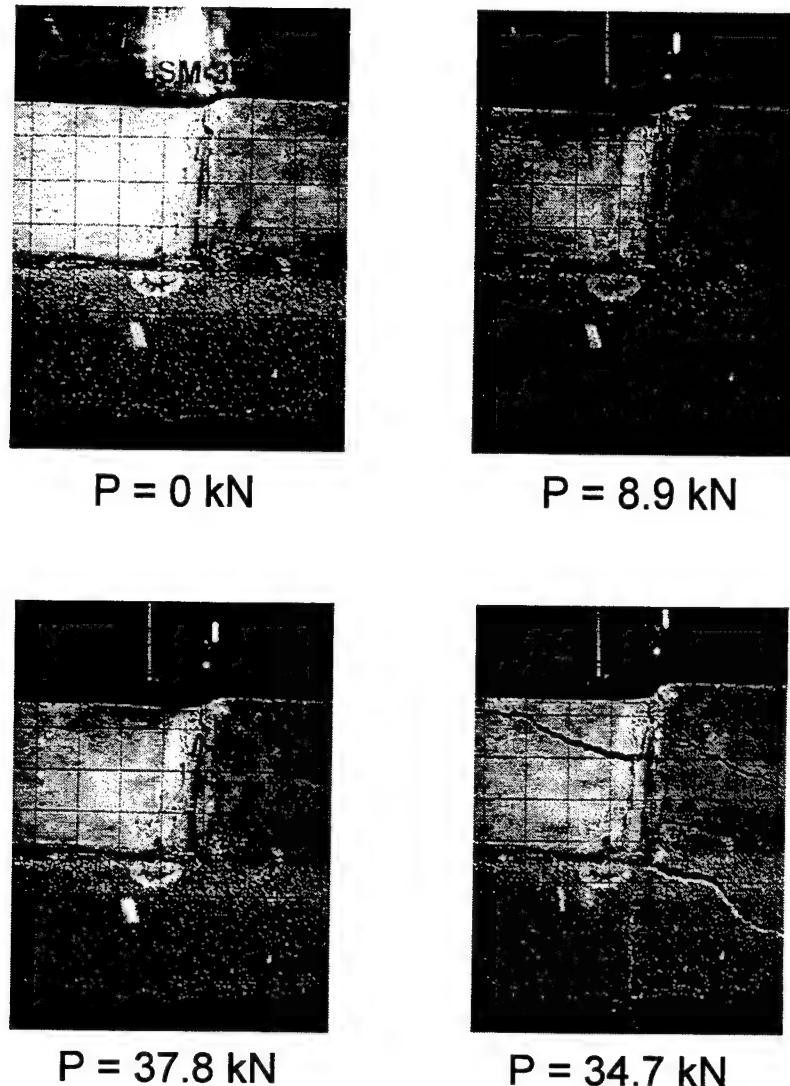


Figure 8.35. Selected photographs of joint region during testing, Experiment LSM-3R

near the first peak in the load-deflection curve. The lower right photograph was taken just prior to halting the test. Note that the vertical crack in the base has open considerably, and horizontal cracking is evident in the left- and right-hand slabs and in the base underneath the right-hand slab.

The load-displacement and load-strain traces are presented in Appendix D. The effects of the cracking which occurred near peak load are evident in these data. Selected deflection

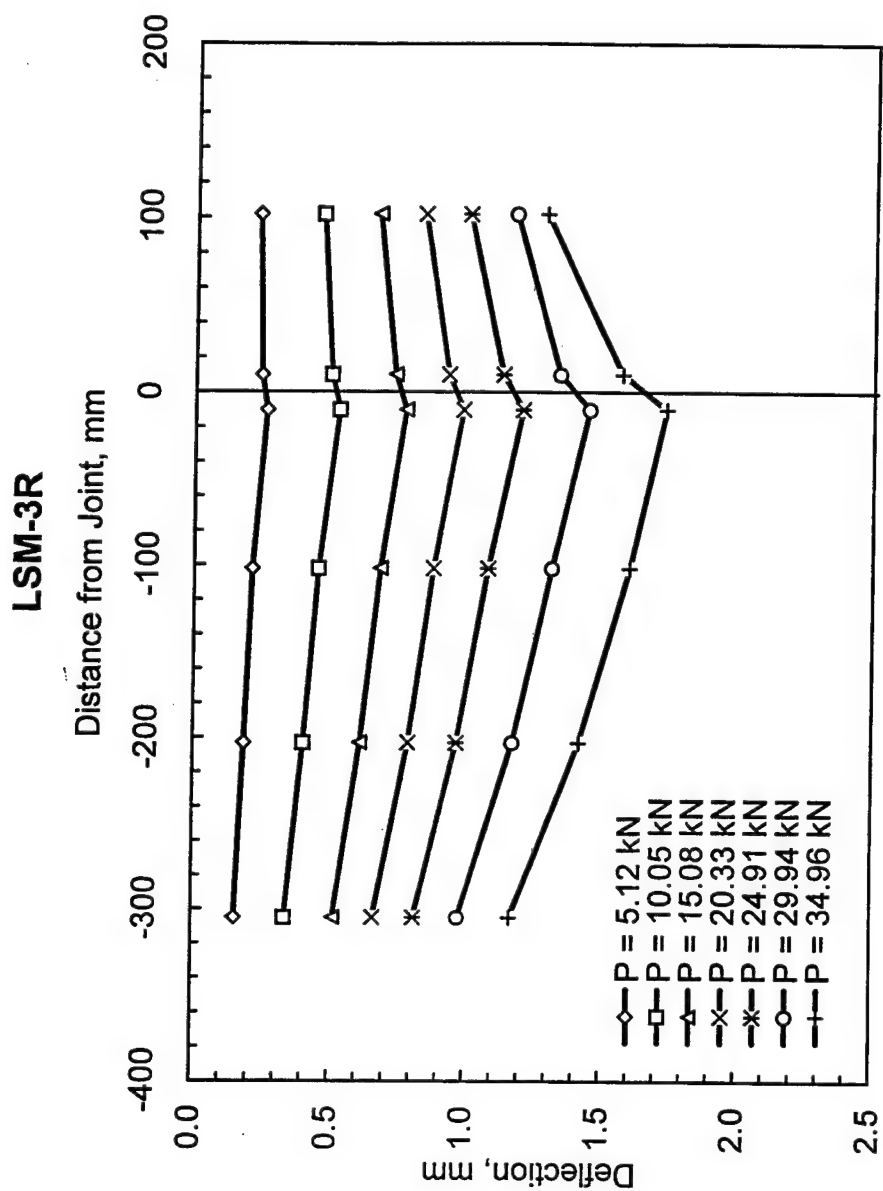


Figure 8.36. Selected deflection basin profiles, Experiment LSM-3R

basin profiles are plotted in Figure 8.36. Insight into the influence of the stabilized base course on the post-cracking response of the slabs can be gained by comparing the deflection basin profiles in Figure 8.36 with those from Experiment LSM-2 (Figure 8.32). The basins from Experiment LSM-2 (with no base course) are highly nonlinear after cracking has occurred indicating the slab is tending to break apart under increasing loads. However, for Experiment LSM-3R (with stabilized base), the post-cracking deflection basins do not indicate that the slab response is nearly as nonlinear as that observed in Experiment LSM-2.

Experiment LSM-4

Two 51-mm (2-in.) thick slabs (separated by a doweled joint) founded on a 38.1-mm (1-1/2 in.) thick cement-stabilized base were constructed and tested for Experiment LSM-4. The base was divided into two equal halves by a cold joint discontinuity directly beneath the slab construction joint. The base was founded directly on the rubber block subgrade model. A Teflon sheet inserted between the two slabs maintained the slab joint opening at 1.58 mm (1/16 in.). A circular load was applied near the corner of the left-hand slab, which contained the bonded end of the dowels. The location and spacing of the dowels is shown in Figure 8.5. Instrumentation type and locations for LSM-4 were identical to that for LSM-2 and LSM-3R (Figure 8.29).

The loading history for LSM-4 (Figure 8.37) is similar in form to that of LSM-3R. A transient reduction in stiffness of the pavement model occurred in the vicinity of a load of 15 kN (3,400 lb). Figure 8.38 is a posttest photograph of the top surface of the model. The cracking highlighted in the photograph occurred on both the loaded and unloaded sides of the joint and is nearly symmetrical about the joint. As was the case for Experiment LSM-3R, the cracking pattern in the slabs was observed to be reflected in the base course as well. Again, no debonding of the slab-base interface was observed.

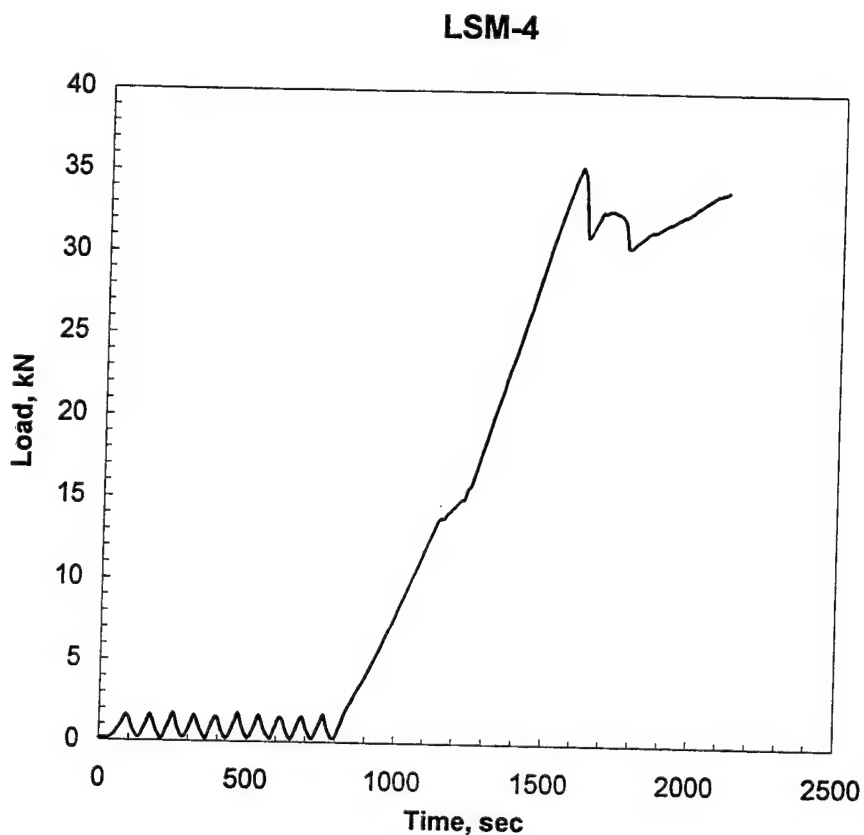


Figure 8.37. Loading history, Experiment LSM-4

Figure 8.39 contains selected photographs of the joint region taken through the transparent window in the side of the reaction box during the experiment. Before the testing commenced, the cold joint discontinuity is visible in the base. As the deflection increased, the cold joint opened up.

The load-displacement traces from the LVDTs are shown in Appendix D. As noted on the plots in Appendix C, Gages D3, D4, and D5 experienced over-ranging before the test was halted. Selected deflection basin profiles are plotted in Figure 8.40. Again, these data indicate, as was the case for Experiment LSM-3R, the presence of the stabilized base course, even though it was initially cracked, led to a much more ductile response than that observed

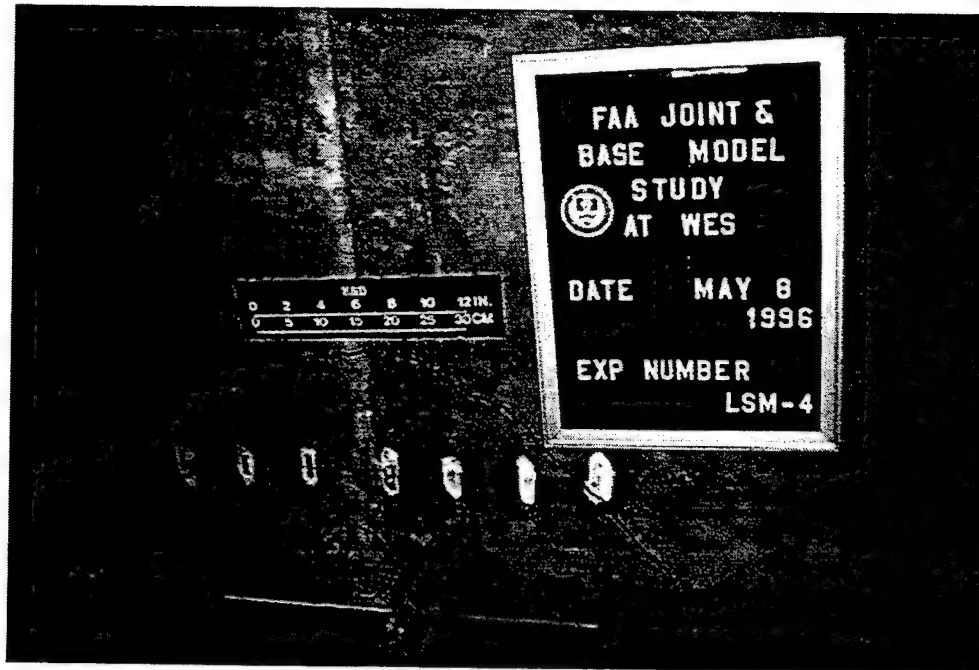
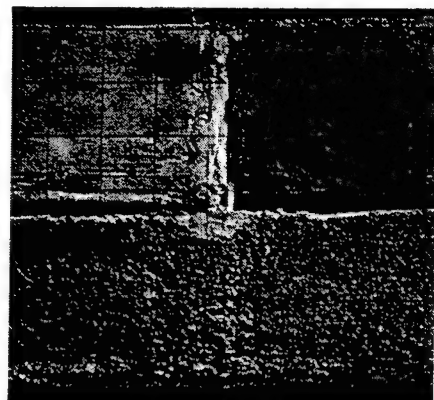


Figure 8.38. Posttest photograph of top surface of slabs, Experiment LSM-4

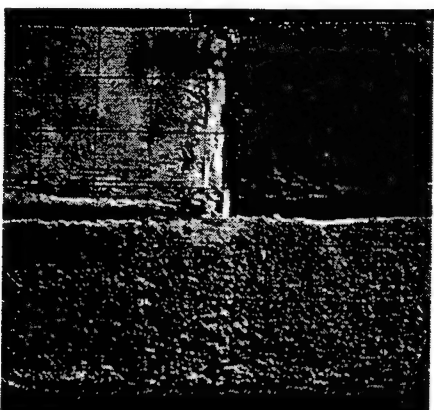
for the slabs founded directly on the rubber pad (Experiment LSM-2). Strain gage traces are also presented in Appendix D. Gage S5 failed during the test. It was postulated that the gage was inadequately bonded to the slab.

Experiment LSM-5

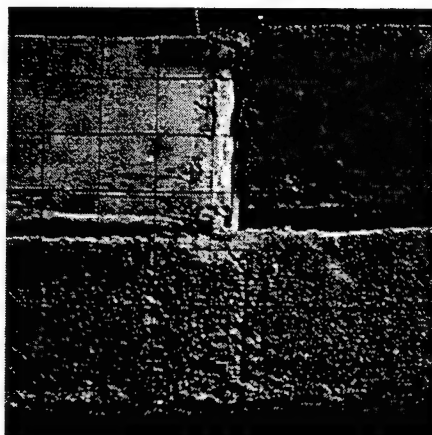
A polyethylene-sand-polyethylene sandwich was constructed as a bond-breaking layer between the two 51-mm (2-in.) thick slabs (separated by a doweled joint) and the 38.1-mm (1-1/2 in.) thick cement-stabilized base for Experiment LSM-5. The monolithic base was founded directly on the rubber block subgrade model. A Teflon sheet inserted between the two slabs maintained the slab joint opening at 1.58 mm (1/16 in.). A circular load was applied near the corner of the left-hand slab, which contained the bonded end of the dowels. The location and spacing of the dowels is shown in Figure 8.5. Instrumentation type and locations for LSM-5 were identical to that for LSM-2, LSM-3R, and LSM-4 (Figure 8.26).



$P = 0 \text{ kN}$



$P = 33.4 \text{ kN}$



$P = 33.9 \text{ kN}$

Figure 8.39. Selected photographs of joint region during testing, Experiment LSM-4

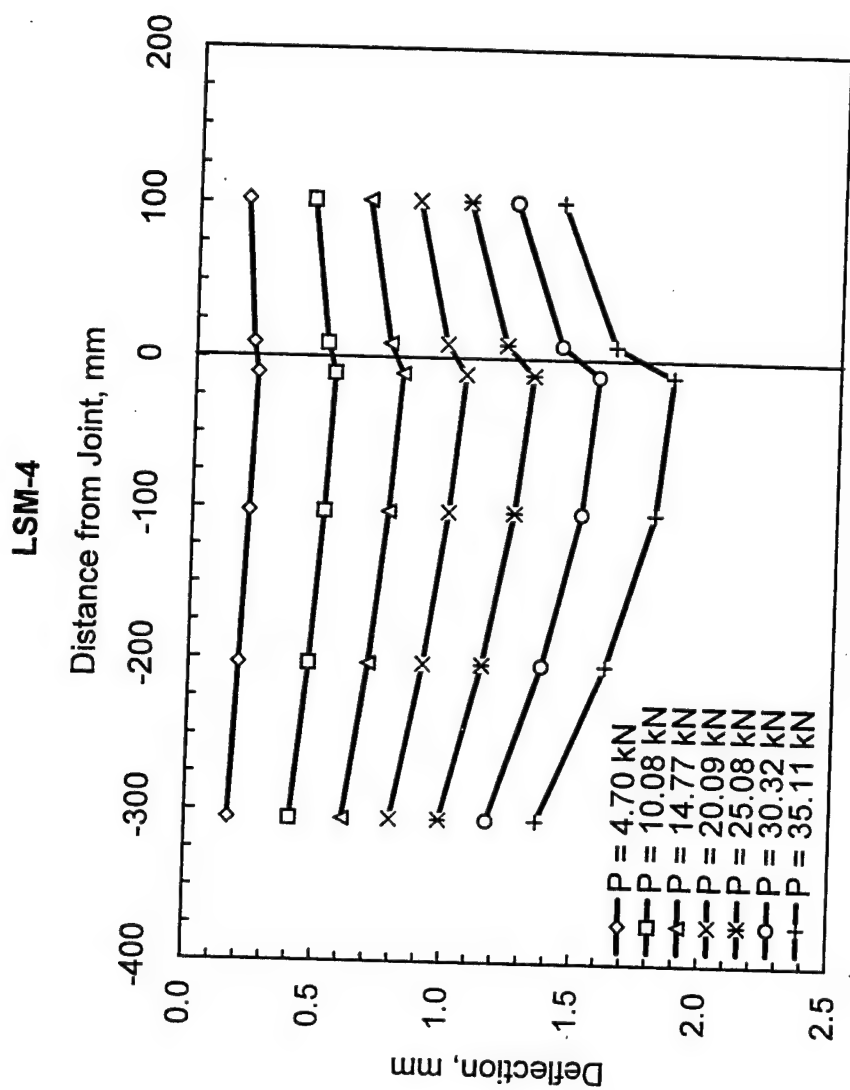


Figure 8.40. Selected deflection basin profiles, Experiment LSM-4

The loading history for LSM-5 is presented in Figure 8.41. As was the case for Experiments LSM-3R and LSM-4, a transient reduction in stiffness of the pavement model occurred in the vicinity of a load of 15 kN (3,400 lb). A posttest photograph of the top surface of the

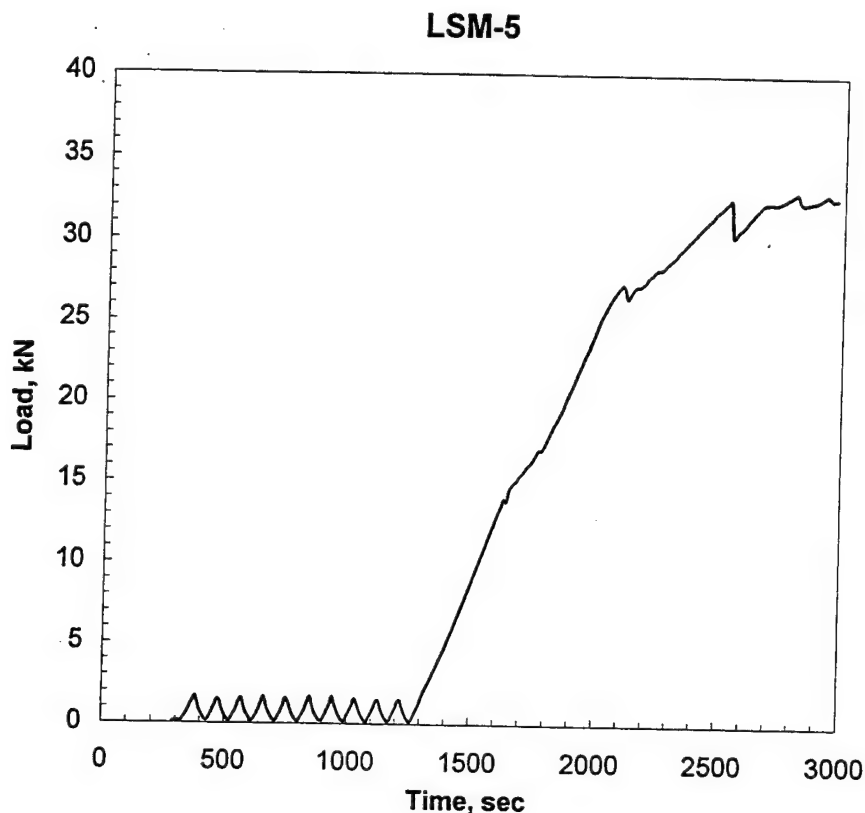


Figure 8.41. Loading history, Experiment LSM-5

model is presented in Figure 8.42. Several corner breaks are evident on the surface of the left-hand or loaded slab and a single corner break on the right-hand or unloaded slab. The occurrence of the outermost corner break on the left side occurred at a load of approximately 25 kN (5,600 lb), and the corner break on the left occurred at a load of approximately 28 kN (6,300 lb). The interior corner breaks on the loaded side happened progressively as the load dropped from its maximum value of approximately 33 kN (7,400 lb).

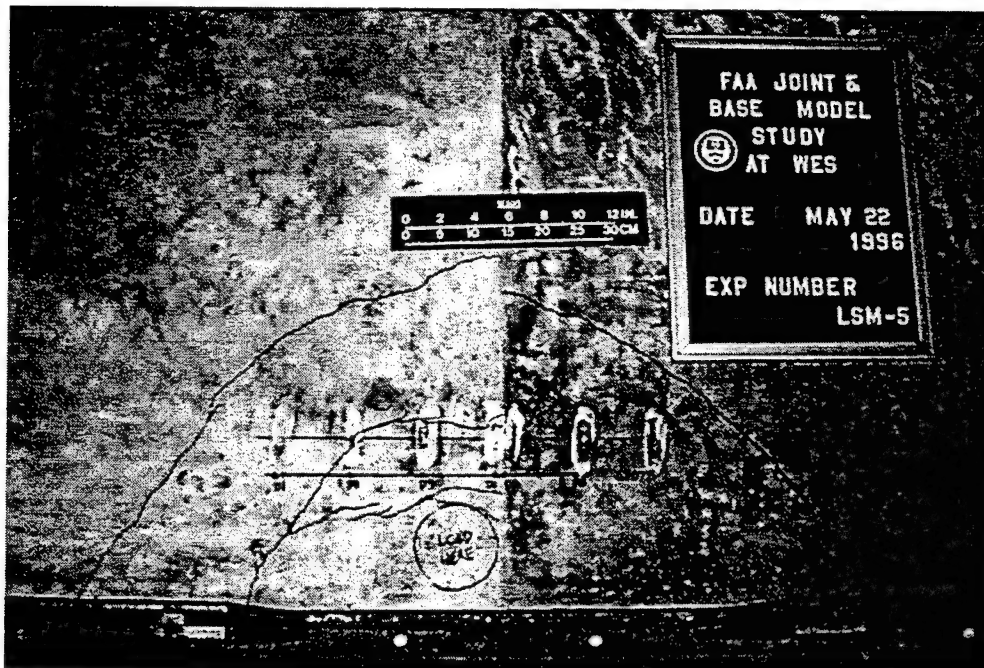
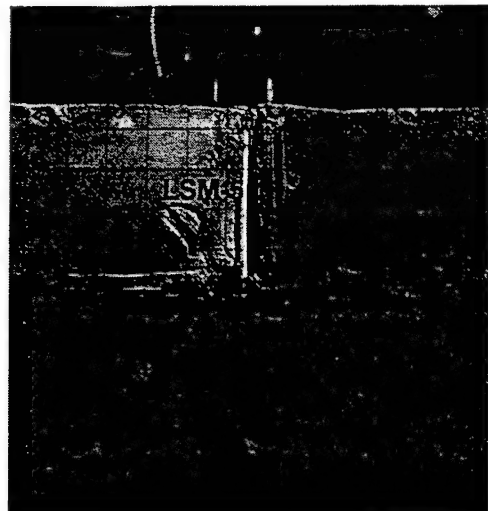


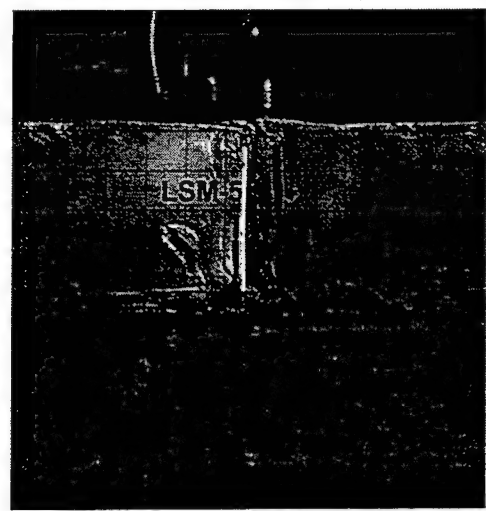
Figure 8.42. Posttest photograph of top surface of slabs, Experiment LSM-5

Figure 8.43 contains selected photographs taken through the transparent window in the side of the reaction box. Perhaps the most interesting observation from these photographs is that no visible cracking was observed in the cement-stabilized base. Based upon the results of the previous experiments, it can be concluded that breaking the bond between the slabs and base may reduce the potential for cracking beneath the surface joint.

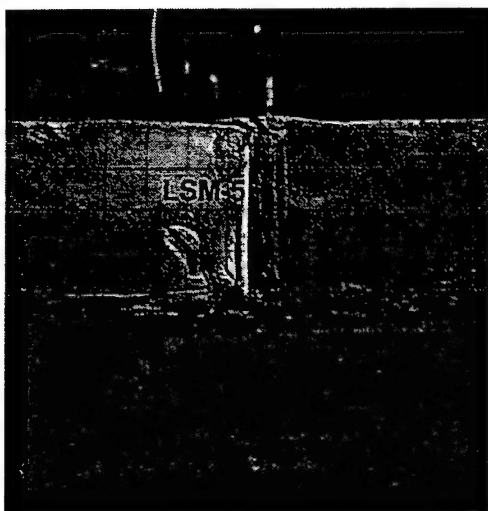
The load-displacement and strain traces from the experiment are presented in Appendix D. Gages D3, D4, and D5 experienced over-ranging before the test was halted. Selected deflection basin profiles are plotted in Figure 8.44. It can be noted from Figure 8.44 that the response was less ductile than that observed in Experiments LSM-3R and LSM-4 in which bonding between the slabs and base was not prevented.



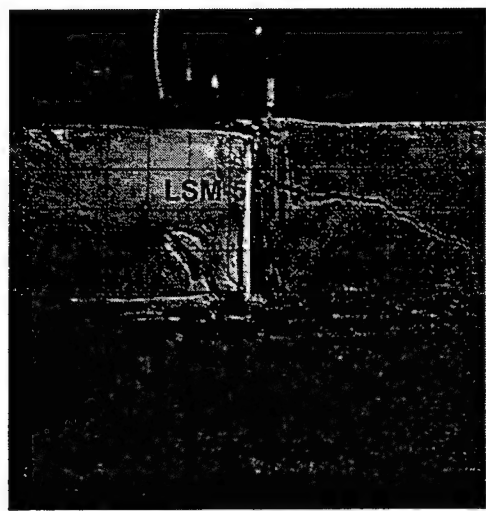
$P = 0 \text{ kN}$



$P = 32.2 \text{ kN}$



$P = 30.8 \text{ kN}$



$P = 32.6 \text{ kN}$

Figure 8.43. Selected photographs of joint region during testing,
Experiment LSM-5

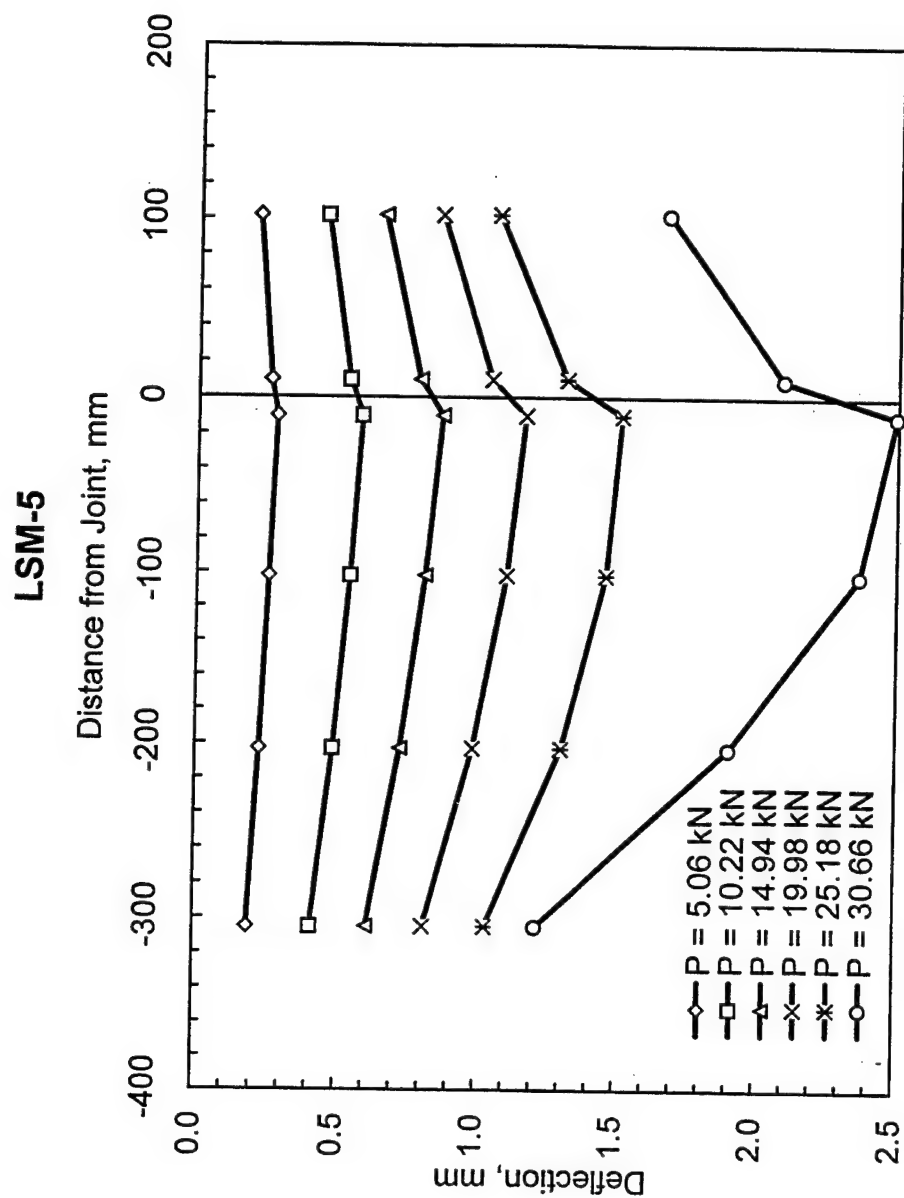


Figure 8.44. Selected deflection basin profiles, Experiment LSM-5

COMPARISON OF EXPERIMENTAL RESULTS

In Figures 8.45 and 8.46, the load-deformation traces from D4 and D5, respectively, from Experiments LSM-2, LSM-3R, LSM-4, and LSM-5 have been plotted on the same graphs.

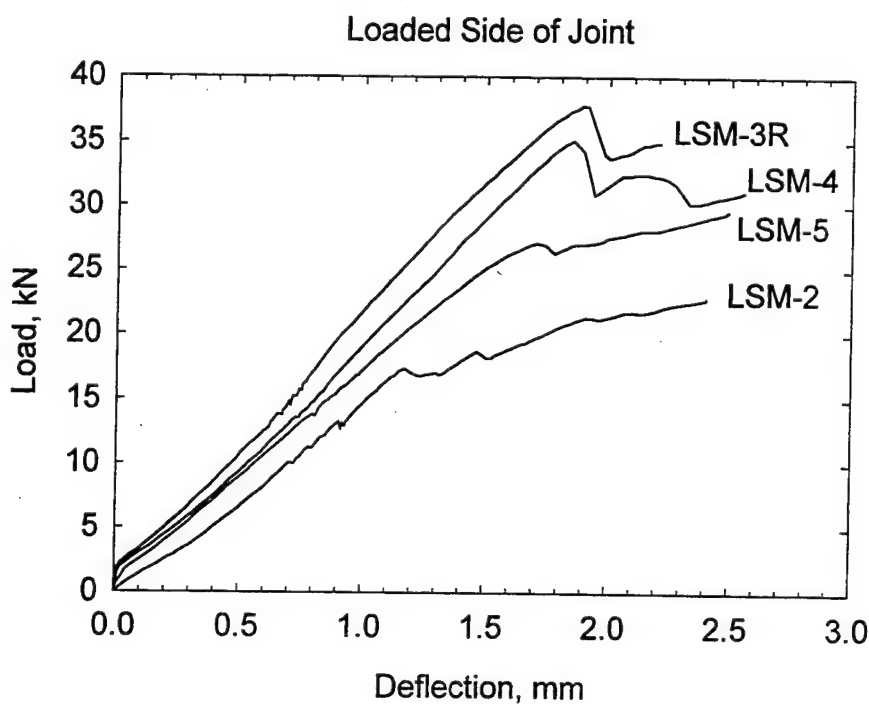


Figure 8.45. Load-deflection curves from experiments, loaded side of joint

These plots indicate the relative stiffness and strength of the various experimental model configurations. To compare the slopes of the four curves, instantaneous slope values were calculated for loads between 5 and 10 kN (1,125 and 2,250 lb) for the cases of the loaded and unloaded sides of the joint. ANOVA techniques were subsequently used to determine if a

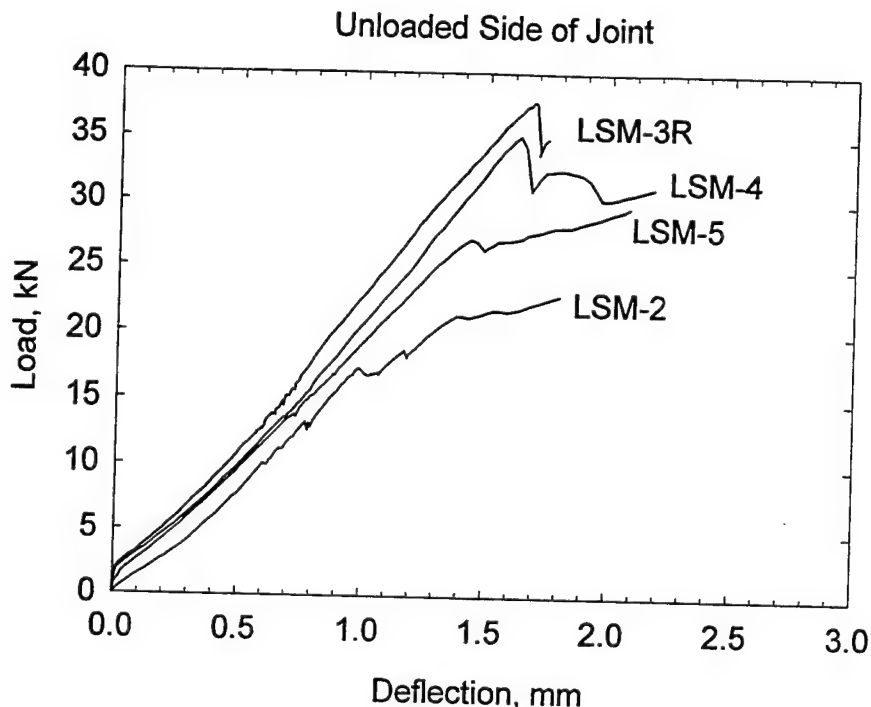


Figure 8.46. Load-deflection curves from experiments, unloaded side of joint

statistically significant difference in the pre-cracking slopes could be observed. The instantaneous slope measurements failed a normality test; therefore the ANOVA was conducted based upon ranks. The differences in the median values among the experiments were not great enough to exclude the possibility that the difference in slopes was due to random sampling variability; therefore, the ANOVA failed to detect any statistically significant difference in the slopes of the load-deflection curves between the four experiments at the 0.05 significance level.

The post-cracking responses of the four experiments revealed some striking differences. As expected, the load carrying capacity of the models with stabilized bases exceeded that of

experiment without a stabilized base (Experiment LSM-2). For the two experiments in which bonding between the slabs and base was allowed (LSM-3R and LSM-4), the strength was enhanced over the experiment in which the bond breaker was employed (LSM-5). The slabs with stabilized bases sustained greater deflections prior to experiencing softening of the load-deflection curves. Thus, it can be observed from these plots that composite action of the slabs and stabilized bases provided an increase in structural capacity and ductility over slabs cast directly on grade.

Figure 8.47 shows a composite plot of deflection load transfer efficiencies (LTE_{δ}) versus load for each of the experiments. These values were calculated by forming the ratios of the measured deflections at LVDT locations D4 and D5. Calculated values of LTE_{δ} for loads

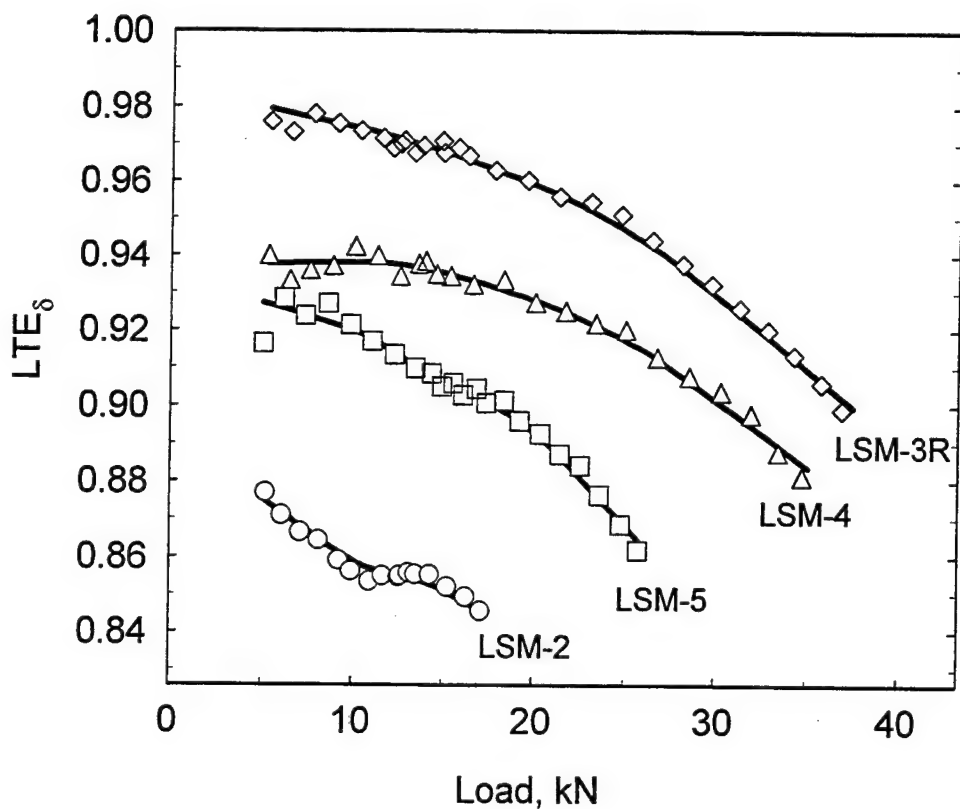


Figure 8.47. Deflection load transfer efficiencies from experiments

less than 5 kN (1,125 lb) were unreliable due to the small levels of deformation at low load levels and due to seating of the slabs on the foundation. Thus, these measurements are not plotted in Figure 8.47. Similarly, once the initial peak loads occurred (typically associated with visible cracking of the slabs), the calculated values of LTE_{δ} became unreliable. Therefore, these values are also not plotted in Figure 8.47.

Several important observations can be made from Figure 8.47. First, it can be observed that the greatest values of LTE_{δ} were obtained from the slabs founded on the monolithic stabilized base (LSM-3R), followed, in order, by slabs founded on a cracked monolithic base, founded on a monolithic base with a bond breaker, and finally, founded directly on the rubber pad. Secondly, each of the curves seem to have the same general shape indicating the maximum load transfer efficiency occurred at low loads with decreasing effectiveness for increasing load. This phenomenon is likely caused by localized crushing of the slabs' concrete in the region of the dowels as the loads and resulting displacements increase. This crushing occurs where high localized loads are being transferred from the concrete to the bars or vice versa. This effect has been predicted by finite element modelers (Channakeshava, Barzegar, and Voyiadjis 1993) and can also occur as the result of localized fatigue in pavement slabs under the influence of repeated service loads.

The data in Figure 8.48 were used to evaluate the effectiveness of the structural steel angles in restraining vertical translation of the ends of the slabs. These angles were placed on the upper surface of the slabs in each experiment and bolted to the reaction box. Their primary purpose was to prevent rigid body translation of the slabs due to the imposed corner loading. LVDTs were installed at gage locations D7, D8, D9, and D10 (Figure 8.29) to monitor to vertical movements of the far corners of each slab.

Data from Experiments LSM-2, LSM-3R, LSM-4, and LSM-5 are compared in Figure 8.48. The upper plot shows the deflection at the gage locations D7 and D8 on the left (loaded) slab, while the lower plot shows the deflections at gage locations D9 and D10 on the right (unloaded) slab. The deflections shown in Figure 8.48 at a load of approximately 10 kN. In the case of Experiment LSM-2, very small movements either upward or downward were observed. However, downward displacements were observed at gage location D7 in Experiments LSM-3R, LSM-4, and LSM-5. For Experiment LSM-4 an upward displacement near the front of the right (unloaded) slab was observed at gage location D10; however, for all other experiments either very small displacements or downward displacements were observed on the unloaded slab. Therefore, it can be concluded that the angles were marginally effective in preventing upward displacement of the slab corners. However, downward deflections of the slab corners were commonly observed.

Certain observations from this experimental program point to some significant challenges for modelers seeking to predict rigid pavement behavior and performance. Among these are the following challenges:

- The presence of bonding between the slabs and base has an effect on the strength and ductility of the rigid pavement structure. The concept of the composite or “top of the base” modulus of subgrade reaction, which substitutes an inflated value of the subgrade modulus to account for stabilized bases, ignores the composite action of the slab-stabilized base structural system. This concept, which was adopted out of necessity when the most reliable method of predicting rigid pavement behavior was the Westergaard theory, should be abandoned in favor of a more realistic model that explicitly includes the structural benefits of the stabilized base.

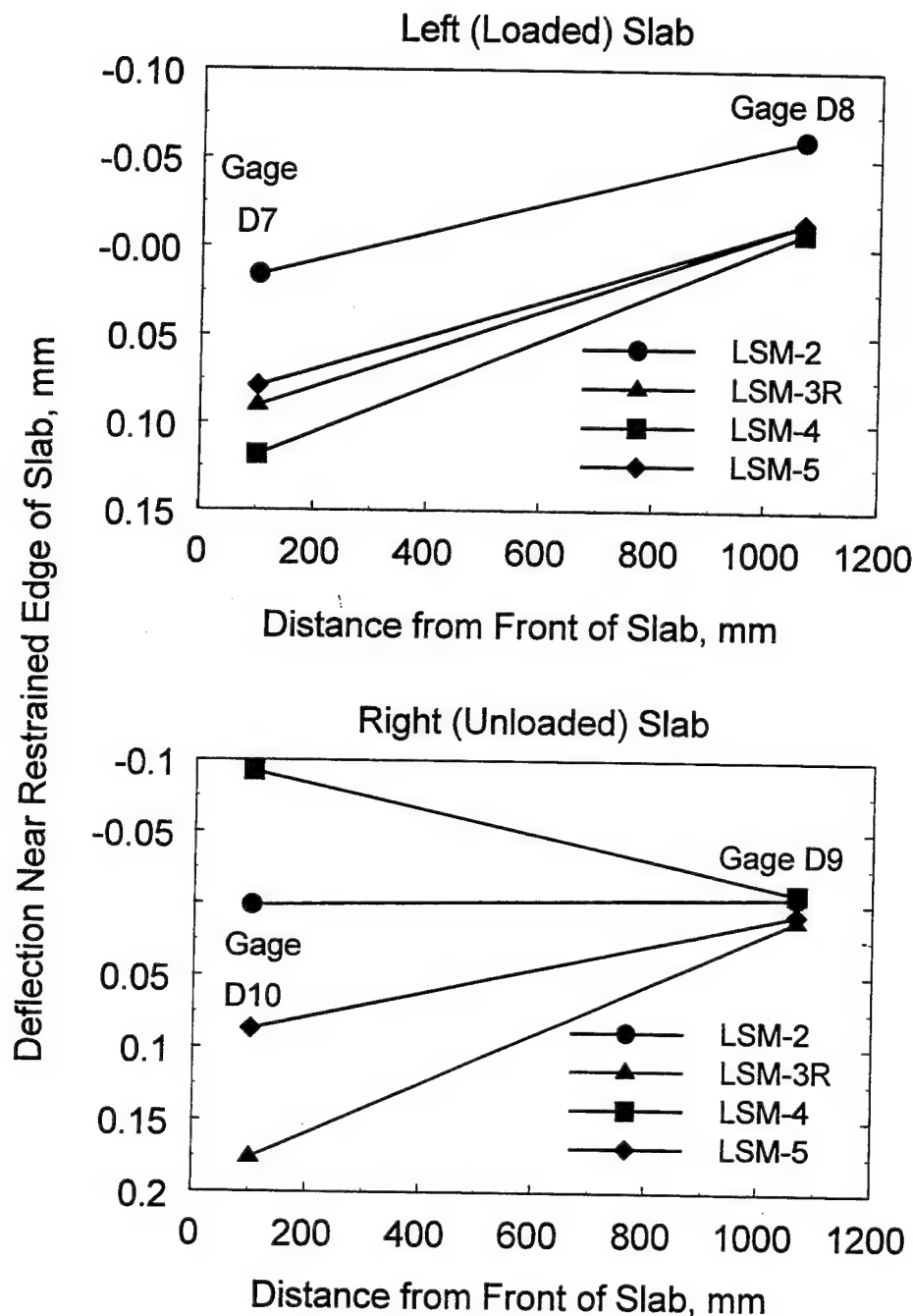


Figure 8.48. Effectiveness of slab end restraint

- The presence and quality of stabilized base has an influence on the load transfer effectiveness of a rigid pavement joint. From the experimental data, it appears that a monolithic stabilized base provides superior joint performance. However, field observations by Grogan, Weiss, and Rollings (1996) at Dallas-Fort Worth, Stapleton (Denver), and Hartsfield (Atlanta) International Airports have indicated that the majority of both the longitudinal and transverse cracking in cement stabilized bases was found to occur under the joints in the rigid pavement surface. Thus, it may reasonably be expected that, for the majority of in-service rigid pavements, cracks are present in the stabilized base in a pattern matching the jointing pattern of the slabs. The net effect of this cracking is that the load transfer mechanism includes not only the load transfer devices (dowels, aggregate interlock, key ways) in the slab, but also some degree of load transfer due to aggregate interlock in the stabilized base. The effectiveness of this aggregate interlock in the base is likely to depend upon the magnitude and cycles of loading, quality of the stabilized base materials, and moisture and temperature (and attending volume changes) in the base.
- The presence and degree of bonding between the slabs and stabilized base course has an influence on the structural capacity and load transfer capability of the rigid pavement structure. Research by Wesivich, McCullough, and Burns (1987) has shown that the magnitude of friction between the slab and base is dependent upon bearing, shear, and adhesion between the slab and base. They also concluded that if the adhesion is great enough, the failure plane will not be at the interface between the slab and base, but rather within the base. Observations by Grogan, Weiss, and Rollings (1996) indicated where slabs were being reconstructed at Hartsfield (Atlanta) Inter-

national Airport that in some instances the cement stabilized base was adhered to the slabs, while in other instances it was not.

- The experiments conducted in this investigation confirmed the observations and predictions of other researchers that the effectiveness of the load transfer mechanism decreases with localized damage in the immediate vicinity of the joint. This has significant implications in the modeling of the performance of rigid pavements. A non-linear model of decreasing joint effectiveness with repetitions of load would be necessary to model this aspect of rigid pavement performance. Additional testing and research would be required to develop and calibrate such a model.

CHAPTER 9: ANALYTICAL MODEL DEVELOPMENT AND VERIFICATION

ANALYTICAL MODEL DESCRIPTION

As described in Chapters 4 and 5, most response models for rigid pavements, including the Westergaard model and 2D finite element models, assume a single man-made layer rests directly on a foundation that can be represented by a bed of springs. However, most modern airport pavements are constructed on cement-stabilized bases that are of high quality and substantial strength. The contribution of the base course to the strength of the pavement structure is poorly understood. To account for the increased capacity of the foundation caused by a stabilized layer, the modulus of subgrade reaction is increased in the Westergaard model. This approach, in which the "top-of-the-base" modulus is determined empirically, is required by the assumptions implied in the Westergaard solution. Similarly, 2D finite element plate programs such as ILLI-SLAB may account for the stabilized layer by adding additional stiffness to the plate elements based upon the concept of the transformed section.

The primary deficiency of these approaches is that neither directly addresses the influence of the base course on the load transfer efficiency at a joint. In almost all instances stabilized layers are constructed to be monolithic. However, field observations (Grogan, Weiss, and Rollings, 1996) have indicated that cracks occur in the stabilized base in a pattern that directly matches the jointing pattern in the surface layer. It is likely that some load transfer occurs across these cracks by aggregate interlock.

As a part of the construction process, a bond breaker may be used between the surface slabs and the base course; thus, it is possible that gaps may open between the slab and base course. For those areas which remain in contact, shear stress may be transferred across the

boundary by friction. In other cases, delamination of an initially bonded base course and slab may occur from volume changes caused by moisture and temperature variations. In some instances field investigations have indicated that delaminations have occurred, usually somewhere beneath the interface between the slab and base course (Grogan, Weiss, and Rollings 1996). It is likely that shear stresses are transmitted across these delaminations by aggregate interlock. It is also possible that gaps may form between the slabs and base. In order to make a contribution to the state of the art in rigid pavement response modeling, these factors must be considered.

Table 9.1 contains a matrix that summarizes these conditions and compares them to the experiments described in Chapter 8. To develop an analysis methodology that takes into consideration the influence of the stabilized base course on the joint response, a series of finite element models were generated and executed. Figure 9.1 summarizes the cases described and the model options chosen to represent the behavior of the major features of each case.

Table 9.1
Considerations for Model Development

Case	Are base and slabs bonded?	Is base course cracked beneath slab joint?	Experiment Most Closely Matching Case
I	No Base	No Base	LSM-2
II	Yes	No	LSM-3R
III	Yes	Yes	LSM-4
IV	No	No	LSM-5
V	No	Yes	Not in experimental matrix

A sample ABAQUS input file with explanatory comments is listed in Appendix E. The slabs and base course continua were modeled by C3D27R reduced-integration Lagrangian hexahedral elements. The joint between the slabs was modeled by JOINTC elements with

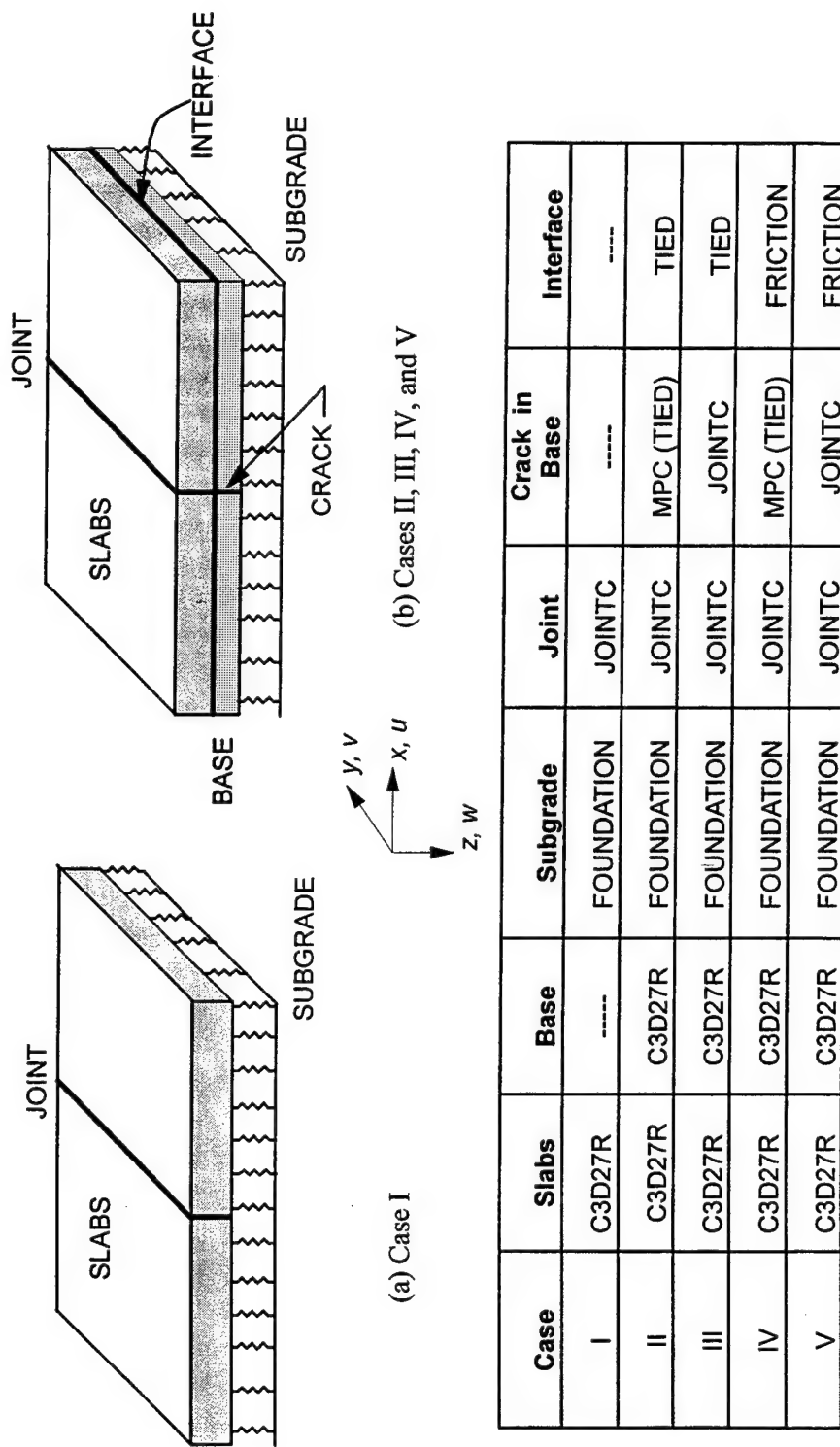


Figure 9.1. Analytical model case descriptions

stiffnesses assigned in the z-direction direction only. Thus, the load transfer mechanism was implicitly a shear only mechanism, with no load transfer due to bending. The interface between the slabs and base course was modeled by the ABAQUS contact interaction feature. Where the base and slabs were bonded (Cases II and III), the "TIED" option was invoked to force the displacements of all three degrees-of-freedom (u , v , and w) equal for all node pairs across the interface. Where the slabs and base were not bonded (Cases IV and V), the "FRICTION" option was used allow transfer of shear contact stresses across the interface. For Cases II and IV in which the base course was not cracked, ABAQUS MPCs with the "TIE" option invoked was used to set displacements (u , v , and w) of corresponding node pairs across the crack equal. Conversely, for Cases III and V in which a crack was present in the base course, JOINTC elements were employed to allow load transfer across to the crack. Again, stiffnesses were assigned to the JOINTC elements in the z-direction only, limiting them to load transfer due to shear only. For each of the cases, the subgrade was modeled as a bed of springs using the ABAQUS "FOUNDATION" option. In all cases the slabs and base were considered to be weightless.

ANALYTICAL MODEL RESULTS

Case I

The material and structural parameters from the experimental pavement models (summarized in Table 9.2) were used to develop the analytical model. Because of concerns about execution times and memory requirements, a relatively coarse mesh (Figure 9.2) was adopted. The aspect ratio for the elements in the plane of the slab surface were 1:1, while the aspect ratio in the plane of the slab thickness was 4:1. The spring stiffnesses assigned to the individual JOINTC elements were calculated from the data in Table 9.2 using Equations 7.13 and 7.14. The loaded area was equal to that of the circular loaded area in the

Table 9.2
Experimental Model Parameters

Parameter	Equation No.	Dimensions	Value
Slabs-on-Grade Material Parameters			
E_s	--	F/L^2	27,600 MPa (4,000,000 psi)
v_s	--	--	0.18
h	--	L	0.051 m (2 in.)
k	--	F/L^3	90 MPa/m (330 psi/in.)
Slabs-on-Grade Structural Parameters			
ℓ	4.1	L	0.243 m (9.57 in.)
ϵ	--	L	0.0508 m (2 in.)
ϵ/ℓ	--	--	0.209
Joint Material Parameters			
E_d	--	F/L^2	200,000 MPa (29,000,000 psi)
v_d	--	--	0.30
K	--	F/L^3	407,000 MPa/m (1,500,000 psi/in.)
Joint Structural Parameters			
s	--	L	0.102 m (4 in.)
d	--	L	0.00635 m (0.25 in.)
I_d	--	L^4	$0.798 \times 10^{-12} \text{ m}^4$ ($0.192 \times 10^{-3} \text{ in.}^4$)
A_z	5.6	L^2	$28.5 \times 10^{-6} \text{ m}^2$ (0.044 in. ²)
G_d	5.5	F/L^2	76,900 MPa (1,115,000 psi)
ω	--	L	0.00159 m (0.0625 in.)
ϕ	5.4	--	34.7
C	5.3	F/L	112 MN/m (640,000 lb/in.)
β	4.5	L^{-1}	79.8 m^{-1} (2.03 in. ⁻¹)
DCI	5.2	F/L	15.2 MN/m (86,800 lb/in.)
D	5.1	F/L	15.1 MN/m (86,200 lb/in.)
$f = D/sk\ell$	--	--	6.79
$q = D/s$	--	F/L^2	148 MN/m/m (21,460 lb/in./in.)

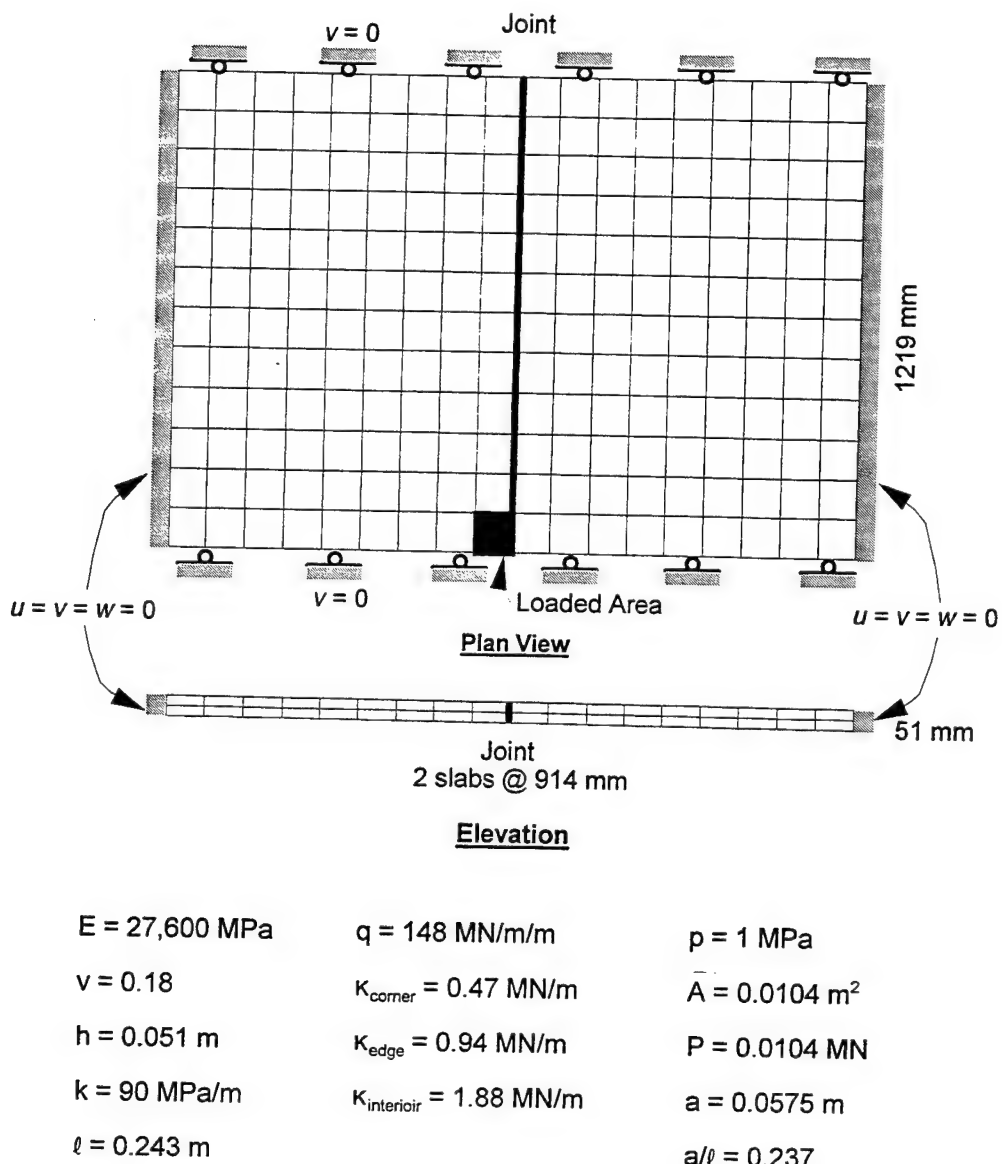


Figure 9.2. Finite element model, Case I

experimental program. The load consisted of an uniform pressure of 1 MPa (145 psi), and the loaded area was 0.0104 m^2 (16 in.^2) resulting in a total load of 10.4 kN (2,340 lb).

The boundary conditions for the finite element model were selected to match those of the experiment as closely as possible. The ends of the experimental slabs were restrained by the

stiff steel reaction box and by structural steel angles embedded in the top surface of each slab and bolted to the reaction box. Thus, all three degrees of freedom were restrained ($u = v = w = 0$) along these ends in the finite element model. The other sides of the experimental slabs were prevented from deforming laterally by the steel reaction box. Therefore, in the finite element model translation perpendicular to these sides of the box was restrained ($v = 0$). Because the sides of the box were coated with a form-release agent prior to casting the slabs, the other two degrees of freedom were not restrained.

The results from the finite element analysis was compared with results from Experiment LSM-2. In order to directly compare the load-deflection results from the finite element model to the experiment, the experimental load-deflection data were corrected to remove the nonlinearity introduced by the rubber subgrade. This was accomplished in a manner identical to that described in Chapter 8 for Experiments LSM-1A and LSM-1B. The original experimental data along with the corrected experimental data (up to a load of 10 kN (2,250 lb)) are shown in Figure 9.3. The resulting experimental deflection basin profiles at a load of approximately 10 kN (2,250 lb) are shown in Figure 9.4 along with the deflection basin profile from the finite element model. These data indicate that the finite element model matches the corrected experimental data well.

Figure 9.5 shows a plot of LTE_{δ} (calculated as the ratio of LVDTs D5 and D4) as a function of applied load. Superimposed on this data is the deflection load transfer efficiency predicted at the location of LVDTs D5 and D4 by the finite element model. Again, the agreement between the model and the experimental data is acceptable over the linear range of response of the experimental slabs. At loads above approximately 17 kN (3,820 lb), significant cracking occurred in the experiment, thus changing the experimental boundary conditions.

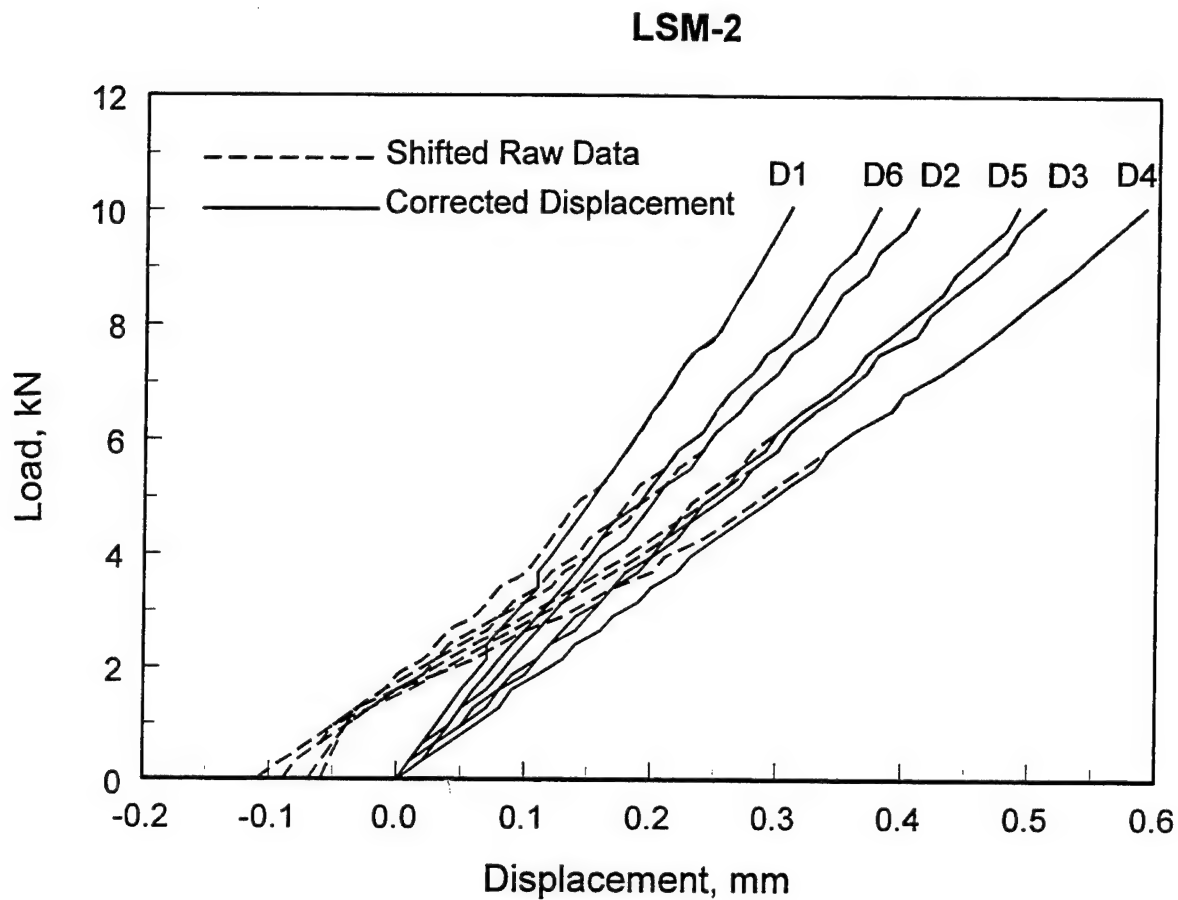


Figure 9.3. Raw and corrected displacements, Experiment LSM-2

Based upon these results it was concluded that all aspects of the finite element model including the density of finite element mesh, the modeling of the load transfer at the joints, and the boundary conditions imposed on the slab by the reaction box were adequate.

Case II

Figure 9.6 shows a diagram of the 3D finite element mesh used to predict the response from Experiments LSM-3R. In plan view the mesh was identical to the mesh employed for Experiment LSM-2. The surface layer consisted of two slabs were separated by a joint, which was modeled using the ABAQUS JOINTC elements. The individual spring stiffnesses

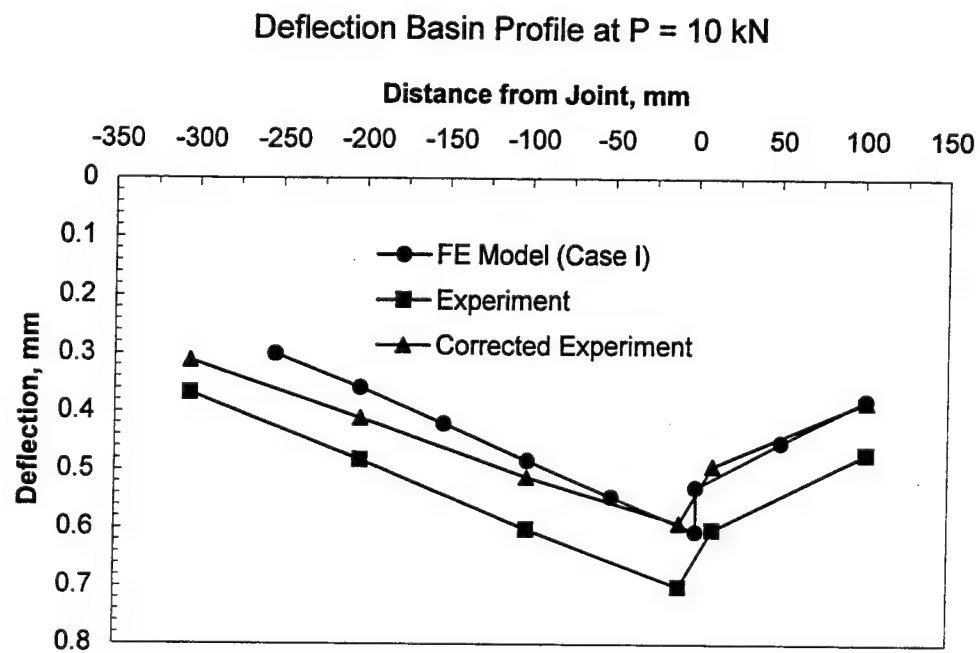


Figure 9.4. Experimental and analytical deflection basin profiles, Experiment LSM-2

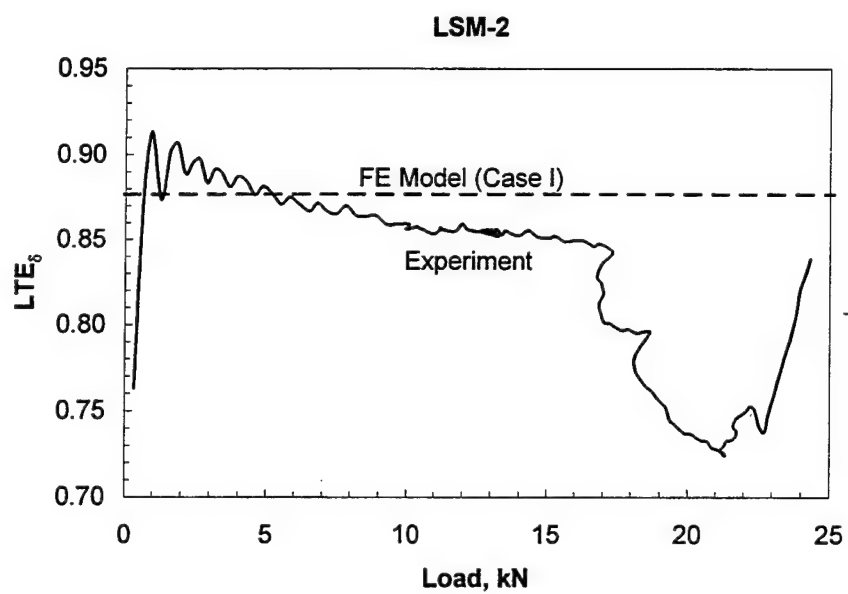


Figure 9.5 Comparison of experimental deflection load transfer efficiency with analytical value, Experiment LSM-2

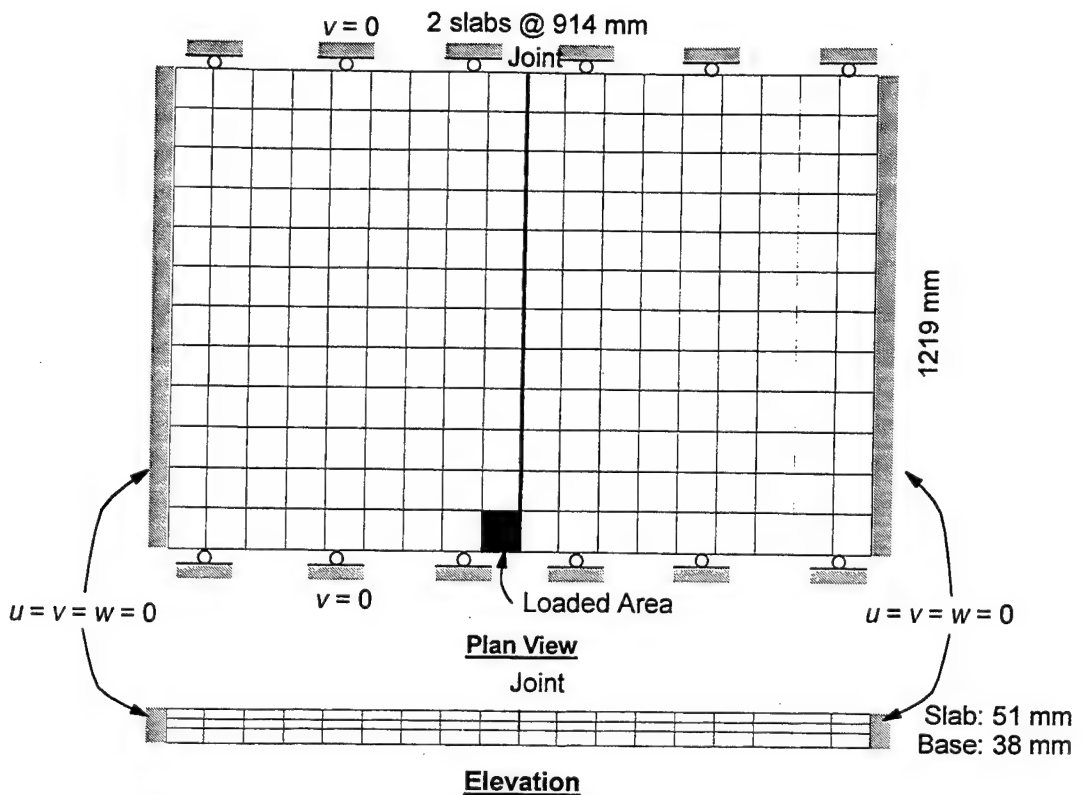


Figure 9.6. Finite element model, Cases II, III, IV, and V

assigned to the JOINTC elements across the joint in the slabs were identical to those employed for the finite element model of Case I (Experiment LSM-2).

The material and structural properties of the slabs and subgrade were identical to those described in Table 9.2. Additional material and structural parameters for the base course are listed in Table 9.3. Two additional structural parameters, used by Kuo (1994) were introduced to describe the structural properties of the base course. The radius of relative stiffness of the base, a parameter related to the relative stiffness of the base and subgrade, defined as follows

$$\ell_b = \frac{E_b}{k(1 - v_b)} \quad (9.1)$$

Table 9.3
Experimental Model Parameters for Base

Parameter	Equation No.	Dimensions	Value
Base Material Parameters			
E_b	--	F/L^2	1,410 MPa (204,000 psi)
v_b	--	--	0.20
h	--	L	0.038 m (1.5 in.)
Base Structural Parameters			
ℓ_b	9.1	L	13.056 m (514 in.)
B	9.2	--	2.903

The base factor includes the structural properties of the base and slab as follows:

$$B = \frac{\sqrt{\ell_b h_b}}{\ell} \quad (9.2)$$

The finite element model was extended in the vertical direction (z-direction) to include the base course. The base course was modeled by a single layer of ABAQUS C3D27R hexahedral elements with aspect ratios of 1:1 in the plane of the base surface and 2.67:1 in the plane of the base thickness. The nodes along the interface between the slab and base were tied so that no delaminations or slip occurred between the slabs and base course. The lower surfaces of the elements in the base course were supported by a bed of springs using the ABAQUS "FOUNDATION" option.

As was the case for the Case I finite element model, the boundary conditions were chosen to match as closely as possible the experimental conditions. The boundary conditions, as indicated in Figure 9.6, were thus the same as those used for Case I.

The results from the finite element model were compared with data from Experiment LSM-3R. Figure 9.7 shows a plot of LTE_δ versus load from Experiment LSM-3R along with the value of LTE_δ predicted from the Case II finite element model at the location of the LVDT array in the experiment. The finite element model predicted almost perfect joint

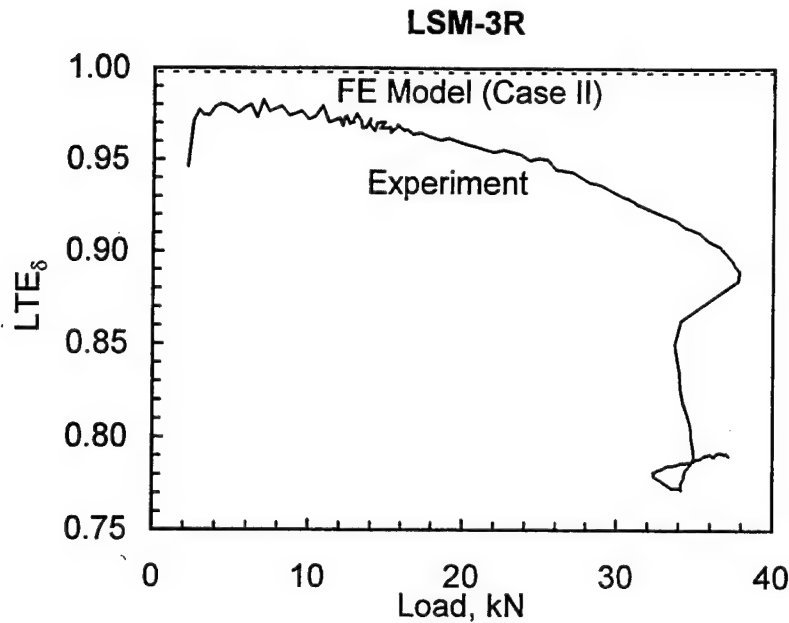


Figure 9.7. Comparison of experimental deflection load transfer efficiency with analytical value, Experiment LSM-3R

efficiency ($LTE_\delta = 0.998$). Figure 9.8 shows the deflection basin profile (raw data, no corrections applied) from Experiment LSM-3R at a load of approximately 10 kN plotted alongside the analytical deflection basin profile for that load. The magnitude of the deflections predicted by the analytical model was less than that observed in the experiment. This discrepancy is due to the boundary conditions imposed on the model, which limited both upward and downward displacement of the slab ends. However, as demonstrated in Figure 8.48, the slabs experienced some downward deflections at their ends which added to the magnitude of the deflections near the joint. However, it is not likely that the joint efficiency was affected.

A second finite element run was made with the Case II model. In this run the stiffness of the joint was decreased by a factor of 100 from $q = 148 \text{ MN/m/m}$ (21,460 lb/in./in.) to $q =$

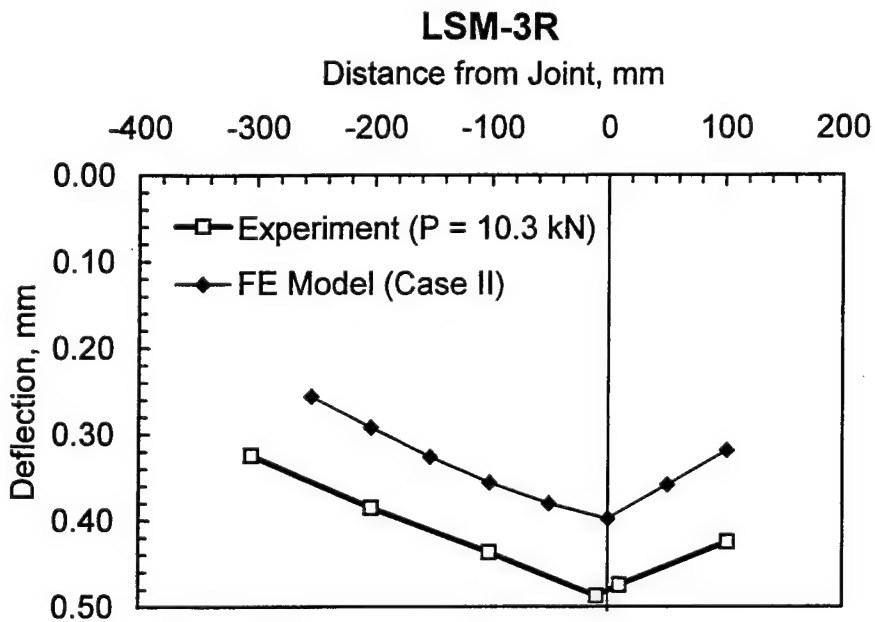


Figure 9.8. Experimental and analytical deflection basin profiles, Experiment LSM-3R

1.48 MN/m/m (214.6 lb/in./in.). As indicated in Figure 9.9, decreasing the stiffness of the joint by two orders of magnitude had little effect on the resulting LTE_{δ} . In Case II the slabs and base were not free to separate. Furthermore, the base was monolithic, and thus the slabs are forced to have equal displacements at the intersection of the joint with the slab/base course interface. Because of this effect, there was essentially no differential movement across the joint. Thus, the magnitude of the stiffness of the JOINTC elements makes virtually no difference, because the differential displacements across the joint are small.

Case III

The finite element model employed for Case III was identical to that employed for Case II with one major exception: a crack with aggregate interlock was present in the base course model. Material and structural properties for the model were identical to those listed in

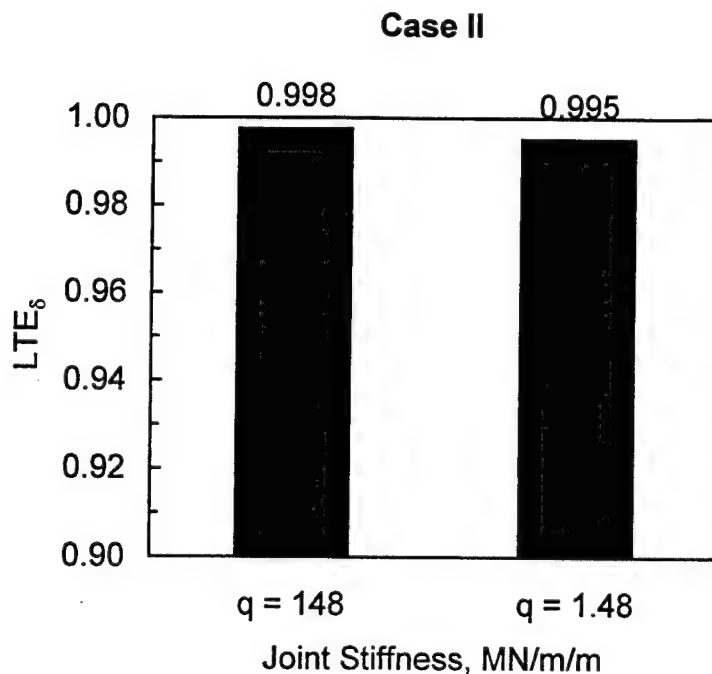


Figure 9.9. Variation of analytical deflection load transfer efficiency with joint stiffness, Case II

Tables 9.1 and 9.3. The stiffness of the joint, q_{joint} , for Case III was identical to that for Cases I and II.

The effect of aggregate interlock in the base course on joint response was investigated. Aggregate interlock across the crack was modeled using ABAQUS JOINTC elements connecting corresponding node pairs across the crack. A range of conditions were modeled varying from the case of an open crack in the base with no load transfer to the case a monolithic base by choosing a spectrum of values of the crack stiffness parameter q_{base} . The individual spring constants (κ) for the joint and base were calculated from the q_{base} and q_{joint} using Equations 7.13 and 7.14.

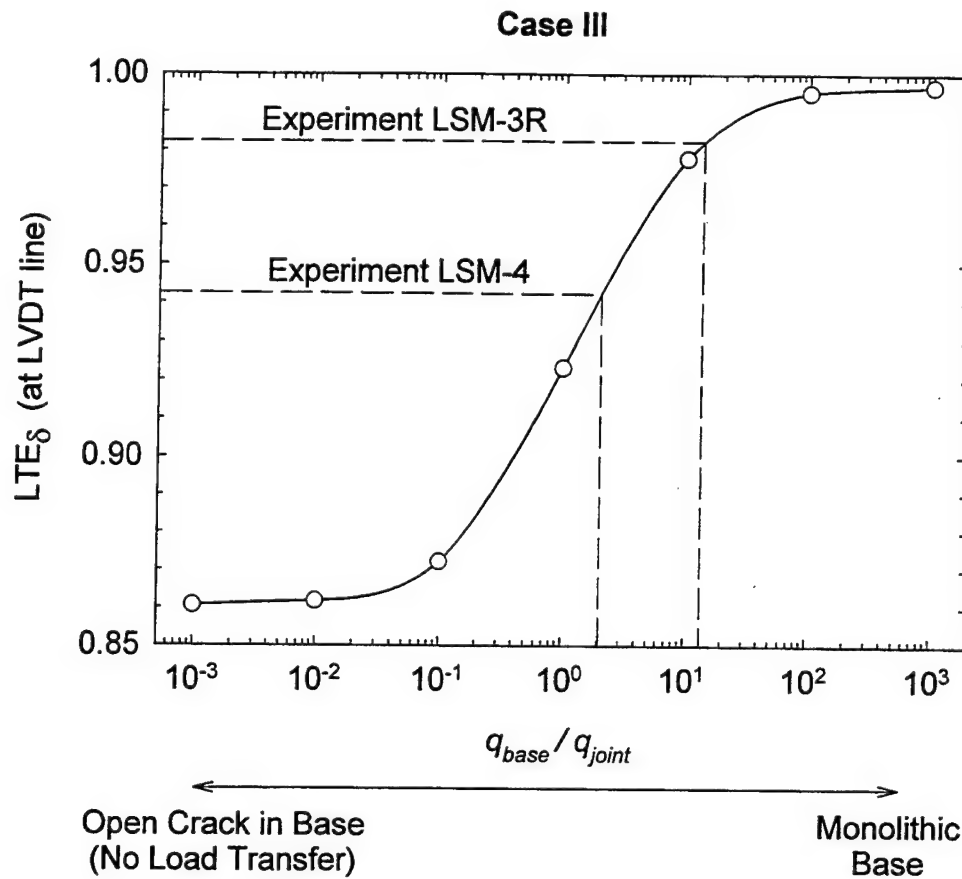


Figure 9.10. Variation of analytical deflection load transfer efficiency with changes in aggregate interlock in cracked base, Case III

The results from these analyses are plotted in Figure 9.10. The horizontal axis is the ratio of q_{base} to q_{joint} , while the vertical axis is LTE_{δ} calculated at the location of the LVDT array in the experimental program. For the case of a doweled joint with no aggregate interlock, q_{joint} is a function of the dowel diameter, dowel spacing, and joint opening. However, q_{base} is an unknown quantity which may approach zero in the case of an open crack (no aggregate interlock) to near infinity in the case of a monolithic base course.

Several important observations can be made concerning the analytical curve in Figure 9.10. Results from the finite element analyses indicate that the amount of load transfer in the base influences the deflection load transfer at the joint. As would be intuitively expected, the deflection load transfer efficiency increases with increasing shear stiffness across the crack in the base course.

The deflection load transfer efficiencies from Experiments LSM-3R and LSM-4 and the predicted q ratio values are indicated by the dashed lines in Figure 9.10. The data from LSM-4 indicates that one would predict that the crack stiffness due to aggregate interlock in the base course was in excess of two times the stiffness of the doweled joint. However, this result is irrational, because the dowels in the slabs should provide more shear stiffness than the aggregate interlock in the base. Similarly, the data from LSM-3R indicates that the experimental deflection load transfer efficiency intersects the curve in a location somewhat below the point predicted for a monolithic base.

The stiffness of the doweled joint can be decomposed into components from shearing action in the dowel, bending action in the dowel, and from direct bearing (or aggregate interlock) across the joint as follows:

$$q_{joint} = q_{dowel\ shear} + q_{dowel\ bending} + q_{aggregate\ interlock} \quad (9.3)$$

Most researchers have concluded that the component due to dowel bending is negligible, particularly for the ranges of joint openings which typically occur in airport pavements. Therefore, the joint stiffness can be thought of as the sum of the components from dowel shear and from aggregate interlock. In the case of the experimental program, the dowel shear component may be calculated directly from the dowel diameter, dowel spacing, and joint opening. Even though the joint opening in the experiments contained a Teflon strip to minimize load transfer due to direct bearing, it is likely that direct bearing made some contribution to the

stiffness of the joint. If direct bearing contributed to the stiffness of the joint, q_{joint} is greater than that calculated from the dowels alone. As q_{joint} increases, the ratio of q_{base} to q_{joint} decreases. Thus, the curve in Figure 9.10 would be translated to the left, as indicated in Figure 9.11. The maximum LTE_δ values from the experiment and the predicted q ratio values from the postulated curve are indicated by dashed lines in Figure 9.11. This postulated shift in the locus of the curve would result in a rational intersection of the experimental data with the analytical curve.

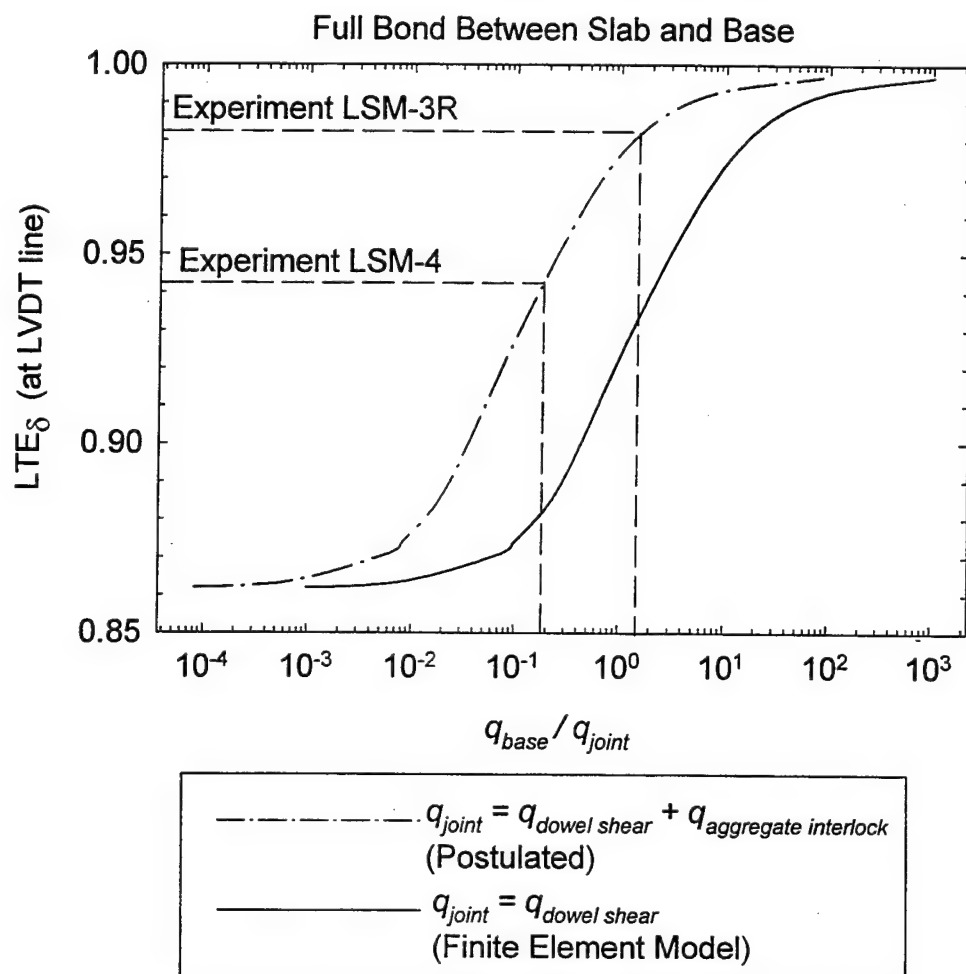


Figure 9.11. Postulated shift in analytical curve due to direct bearing in joint, Case III

Deflection basins from selected Case III runs along the location of the experimental LVDT array are plotted versus the experimental deflection basin profile from Experiment LSM-4 at a load of approximately 10 kN (2,250 lb) in Figure 9.12. The differences in magnitude of deflections between the experiment and the analytical models was likely due to the boundary conditions imposed on the models which limited both upward and downward displacement of the slab ends. However, the experimental evidence, as discussed in Chapter 8, indicated that this condition was not perfectly achieved in the experiment. The deflection on the loaded (left side) of the joint for the case where $q_{base}/q_{joint} = 0.1$ is very nearly the same as the experimental deflection at that location. However, the deflection just across the joint is less than that observed in the experiment. Also note that as the q ratio increases, the ratio of deflections across the joint becomes closer to unity.

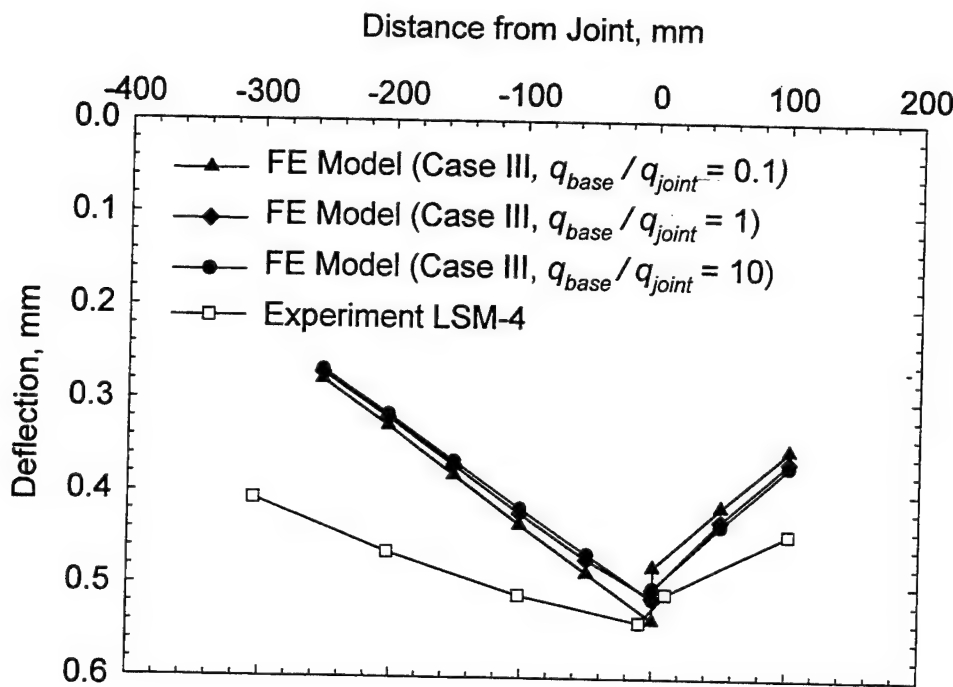


Figure 9.12. Experimental and analytical deflection basin profiles, Experiment LSM-4

Case IV

In Case IV the base was considered to be monolithic. However, the contact interaction feature was implemented between the base course and the slabs allowing slip to occur between the slabs and base as well as allowing gaps to open. Coulomb friction was modeled on the contact surfaces with a range of coefficients of static friction (μ) from 0.1 to 100. A coefficient of friction greater than unity represents a shear stress which is greater than the normal pressure causing the shear stress. This condition, which may not be realistic, is nonetheless instructive to consider as a modeling tool.

Figure 9.13 shows a plot of LTE_{δ} versus μ . The values of LTE_{δ} obtained from these analyses were at least 8 percent less than those for Case II (fully bonded slabs and base, no crack

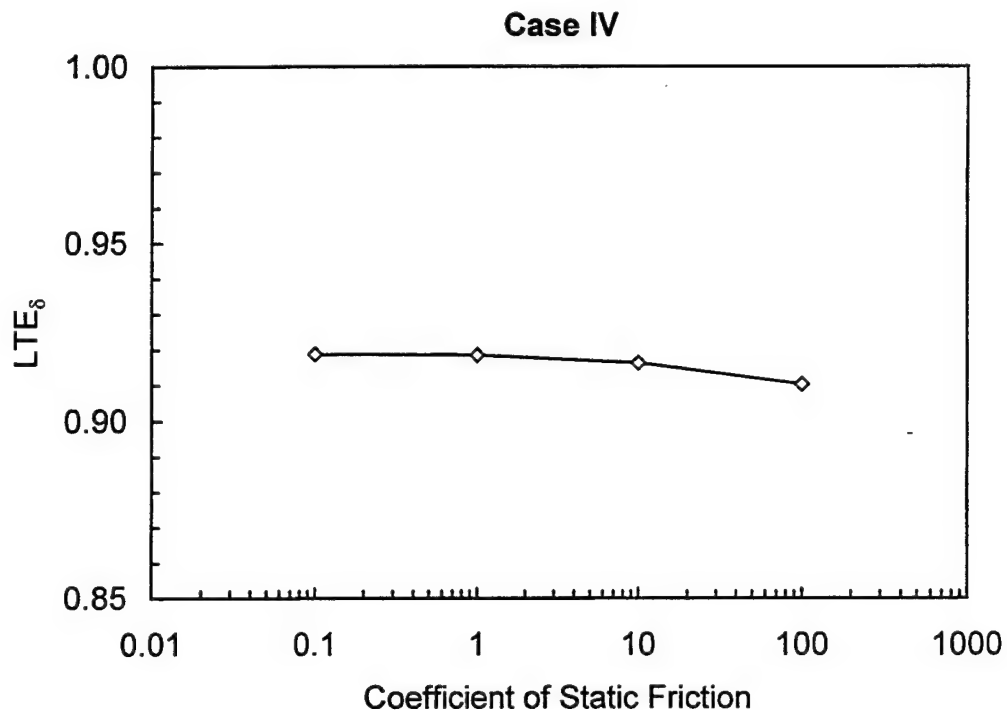


Figure 9.13. Variation of analytical deflection load transfer efficiency with friction between base course and slab, Case IV

in base). Also, there was a trend of decreasing joint efficiency with increasing μ ; however, a less than 1 percent difference in LTE_s was predicted between a μ of 0.1 and 100.

Figure 9.14 shows a plot of the vertical deflection profiles calculated along the edge of the model at the top of the base course and the bottom of the slabs for $\mu = 1$. These curves clearly indicate that gaps were forming between the slabs and base course on both the loaded and unloaded side of the joint. The largest gap was located on the unloaded side of the joint. This response was typical of that predicted across the range of μ studied. Figure 9.15 shows a plot of the gap between the slabs and base course, denoted as Δz , as a function of distance from the joint and friction. Clearly, gaps were present in all cases; the largest gaps occurred

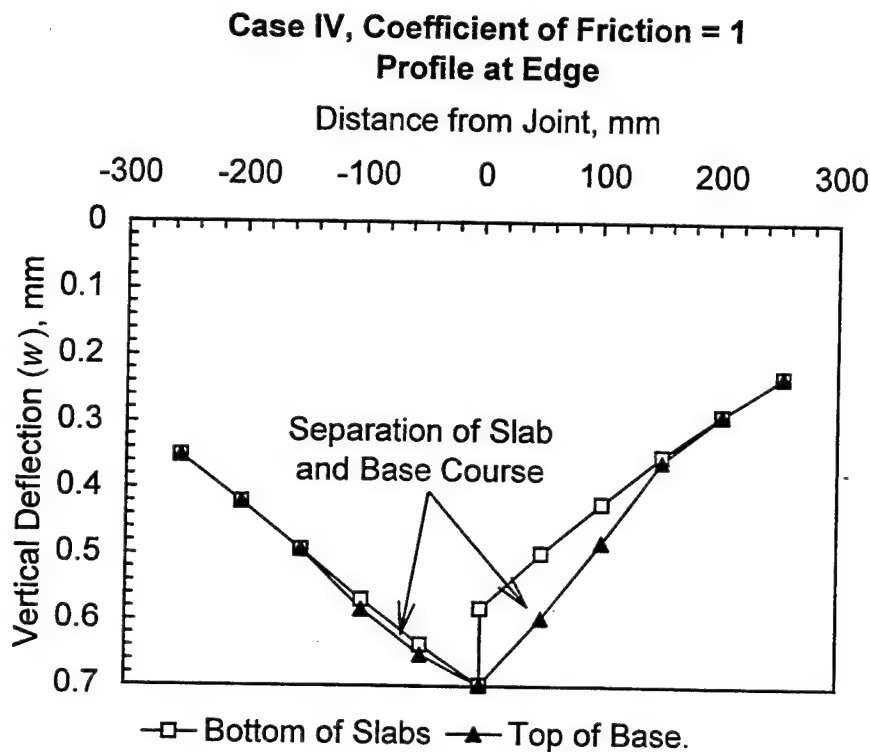


Figure 9.14. Vertical deflection profiles along edge illustrating gap between slab and base, Case IV

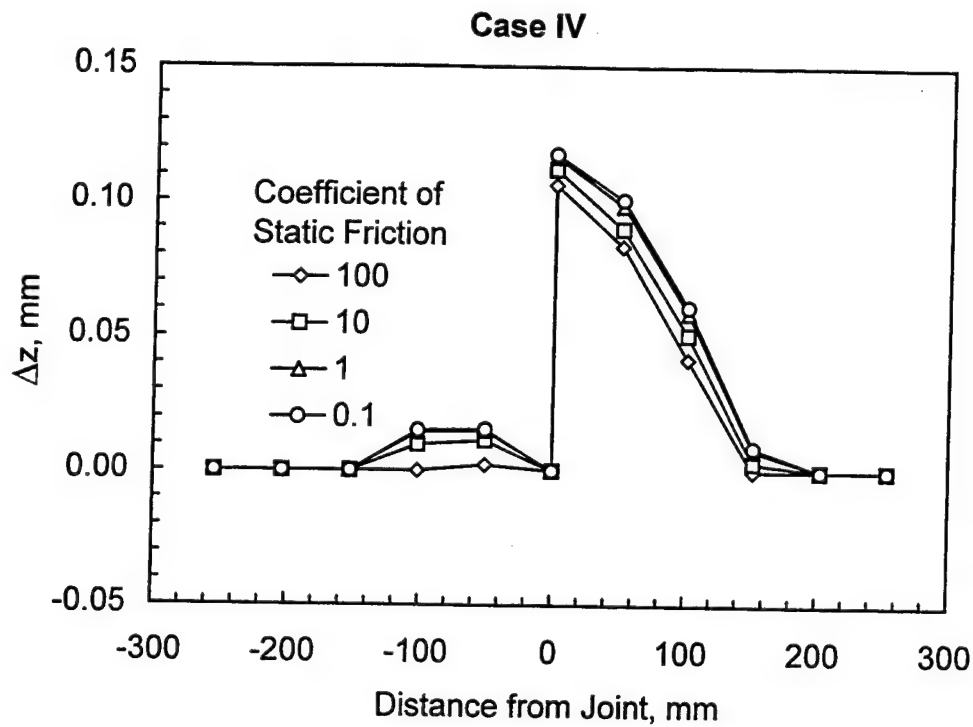


Figure 9.15. Gap opening between slab and base, Case IV

for the lowest value of μ . Because strain compatibility between the slabs and base course was not imposed, and because the slabs and base course have different deflection basin profiles and inflection points, a gap forms between the slab and base course on the loaded side of the joint. The magnitude of the gap opening depends on the degree of shear transfer between the slab and base.

Figure 9.16 shows profiles of the horizontal deformations for selected nodes on the top of the base course and on the bottom of the slab. A positive deformation indicates movement to the right while negative values indicate movement to the left. This plot indicates that the slabs were moving relative to one another. The top of the base was moving right on the loaded side of the joint and left on the unloaded side. Conversely, the loaded side moved

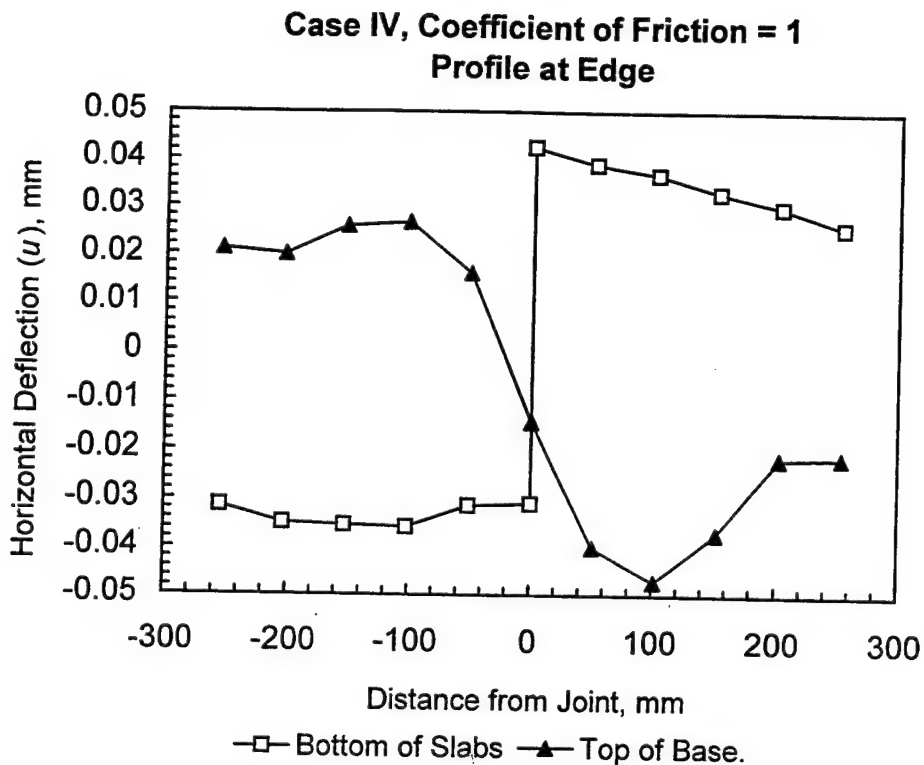


Figure 9.16. Horizontal deflection profiles along edge illustrating slip between slab and base, Case IV

left, while the unloaded slab moved right. The discontinuity between the slabs at the joint shows clearly in this plot. Figure 9.17 shows a plot of differential horizontal movement between the slabs and base as a function of distance from the joint and friction. As expected, the largest differential movements occurred for the lowest value of μ .

Figure 9.18 shows plots of the deflection basin profiles from Cases IV and II compared with the deflection basin profiles from Experiment LSM-5. As was noted for Cases II and III, the differences in magnitude of deflections between the experiment and the analytical models was likely due to the restrictive boundary conditions imposed on the models which

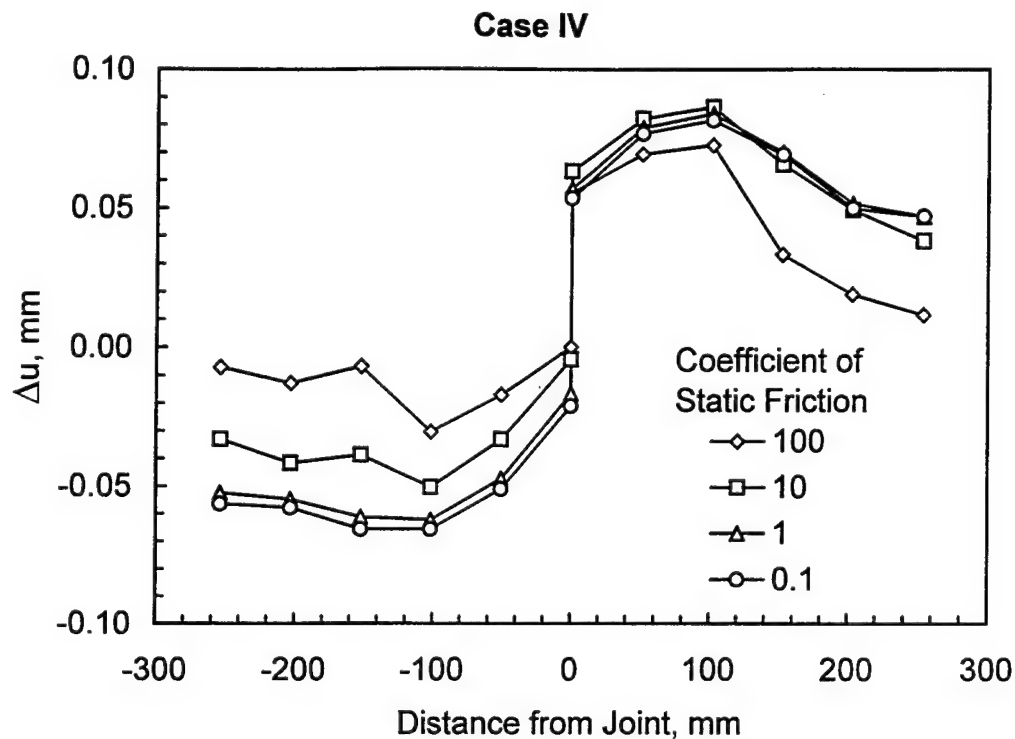


Figure 9.17. Relative slip between slab and base, Case IV

varied somewhat from those of the experiment. It is obvious that the deflection basin from the run with the lowest μ most closely matches that of the experiment.

Case V

Case V was distinguished from the other four cases in that the base course was considered to be cracked with some value of aggregate interlock across the crack, and the base course and slabs were not bonded allowing gaps to form between the slabs and base. Where the slabs and base were in contact, shear stress was transmitted via friction between the slabs and base course.

The joint response over a range of μ and aggregate interlock across the crack in the base are plotted in Figure 9.19. As expected, these results indicate that joint efficiency decreases

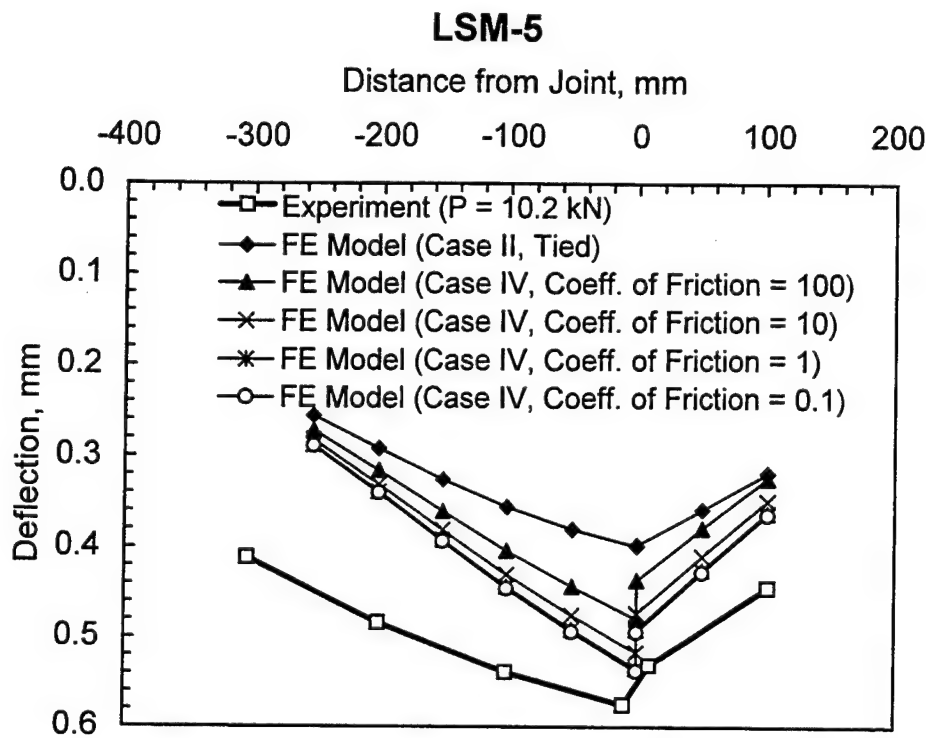


Figure 9.18. Experimental and analytical deflection basin profiles, Experiment LSM-5

as aggregate interlock across the crack in the base decreases. It also indicates that the joint efficiency decreases with increasing values of μ as was found for Case IV. In Figure 9.20, results from the Case III analyses have been plotted along with the results from Case V. It can be seen from Figure 9.20 that allowing gaps to form between the slab and base course tends to flatten the joint response curves and thereby reduces the range of possible joint efficiencies compared to a cracked base.

SLAB/BASE INTERACTION AND JOINT RESPONSE

The analytical results reported in this chapter indicate that a wide range of joint efficiencies are possible from a given joint subjected to a given loading depending on the presence of a stabilized base layer present and:

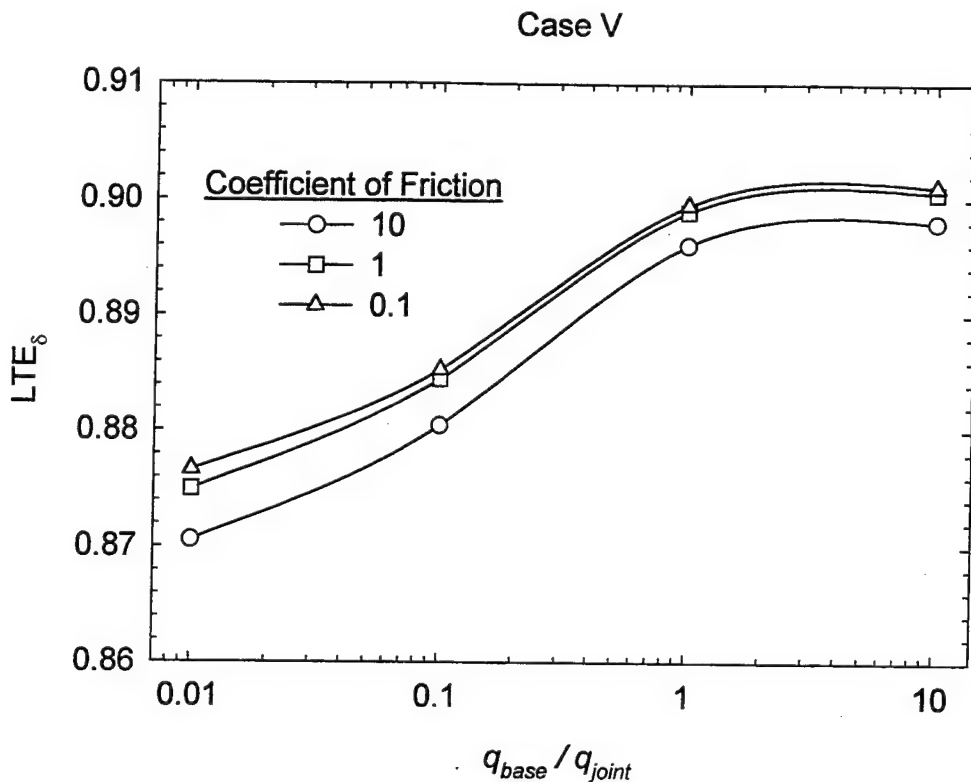


Figure 9.19. Variation of analytical deflection load transfer efficiency with friction between base course and slab and aggregate interlock across crack, Case V

- Is the base cracked below the joint? If so how much load is transferred across the crack by aggregate interlock?
- Are the slabs and base bonded, or can gaps open between the slabs and base? If the slabs and base are not bonded, how much shear stress can be transmitted across the interface by friction?

These effects are illustrated by the bar chart shown in Figure 9.21. This plot compares the calculated joint efficiencies from Cases III, IV, and V. It can be seen from this graph that the case of the monolithic base bonded to the slabs gives nearly perfect joint efficiency. If the monolithic base is cracked the joint efficiency is decreased with a trend of decreasing

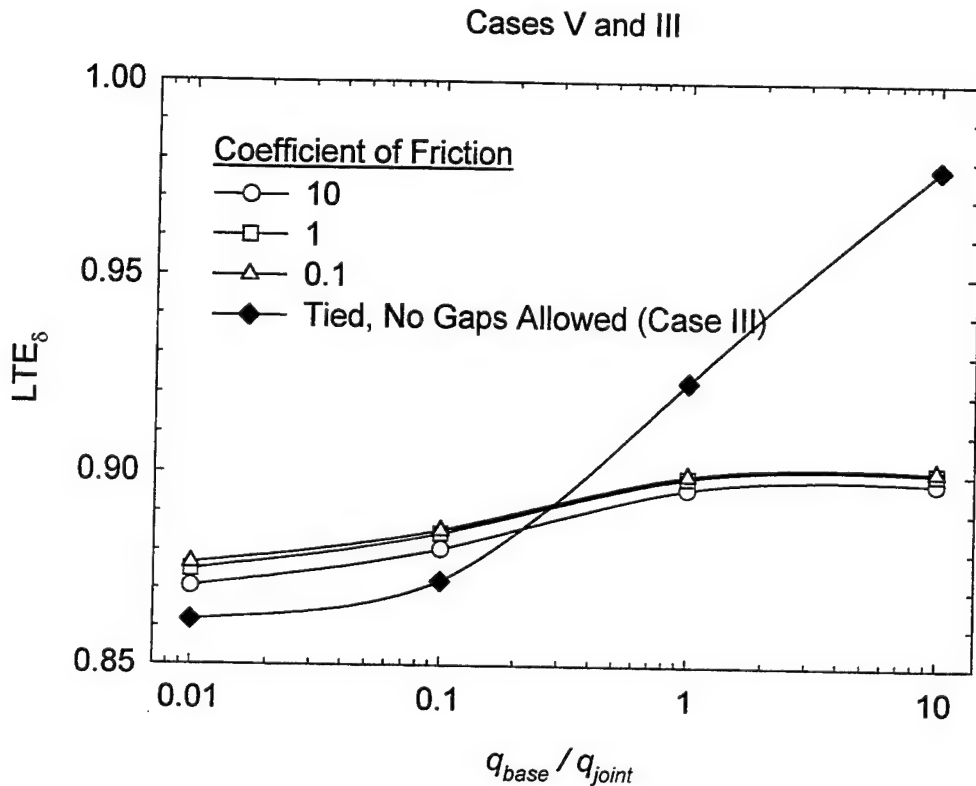


Figure 9.20. Comparison of joint responses from Cases III and V

joint efficiency as the aggregate interlock across the crack decreases. If gaps are allowed to form between the base and slabs, joint efficiency is decreased compared to the bonded cases, and the coefficient of friction between the slabs and base has only a small effect on the load transfer obtained.

Figure 9.22 shows a plot of the maximum load transfer values obtained in the experimental program (Chapter 8) compared with the ranges of values calculated from the analyses described in this chapter. For the analytical data the solid bar represents the lower bound of possible values of LTE_δ , while the error bar represents the upper bound values. In all cases, with the exception of Case IV, the experimental response is within the range of possible

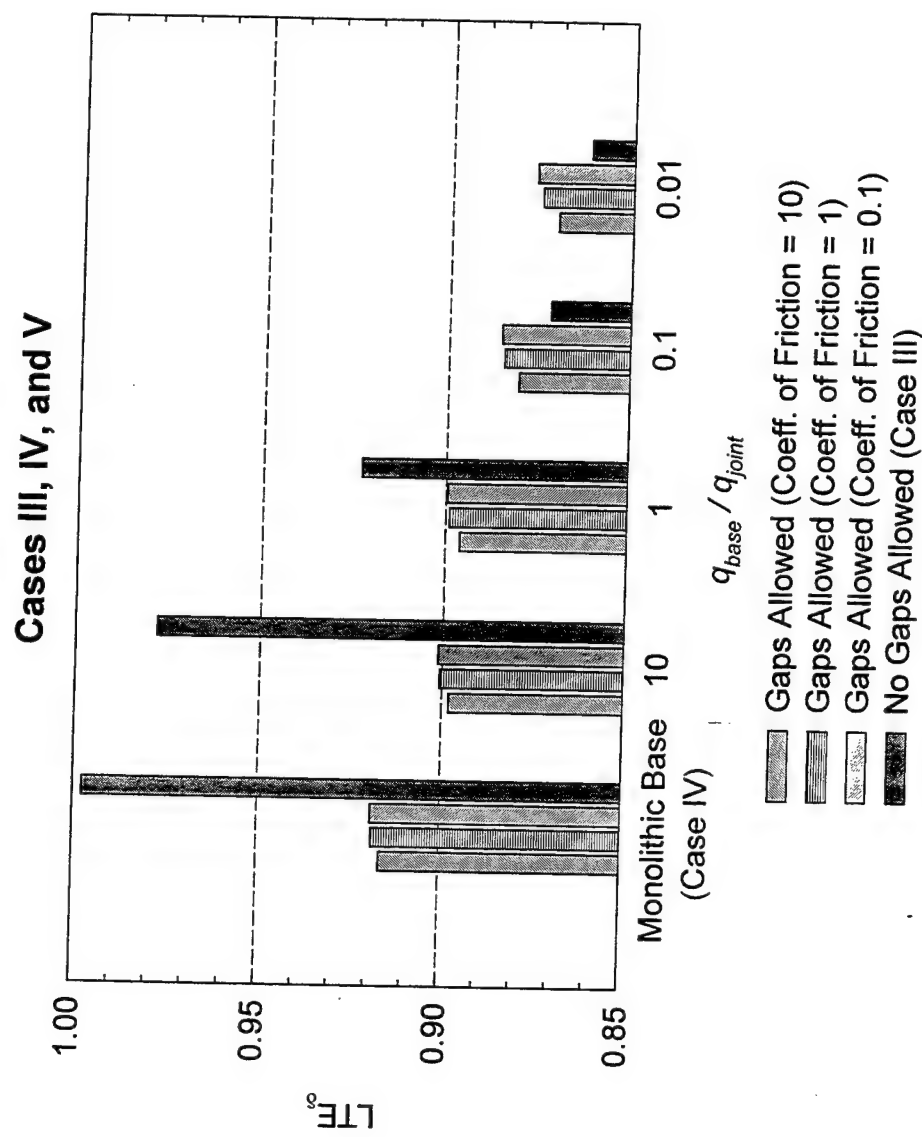


Figure 9.21. Comparison of joint responses from Cases III, IV, and V

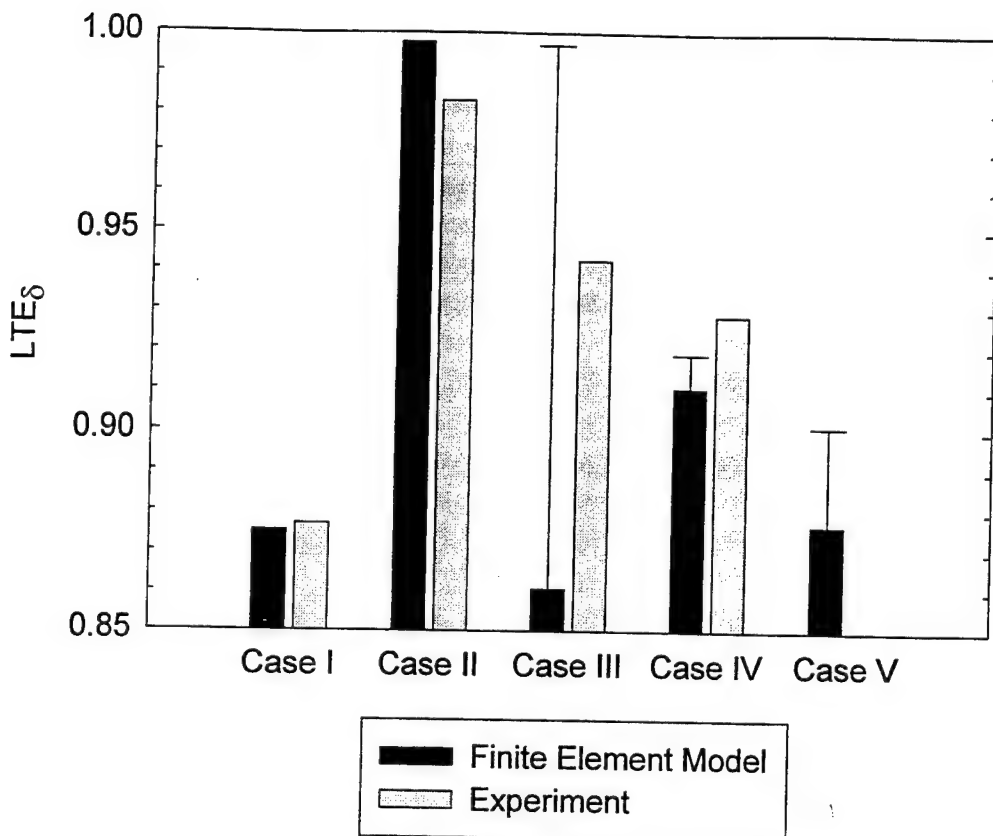


Figure 9.22. Comparison of joint responses from finite element models and experiments

responses predicted by the experiments. This experimental and analytical agreement lend credibility to the validity of the analytical models.

The implications of these responses upon the response and performance of rigid pavements in the field is not explicitly predicted by the analytical model. However, it is possible to discuss in general terms the potential impact. Refer to Figure 9.23. Suppose a particular joint were constructed on a stabilized base such that the base course was initially monolithic and the base and slabs were initially bonded. Over a period of time, here indicated by aircraft departures, repeated cycles of aircraft and/or environmental loading may result in cracking of the base directly beneath the joint. Depending upon the degree of aggregate interlock

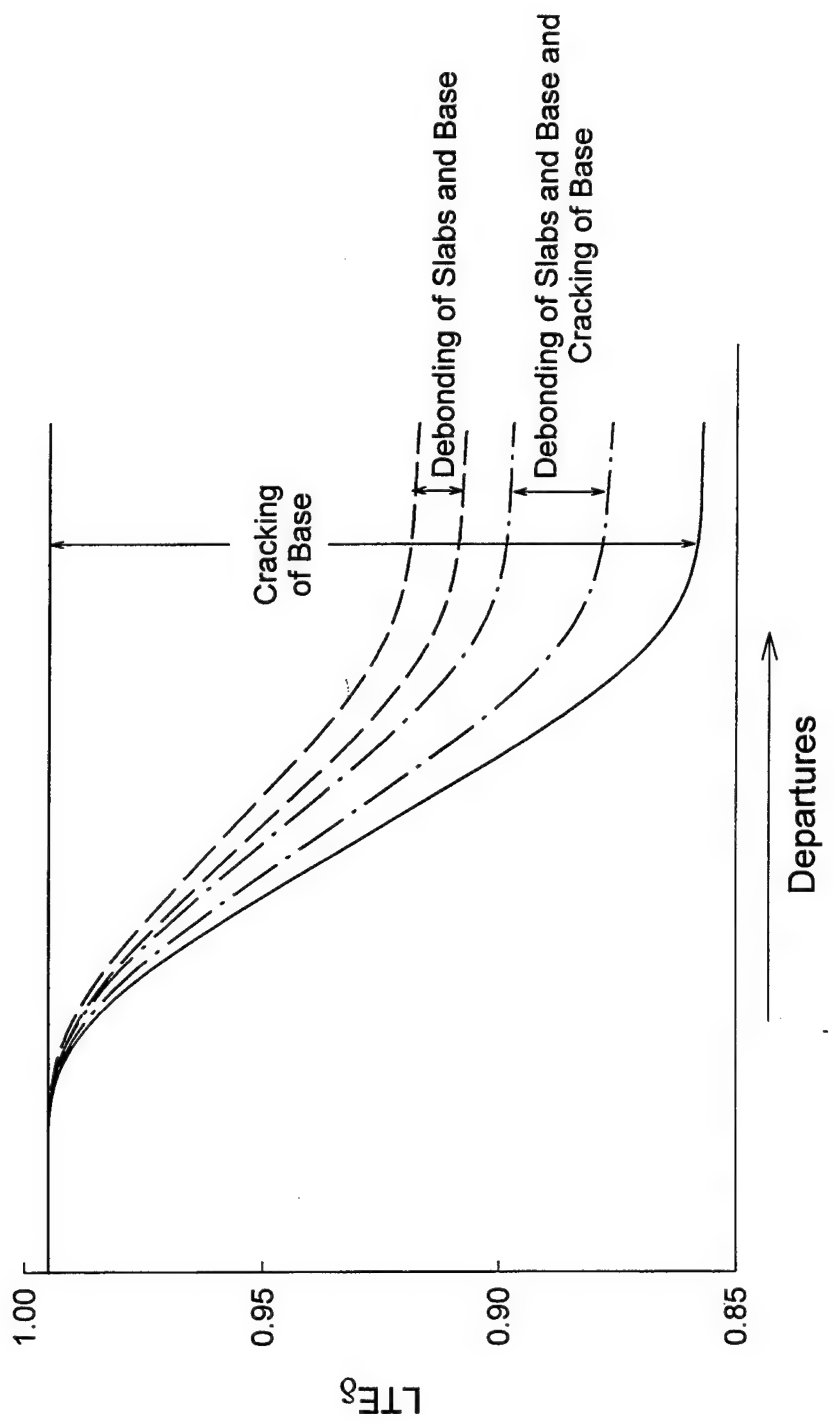


Figure 9.23. Possible implications of slab/base interaction on joint performance

across the crack in the base, the finite element analyses indicated that a range of responses (indicated by the two solid curves in the Figure 9.23) is possible.

Next, suppose that an identical joint were constructed in the same manner. However, in this case suppose that the base and slabs were debonded by repeated cycles of aircraft or environmental loading such that it was possible that gaps could form between the slabs and base in the vicinity of the joint. For the sake of argument suppose that the base were monolithic. The finite element analyses indicate a range of possible responses, depending upon the amount of shear stresses transmitted across the interface by friction, denoted by the dashed curves in Figure 9.23. Note that the range of possible responses is much less than that possible due to cracking of the base.

Finally, suppose that the identical joint were again constructed in the same manner. Now, in this case suppose that aircraft or environmental loadings cause the base to crack beneath the joint and also cause delamination or debonding between the slabs and base. Again the finite element models indicated a range of possible responses plotted as dash-dot curves in Figure 9.23. The range of potential responses is much less than that for the cracked base alone. However, as expected, the efficiency of a joint associated with a cracked and debonded base is predicted to be less than that of the joint associated with a debonded base without a crack.

It should be noted that the exact values of LTE_{δ} obtained in a particular case depend not only on the slab/base interaction factors, but also upon the slab and base geometry, subgrade strength, material properties, and load geometry. Therefore, the values plotted on the vertical axis in Figure 9.23 are intended to be representative values of the LTE_{δ} obtained in these analytical cases.

CHAPTER 10: CONCLUSIONS AND RECOMMENDATIONS

CONCLUSIONS

The response of the rigid pavement slab-joint-base structural system is complex, and accurately predicting the response of such a system requires a significant degree of analytical sophistication. The research reported in this dissertation has defined some features required to adequately model the system and has demonstrated a technique to develop a comprehensive 3D finite element model of the rigid pavement slab-joint-foundation structural system. These findings represent a significant advancement in the state of the art of rigid pavement response modeling. Specifically, the following conclusions can be drawn from this study:

- Analysis of experimental data obtained by the Corps of Engineers in the 1950s confirms the usefulness of the concepts of dimensionless joint stiffness as a means of characterizing the response of the doweled joint. Thus, the response of both the aggregate interlock joint and the doweled joint can be characterized by the same family of curves. Explicit modeling of the dowel in the 3D finite element model, while perhaps useful for research purposes, is unnecessary for predicting the gross response of the structural system. The usefulness of the dimensionless joint stiffness for characterizing the response of the keyed joint was not addressed by this research. The ease of application of the concepts of dimensionless joint stiffness has been increased by the development of closed-form equations (Equations 4.11, 4.12, and 4.13) based upon the theoretical developments of Skarlatos (1949).
- For most practical rigid pavement slabs, the classical Kirchhoff assumptions, adopted by Westergaard and Skarlatos, lead to small errors in predicting edge stresses.

Results from 3D finite element models show that the maximum edge stress does not occur at the edge of the slab but at some finite distance from the edge. Fortunately, the Westergaard edge stress is conservative; the analytical models predict that, for most rigid pavement slabs, the maximum edge stress will occur within 0.1ℓ of the edge of the slab and will be approximately 10 percent less than that predicted by the Westergaard theory.

- Experimental evidence from this research suggests that the joint efficiency is significantly affected by the presence and condition of a stabilized base. The presence of cracking in the base and the degree of bonding between the slabs and stabilized base course influences the structural capacity and load transfer capability of the rigid pavement structure. The greatest experimental values of joint efficiency were obtaining from slabs founded on a monolithic stabilized base followed, in order, by slabs founded on a cracked monolithic base, founded on a monolithic base with a bond breaker, and finally, founded directly on a granular base or on a subgrade. Maximum load transfer efficiency occurs at low loads with decreasing effectiveness for increasing load. This phenomenon is likely caused by localized crushing of the concrete in the region of the dowels as the loads and resulting displacements increase.
- The finite element models developed in this research indicate that a comprehensive 3D finite element modeling technique provides a rational approach to modeling the structural response of the jointed rigid airport pavement system. Modeling features which are required include explicit 3D modeling of the slab continua, load transfer capability at the joint (modeled by springs between the slabs), explicit 3D modeling of the base course continua, aggregate interlock capability across the cracks in the base course (again, modeled by springs across the crack), and contact interaction between

the slabs and base course. The contact interaction model feature must allow gaps to open between the slab and base. Furthermore, where the slabs and base are in contact, transfer of shear stresses across the interface via friction should be modeled.

RECOMMENDATIONS

The following recommendations are drawn from this research:

- Mechanistic design criteria for doweled joints should be developed using the concepts of dimensionless joint stiffness in concert with the closed-form Westergaard-type solution for load transfer in rigid pavements. Given the slab thickness, support conditions, and loading, it is possible to use these developments to establish criteria for dowel diameter and spacing for a critical joint opening. These criteria should then be verified by full-scale testing.
- The concept of the composite or "top of the base" modulus of subgrade reaction ignores the composite action of the slab-stabilized base structural system. This concept should be abandoned in favor of a more realistic model that explicitly includes the structural benefits of the stabilized base. It may be possible to develop improved design criteria which allow a reduction in the thickness of the portland cement concrete surface layer if the increased strength, ductility, and load transfer capabilities provided by the stabilized layer are considered in the structural analysis.
- Certain issues pertaining to the effects on new- and future-generation aircraft and rigid pavement behavior and performance can be addressed by the finite element modeling techniques developed in this research. A research study should be initiated to study the effects of multiple-wheel loadings on the response of jointed rigid pavements.

- For rigid pavements the magnitude of responses due to environmental loadings may be as great as those responses due to traffic loading. Thus, the effects of environmental factors on the findings of this research should be investigated. It should be possible to add to the analytical complexity of this research by superimposing the effects of temperature and moisture gradients on the response of the rigid pavement structure. With the tools presented in this study, it is possible to develop and implement an algorithm which could change the joint efficiency with joint opening.
- The 3D finite element model developed as a part of this study is limited to linear elastic material behavior, yet fracture and nonlinear material response clearly controls failure of the rigid pavement system. Future model developments should include more sophisticated material models. For example fracture mechanics concepts should be employed to study the effects of repeated traffic loading on the slabs and cement-stabilized base course. Furthermore, a micro-mechanics approach should be implemented to model localized damage in the vicinity of the dowel-concrete interface.
- The results of this study point to some critical issues which should be considered by the FAA in developing test plans for its full-scale, instrumented test facility currently under construction. Specifically, instrumentation should be installed to detect the presence of cracking in the stabilized base course, particularly directly beneath the joint. Also, instrumentation should be selected and installed to detect the presence of gaps between the slabs and base course.
- The incremental finite element analysis procedure used to solve the contact interaction problem can be computer intensive. In the event that solution times and memory requirements exceed the available computer resources, the slabs can be modeled by thick plate or shell elements with little sacrifice in accuracy. However, the capability

to predict load transfer across cracks in the base course and debonding between the slabs and base are critical and must be retained.

REFERENCES

- Ahlvin, R. G. 1971. "Multiple-Wheel Heavy Gear Load Pavement Tests," AFWL-TR-70-113, Vol. I. Kirtland Air Force Base: Air Force Weapons Laboratory.
- Ahlvin, R. G. 1991. "Origin of Developments for the Structural Design of Pavements," Technical Report GL-91-26. Vicksburg, MS: U.S. Army Engineer Waterways Experiment Station.
- American Concrete Institute. 1994. State-of-the-Art Report on Soil Cement. ACI 230.1R-90, *Manual of Concrete Practice*, Vol. 1. Detroit: American Concrete Institute.
- Barker, W. R. and C. R. Gonzalez. 1991. "Pavement Design by Elastic Layer Theory," *Aircraft/Pavement Interaction: An Integrated System*. New York: American Society of Civil Engineers, pp. 21-43.
- Bathe, K. J. 1982. *Finite Element Procedures in Engineering Analysis*. Englewood Cliffs, NJ: Prentice-Hall, Inc.
- Behrmann, R. M. 1966. "Small-Scale Model Study to Determine the Effects of Sawkerfs and Bored Recesses of Load-Carrying Capacity of Rigid Pavement," Technical Report No. 4-38. Cincinnati: Ohio River Division Laboratories.
- Behrmann, R. M. 1972. "Small-Scale Static Load Model Study: Behavior of Rigid Pavement Loaded Near the Edge," Technical Report No. S-4. Champaign, IL: Construction Engineering Research Laboratory.
- Burns, C. D. 1971. "Multiple-Wheel Heavy Gear Load Pavement Tests," AFWL-TR-70-113, Vol. II. Kirtland Air Force Base: Air Force Weapons Laboratory.
- Carlton, P. F. and R. M. Behrmann. 1956. "A Model Study of Rigid Pavement Behavior Under Corner and Edge Loadings," *Proceedings, Highway Research Board*, No. 35. Washington: Highway Research Board, pp. 139 - 146.
- Channakeshava, C., F. Barzegar, and G. Z. Voyiadjis. 1993. "Nonlinear FE Analysis of Plain Concrete Pavements with Dowel Joints," *Journal of Transportation Engineering*, Vol. 119, No. 5, pp. 763-781.
- Chatti, K. 1992. "Dynamic Analysis of Jointed Concrete Pavements Subjected to Moving Transient Loads," PhD dissertation. Berkeley: University of California at Berkeley.
- Chou, Y. T. 1981. "Structural Analysis Computer Programs for Rigid Multicomponent Pavement Structures with Discontinuities: WE\$LIQID and WESLAYER." Technical Report GL-81-6. Vicksburg, MS: U.S. Army Engineer Waterways Experiment Station.

- Corps of Engineers. 1954. "A Model Study of the Effect of High Contact Pressures on Stresses in Rigid Pavements." Mariemont, OH: Ohio River Division Laboratories.
- Corps of Engineers. 1962. "Small Scale Model Studies of Prestressed Rigid Pavements for Military Airfields, Part I, Development of the Model and Results of Exploratory Tests," Technical Report 4-13. Cincinnati: Ohio River Division Laboratories.
- Corps of Engineers. 1963. "Small Scale Model Studies of Prestressed Rigid Pavements for Military Airfields, Part II, Single-Wheel Loadings on Pre-tensioned and Post-tensioned Slabs," Technical Report 4-25. Cincinnati: Ohio River Division Laboratories.
- Crawford, J. E. and M. G. Katona. 1975. "State-of-the-Art for Prediction of Pavement Response," Contract Report S-75-8. Vicksburg, MS: U.S. Army Engineer Waterways Experiment Station.
- Darter, M. I., K. T. Hall, and C. H. Kuo. 1995. "Support Under Portland Cement Concrete Pavements," National Cooperative Highway Research Program Report 372, Washington: National Academy Press.
- Desai, C. S. and J. F. Able. 1972. *Introduction to the Finite Element Method*. New York: Van Nostrand Reinhold Company.
- Department of the Army. 1987. "Materials Testing." FM 5-530. Washington: Headquarters, Department of the Army.
- Departments of the Army and the Air Force. 1988. "Rigid Pavement Design for Airfields: Elastic Layered Method," Army TM 5-825-3-1 and Air Force AFM 88-6, Chapter 3, Section A. Washington: Headquarters, Departments of the Army and the Air Force.
- Departments of the Army and the Air Force. 1989. "Flexible Pavement Design for Airfields: Elastic Layered Method," Army TM 5-825-2-1 and Air Force AFM 88-6, Chapter 2, Section A. Washington: Headquarters, Departments of the Army and the Air Force.
- Federal Aviation Administration. 1989. "Standards for Specifying Construction of Airports." Advisory Circular 150/5370-10A. Washington: Department of Transportation.
- Federal Aviation Administration. 1995. "Airport Pavement Design for the Boeing 777 Airplane," Advisory Circular No. 150/5320-16. Washington: Federal Aviation Administration.
- Fagan, M. J. 1992. *Finite Element Analysis*. Essex, UK: Longman Scientific and Technical.
- Friberg, B. F. 1940. "Design of Dowels in Transverse Joints of Concrete Pavements," *Transactions of the American Society of Civil Engineers*, Vol. 105, pp. 1076-1095.

- Grinter, L. E. 1931. "Design of Reinforced Concrete Road Slabs," Bulletin No. 39. College Station, TX: Texas Engineering Experiment Station.
- Grogan, W. P., C. A. Weiss, Jr., and R. S. Rollings. 1996. "Stabilized Base Courses for Advanced Pavement Design Report 1: Literature Review and Field Performance Data." DOT/FAA/CT-96/XX. Atlantic City: FAA Technical Center.
- Huang, Y. H. 1993. *Rigid Pavement Analysis and Design*. Englewood Cliffs, NJ: Prentice-Hall, Inc.
- Hutchinson, R. L. 1966. "Basis for Rigid Pavement Design for Military Airfields," Miscellaneous Paper No. 5-7. Cincinnati: Ohio River Division Laboratories.
- Ioannides, A. M. 1984. "Analysis of Slabs-On-Grade for a Variety of Loading and Support Conditions," PhD Dissertation. Urbana, IL: University of Illinois.
- Ioannides, A. M., M. R. Thompson, and E. J. Barenberg. 1985. "Westergaard Solutions Reconsidered," *Transportation Research Record* 1043. Washington: Transportation Research Board, pp. 13-23.
- Ioannides, A. M., M. R. Thompson, J. Donnelly, and E. J. Barenberg. 1986. "Three-Dimensional Finite Element Analysis of a Slab on Stress Dependent Elastic Solid Foundation." Urbana, IL: University of Illinois.
- Ioannides, A. M., Y. H. Lee, and M. I. Darter. 1990. "Control of Faulting Through Joint Load Transfer Design," *Transportation Research Record* No. 1286. Washington: Transportation Research Board, pp. 49-56.
- Ioannides, A. M. and G. T. Korovesis. 1990. "Aggregate Interlock: A Pure-Shear Load Transfer Mechanism," *Transportation Research Record* 1286. Washington: Transportation Research Board, pp. 14-24.
- Ioannides, A. M. and G. T. Korovesis. 1992. "Analysis and Design of Dowelled Slab-on-Grade Pavement Systems," *Journal of Transportation Engineering*, Vol 118, No. 6, pp. 745-768.
- Ioannides, A. M. 1994. "Concrete Pavement Backcalculation using ILLI-BACK 3.0," *Nondestructive Testing of Pavements and Backcalculation of Moduli*, STP 1198, Vol. 2. Philadelphia: American Society for Testing and Materials, pp. 103-124.
- Ioannides, A. M. and M. I. Hammons. 1996. "A Westergaard - Type Solution for the Load Transfer Problem," *Transportation Research Record* 1525. Washington: Transportation Research Board, pp. 28-34.
- Kerr, A. D. 1964. "Elastic and Viscoelastic Foundation Models," *Journal of Applied Mechanics*, Vol. 31, No. 3.
- Kerr, A. D. 1965. "A Study of a New Foundation Model," *Acta Mechanical*, Vol. I/2.

- Kerr, A. D. 1993. "Mathematical Modeling of Airport Pavements," *Airport Pavements Innovations: Theory to Practice*. New York: American Society of Civil Engineers, pp. 31-45.
- Khazanovich, L. and A. M. Ioannides. 1993. "Finite Element Analysis of Slabs-On-Grade Using Higher Order Subgrade Models," *Airport Pavements Innovations: Theory to Practice*. New York: American Society of Civil Engineers.
- Korovesis, G. T. 1990. "Analysis of Slab-On-Grade Pavement Systems Subjected to Wheel and Temperature Loadings," PhD Dissertation. Urbana, IL: University of Illinois.
- Kuo, C. M. 1994. "Three-Dimensional Finite Element Analysis of Concrete Pavement," PhD Dissertation. Urbana, IL: University of Illinois.
- Kushing, J. W., and W. O. Fremont. 1940. "Design of Load Transfer Joints in Concrete Pavements," *Proceedings, Highway Research Board*, No. 20. Washington: Highway Research Board, pp. 481-493.
- Larralde, J. and W. F. Chen. 1985. "Computer Model for Analysis of Rigid Pavements with Fatigue," *Proceedings, Third International Conference on Concrete Pavement Design and Rehabilitation*. West Lafayette, IN: Purdue University.
- Ledbetter, R. H. 1971a. "Multiple-Wheel Heavy Gear Load Pavement Tests," AFWL-TR-70-113, Vol. IIIA. Kirtland Air Force Base: Air Force Weapons Laboratory.
- Ledbetter, R. H. 1971b. "Multiple-Wheel Heavy Gear Load Pavement Tests," AFWL-TR-70-113, Vol. IIIB. Kirtland Air Force Base: Air Force Weapons Laboratory.
- Majidzadeh, K., G. H. Ilves, and R. McComb. 1981. "Mechanistic Design of Rigid Pavements," *Proceedings, Second International Conference on Concrete Pavement Design*. West Lafayette, IN: Purdue University.
- Mellinger, F. M. and P. F. Carlton. 1955. "Application of Models to Design Studies of Concrete Airfield Pavements," *Proceedings, Highway Research Board*, No. 34. Washington: Highway Research Board, pp. 57-64.
- Nishizawa, T., T. Fukuda, and S. Matsumo. 1989. "A Refined Model of Dowelled Joints for Concrete Pavement Using FEM Analysis," *Proceedings, Fourth International Conference on Concrete Pavement Design*. West Lafayette, IN: Purdue University.
- Packard, R. G. No date. "Computer Program for Airport Pavement Design." Skokie, IL: Portland Cement Association.
- Pickett, G. and G. K. Ray. 1951. "Influence Charts for Concrete Pavements," *Transactions of the American Society of Civil Engineers*, Vol. 116, pp. 49-73.

- Pickett, G., M. E. Rayville, W. C. Jones, and F. J. McCormick. 1951. "Deflections, Moments, and Reactive Pressures for Concrete Pavements," Kansas State College Bulletin No. 65. Manhatten KS: Kansas State College.
- Rollings, R. S. 1989. "Developments in the Corps of Engineers Rigid Pavement Design Procedure," *Proceedings, Fourth International Conference on Concrete Pavement Design and Rehabilitation*. West Lafayette, IN: Purdue University, pp. 405-418.
- Rollings, R. W. and D. W. Pittman. 1992. "Field Instrumentation and Performance Monitoring of Rigid Pavements," *Journal of Transportation Engineering*, Vol 118, No. 3, pp. 361-370.
- Sale, J. P., and R. L. Hutchinson. 1959. "Development of Rigid Pavement Design Criteria for Military Airfields," *Journal of the Air Transport Division*, Vol. 85, No. AT3, pp. 129-151.
- Sale, J. P. 1977. "Rigid Pavement Design for Airfields," *Proceedings, First International Conference on Concrete Pavement Design*. West Lafayette, IN: Purdue University, pp. 3-18.
- Schnobrich, W. C. 1990. "Structural Analysis, Part 2. Continua: The Finite Element Method," In *Structural Engineering Handbook*, Third Edition, E. H. Gaylord, Jr. and C. N. Gaylord, ed., New York: McGraw-Hill.
- Skarlatos, M. S. 1949. "Deflections and Stresses in Concrete Pavements of Airfields with Continuous Elastic Joints." Mariemont, OH: Ohio River Division Labs.
- Tabatabaie, A. M. 1978. "Structural Analysis of Concrete Pavement Joints," PhD Dissertation. Urbana, IL: University of Illinois.
- Tayabji, S. D. and B. E. Colley. 1984. "Analysis of Jointed Concrete Pavements," Report No. FHWA/RD-86/041. McClean, VA: Federal Highway Administration.
- Tia, M., J. M. Armaghani, C. Wu, and K. L. Toye. 1987. "FEACONS III Computer Program for Analysis of Jointed Concrete Pavements," *Transportation Research Record No 1136*. Washington: Transportation Research Board.
- Timoshenko, S. and J. M. Lessels. 1925. *Applied Elasticity*. Pittsburgh: Westinghouse Technical Night School Press.
- Timoshenko, S. and S. Woinowsky-Krieger. 1959. *Theory of Plates and Shells*. New York: McGraw-Hill Book Company.
- Wesevich, J. W., McCullough, B. F., and Burns, N. H. 1987. "Stabilized Subbase Friction Study for Concrete Pavements." Research Report 459-1. Austin, Texas: Center for Transportation Research, University of Texas at Austin.

- Westergaard, H. M. 1923. "Om Beregning Af Plader Paa Elastisk Underlag Med Særligt Henblik Pass Ppørgsmalet Om Spændinger I Betonveje," *Ingeniøren*, No. 42, pp. 513-524. (In Danish).
- Westergaard, H. M. 1926. "Stresses in Concrete Pavements Computed by Theoretical Analysis," *Public Roads*, Vol. 7, No. 2, pp. 25-35.
- Westergaard, H. M. 1928. "Spacing of Dowels," *Proceedings*, Highway Research Board, No. 8. Washington: Highway Research Board, pp. 154-158.
- Westergaard, H. M. 1933. "Analytical Tools for Judging Results of Structural Tests of Concrete Pavements," *Public Roads*, Vol. 14, No. 10, pp. 129-151.
- Westergaard, H. M. 1939. "Stresses in Concrete Runways of Airports," *Proceedings, Highway Research Board No. 19*. Washington: National Research Council, pp. 197-205.
- Westergaard, H. M. 1948. "New Formulas for Stresses in Concrete Pavements of Airfields," *Transactions, American Society of Civil Engineers*, Vol. 113, pp. 425-444.
- Zaghoul, S. and T. White. 1993. "Non-Linear Dynamic Analysis of Concrete Pavements," *Proceedings, Fifth International Conference on Concrete Pavement Design and Rehabilitation*, Vol. 1. West Lafayette, IN: Purdue, University, pp. 277-292.
- Zienkiewicz, O. C. and Y. K. Cheung. 1967. *The Finite Element Method of Structural and Continuum Mechanics*. London: McGraw-Hill Publishing Company Limited.

APPENDIX A
STRAIN PLOTS FROM 1950S MODEL TESTS

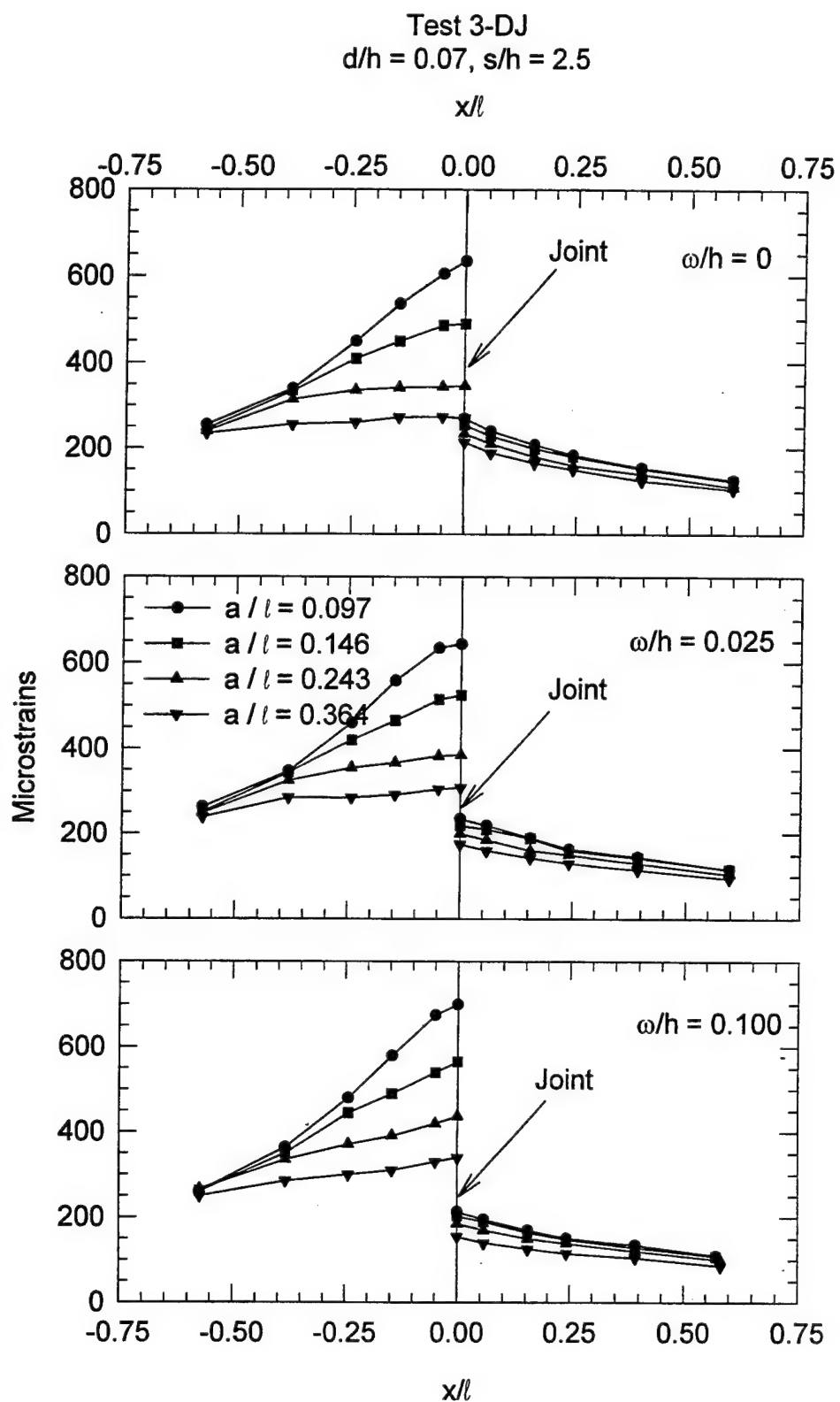


Figure A-1. Test 3-DJ

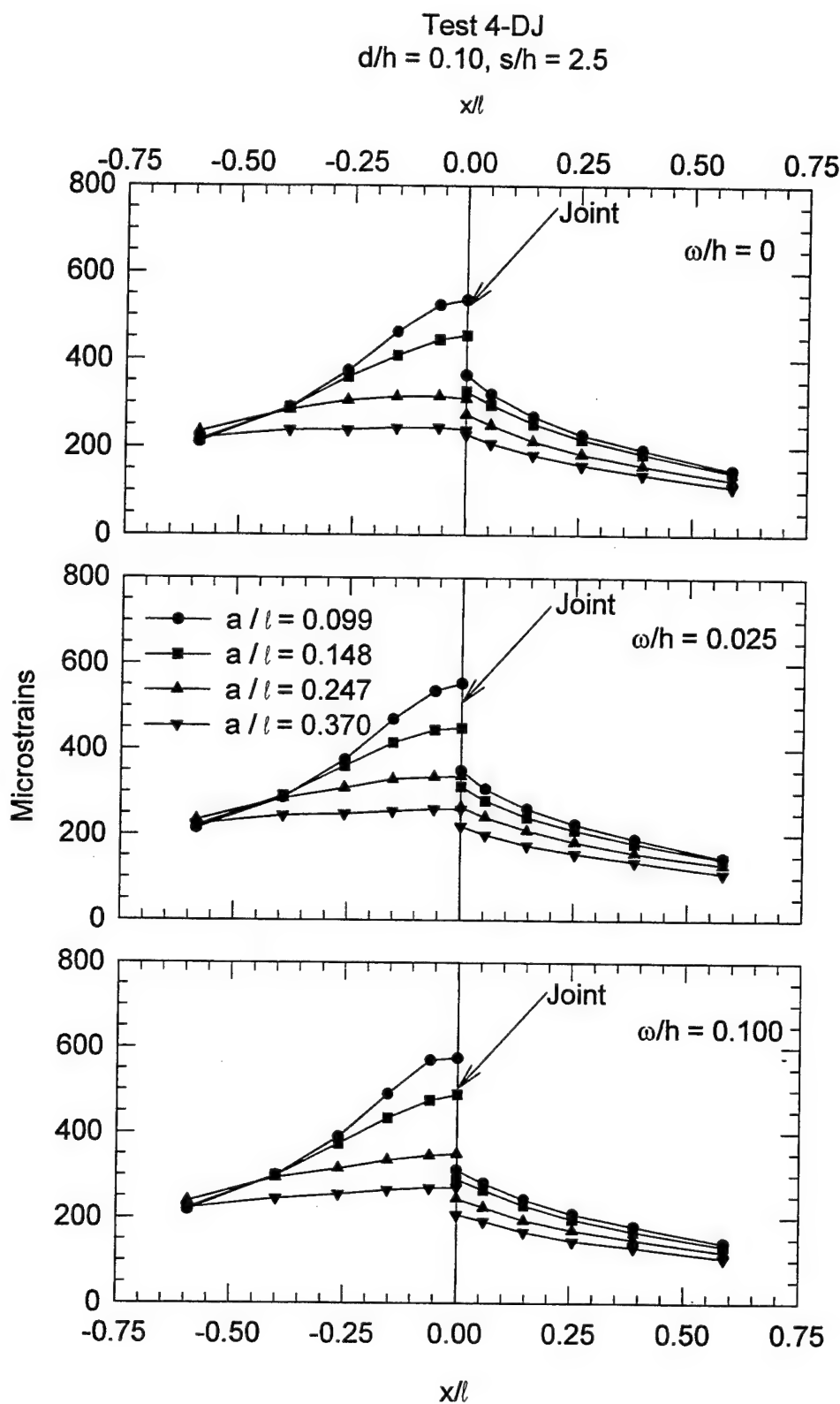


Figure A-2. Test 4-DJ

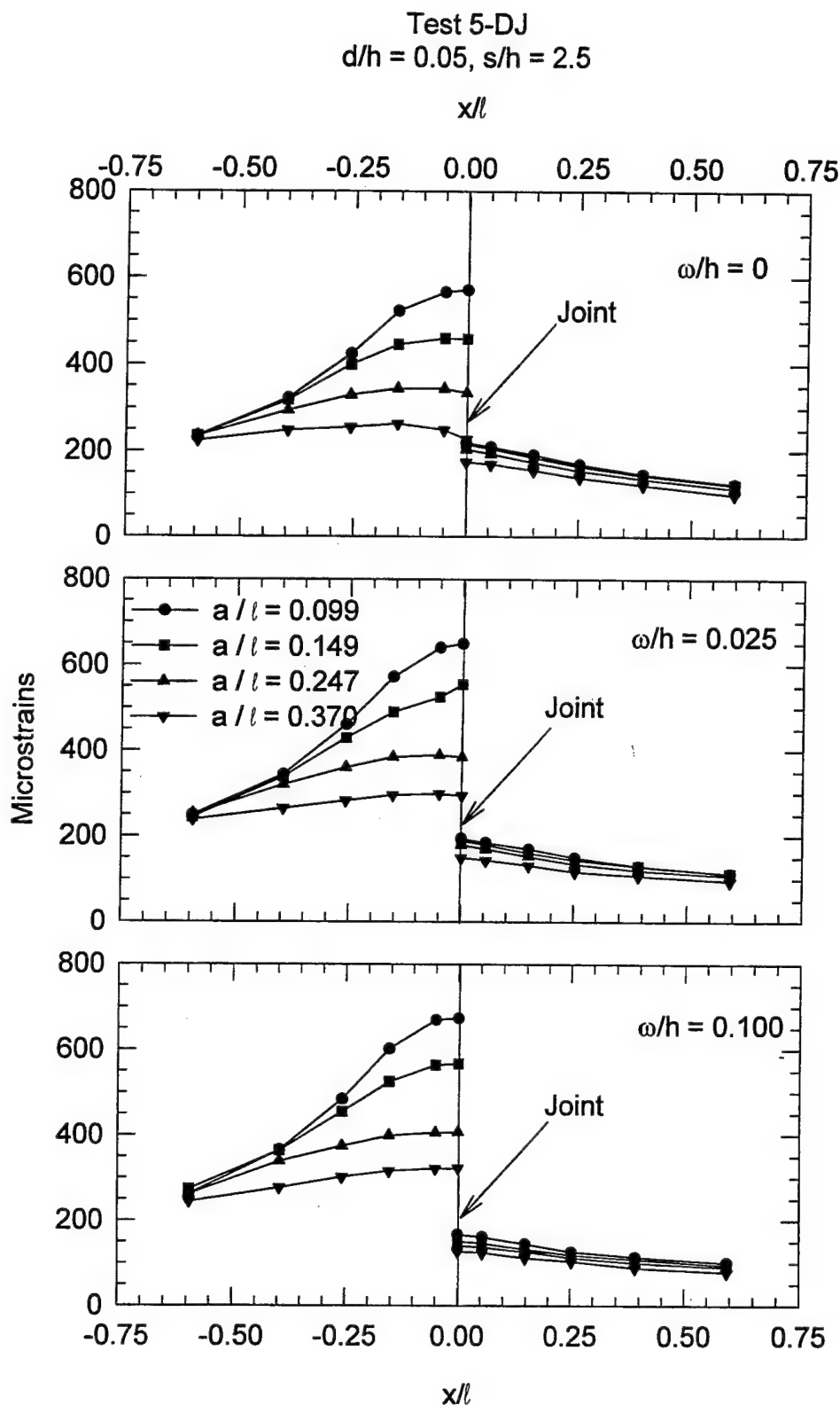


Figure A-3. Test 5-DJ

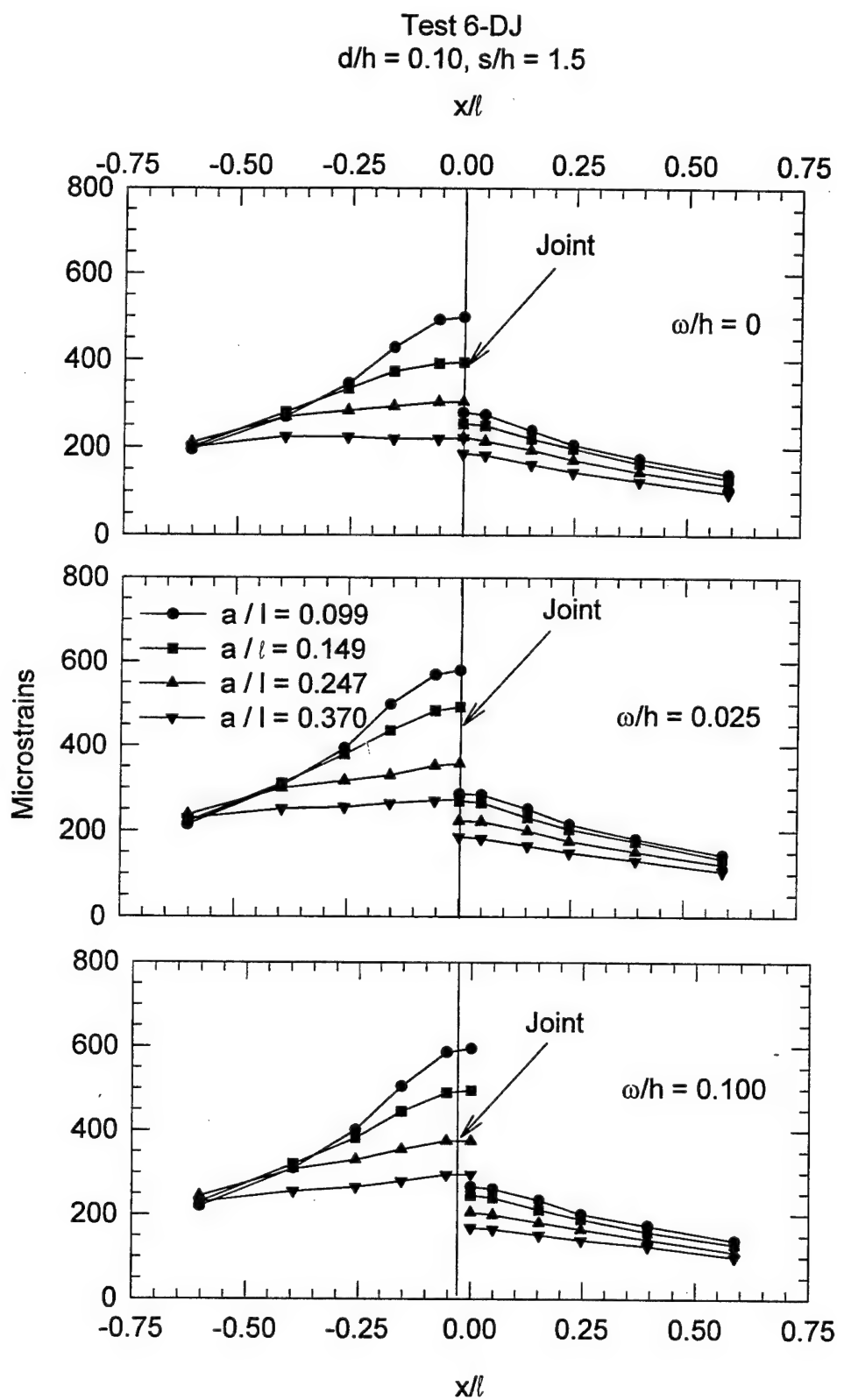


Figure A-4. Test 6-DJ

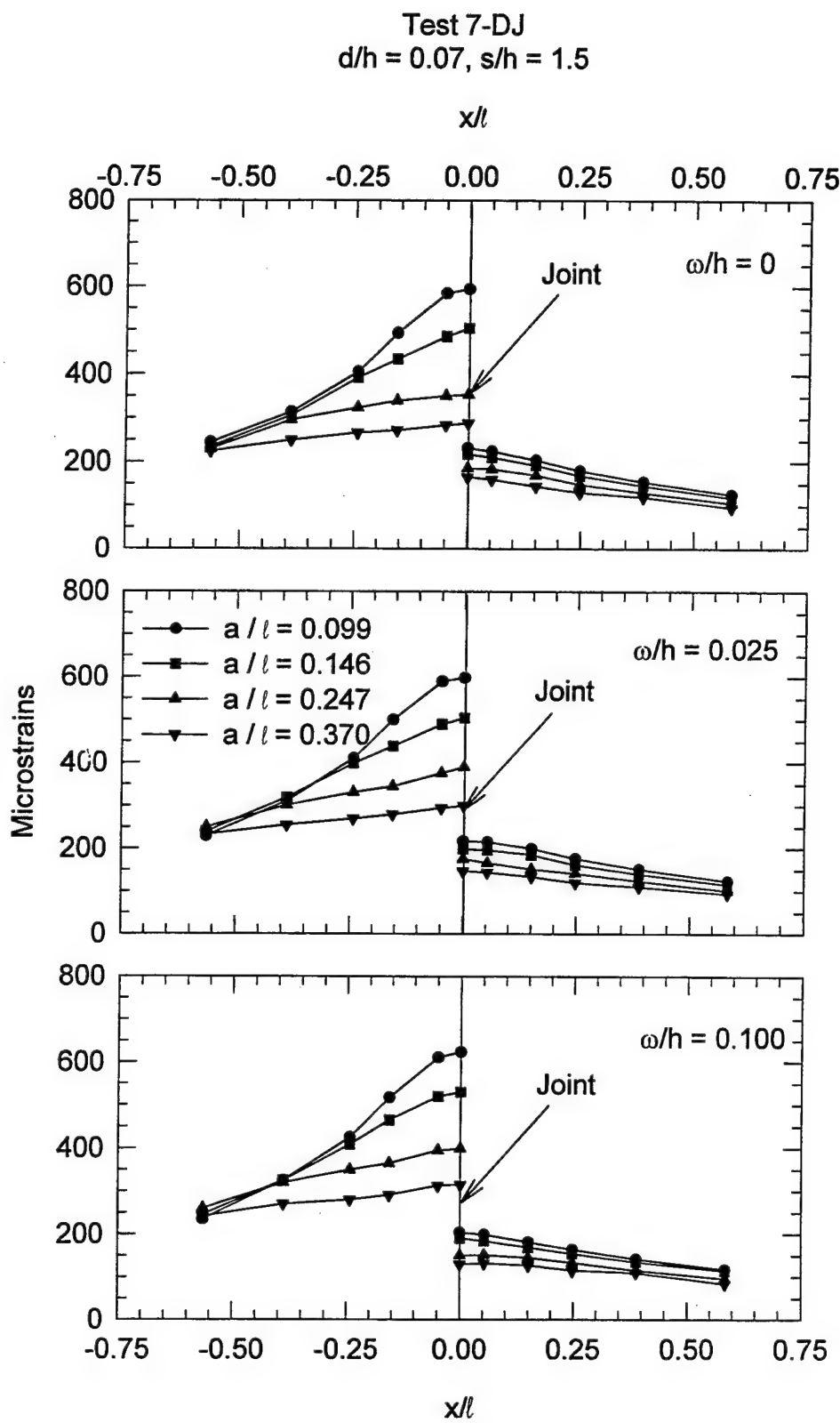


Figure A-5. Test 7-DJ

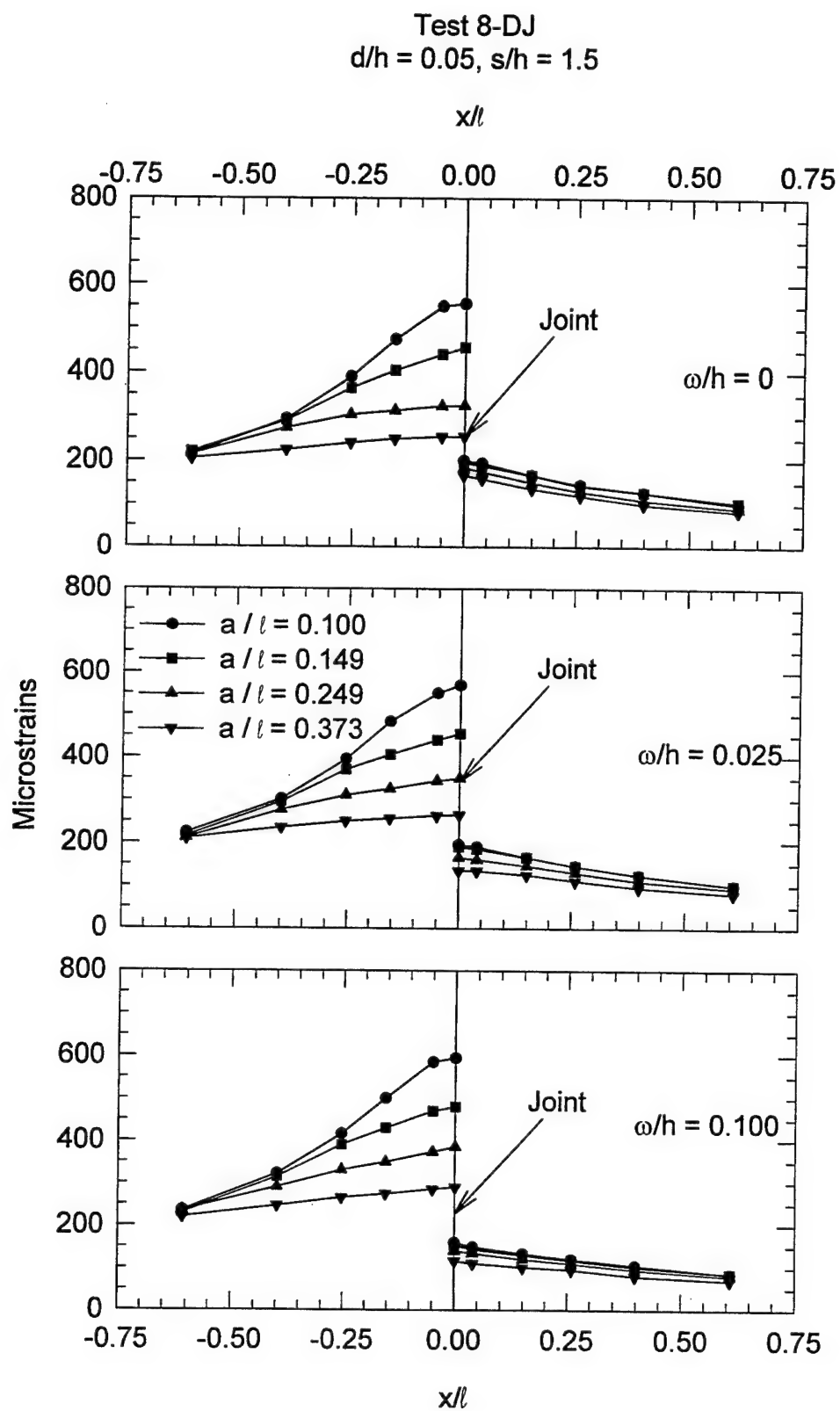


Figure A-6. Test 8-DJ

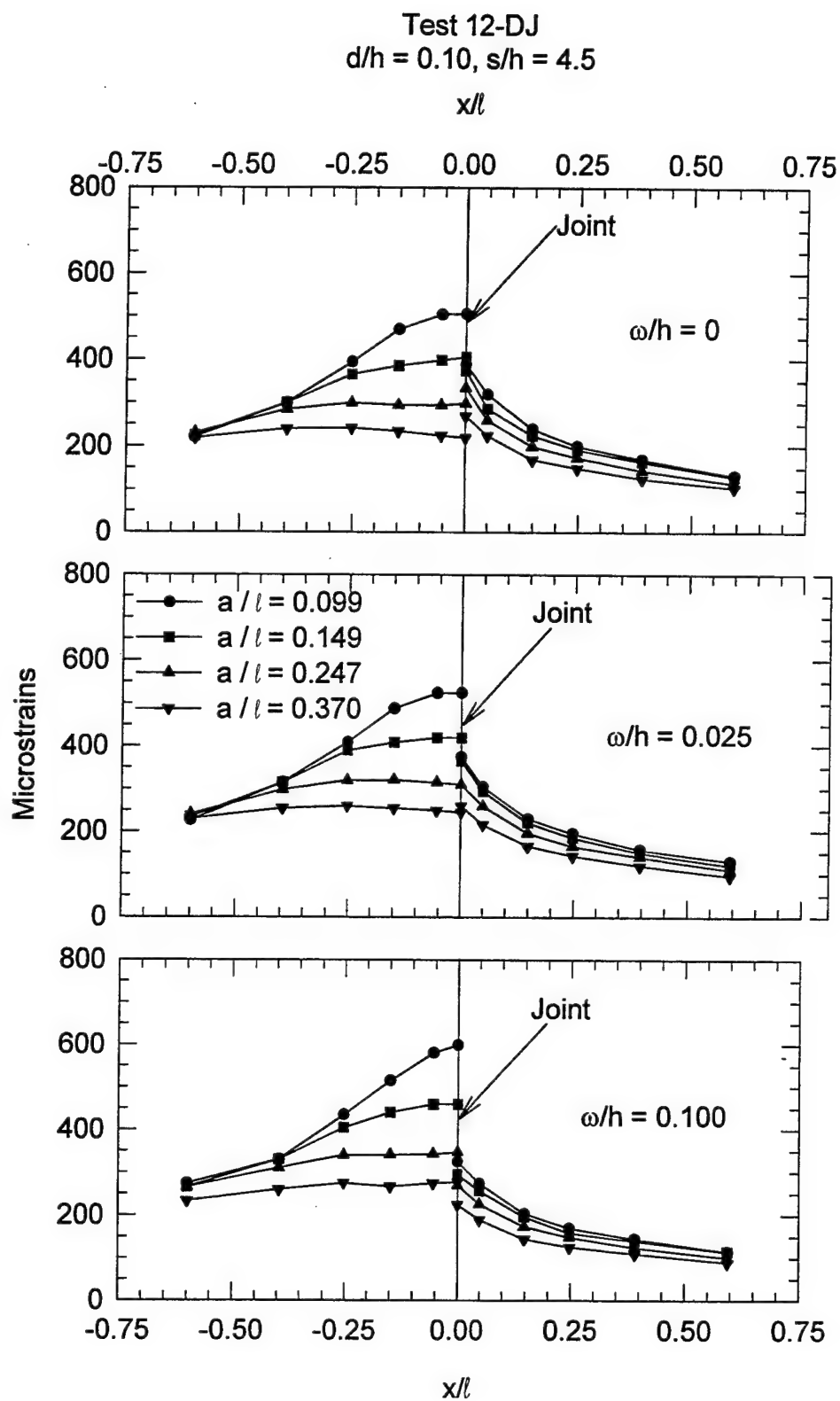


Figure A-7. Test 12-DJ

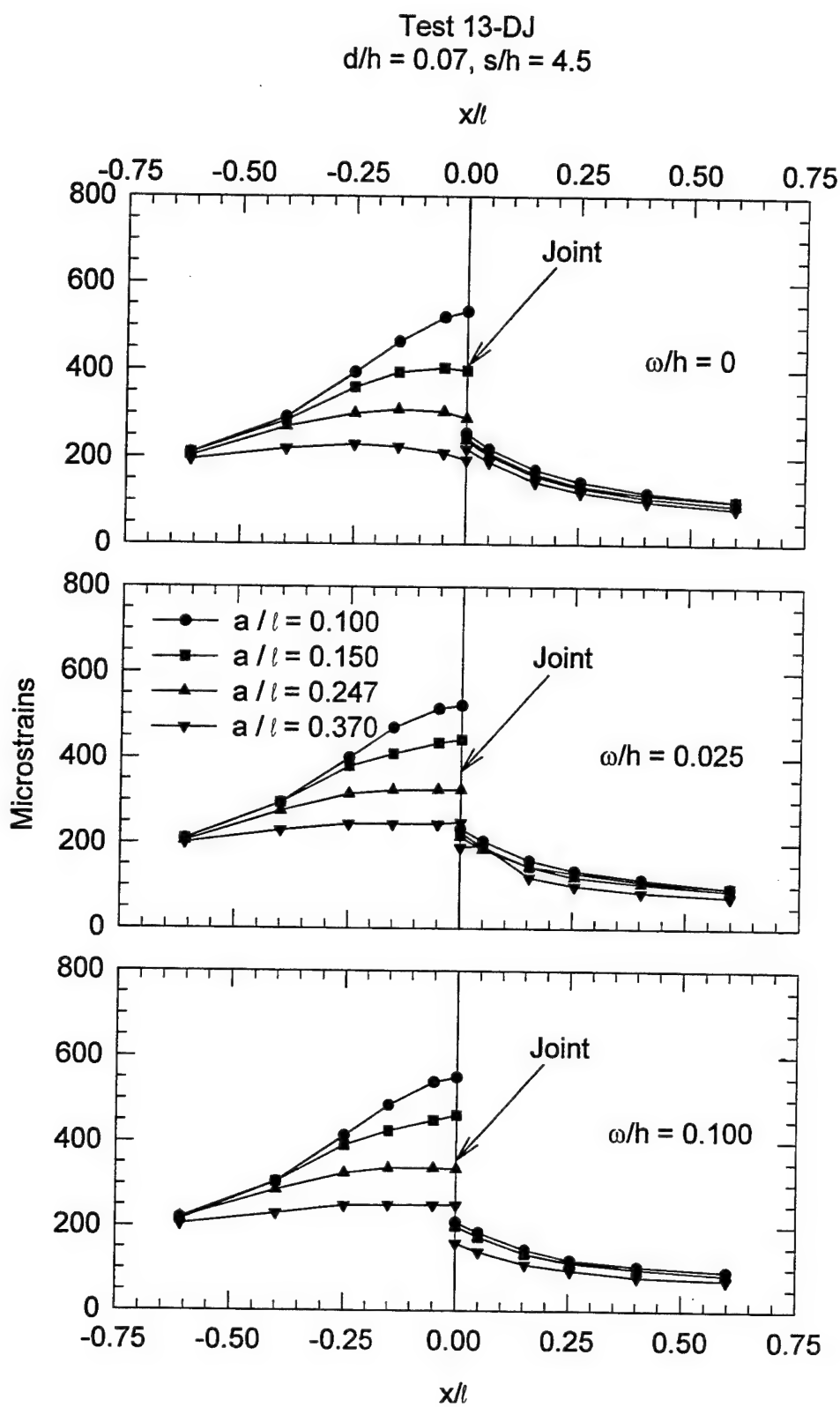


Figure A-8. Test 13-DJ

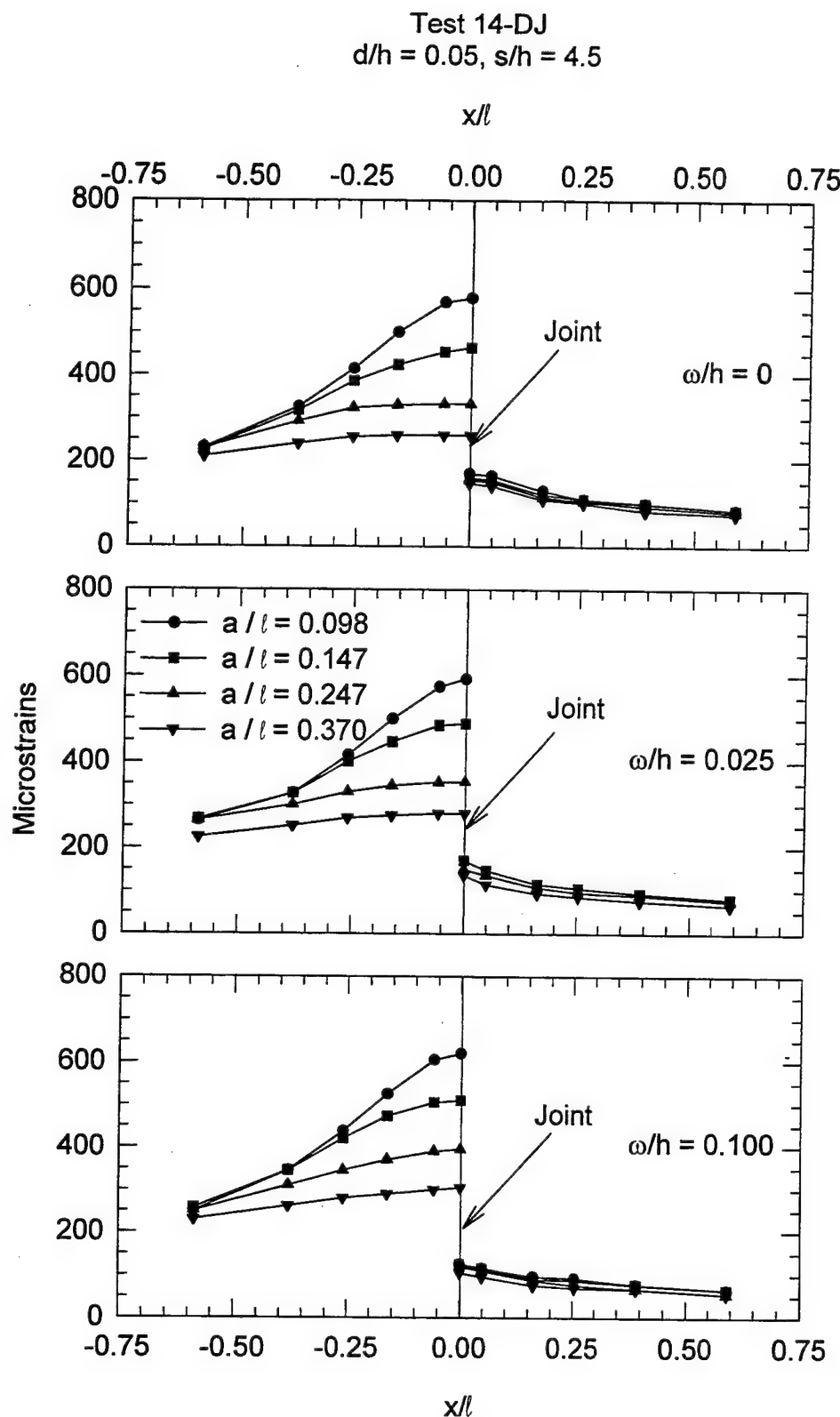


Figure A-9. Test 14-DJ

APPENDIX B
TABULATED JOINT RESPONSES FROM 1950S MODEL TESTS

Table B1

Percent Load Transfer at Doweled Joint, Test 3-DJ

Percent Load Transfer at Doweled Joint, Test 3-DJ								
Footprint Radius a mm (in.)	Load Ratio a/l	Based on Strains 3 mm (0.12 in.) from Edge (by interpolation)			Based on Strains at Edge (by extrapolation)			
		Joint Opening, mm (in.)						
		0	0.127 (0.005)	0.508 (0.020)	0	0.127 (0.005)	0.508 (0.020)	
At Dowels								
Load on Bonded-Dowel Side of Joint								
19 (0.75)	0.364	43.2	38.4	33.9	46.7	40.4	37.2	
13 (0.50)	0.243	39.8	35.6	32.2	42.6	38.3	33.9	
7.6 (0.30)	0.146	36.1	32.8	29.2	39.0	35.2	30.8	
5.1 (0.20)	0.097	31.5	28.7	24.7	34.2	30.4	26.1	
Load on Unbonded-Dowel Side of Joint								
19 (0.75)	0.364	41.0	34.2	30.3	44.2	36.0	31.3	
13 (0.50)	0.243	37.3	32.9	29.1	40.4	34.1	29.7	
7.6 (0.30)	0.146	33.4	29.9	26.6	35.6	30.9	26.8	
5.1 (0.20)	0.097	27.5	24.8	22.1	28.6	25.2	22.5	
Between Dowels								
Load on Bonded-Dowel Side of Joint								
19 (0.75)	0.364	36.7	34.4	32.6	36.2	34.3	32.1	
13 (0.50)	0.243	34.9	32.5	29.8	33.9	32.3	28.7	
7.6 (0.30)	0.146	33.8	29.2	27.1	32.9	28.1	26.1	
5.1 (0.20)	0.097	29.5	25.8	24.3	28.3	24.2	23.9	
Load on Unbonded-Dowel Side of Joint								
19 (0.75)	0.364	37.6	34.5	29.6	37.6	34.3	28.9	
13 (0.50)	0.243	35.4	31.8	27.5	35.2	31.8	26.5	
7.6 (0.30)	0.146	31.9	28.3	24.8	31.6	27.4	24.2	
5.1 (0.20)	0.097	27.3	24.4	21.1	26.8	23.8	20.6	

Table B2

Percent Load Transfer at Doweled Joint, Test 4-DJ

Table B3

Percent Load Transfer at Dowelled Joint, Test 5-DJ

Percent Load Transfer at Doweled Joint, Test 5-DJ							
Footprint Radius a mm (in.)	Load Ratio a/l	Based on Strains 3 mm (0.12 in.) from Edge (by interpolation)			Based on Strains at Edge (by extrapolation)		
		Joint Opening, mm (in.)					
19 (0.75)	0.371	40.9	31.0	26.1	42.8	31.8	26.7
13 (0.50)	0.248	32.4	28.4	22.4	32.2	29.8	22.5
7.6 (0.30)	0.149	27.2	23.8	19.4	26.0	24.3	19.3
5.1 (0.20)	0.099	23.6	20.9	17.3	22.7	21.3	17.2
At Dowels							
Load on Bonded-Dowel Side of Joint							
19 (0.75)	0.371	40.3	32.3	27.4	43.4	33.6	28.4
13 (0.50)	0.248	35.9	30.0	25.0	38.1	31.8	25.7
7.6 (0.30)	0.149	30.9	26.1	20.5	32.1	26.9	21.0
5.1 (0.20)	0.099	27.0	21.8	19.4	27.8	23.0	20.0
Between Dowels							
Load on Bonded-Dowel Side of Joint							
19 (0.75)	0.371	34.2	30.7	24.7	33.8	29.0	23.8
13 (0.50)	0.248	30.2	27.9	21.8	29.9	27.0	20.7
7.6 (0.30)	0.149	26.1	24.1	18.4	25.6	23.3	17.2
5.1 (0.20)	0.099	22.7	20.5	17.0	20.9	19.3	15.9
Load on Unbonded-Dowel Side of Joint							
19 (0.75)	0.371	34.1	28.7	23.0	34.4	28.2	21.6
13 (0.50)	0.248	30.7	27.2	21.0	30.8	26.9	20.1
7.6 (0.30)	0.149	27.2	23.5	16.6	26.7	22.8	16.0
5.1 (0.20)	0.099	22.7	19.3	15.8	22.2	18.3	15.4

Table B4

Percent Load Transfer at Doweled Joint, Test 6-DJ

Percent Load Transfer at Doweled Joint, Test 6-DJ								
Footprint Radius a mm (in.)	Load Ratio a/l	Based on Strains 3 mm (0.12 in.) from Edge (by interpolation)			Based on Strains at Edge (by extrapolation)			
		Joint Opening, mm (in.)						
		0	0.127 (0.005)	0.508 (0.020)	0	0.127 (0.005)	0.508 (0.020)	
At Dowels								
Load on Bonded-Dowel Side of Joint								
19 (0.75)	0.370	47.2	44.5	42.4	51.0	46.7	43.8	
13 (0.50)	0.247	44.3	42.7	40.4	47.2	44.7	42.6	
7.6 (0.30)	0.148	41.5	39.2	36.5	45.1	40.1	37.9	
5.1 (0.20)	0.099	38.4	36.2	33.9	40.1	37.2	33.9	
Load on Unbonded-Dowel Side of Joint								
19 (0.75)	0.370	45.3	40.3	36.0	45.6	40.7	36.3	
13 (0.50)	0.247	41.3	38.5	34.5	42.2	38.4	35.2	
7.6 (0.30)	0.148	38.8	35.2	32.7	39.2	35.3	33.2	
5.1 (0.20)	0.099	35.7	33.2	30.8	36.0	33.0	30.9	
Between Dowels								
Load on Bonded-Dowel Side of Joint								
19 (0.75)	0.370	44.6	41.8	40.2	45.7	42.7	41.6	
13 (0.50)	0.247	42.2	39.6	37.5	43.3	40.0	39.4	
7.6 (0.30)	0.148	39.1	36.9	35.4	40.2	37.2	36.9	
5.1 (0.20)	0.099	35.4	34.0	32.4	35.1	34.4	31.9	
Load on Unbonded-Dowel Side of Joint								
19 (0.75)	0.370	44.4	40.1	36.8	45.3	39.6	36.4	
13 (0.50)	0.247	42.1	38.8	35.0	42.9	38.7	34.8	
7.6 (0.30)	0.148	38.7	35.5	32.7	39.0	35.5	32.5	
5.1 (0.20)	0.099	36.3	32.7	30.7	36.0	32.3	30.6	

Table B5

Percent Load Transfer at Dowelled Joint, Test 7-DJ

Percent Load Transfer at Doweled Joint, Test 7-DJ							
Footprint Radius a mm (in.)	Load Ratio a/l	Based on Strains 3 mm (0.12 in.) from Edge (by interpolation)			Based on Strains at Edge (by extrapolation)		
		Joint Opening, mm (in.)					
19 (0.75)	0.365	39.8	36.7	34.8	40.4	37.8	35.1
At Dowels							
Load on Bonded-Dowel Side of Joint							
19 (0.75)	0.365	39.8	36.7	34.8	40.4	37.8	35.1
13 (0.50)	0.243	36.4	35.1	33.5	37.0	35.9	33.6
7.6 (0.30)	0.146	32.5	32.2	30.3	33.8	33.1	30.5
5.1 (0.20)	0.097	29.6	29.5	27.3	30.1	31.0	27.1
Load on Unbonded-Dowel Side of Joint							
19 (0.75)	0.365	36.2	32.8	29.7	36.6	33.0	29.2
13 (0.50)	0.243	34.2	30.8	27.8	34.6	31.0	27.5
7.6 (0.30)	0.146	30.5	28.8	26.0	30.1	28.2	26.2
5.1 (0.20)	0.097	27.8	26.8	24.5	28.2	26.7	24.5
Between Dowels							
Load on Bonded-Dowel Side of Joint							
19 (0.75)	0.365	34.9	31.4	31.1	35.1	31.4	31.4
13 (0.50)	0.243	31.9	29.9	28.6	31.4	30.0	28.1
7.6 (0.30)	0.146	28.5	27.5	25.9	27.9	28.0	25.9
5.1 (0.20)	0.097	25.7	25.4	23.0	25.2	25.5	22.7
Load on Unbonded-Dowel Side of Joint							
19 (0.75)	0.365	41.1	36.2	33.3	42.2	37.3	33.8
13 (0.50)	0.243	38.3	34.8	30.6	38.7	35.3	30.3
7.6 (0.30)	0.146	34.0	31.8	28.6	34.8	31.6	28.0
5.1 (0.20)	0.097	30.6	29.6	26.7	31.3	30.3	26.1

Table B6

Percent Load Transfer at Dowelled Joint, Test 8-DJ

Percent Load Transfer at Doweled Joint, Test 8-DJ								
Footprint Radius a mm (in.)	Load Ratio a/l	Based on Strains 3 mm (0.12 in.) from Edge (by interpolation)			Based on Strains at Edge (by extrapolation)			
		Joint Opening, mm (in.)						
		0	0.127 (0.005)	0.508 (0.020)	0	0.127 (0.005)	0.508 (0.020)	
At Dowels								
Load on Bonded-Dowel Side of Joint								
19 (0.75)	0.373	35.1	32.9	30.6	35.5	32.3	31.5	
13 (0.50)	0.249	31.9	31.5	27.4	31.6	30.9	27.3	
7.6 (0.30)	0.149	28.6	28.8	23.9	27.8	28.8	23.7	
5.1 (0.20)	0.100	25.2	24.6	20.5	25.2	24.1	21.3	
Load on Unbonded-Dowel Side of Joint								
19 (0.75)	0.373	37.8	33.5	27.6	39.2	33.7	28.6	
13 (0.50)	0.249	34.3	31.9	26.2	36.1	31.9	26.8	
7.6 (0.30)	0.149	30.1	29.7	23.6	30.7	30.2	24.8	
5.1 (0.20)	0.100	25.2	24.9	19.5	26.1	25.0	20.4	
Between Dowels								
Load on Bonded-Dowel Side of Joint								
19 (0.75)	0.373	33.3	31.1	28.4	32.7	31.0	28.7	
13 (0.50)	0.249	29.8	29.6	25.4	29.3	29.2	25.0	
7.6 (0.30)	0.149	26.7	26.1	21.9	25.8	25.8	21.0	
5.1 (0.20)	0.100	22.5	22.3	18.6	21.4	21.4	17.8	
Load on Unbonded-Dowel Side of Joint								
19 (0.75)	0.373	33.1	28.2	24.4	33.0	28.5	23.9	
13 (0.50)	0.249	29.6	27.7	23.0	29.2	27.4	22.4	
7.6 (0.30)	0.149	26.5	25.2	20.7	25.4	24.8	20.2	
5.1 (0.20)	0.100	21.2	20.3	17.0	20.2	19.4	16.1	

Table B7

Percent Load Transfer at Doweled Joint, Test 12-DJ

Percent Load Transfer at Doweled Joint, Test 12-DJ								
Footprint Radius a mm (in.)	Load Ratio a/l	Based on Strains 3 mm (0.12 in.) from Edge (by interpolation)			Based on Strains at Edge (by extrapolation)			
		Joint Opening, mm (in.)						
		0	0.127 (0.005)	0.508 (0.020)	0	0.127 (0.005)	0.508 (0.020)	
At Dowels								
Load on Bonded-Dowel Side of Joint								
19 (0.75)	0.371	47.2	43.2	40.0	53.1	49.0	44.9	
13 (0.50)	0.248	42.9	40.9	37.4	50.2	47.4	41.7	
7.6 (0.30)	0.149	39.2	38.2	33.9	44.4	44.0	37.8	
5.1 (0.20)	0.099	34.2	33.0	28.8	39.3	37.9	31.5	
Load on Unbonded-Dowel Side of Joint								
19 (0.75)	0.371	48.9	45.5	40.1	54.3	51.3	39.7	
13 (0.50)	0.248	46.1	44.1	38.6	51.5	49.9	38.6	
7.6 (0.30)	0.149	41.2	40.5	35.1	45.1	46.4	35.0	
5.1 (0.20)	0.099	38.0	36.1	31.4	42.5	41.6	30.6	
Between Dowels								
Load on Bonded-Dowel Side of Joint								
19 (0.75)	0.371	35.0	34.0	31.9	33.7	34.1	32.8	
13 (0.50)	0.248	32.0	31.1	28.4	31.4	30.3	27.5	
7.6 (0.30)	0.149	29.2	27.6	25.4	28.7	27.5	25.0	
5.1 (0.20)	0.099	24.6	24.2	22.0	24.0	23.2	20.8	
Load on Unbonded-Dowel Side of Joint								
19 (0.75)	0.371	37.4	33.9	30.5	36.9	33.3	30.4	
13 (0.50)	0.248	33.2	31.6	28.1	32.9	30.8	28.1	
7.6 (0.30)	0.149	32.8	27.8	25.1	32.0	27.2	23.9	
5.1 (0.20)	0.099	27.0	24.9	22.1	26.5	24.4	21.7	

Table B8

Percent Load Transfer at Dowelled Joint, Test 13-DJ

Percent Load Transfer at Doweled Joint, Test 13-DJ								
Footprint Radius a mm (in.)	Load Ratio a/l	Based on Strains 3 mm (0.12 in.) from Edge (by interpolation)			Based on Strains at Edge (by extrapolation)			
		Joint Opening, mm (in.)						
		0	0.127 (0.005)	0.508 (0.020)	0	0.127 (0.005)	0.508 (0.020)	
At Dowels								
Load on Bonded-Dowel Side of Joint								
19 (0.75)	0.374	50.3	43.1	40.5	58.6	48.5	46.4	
13 (0.50)	0.249	44.9	40.6	37.1	52.4	47.2	42.0	
7.6 (0.30)	0.150	39.3	36.0	32.1	45.8	40.5	36.1	
5.1 (0.20)	0.100	35.0	33.8	29.2	40.8	37.7	32.4	
Load on Unbonded-Dowel Side of Joint								
19 (0.75)	0.374	46.3	36.7	35.6	52.8	40.0	39.7	
13 (0.50)	0.249	39.3	35.5	33.5	45.0	39.8	37.3	
7.6 (0.30)	0.150	33.5	29.6	27.5	36.8	33.6	30.2	
5.1 (0.20)	0.100	29.4	28.3	25.2	31.6	31.2	27.5	
Between Dowels								
Load on Bonded-Dowel Side of Joint								
19 (0.75)	0.374	31.7	28.5	26.7	30.9	26.9	25.5	
13 (0.50)	0.249	28.5	26.5	24.3	27.2	25.4	22.6	
7.6 (0.30)	0.150	24.4	22.7	20.7	23.1	20.8	19.8	
5.1 (0.20)	0.100	21.3	20.8	18.4	20.2	19.8	17.4	
Load on Unbonded-Dowel Side of Joint								
19 (0.75)	0.374	32.2	28.2	25.1	29.1	26.9	23.7	
13 (0.50)	0.249	27.3	25.6	22.6	25.3	24.2	20.6	
7.6 (0.30)	0.150	24.0	22.5	18.9	22.2	19.4	18.1	
5.1 (0.20)	0.100	19.8	20.6	17.3	18.0	18.5	16.1	

Table B9

Percent Load Transfer at Dowelled Joint, Test 14-DJ

Percent Load Transfer at Doweled Joint, Test 14-DJ																	
Footprint Radius a mm (in.)	Load Ratio a/l	Based on Strains 3 mm (0.12 in.) from Edge (by interpolation)			Based on Strains at Edge (by extrapolation)												
		Joint Opening, mm (in.)															
At Dowels																	
Load on Bonded-Dowel Side of Joint																	
19 (0.75)	0.367	38.6	30.4	24.7	41.3	34.5	26.4										
13 (0.50)	0.244	32.0	28.0	23.3	34.0	31.6	24.6										
7.6 (0.30)	0.147	26.9	23.1	19.2	28.0	26.8	20.3										
5.1 (0.20)	0.098	22.5	21.5	17.1	23.2	24.3	18.0										
Load on Unbonded-Dowel Side of Joint																	
19 (0.75)	0.367	34.9	28.4	23.6	36.0	32.3	25.5										
13 (0.50)	0.244	30.2	27.3	22.4	31.6	30.5	23.9										
7.6 (0.30)	0.147	26.2	21.5	17.5	26.8	24.8	18.9										
5.1 (0.20)	0.098	20.9	19.9	15.4	21.7	22.8	16.4										
Between Dowels																	
Load on Bonded-Dowel Side of Joint																	
19 (0.75)	0.367	26.5	24.3	18.9	24.4	24.2	17.8										
13 (0.50)	0.244	22.7	21.8	16.6	21.0	21.3	15.7										
7.6 (0.30)	0.147	19.3	17.7	14.5	17.9	16.6	13.8										
5.1 (0.20)	0.098	15.0	16.1	12.9	14.0	15.3	11.8										
Load on Unbonded-Dowel Side of Joint																	
19 (0.75)	0.367	25.8	21.8	17.2	24.3	20.7	16.5										
13 (0.50)	0.244	22.4	20.1	15.4	21.5	19.0	14.6										
7.6 (0.30)	0.147	17.9	15.8	11.5	16.9	15.2	10.9										
5.1 (0.20)	0.098	13.6	13.9	11.7	12.8	13.0	11.1										

APPENDIX C: ALGORITHM FOR ASSIGNING SPRING STIFFNESSES TO NODES USING THE ABAQUS "JOINTC" OPTION

PROBLEM STATEMENT

It is desired to represent the stiffness of a rigid pavement joint in ABAQUS using a 3D finite element model of the rigid pavement slabs. Each node on the joint face of a slab will be connected to the corresponding node on the joint face of the adjacent slab with a spring element. The algorithm described in this appendix provides a rational way to distribute the joint stiffness per unit length along the joint to the nodes along the joint. The ABAQUS element chosen for this study is the "JOINTC" element, a general, non-linear spring and dashpot element which can have stiffness (and damping, as well) in three orthogonal directions. For most purposes of this study, the elements will be assigned stiffness values assigned in the vertical direction only. Furthermore, a linear force-displacement relationship will be assumed. Because all analyses are static, damping will be of no consequence.

ASSUMPTIONS

- a. Let nodes be equally spaced in the y-direction. Let the distance between nodes be given by 2a (Figure C1).
- b. Let nodes be equally spaced in the z-direction. Let the distance between nodes be given by 2b.
- c. Let the number of rows of nodes be given by N_R and the number of columns of nodes be given by N_C .
- d. Let the length of the joint to be modeled be given by λ .
- e. Let the joint stiffness per unit length be given by q (Units: F/L^2).
- f. Let κ be the unit spring stiffness (Units: F/L).

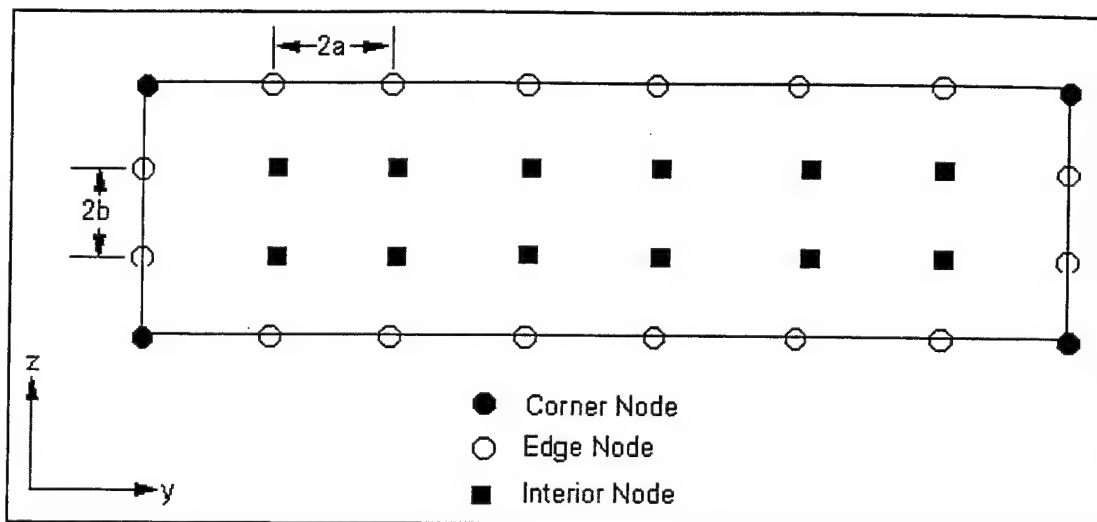


Figure C1. Face of typical one-layer 3D finite element mesh showing location of nodes

GEOMETRY

- a. There are three types of nodes: corner, edge, and interior (See Figure D1).
- b. The contributing areas for each type of node are the following:
 - (1) Corner node: $A_C = ab$
 - (2) Edge node: $A_E = 2ab$
 - (3) Interior node: $A_I = 4ab$
- c. Develop general statements for the number of each type of node as a function of N_C and N_R .
 - (1) Number of corner nodes = 4
 - (2) Number of edge nodes = $2(N_R + N_C - 4)$
 - (3) Number of interior nodes = $(N_R - 2)(N_C - 2)$

SOLVE FOR SPRING STIFFNESSES AS A FUNCTION OF q :

- a. Assign spring stiffness to types of node based on contributing areas:
 - (1) Corner node: κ

(2) Edge node: 2κ

(3) Interior node: 4κ

b. Set joint stiffness equal to sum of spring stiffnesses.

$$\begin{aligned}
 q \times \lambda &= \kappa \times (\text{Number of corner nodes}) + 2\kappa \times (\text{Number of edge nodes}) + \\
 &\quad 4\kappa \times (\text{Number of interior nodes}) \\
 &= \kappa(4) + 2\kappa[2(N_R + N_C - 4)] + 4\kappa(N_R - 2)(N_C - 2) \\
 &= 4\kappa(1 + N_R + N_C - 4 + N_R N_C - 2N_R - 2N_C + 4) \\
 &= 4\kappa(N_R - 1)(N_C - 1)
 \end{aligned}$$

Therefore:

$$\kappa = \frac{q\lambda}{4(N_R - 1)(N_C - 1)}$$

APPENDIX D

COMPILATION OF INSTRUMENTATION TRACES FROM EXPERIMENTS

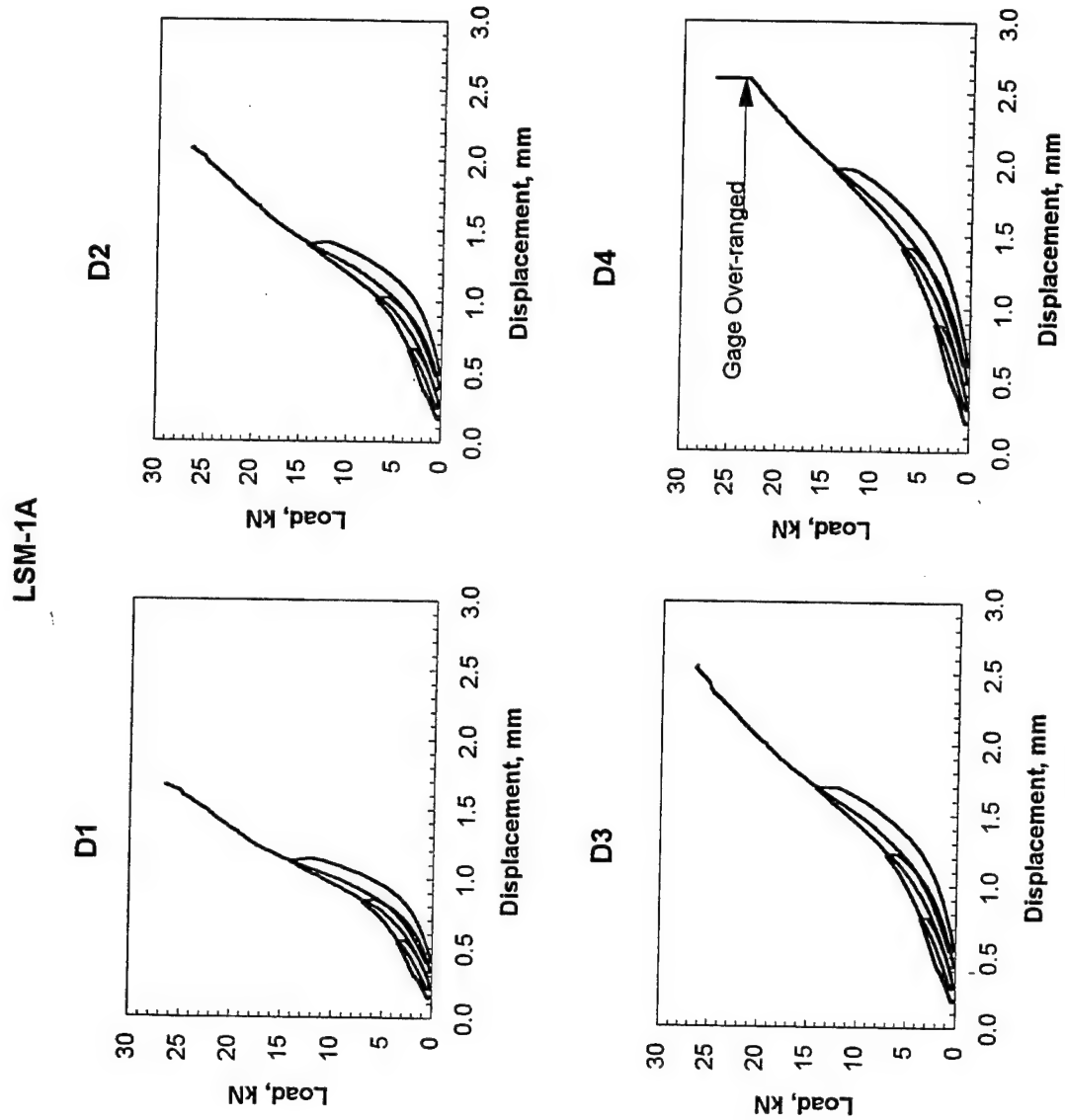


Figure D.1. Gages D1 through D4, Experiment LSM-1A

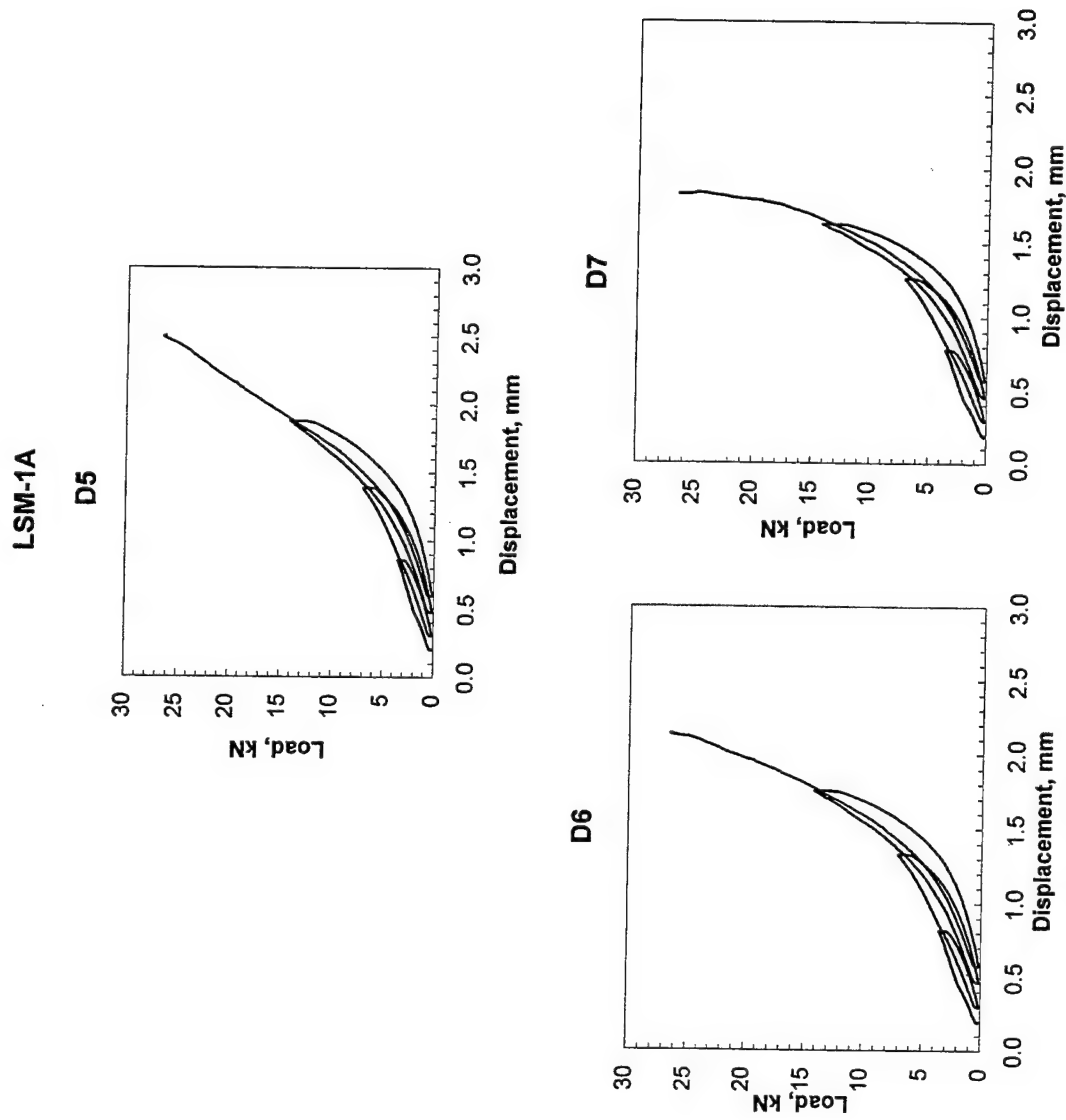


Figure D.2. Gages D5 through D7, Experiment LSM-1A

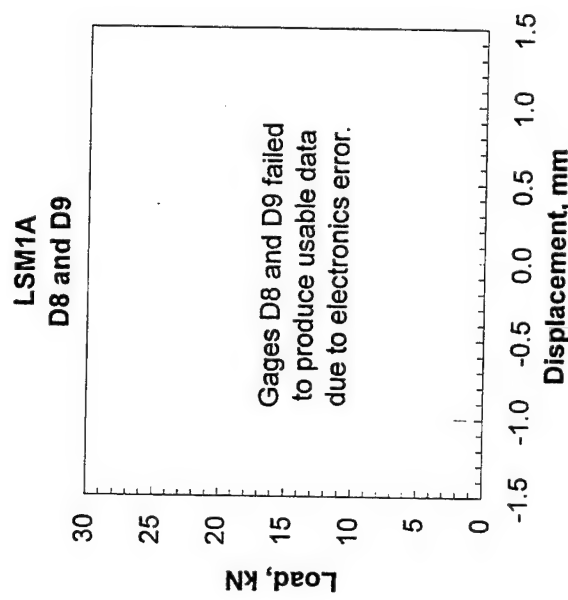


Figure D.3. Gages D8 through D9, Experiment LSM-1A

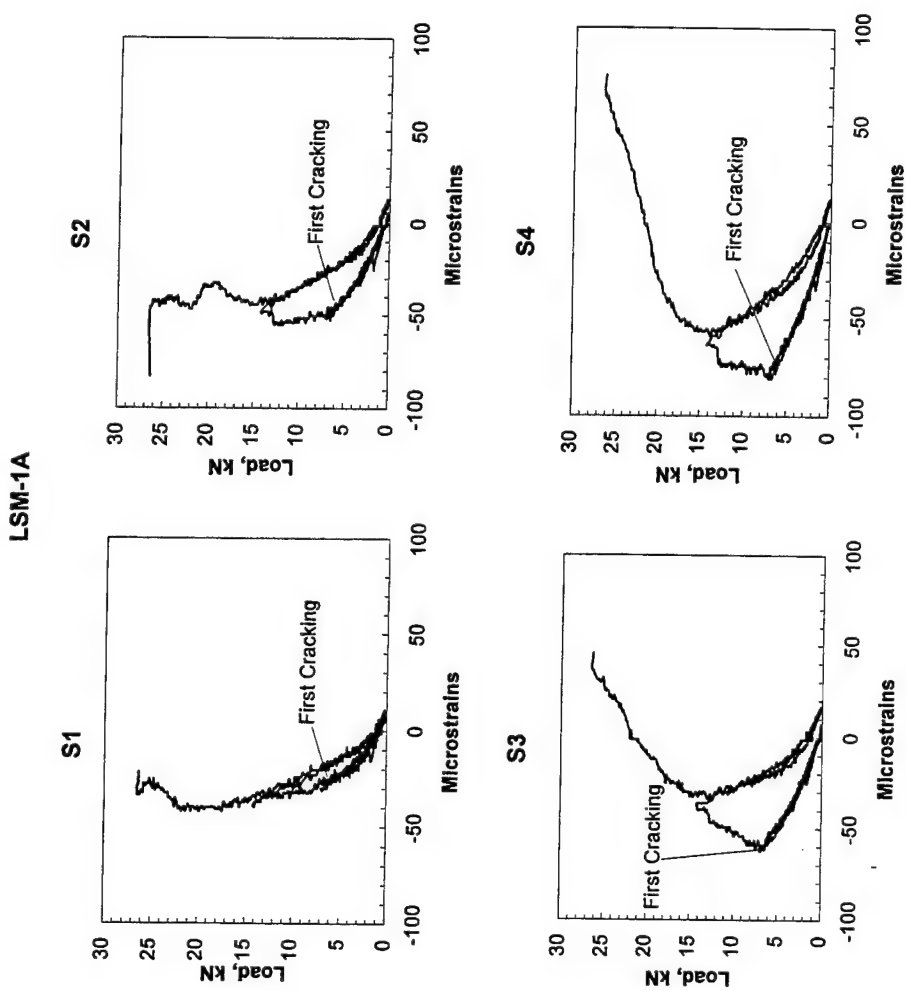


Figure D.4. Gages S1 through S4, Experiment LSM-1A

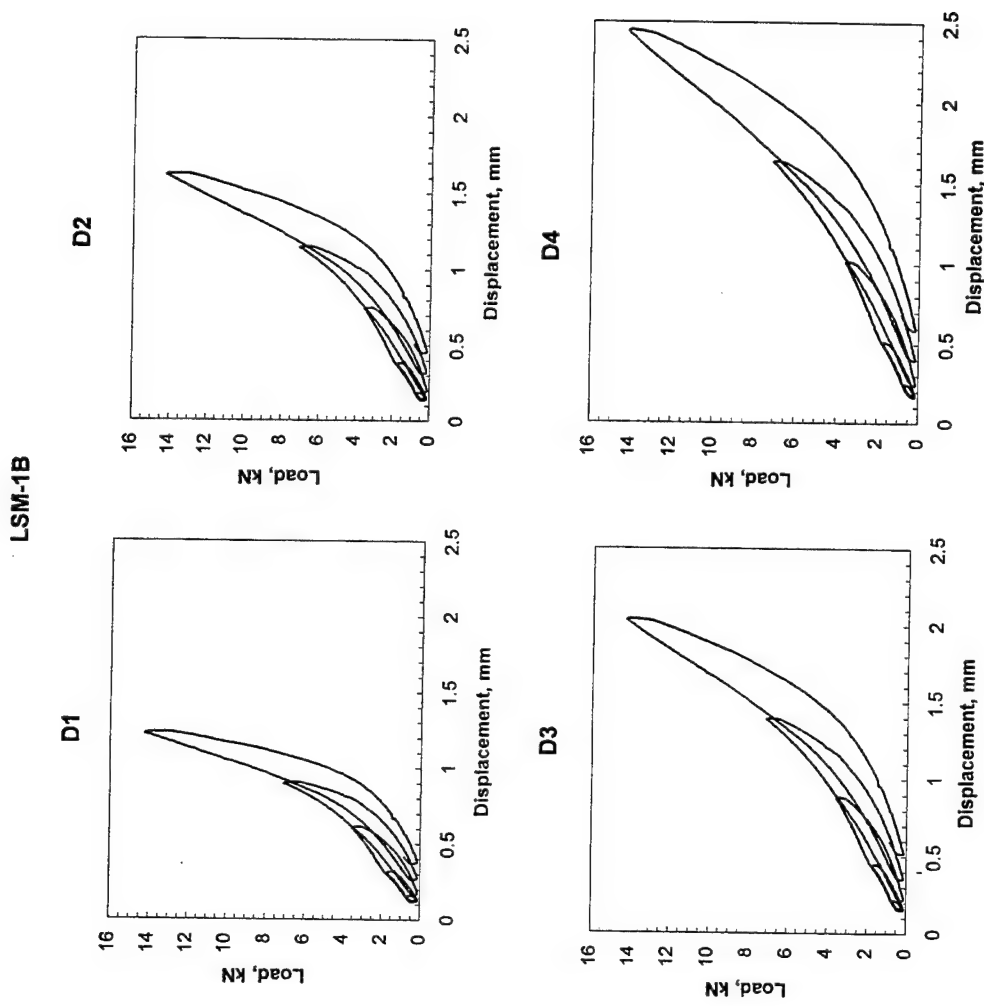


Figure D.5. Gages D1 through D4, Experiment LSM-1B

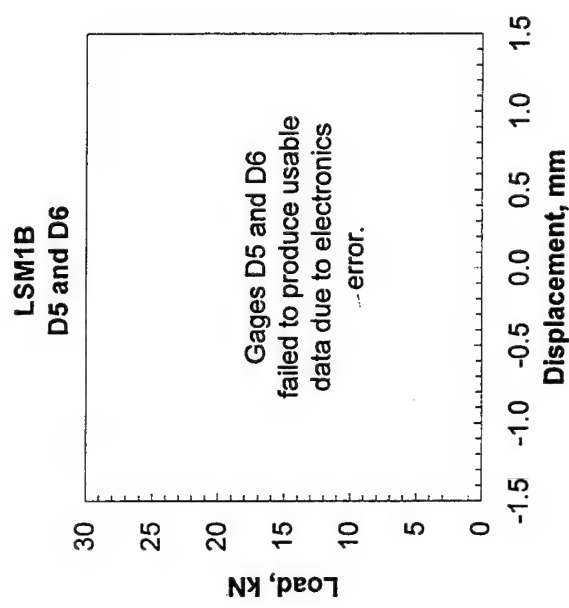


Figure D.6. Gages D5 and D6, Experiment LSM-1B

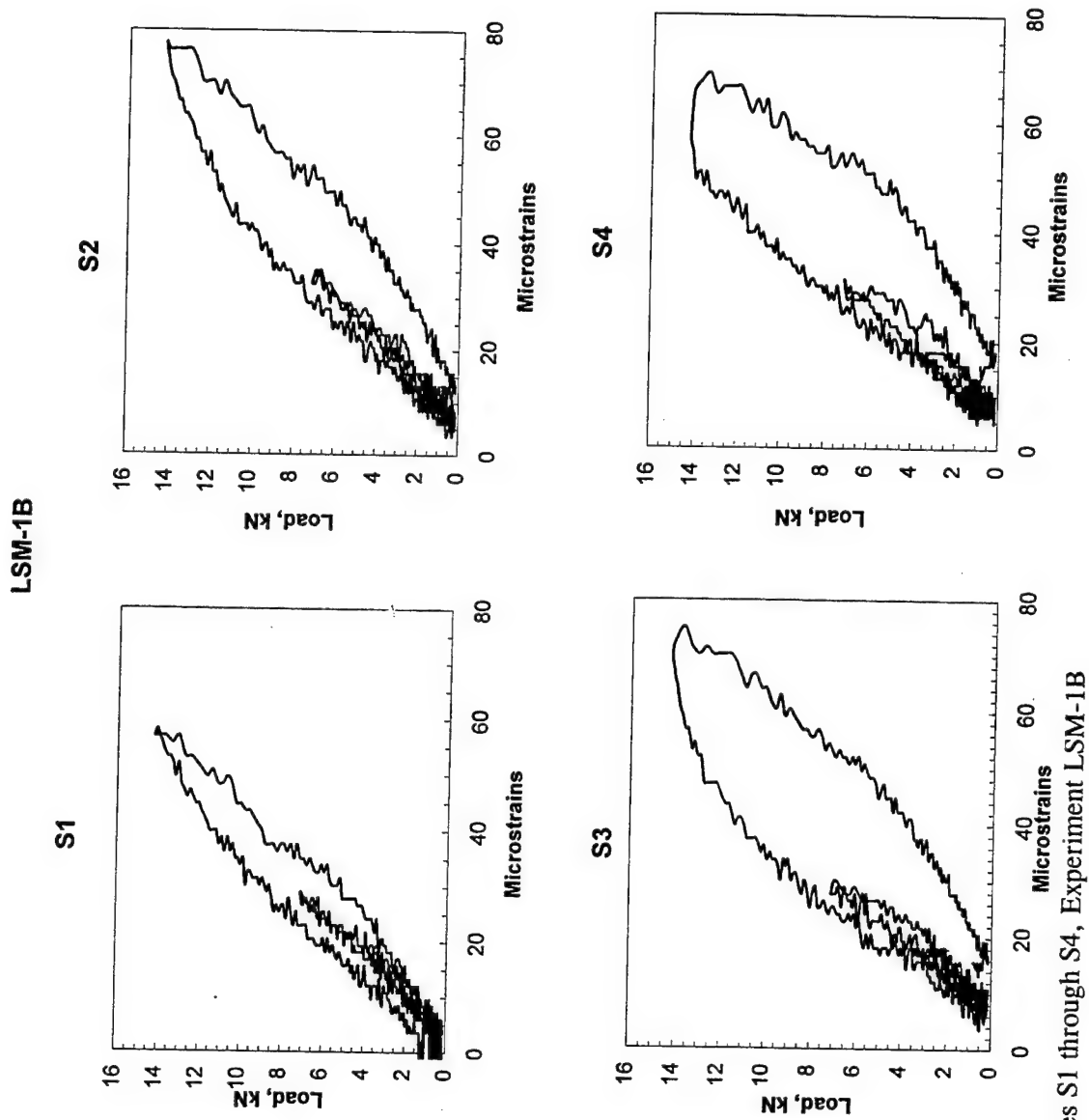


Figure D.7. Gages S1 through S4, Experiment LSM-1B

LSM-2

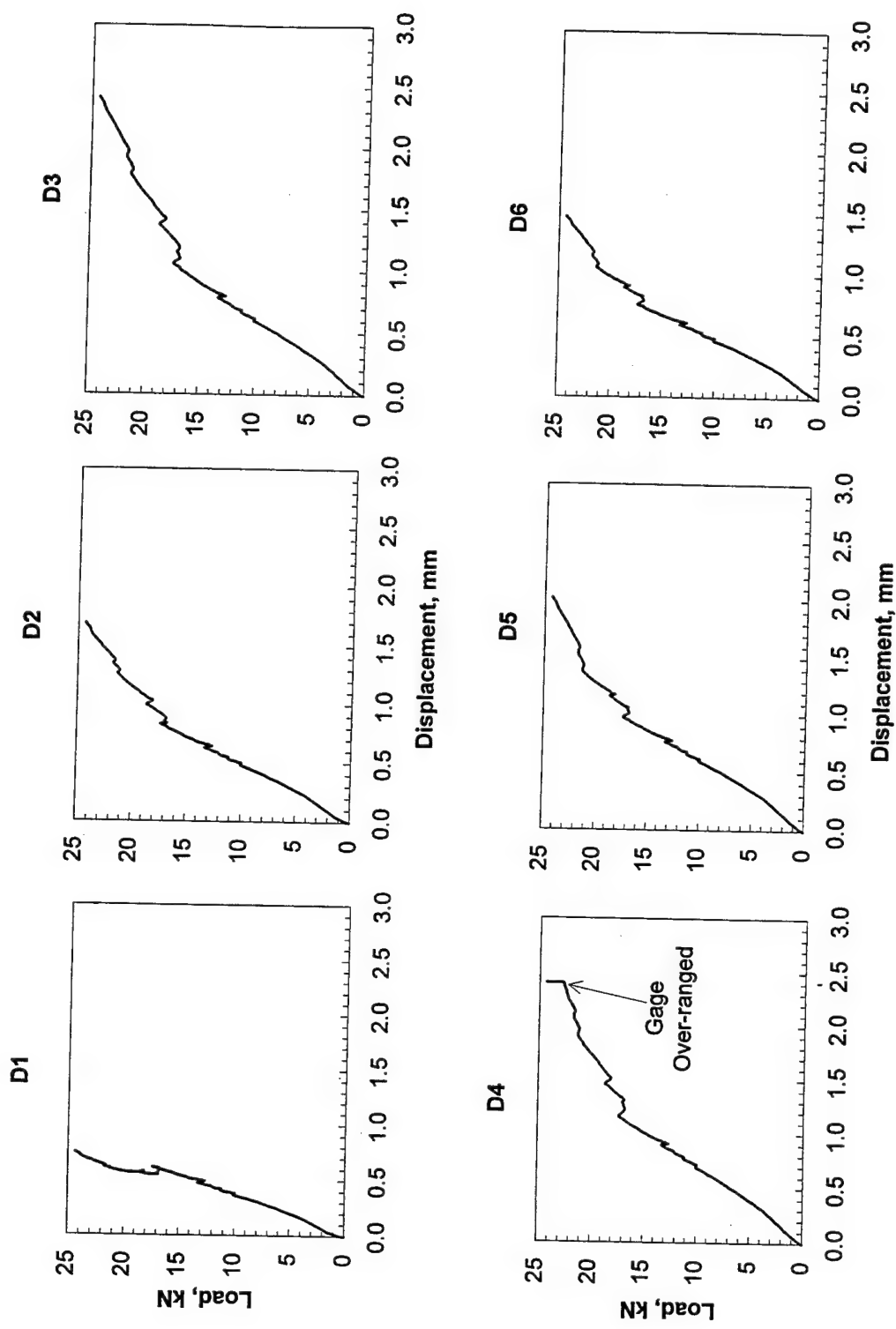


Figure D.8. Gages D1 through D6, Experiment LSM-2

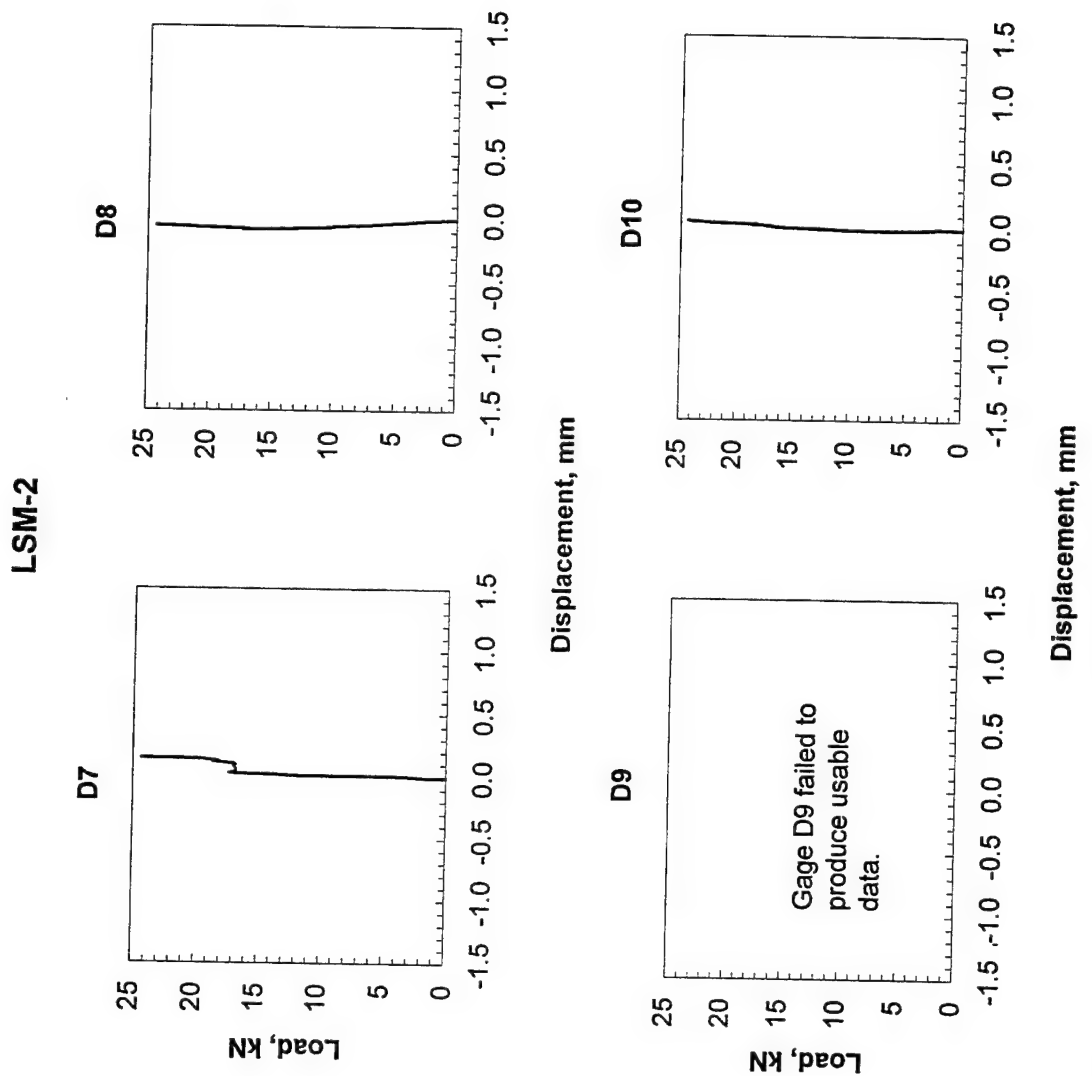


Figure D.9. Gages D7 through D10, Experiment LSM-2

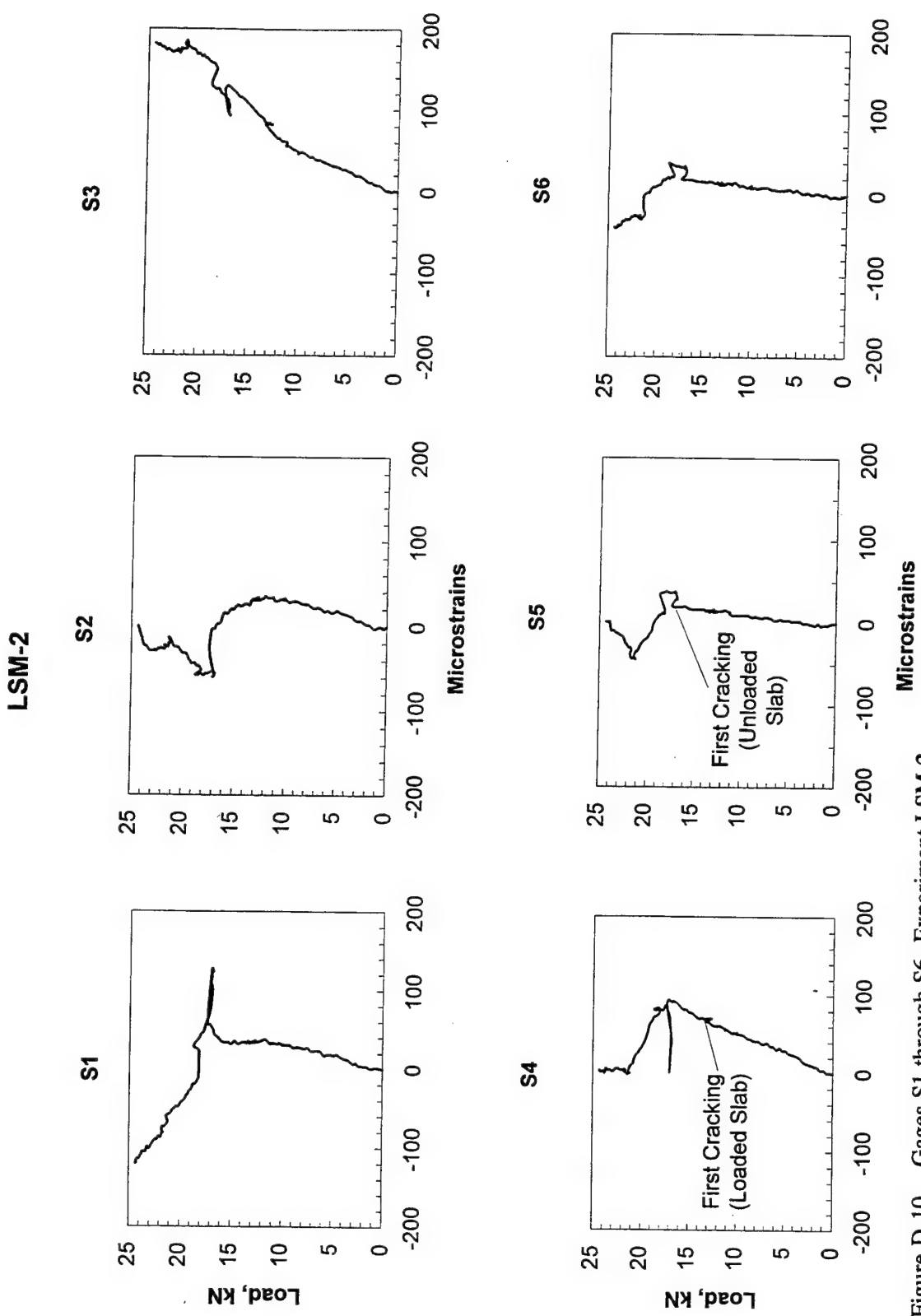


Figure D.10. Gages S1 through S6, Experiment LSM-2

LSM-2

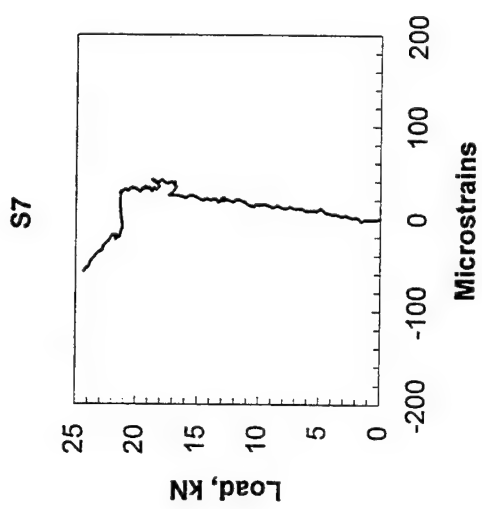


Figure D.11. Gage S7, Experiment LSM-2

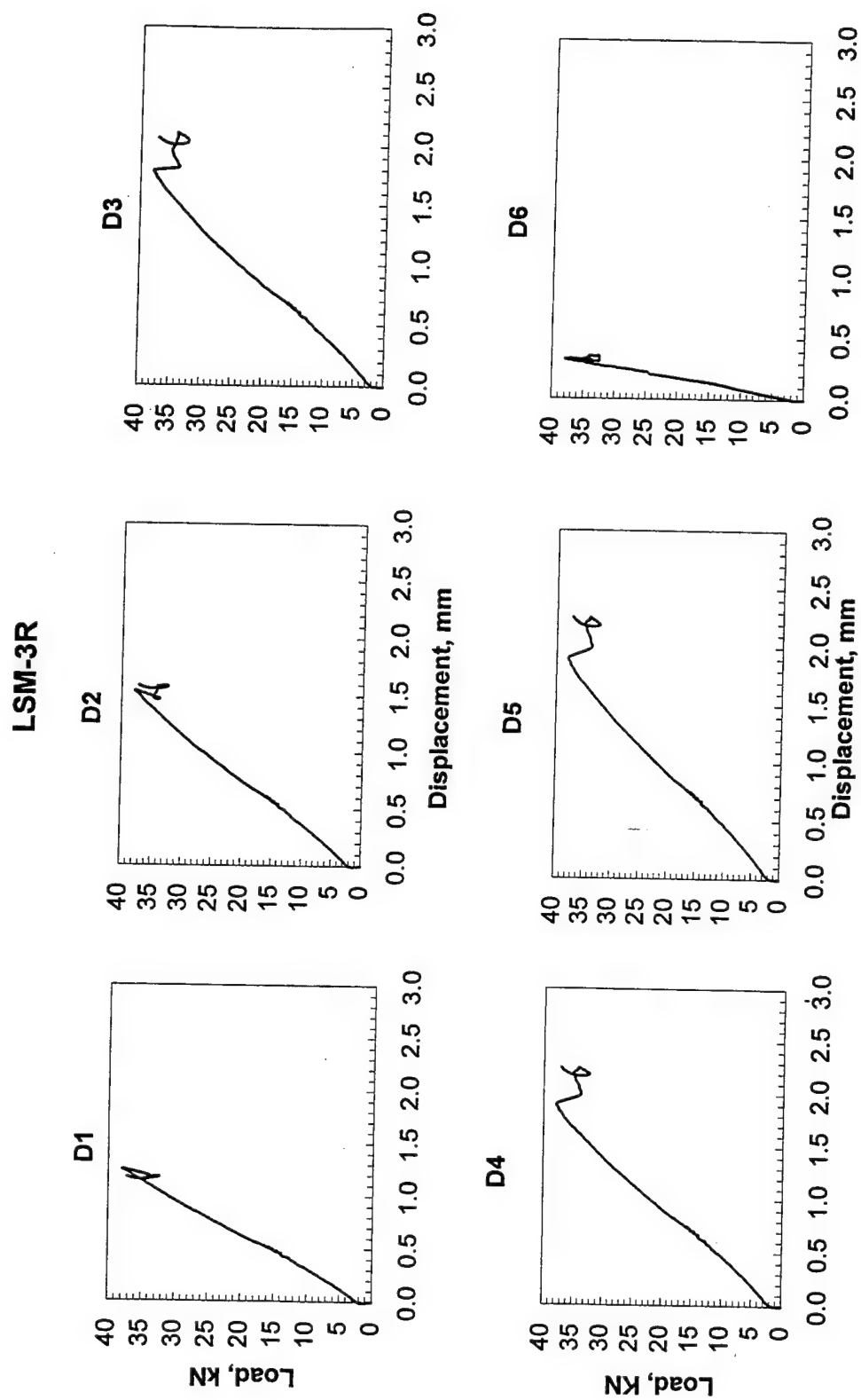


Figure D.12. Gages D1 through D6, Experiment LSM-3R

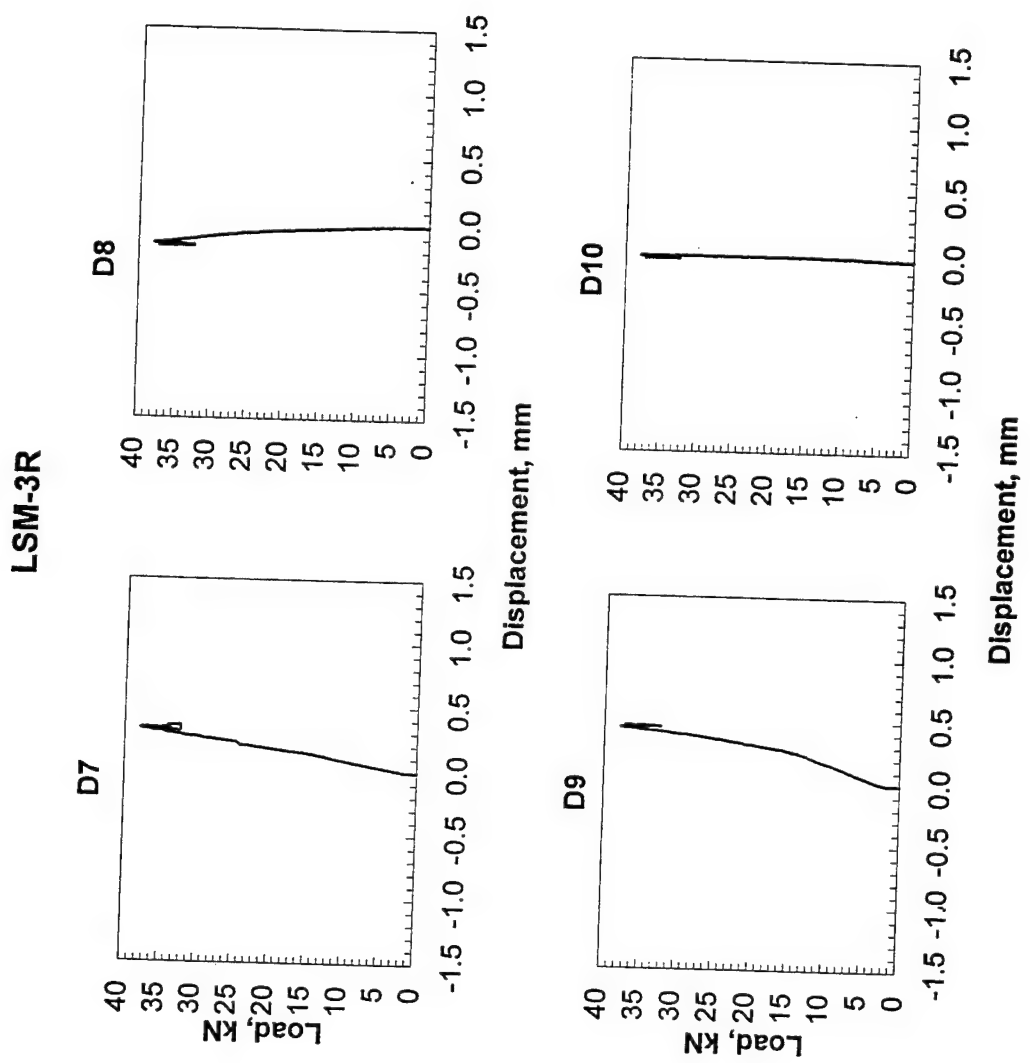


Figure D.13. Gages D7 through D10, Experiment LSM-3R

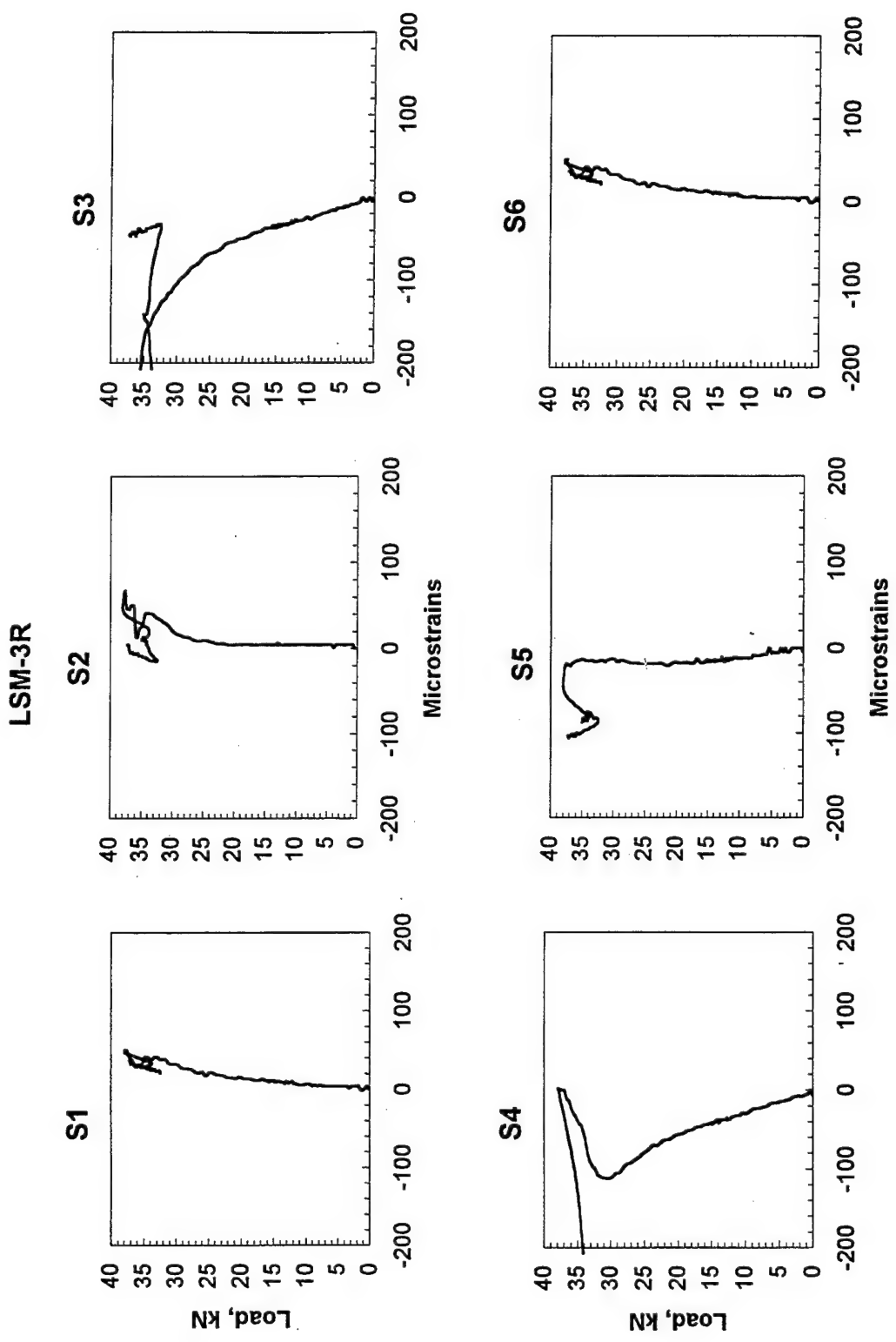


Figure D.14. Gages S1 through S6, Experiment LSM-3R

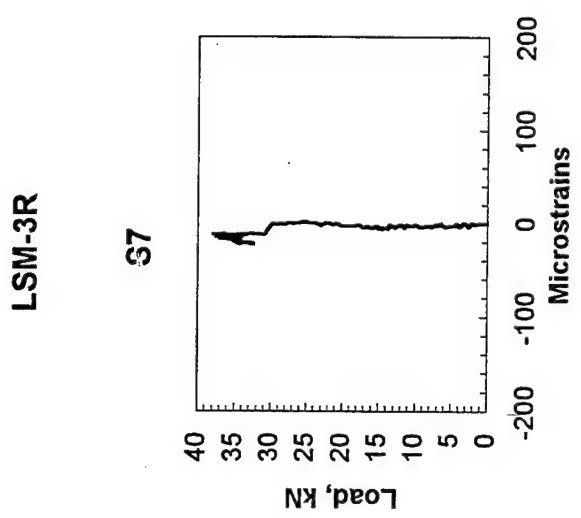


Figure D.15. Gage S7, Experiment LSM-3R

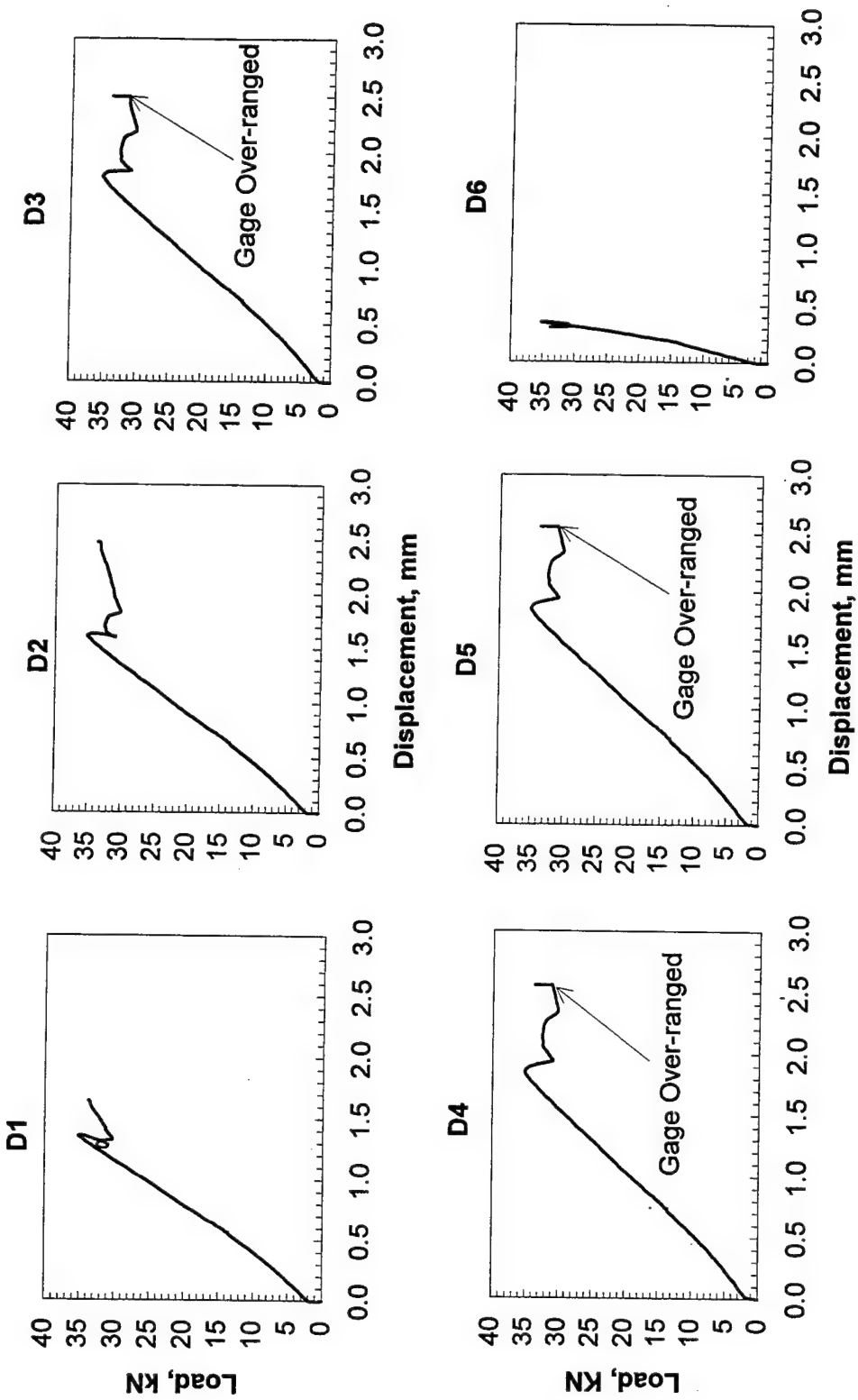
LSM-4

Figure D.16. Gages D1 through D6, Experiment LSM-4

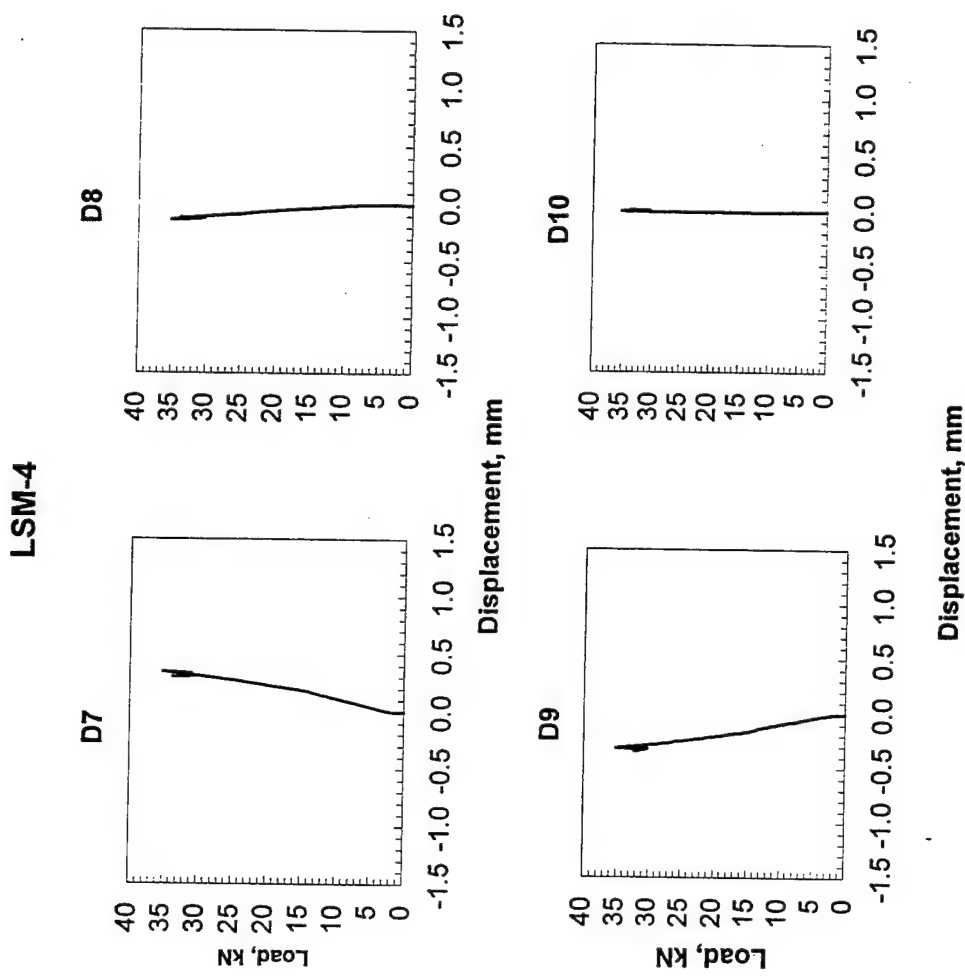


Figure D.17. Gages D7 through D10, Experiment LSM-4

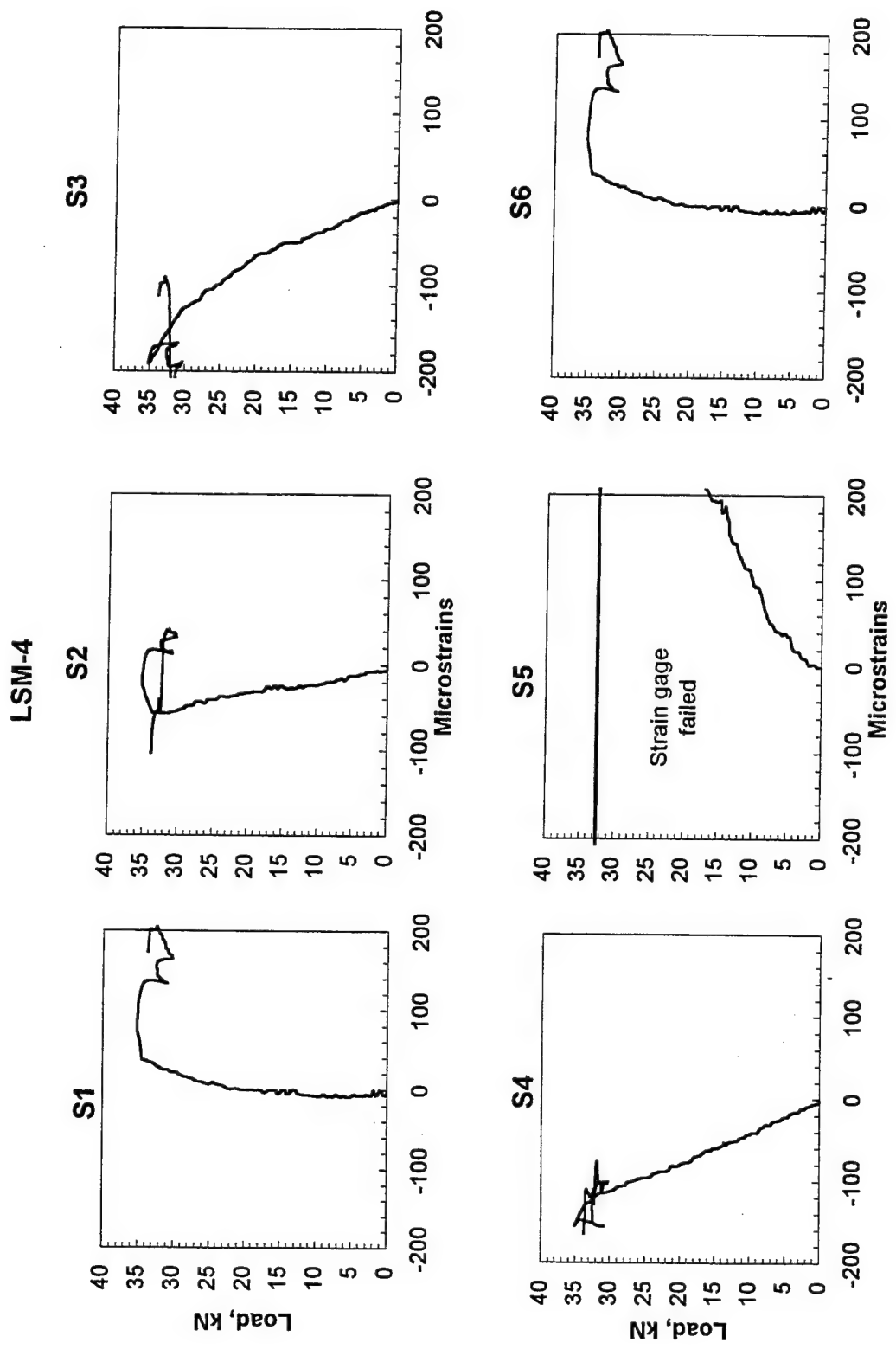


Figure D.18. Gages S1 through S6, Experiment LSM-4

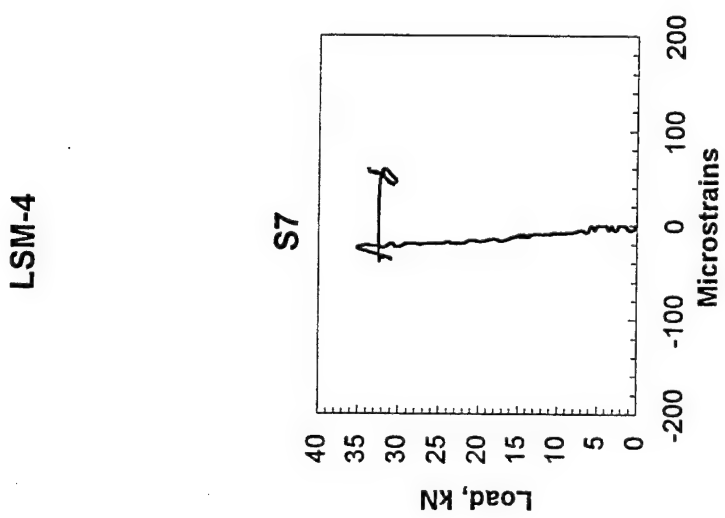


Figure D.19 Gage S7, Experiment LSM-4

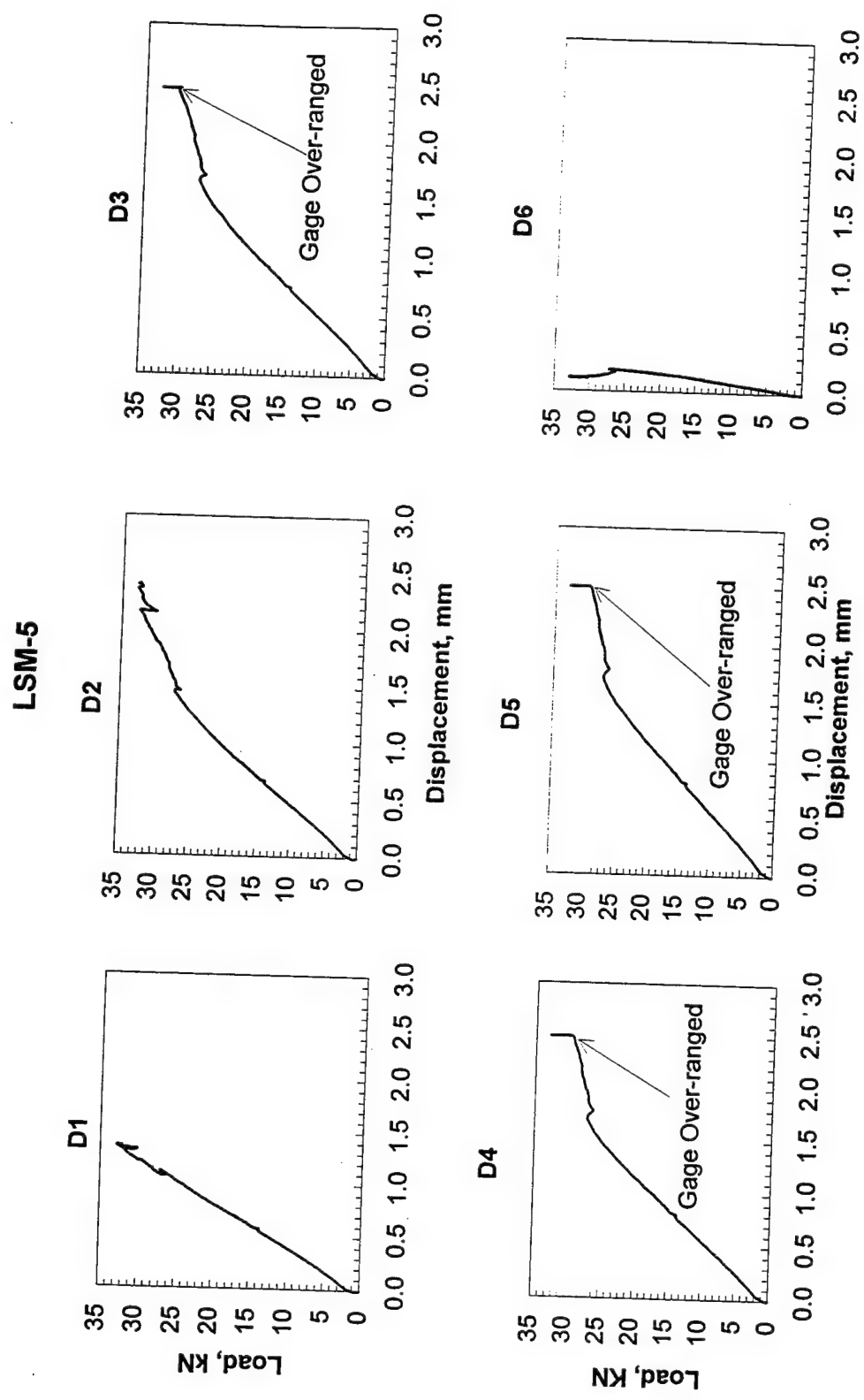


Figure D.20. Gages D1 through D6, Experiment LSM-5

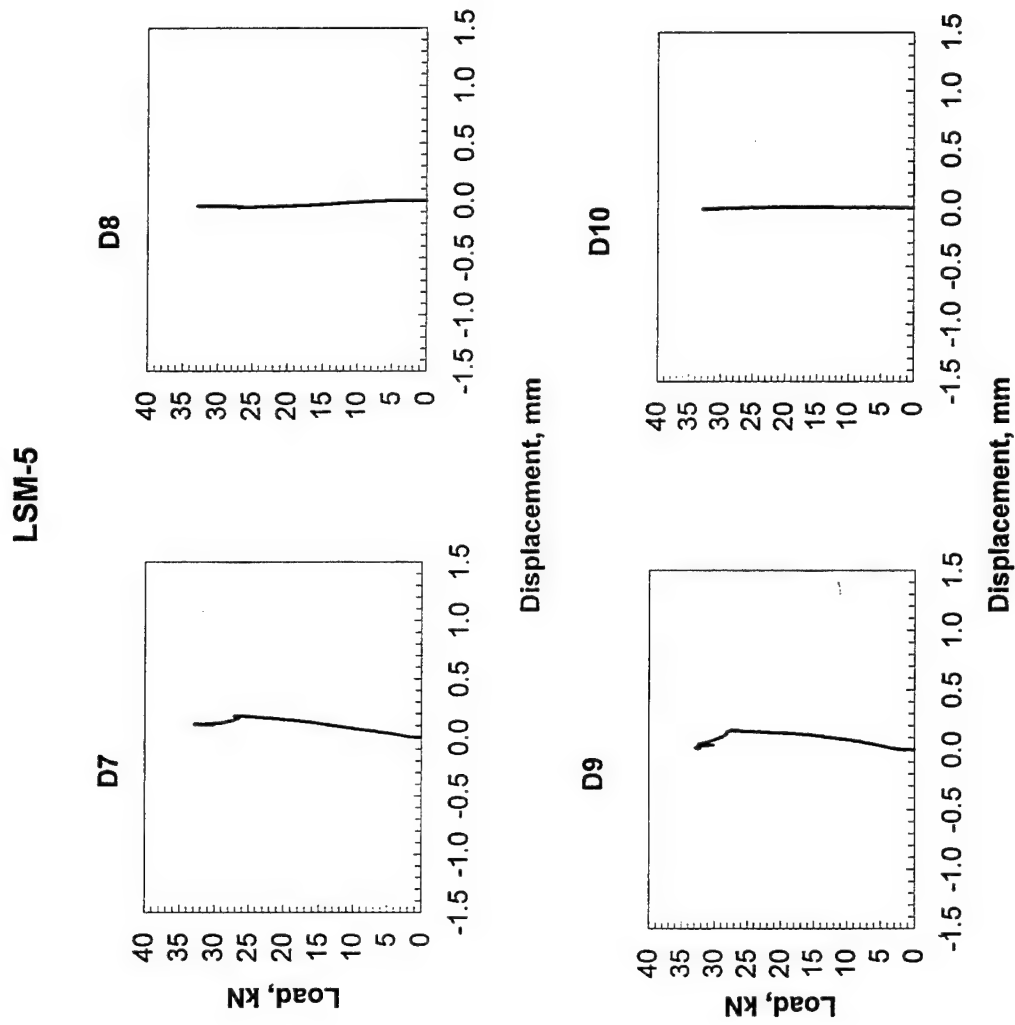


Figure D.21. Gages D7 through D10, Experiment LSM-5

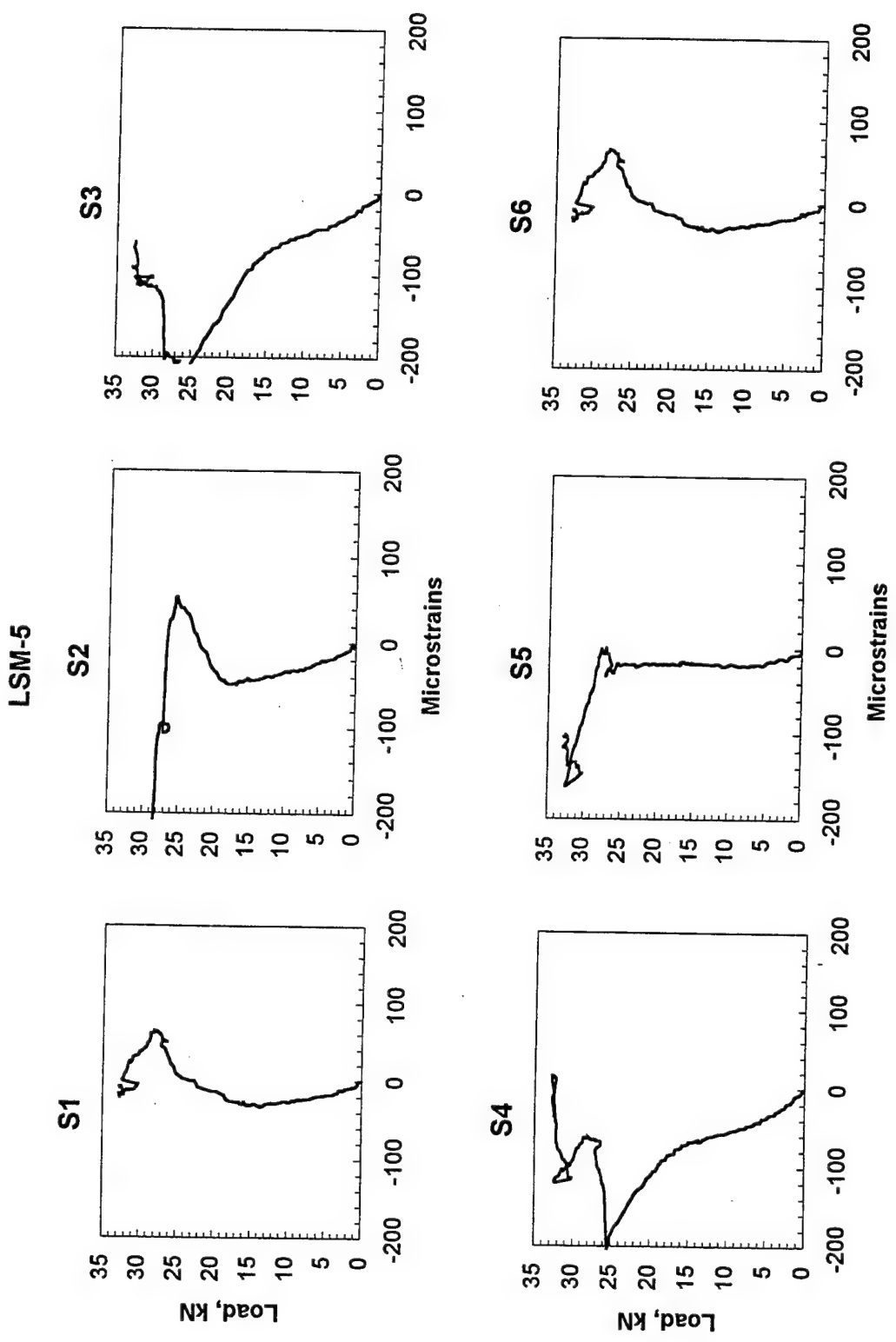


Figure D.22. Gages S1 through S6, Experiment LSM-5

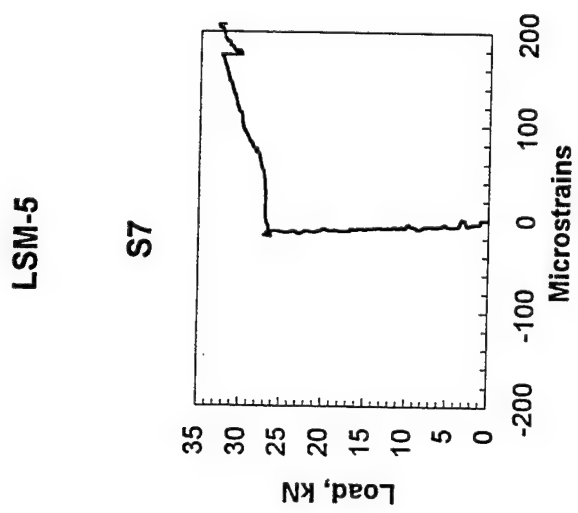


Figure D.23. Gage S7, Experiment LSM-5

APPENDIX E: SAMPLE ABAQUS INPUT FILE

A sample ABAQUS input file is listed in this appendix along with limited explanatory comments. The purpose of including this sample input file is to assist analysts familiar with ABAQUS in duplicating the results described in this dissertation. An ABAQUS input file consists of three types of input lines:

- Comment lines, which always begin with double asterisks (**)
- Keyword input lines, which always begin with a single asterisk (*)
- Data input lines

The outline of the input file is as follows:

- Model Definition
 - Node Definitions
 - Element Definitions
 - Joint Property Definitions
 - Multi-Point Constraint Definitions
 - Contact Interaction Definitions
- Material Definition
 - Solid Element Property Specifications
 - Foundation Specification
- Boundary Condition Definition
 - Specify Nodal Displacement Constraints
- Solution Step Definition
 - Define Iterative Solution Step
- Output Requests
 - Specify displacement, stress, and strain output

In the sample input file those lines which are common to all cases are printed in normal font. Those lines which are used optionally to define each of the cases described in Chapter 9 are printed in *italic* font. Because the input file is quite lengthy, selected lines have been removed from the sample file for the sake of brevity. These locations are denoted in the comments column.

SAMPLE INPUT FILE**COMMENTS**

```
*HEADING
*Sample input file for Appendix E
*WAVEFRONT MINIMIZATION, NODES, METHOD=3
1,1498
**
```

```
*NODE
1,          0.,
2, 0.0507778, 0.
3, 0.101556, 0.
4, 0.1523333, 0.
5, 0.203111, 0.
6, 0.253889, 0.
7, 0.304667, 0.
8, 0.355444, 0.
9, 0.406222, 0.
10, 0.457, 0.
11, 0.507778, 0.
12, 0.558556, 0.
```

- 7588, 1.21867, 1.219, 0.089
- 7589, 1.26944, 1.219, 0.089
- 7590, 1.32022, 1.219, 0.089
- 7591, 1.371, 1.219, 0.089
- 7592, 1.42178, 1.219, 0.089
- 7593, 1.47256, 1.219, 0.089
- 7594, 1.52333, 1.219, 0.089

(Lines deleted for sake of brevity.)

Used to reduce the solution time in ABAQUS

Continued on Next Page

SAMPLE INPUT FILE	COMMENTS
<pre> 7595, 1.57411, 1.219, 0.089 7596, 1.62489, 1.219, 0.089 7597, 1.67567, 1.219, 0.089 7598, 1.72644, 1.219, 0.089 7599, 1.77722, 1.219, 0.089 7600, 1.828, 1.219, 0.089 ** ** base ** *ELEMENT, TYPE=C3D27R, ELSET=BASE 1, 1, 3, 41, 39, 951, 953, 991, 989, 2, 22, 40, 20, 952, 972, 990, 970, 476, 478, 516, 514, 496, 21, 971, 477, 497, 515, 495 ** 2, 3, 5, 43, 41, 953, 955, 993, 991, 4, 24, 42, 22, 954, 974, 992, 972, 478, 480, 518, 516, 498, 23, 973, 479, 499, 517, 497 ** 3, 5, 7, 45, 43, 955, 957, 995, 993, 6, 26, 44, 24, 956, 976, 994, 974, 480, 482, 520, 518, 500, 25, 975, 481, 501, 519, 499 • • • ** </pre>	<p>C3D27R Element Definitions:</p> <p>Element No., List of nodes defining element</p> <p>(Lines deleted for sake of brevity.)</p>

Continued on Next Page

SAMPLE INPUT FILE**COMMENTS**

```

214, 1856, 1858, 1896, 1894, 2806, 2808, 2846,
2844, 1857, 1877, 1895, 1875, 2807, 2827, 2845,
2825, 2331, 2333, 2371, 2369, 2351, 1876, 2826,
** 2332, 2352, 2370, 2350

215, 1858, 1860, 1898, 1896, 2808, 2810, 2848,
2846, 1859, 1879, 1897, 1877, 2809, 2829, 2847,
2827, 2333, 2335, 2373, 2371, 2353, 1878, 2828,
** 2334, 2354, 2372, 2352

216, 1860, 1862, 1900, 1898, 2810, 2812, 2850,
2848, 1861, 1881, 1899, 1879, 2811, 2831, 2849,
2829, 2335, 2337, 2375, 2373, 2355, 1880, 2830,
** 2336, 2356, 2374, 2354

** slabs
**

*ELEMENT, TYPE=C3D27R, ELSET=SLABS
217, 2851, 2853, 2891, 2889, 3801, 3803, 3841,
3839, 2852, 2872, 2890, 2870, 3802, 3822, 3840,
3820, 3326, 3328, 3366, 3364, 3346, 2871, 3821,
3327, 3347, 3365, 3345
**

218, 2853, 2855, 2893, 2891, 3803, 3805, 3843,
3841, 2854, 2874, 2892, 2872, 3804, 3824, 3842,
3822, 3328, 3330, 3368, 3366, 3348, 2873, 3823,
3329, 3349, 3367, 3347

```

Continued on Next Page

SAMPLE INPUT FILE	COMMENTS
** 219, 2855, 2857,	
3843, 2856, 2876,	2893, 3805, 3807, 3845,
3824, 3330, 3332,	2894, 2874, 3806, 3826, 3844,
3331, 3351, 3369,	3370, 3368, 3350, 2875, 3825,
** 220, 2857, 2859,	2897, 2895, 3807, 3809, 3847,
3845, 2858, 2878,	2896, 2876, 3808, 3828, 3846,
3826, 3332, 3334,	3372, 3370, 3352, 2877, 3827,
3333, 3353, 3371,	3351
• •	
** 646, 6606, 6608,	6646, 6644, 7556, 7558, 7596,
7594, 6607, 6627,	6645, 6625, 7557, 7577, 7595,
7575, 7081, 7083,	7121, 7119, 7101, 6626, 7576,
7082, 7102, 7120,	7100
** 647, 6608, 6610,	6648, 6646, 7558, 7560, 7598,
7596, 6609, 6629,	6647, 6627, 7559, 7579, 7597,
7577, 7083, 7085,	7123, 7121, 7103, 6628, 7578,
7084, 7104, 7122,	7102
** 648, 6610, 6612,	6650, 6648, 7560, 7562, 7600,
7598, 6611, 6631,	6649, 6629, 7561, 7581, 7599,
7579, 7085, 7087,	7125, 7123, 7105, 6630, 7580,
7086, 7106, 7124,	7104

(Lines deleted for sake of brevity.)

Continued on Next Page

SAMPLE INPUT FILE**COMMENTS**

JOINTC Element Definitions:	Element No., List of nodes defining element
*ELEMENT, TYPE=JOINTC, ELSET=CNR	
649, 2869, 5226	
673, 3325, 5682	
749, 4769, 7126	
773, 5225, 7582	
*JOINT, ELSET=CNR	
*SPRING	
3	
0.47	
**	
** edg	
*ELEMENT, TYPE=JOINTC, ELSET=EDG	
650, 2888, 5245	
651, 2907, 5264	
652, 2926, 5283	
653, 2945, 5302	
654, 2964, 5321	
655, 2983, 5340	
•	
•	
768, 5130, 7487	
769, 5149, 7506	
770, 5168, 7525	

(Lines deleted for sake of brevity.)

Continued on Next Page

SAMPLE INPUT FILE**COMMENTS**

```

771, 5187, 7544
772, 5206, 7563
*JOINT, ELSET=EDG
*SPRING
3
0.940
**
** int
**
*ELEMENT, TYPE=JOINTC, ELSET=INT
    675, 3363, 5720
    676, 3382, 5739
    677, 3401, 5758
    678, 3420, 5777
    679, 3439, 5796
    680, 3458, 5815
    •
    •
    742, 4636, 6993
    743, 4655, 7012
    744, 4674, 7031
    745, 4693, 7050
    746, 4712, 7069
    747, 4731, 7088
*JOINT, ELSET=INT
*SPRING
3

```

(Lines deleted for sake of brevity.)

Continued on Next Page

SAMPLE INPUT FILE**COMMENTS**

```

1.880
***** This section is used to define crack in base course with
***** aggregate interlock capabilities
***** This option is used to define crack in base course with
***** aggregate interlock capabilities
****

** base_cmr
**
*ELEMENT, TYPE=JOINTC, ELSET=B_CNR
  774, 19, 1426
  798, 475, 1882
  824, 969, 2376
  848, 1425, 2832
*JOINT, ELSET=B_CNR
*SPRING
  3      0.94
**
** b_edg
**
*ELEMENT, TYPE=JOINTC, ELSET=B_EDG
  775, 38, 1445
  776, 57, 1464
  777, 76, 1483
  778, 95, 1502
  779, 114, 1521
  780, 133, 1540
  .

```

OPTION to define crack in base course
 (JOINTC elements)
THIS OPTION USED FOR CASES III AND V.

Continued on Next Page

SAMPLE INPUT FILE

COMMENTS

(Lines deleted for sake of brevity.)

843,	1330,	2737
844,	1349,	2756
845,	1368,	2775
846,	1387,	2794
847,	1406,	2813

*JOINT, ELSE_T=B_EDG
*SPRING

(Lines deleted for sake of brevity.)

•

843, 1330, 2737
844, 1349, 2756
845, 1368, 2775
846, 1387, 2794
847, 1406, 2813
*JOINT, ELSESET=B_EDG
*SPRING
3
1.88
**
** b int
**
*ELEMENT, TYPE=JOINTC, ELSESET=B_INT
800, 513, 1920
801, 532, 1939
802, 551, 1958
803, 570, 1977
804, 589, 1996
805, 608, 2015

(Lines deleted for sake of brevity.)

Continued on Next Page

SAMPLE INPUT FILE**COMMENTS**

```

820, 893, 2300
821, 912, 2319
822, 931, 2338
*JOINT, ELSET=B INT
*SPRING
3

3.76
***** This section is used to tie nodes across crack in base course
** so that the base course acts as if monolithic
*****  

** MPC_ID=1
**  

*MPC
TIE , 1426, 19
TIE , 1445, 38
TIE , 1464, 57
TIE , 1483, 76
•
•
•
TIE , 2756, 1349
TIE , 2775, 1368
TIE , 2794, 1387
TIE , 2813, 1406
TIE , 2832, 1425
*****
```

**OPTION to "TIE" crack in base course so that
it acts monolithically (MPC)**
THIS OPTION USED FOR CASES II and IV.

(Lines deleted for sake of brevity.)

Continued on Next Page

SAMPLE INPUT FILE**COMMENTS**

```
**
** lh_b
**
*ELSET, ELSET=LH_B
  1,      2,      3,      4,      5,      6,      7,      8,
  9,     10,     11,     12,     13,     14,     15,     16,
 17,     18,     19,     20,     21,     22,     23,     24,
 25,     26,     27,     28,     29,     30,     31,     32,
 33,     34,     35,     36,     37,     38,     39,     40,
 41,     42,     43,     44,     45,     46,     47,     48,
 49,     50,     51,     52,     53,     54,     55,     56,
 57,     58,     59,     60,     61,     62,     63,     64,
 65,     66,     67,     68,     69,     70,     71,     72,
 73,     74,     75,     76,     77,     78,     79,     80,
 81,     82,     83,     84,     85,     86,     87,     88,
 89,     90,     91,     92,     93,     94,     95,     96,
 97,     98,     99,    100,    101,    102,    103,    104,
105,    106,    107,    108
**
** rh_b
**
*ELSET, ELSET=RH_B
 109,    110,    111,    112,    113,    114,    115,    116,
117,    118,    119,    120,    121,    122,    123,    124,
125,    126,    127,    128,    129,    130,    131,    132,
133,    134,    135,    136,    137,    138,    139,    140,
141,    142,    143,    144,    145,    146,    147,    148,
149,    150,    151,    152,    153,    154,    155,    156,
```

Defines an element set needed for FOUNDATION definition

Defines an element set needed for FOUNDATION definition

Continued on Next Page

SAMPLE INPUT FILE	COMMENTS
<pre> 157, 158, 159, 160, 161, 162, 163, 164, 165, 166, 167, 168, 169, 170, 171, 172, 173, 174, 175, 176, 177, 178, 179, 180, 181, 182, 183, 184, 185, 186, 187, 188, 189, 190, 191, 192, 193, 194, 195, 196, 197, 198, 199, 200, 201, 202, 203, 204, 205, 206, 207, 208, 209, 210, 211, 212, 213, 214, 215, 216 ** bot_rhs ** *ELSET,ELSET=BOT_RHS 433, 434, 435, 436, 437, 438, 439, 440, 441, 442, 443, 444, 445, 446, 447, 448, 449, 450, 451, 452, 453, 454, 455, 456, 457, 458, 459, 460, 461, 462, 463, 464, 465, 466, 467, 468, 469, 470, 471, 472, 473, 474, 475, 476, 477, 478, 479, 480, 481, 482, 483, 484, 485, 486, 487, 488, 489, 490, 491, 492, 493, 494, 495, 496, 497, 498, 499, 500, 501, 502, 503, 504, 505, 506, 507, 508, 509, 510, 511, 512, 513, 514, 515, 516, 517, 518, 519, 520, 521, 522, 523, 524, 525, 526, 527, 528, 529, 530, 531, 532, 533, 534, 535, 536, 537, 538, 539, 540 ** ** bot_lhs </pre>	<p>Defines an element set needed for CONTACT PAIR definition</p>

Continued on Next Page

SAMPLE INPUT FILE	COMMENTS
<pre>** *ELSET, ELSET=BOT_LHS 217, 218, 219, 220, 221, 222, 223, 224, 225, 226, 227, 228, 229, 230, 231, 232, 233, 234, 235, 236, 237, 238, 239, 240, 241, 242, 243, 244, 245, 246, 247, 248, 249, 250, 251, 252, 253, 254, 255, 256, 257, 258, 259, 260, 261, 262, 263, 264, 265, 266, 267, 268, 269, 270, 271, 272, 273, 274, 275, 276, 277, 278, 279, 280, 281, 282, 283, 284, 285, 286, 287, 288, 289, 290, 291, 292, 293, 294, 295, 296, 297, 298, 299, 300, 301, 302, 303, 304, 305, 306, 307, 308, 309, 310, 311, 312, 313, 314, 315, 316, 317, 318, 319, 320, 321, 322, 323, 324 *****</pre> <p style="text-align: center;"><i>** Option for defining contact interaction along interface between ** slabs and base coarse</i></p> <pre>***** *SURFACE DEFINITION, NAME=RH_BOT RH_B,S2 *SURFACE DEFINITION, NAME=RH_TOP BOT_RHS,S1 *SURFACE DEFINITION, NAME=LH_BOT LH_B,S2 *SURFACE DEFINITION, NAME=LH_TOP BOT_LHS,S1</pre>	<p>Defines an element set needed for CONTACT PAIR definition</p> <p>OPTION for Contact interaction definition for allowing contact and friction between slabs and base</p> <p>THIS OPTION USED FOR CASES IV and V.</p> <p>Define contact surfaces</p>

Continued on Next Page

SAMPLE INPUT FILE	COMMENTS
<pre>*SURFACE INTERACTION, NAME=FRICT *FRICTION I. *CONTACT PAIR, INTERACTION=FRICT, SMALL SLIDING RH_BOT, RH_TOP *CONTACT PAIR, INTERACTION=FRICT, SMALL SLIDING LH_BOT, LH_TOP ***** ** Option for defining tying nodes along interface between ** slabs and base course ***** *SURFACE DEFINITION, NAME=RH_BOT RH_B,S2 *SURFACE DEFINITION, NAME=RH_TOP BOT RHS,S1 *SURFACE DEFINITION, NAME=LH_BOT LH_B,S2 *SURFACE DEFINITION, NAME=LH_TOP BOT LHS,S1 *SURFACE INTERACTION, NAME=STICK *SURFACE BEHAVIOR, NO SEPARATION *CONTACT PAIR, INTERACTION=STICK, SMALL SLIDING, TIED, ADJUST RH_BOT, RH_TOP *CONTACT PAIR, INTERACTION=STICK, SMALL SLIDING, TIED, ADJUST LH_BOT, LH_TOP</pre>	<p>Define surface interaction Specify coefficient of friction</p> <p>Define contact pairs</p> <p>OPTION for tying nodes across interface between slabs and base</p> <p>THIS OPTION USED FOR CASES II AND III.</p> <p>"TIED" option forces displacements of contact pairs along interface to be equal</p> <p>END MODEL DEFINITION</p>

Continued on Next Page

SAMPLE INPUT FILE	COMMENTS
*****	BEGIN MATERIAL DEFINITION
** base	
** slabs	
**	Specifies element properties for solid elements
*SOLID SECTION, ELSET=BASE, MATERIAL=CSB 1.,	
**	
** slabs	
**	
*SOLID SECTION, ELSET=SLABS, MATERIAL=PCC 1.,	
**	
** pcc	
**	
*MATERIAL, NAME=PCC	PCC slab material properties
**	
*ELASTIC, TYPE=ISO 27600., 0.18	Modulus of elasticity, Poisson's ratio
**	
** csb	
**	
*MATERIAL, NAME=CSB	Base material properties
**	
*ELASTIC, TYPE=ISO 1410., 0.2	Modulus of elasticity, Poisson's ratio
**	
** foundation	
**	

Continued on Next Page

SAMPLE INPUT FILE**COMMENTS**

<pre> *FOUNDATION LH_B, F1, 90. RH_B, F1, 90. ** ** ends ***</pre>	<p>Specify properties of bed of springs foundation</p> <p>Element set, active face of element, modulus of subgrade reaction</p> <p>END MATERIAL DEFINITION</p>
<pre> *BOUNDARY, OP=NEW</pre>	<p>BEGIN BOUNDARY CONDITION</p> <p>DEFINITION</p>
<pre> 1, 1,, 0. 1, 2,, 0. 1, 3,, 0. 20, 1,, 0. 20, 2,, 0. 20, 3,, 0. 39, 1,, 0. 39, 2,, 0. 39, 3,, 0. 58, 1,, 0. 58, 2,, 0. 58, 3,, 0. • • 7524, 1,, 0. 7524, 2,, 0. 7524, 3,, 0. 7543, 1,, 0. 7543, 2,, 0. 7543, 3,, 0.</pre>	<p>Node, degree of freedom, specified displacement</p> <p><i>(Lines deleted for sake of brevity.)</i></p>

Continued on Next Page

SAMPLE INPUT FILE**COMMENTS**

7562, 1,, 0.
7562, 2,, 0.
7562, 3,, 0.
7581, 1,, 0.
7581, 2,, 0.
7581, 3,, 0.
7600, 1,, 0.
7600, 2,, 0.
7600, 3,, 0.

**

** sides

*BOUNDARY, OP=NEW

2, 2,, 0.
3, 2,, 0.
4, 2,, 0.
5, 2,, 0.
6, 2,, 0.
7, 2,, 0.
8, 2,, 0.
9, 2,, 0.
10, 2,, 0.
11, 2,, 0.

•

•

7591, 2,, 0.
7592, 2,, 0.

*(Lines deleted for sake of brevity.)***Continued on Next Page**

SAMPLE INPUT FILE**COMMENTS**

```

7593, 2,,      0.
7594, 2,,      0.
7595, 2,,      0.
7596, 2,,      0.
7597, 2,,      0.
7598, 2,,      0.
7599, 2,,      0.

** Step 1, step_1
** LoadCase, lc1
**
*STEP, AMPLITUDE=RAMP, INC=100
*STATIC
    0.01,      1.
**
** load
**
*DLOAD, OP=NEW
    333, P2,      1.
**
** FILE FORMAT, ASCII
**
*NODE PRINT, FREQ=5
U,
*NODE FILE, FREQ=5
U,
**

```

**END BOUNDARY CONDITION
DEFINITION**

BEGIN SOLUTION STEP DEFINITION

Incremental Solution Step Definition
Static step, minimum load increment, maximum
load increment

Define loads
Element number, active face, pressure

END SOLUTION STEP DEFINITION

BEGIN OUTPUT REQUESTS

Output nodal displacements

Continued on Next Page

SAMPLE INPUT FILE	COMMENTS
*EL FILE, POSITION=INTEGRATION POINT, FREQ=5 S, E, ** *EL PRINT, POSITION=AVERAGED AT NODES, FREQ=5 S E ** *PRINT, FREQ=1 ** *END STEP	Output stresses and strains

REPORT DOCUMENTATION PAGE

*Form Approved
OMB No. 0704-0188*

Public reporting burden for this collection of information is estimated to average 1 hour per response, including the time for reviewing instructions, searching existing data sources, gathering and maintaining the data needed, and completing and reviewing the collection of information. Send comments regarding this burden estimate or any other aspect of this collection of information, including suggestions for reducing this burden, to Washington Headquarters Services, Directorate for Information Operations and Reports, 1215 Jefferson Davis Highway, Suite 1204, Arlington, VA 22202-4302, and to the Office of Management and Budget, Paperwork Reduction Project (0704-0188), Washington, DC 20503.

1. AGENCY USE ONLY (Leave blank)			2. REPORT DATE April 1997		3. REPORT TYPE AND DATES COVERED Final report		
4. TITLE AND SUBTITLE Development of an Analysis System for Discontinuities in Rigid Airfield Pavements			5. FUNDING NUMBERS				
6. AUTHOR(S) Michael I. Hammons							
7. PERFORMING ORGANIZATION NAME(S) AND ADDRESS(ES) U.S. Army Engineer Waterways Experiment Station 3909 Halls Ferry Road Vicksburg, MS 39180-6199			8. PERFORMING ORGANIZATION REPORT NUMBER Technical Report GL-97-3				
9. SPONSORING/MONITORING AGENCY NAME(S) AND ADDRESS(ES) U.S. Department of Transportation, Federal Aviation Administration, DOT/FAA Technical Center, Atlantic City International Airport, NJ 08405			10. SPONSORING/MONITORING AGENCY REPORT NUMBER				
11. SUPPLEMENTARY NOTES Available from National Technical Information Service, 5285 Port Royal Road, Springfield, VA 22161.							
12a. DISTRIBUTION/AVAILABILITY STATEMENT Approved for public release; distribution is unlimited.			12b. DISTRIBUTION CODE				
13. ABSTRACT (Maximum 200 words) The response of the rigid pavement slab-joint-base structural system is complex, and accurately predicting the response of such a system requires a significant degree of analytical sophistication. The research reported in this dissertation has defined some essential features required to adequately model the system and has demonstrated a technique to develop a comprehensive three-dimensional (3D) finite element model of the rigid pavement slab-joint-foundation structural system. Analysis of experimental data from the 1950's confirms that explicit modeling of dowels is not required to model the structural response of the system. Additional experimental data gathered as a part of this research indicates that joint response depends upon the presence and condition of a stabilized base. The presence of cracking in the base and the degree of bonding between the slabs and stabilized base course influences the structural capacity and load transfer capability of the rigid pavement structure. The finite element models developed in this research indicate that a comprehensive 3D finite element modeling technique provides a rational approach to modeling the structural response of the jointed rigid airport pavement system. Modeling features which are required include explicit 3D modeling of the slab continua, load transfer capability at the joint (modeled by springs between the slabs), explicit 3D modeling of the base course continua, aggregate interlock capability across the cracks in the base course (again, modeled by springs across the crack), and contact interaction							
14. SUBJECT TERMS Airfield pavements Contact interaction Dowels Finite element method			 Joints Load transfer Rigid pavements Stabilized bases		15. NUMBER OF PAGES 332		
					16. PRICE CODE		
17. SECURITY CLASSIFICATION OF REPORT UNCLASSIFIED		18. SECURITY CLASSIFICATION OF THIS PAGE UNCLASSIFIED		19. SECURITY CLASSIFICATION OF ABSTRACT		20. LIMITATION OF ABSTRACT	

13. (Concluded).

between the slabs and base course. The contact interaction model feature should allow gaps to open between the slab and base, and, where the slabs and base are in contact, transfer of shear stresses across the interface via friction should be modeled.

Destroy this report when no longer needed. Do not return it to the originator.